

Radiofrequency AC Zeeman Trapping for Neutral Atoms

Andrew P. Rotunno

Liverpool, NY

Master of Science, William & Mary, 2016  
Bachelor of Science, Fordham University, 2014

A Dissertation presented to the Graduate Faculty  
of The College of William & Mary in Candidacy for the Degree of  
Doctor of Philosophy

Department of Physics

College of William & Mary  
August 2021

© Copyright by Andrew P. Rotunno 2021

## APPROVAL PAGE

This Dissertation is submitted in partial fulfillment of  
the requirements for the degree of

Doctor of Philosophy



Andrew P. Rotunno

Approved by the Committee June 2021



Committee Chair  
Seth Aubin, Associate Professor, Physics  
College of William & Mary



Eugeniy Mikhailov, Associate Professor, Physics  
College of William & Mary



Keith Griffioen, Professor, Physics  
College of William & Mary



Todd Averett, Professor, Physics  
College of William & Mary



Nathan Lundblad, Associate Professor, Physics  
Bates College

## ABSTRACT

This thesis presents the first experimental demonstration of a two-wire AC Zeeman trap on an atom chip. Our novel trap is generated by a local minimum in AC Zeeman energy, which is a resonant, bipolar, state-dependent atomic energy shift produced by rotating magnetic fields with frequencies near hyperfine transitions. Using less than one watt of power, we demonstrate trap frequency on the order of a few hundred Hz, trap depth about  $5 \mu\text{K}$ , and quarter-second lifetimes. We also demonstrate that high gradients in this energy, as near an atom chip, can produce a spin-state selective force greater than gravity for ultracold rubidium atoms. Motivated by trapped atom interferometry, this proof of principle AC Zeeman trap can also augment atom and ion experiments as a dynamic spin-dependent potential. Different parameters in the current arrangement can produce regions of linear gradient, flat saddle points, square- and donut-shaped traps, offering a new set of tools for atom chip experiments. This thesis also presents the relevant dressed atomic theory, four AC Zeeman trap designs, Rabi frequency measurements, numerical trap simulations, and the AC skin effect in wide rectangular wires.

## TABLE OF CONTENTS

Acknowledgments . . . . .	vii
Dedication . . . . .	viii
List of Tables . . . . .	ix
List of Figures . . . . .	x
CHAPTER	
1 Introduction . . . . .	1
1.1 Foundation . . . . .	1
1.2 AC Zeeman Overview . . . . .	2
1.3 Toward Atom Interferometry . . . . .	5
1.4 Other Applications . . . . .	9
1.5 Layout . . . . .	10
1.6 Supplements . . . . .	10
2 The Apparatus . . . . .	12
2.1 General Description . . . . .	14
2.2 A Typical Cycle . . . . .	14
2.2.1 Magneto-Optical Trap (MOT) . . . . .	14
2.2.2 Optical Molasses and Pumping . . . . .	16
2.2.3 Magnetic Transport . . . . .	17
2.2.4 Atom Chip . . . . .	17
2.2.5 Radiofrequency Evaporation . . . . .	17
2.2.6 Experiment . . . . .	19
2.2.7 DC Stern-Gerlach Separation . . . . .	19

2.2.8	Imaging . . . . .	21
2.3	Optical Dipole Trap . . . . .	22
2.4	Thermal Stabilization Strategies . . . . .	23
2.5	Cinderella and Other RF Sweeping Sources . . . . .	27
2.6	FlexDDS . . . . .	32
2.7	Fluffy, the Three-headed Amplifier . . . . .	33
2.8	Evaporation Trace Switch . . . . .	34
2.9	Chip VNA Measurements . . . . .	37
2.10	Summary . . . . .	38
3	Dressed Atom Theory . . . . .	40
3.1	Hyperfine Basis . . . . .	41
3.2	Transition Elements . . . . .	43
3.3	Two-Level Theory . . . . .	48
3.4	AC Zeeman Force . . . . .	56
3.5	Five-level Eigenstate Curves . . . . .	57
3.6	Summary . . . . .	60
4	Rabi Frequency Measurement . . . . .	61
4.1	Introduction . . . . .	62
4.2	Rabi Measurement with the Force Experiment . . . . .	64
4.2.1	Flopping Experiment . . . . .	65
4.2.2	Fitting . . . . .	68
4.2.3	Scaling . . . . .	71
4.2.4	Rabi Gradient . . . . .	72
4.2.5	“Sag” . . . . .	74
4.3	Rabi Measurement with the Trap Experiment . . . . .	75
4.3.1	Push Triangulation . . . . .	76

4.4	Compiled Measurements . . . . .	78
4.5	Summary . . . . .	79
5	RF AC Zeeman Force . . . . .	80
5.1	Theory . . . . .	81
5.2	Experiment . . . . .	85
5.3	AC Stern-Gerlach . . . . .	91
5.4	Time Evolution of States . . . . .	92
5.4.1	Detuning Effects . . . . .	96
5.4.2	Power Effects . . . . .	99
5.4.3	Beyond Landau-Zener . . . . .	99
5.4.4	Outlook for Trapping . . . . .	100
5.5	Rabi and Rabi Gradient . . . . .	100
5.5.1	Background $B_{DC}$ Gradient . . . . .	102
5.6	Conclusion . . . . .	103
6	Trap Theory . . . . .	104
6.1	Pedagogical Explanation . . . . .	105
6.2	AC Zeeman Trap Simulation . . . . .	106
6.2.1	Finding Linear Gradients . . . . .	111
6.3	Effect of Detuning . . . . .	111
6.4	Trap Location Theory . . . . .	114
6.4.1	Two-wire Trap . . . . .	115
6.4.2	Two-Microstrip Trap . . . . .	118
6.4.3	Three-Wire Trap . . . . .	119
6.4.4	Three-Microstrip Trap . . . . .	121
6.5	Middle-field Seekers . . . . .	123
6.6	Pyramidal Trap . . . . .	127

6.7	Trap Schemes Using the Existing Atom Chip . . . . .	128
6.7.1	Three-Wire Scheme . . . . .	130
6.7.2	Radiofrequency vs. Microwave Comparison . . . . .	131
6.7.3	AC Skin Effects in Modeling . . . . .	133
6.7.4	Two Wire Trap: U-U / U-Z comparison . . . . .	134
6.7.5	Decision . . . . .	136
6.8	Summary . . . . .	138
7	RF AC Zeeman Trap Demonstration . . . . .	140
7.1	Introduction . . . . .	141
7.2	Theory . . . . .	143
7.2.1	AC Zeeman Energy . . . . .	145
7.2.2	RF Magnetic Near Field . . . . .	146
7.2.3	Trap Simulation . . . . .	148
7.3	Experiment . . . . .	150
7.3.1	Low-Power Field Mapping . . . . .	153
7.3.2	Dipole and Ioffe End-capping . . . . .	156
7.3.3	Throw from F=2 and Catch in F=1 . . . . .	156
7.4	Results . . . . .	157
7.4.1	Trap Frequencies . . . . .	159
7.4.2	Trap Lifetimes . . . . .	161
7.4.3	Methods of Evaporation . . . . .	165
7.5	Trap Position Control . . . . .	169
7.6	Lower Resonance Data . . . . .	170
7.7	Extra Phase Effects . . . . .	170
7.8	Conclusion . . . . .	172

8	AC Skin Effect . . . . .	174
8.1	Abstract . . . . .	177
8.2	Introduction . . . . .	177
8.3	Theory . . . . .	181
8.3.1	Pedagogical Explanation . . . . .	184
8.3.2	Simulations . . . . .	185
8.4	Experimental Method . . . . .	186
8.4.1	Pickup coil . . . . .	189
8.4.2	Measurement Theory . . . . .	189
8.4.3	Calibration . . . . .	190
8.5	Results . . . . .	192
8.6	Conclusion . . . . .	196
8.7	AC Skin Appendix . . . . .	198
8.7.1	Analytic Forms . . . . .	198
8.7.2	The Counterflow Effect . . . . .	200
8.7.3	Calibration . . . . .	202
9	Outlook . . . . .	204
9.1	The Proposed Interferometer . . . . .	206
9.2	Chip Design . . . . .	207
9.3	Questions . . . . .	207
APPENDIX A		
	Five-level Hamiltonian Derivation . . . . .	210
APPENDIX B		
	Microwave Lattice . . . . .	217
APPENDIX C		
	Rabi Maps . . . . .	219
BIBLIOGRAPHY		230

VITA . . . . .	242
----------------	-----

## ACKNOWLEDGMENTS

This work could not have been possible without a village of support.

Many thanks to:

My parents for giving my the freedom to pursue this career path.

The wonderful faculty and staff of the W&M physics department for their continued support and accommodation of all their students.

Seth Aubin for advising me with this project and supplying the lab with pounds of dark chocolate and tea over the years.

Previous graduate students in this lab (AJ, Charlie, Austin, Megan, Jim), who created a stable apparatus for future students to experiment with.

Shuangli Du for years of stimulating conversations and technical support.

Joe Karpie for helping find a solution to the DDS slope problem

Dave Lahneman for helping measure resistivity in the AC skin conductor.

Josh Erlich and Wouter Deconinck for creating the Small Hall Makerspace.

Funding for this project at various times came from W&M, AFOSR, DTRA, NSF, and VMEC.

Dennis Manos for securing funds for a replacement laser when we needed it.

For Sarah and the boys

## LIST OF TABLES

2.1	Timing sequence of a typical experimental cycle. . . . .	15
4.1	Rabi Frequency measurements for the ACZ force experiment . . . . .	78
4.2	Rabi Frequency measurements for the ACZ trap experiment . . . . .	78
8.1	Measured ‘Skin Width’ values, theory vs. experiment . . . . .	194

## LIST OF FIGURES

1.1	A cartoon and photo of the experiment, looking up at the atom chip.	3
1.2	Cartoon diagrams of atom interferometry.	7
2.1	Images of the Apparatus	13
2.2	Hyperfine levels and optical transitions in rubidium-87	16
2.3	A 3-D cartoon of the atom chip and dipole trap.	18
2.4	Simulated DC chip trap	20
2.5	Images of the Apparatus	24
2.6	Dipole trap wander with temperature	26
2.7	Analysis of multiplied DDS signal	29
2.8	Cinderella's Webpage	30
2.9	Cinderella's output spectrum	31
2.10	FlexDDS graphical user interface	33
2.11	Photo and schematic of Fluffy, the RF system	35
2.12	Schematic diagram and image of atom chip traces	36
2.13	VNA measurement of relevant chip wires at high frequencies	37
2.14	VNA measurement of relevant chip wires at low frequency	38
3.1	DC Zeeman energy for ground hyperfine states	43
3.2	Two-Level AC Zeeman energy and population	54
3.3	Bloch sphere	55
3.4	Five- and three-level AC Zeeman states	59
4.1	Atom data fit for a Rabi frequency measurement	67
4.2	Example of Rabi flopping with fits from the force experiment	69
4.3	Chi-squared values for Rabi frequency fits	70
4.4	Rabi gradient measurements	73
4.5	All Rabi flop measurements with fits from the trap experiment	76
4.6	Triangulation of AC Zeeman trap	77
5.1	Illustration of intra-manifold hyperfine transitions	82

5.2	AC Zeeman energy curves . . . . .	84
5.3	A cartoon schematic of the ACZ force experiment . . . . .	85
5.4	High $B_{DC}$ AC Zeeman energy calculations . . . . .	86
5.5	Timing diagram for the main push/pull experiment . . . . .	87
5.6	AC Zeeman force data and theory, from negative detuning . . . . .	88
5.7	AC Zeeman force data and theory, from positive detuning . . . . .	89
5.8	AC Stern-Gerlach demonstration . . . . .	93
5.9	Timing diagram for the AC Stern-Gerlach . . . . .	93
5.10	Sample data of state mixing . . . . .	95
5.11	Timing diagram for the state mixing experiment . . . . .	95
5.12	Detuning dependence of $T_{cross}$ . . . . .	97
5.13	State mixing over power . . . . .	98
5.14	Sample Rabi flopping . . . . .	101
5.15	Rabi gradient measurement . . . . .	102
6.1	Pedagogical trap illustration . . . . .	105
6.2	AC Zeeman trapping potential surfaces . . . . .	107
6.3	AC Zeeman two-trace trap simulations, from MATLAB GUI . . . . .	108
6.4	AC Zeeman three-trace trap simulations, from MATLAB GUI . . . . .	109
6.5	Vertical trap profile, showing linear gradient . . . . .	112
6.6	Illustration of detuning's effect on trap profile . . . . .	113
6.7	Diagram of the multi-wire trap geometries considered . . . . .	114
6.8	Trap location for two-wire and two-microstrip cases . . . . .	117
6.9	Plot of trap height vs. phase in two-wire and two-microstrip cases . . . . .	119
6.10	Trap location for three-wire and three-microstrip cases . . . . .	122
6.11	Simulations of the middle-field seeker AC Zeeman trap . . . . .	124
6.12	Calculations of AC Zeeman energy ‘medium-field seeking’ of the $ +\rangle$ state . . . . .	125
6.13	Simulations of the pyramid trap . . . . .	126
6.14	Estimate of current from applied RF power . . . . .	129
6.15	Comparison of RF and $\mu$ w for trapping in the three-wire scheme . . . . .	131
6.16	Comparison of AC Skin approximations . . . . .	132
6.17	Comparison of the U-U and U-Z trap depth vs. detuning . . . . .	135
6.18	Comparison of trap depth vs. distance to chip . . . . .	137
7.1	Evidence of opposite- $m_F$ trapping, via oscillation data . . . . .	142
7.2	DC and AC Zeeman atomic states and energies . . . . .	144

7.3	Pedagogical trap explanation and sample AC Zeeman trapping potentials . . . . .	149
7.4	Cartoon schematic diagram of the experiment, and timing diagram .	151
7.5	Rabi maps across a cycle of phase . . . . .	153
7.6	Rabi maps of $F_+ = 2$ and $F_- = 1$ , for two phases . . . . .	155
7.7	Evidence of opposite- $m_F$ trapping, via oscillation data . . . . .	160
7.8	Measurements of trap frequency vs. applied RF frequency . . . . .	162
7.9	Measurements of trap lifetime vs. applied RF frequency . . . . .	163
7.10	Three demonstrations of forced evaporation in an AC Zeeman trap .	166
7.11	Phase-space density of evaporation examples. . . . .	168
7.12	Demonstration of trap position control with current ratio and phase difference . . . . .	169
7.13	Trap frequency and lifetime data at a lower resonance . . . . .	171
8.1	Cover image from AJP, featuring our work . . . . .	175
8.2	3D model, and comparison of simulation methods . . . . .	178
8.3	Pedagogical explanation of the AC skin effect . . . . .	183
8.4	Schematic and photos of the experimental setup . . . . .	187
8.5	Theory comparison of magnetic field and current density . . . . .	191
8.6	Magnetic field data comparison at low and high frequency . . . . .	193
8.7	Lateral AC skin data at all measured frequencies . . . . .	195
8.8	Phase measurements vs. position at 5 kHz . . . . .	197
8.9	Sequential values of the coefficients $C_n$ . . . . .	199
8.10	Phase distributions for all frequencies . . . . .	201
B.1	Microwave lattice demonstration . . . . .	218
C.1	Rabi map explanation . . . . .	221
C.2	Rabi map initial population . . . . .	222
C.3	Rabi map for 2 $\mu$ s . . . . .	222
C.4	Rabi map for 4 $\mu$ s . . . . .	223
C.5	Rabi map for 6 $\mu$ s . . . . .	223
C.6	Rabi map for 8 $\mu$ s . . . . .	224
C.7	Rabi map for 10 $\mu$ s . . . . .	224
C.8	Rabi map for 12 $\mu$ s . . . . .	225
C.9	Rabi map for 14 $\mu$ s . . . . .	225
C.10	Rabi map for 16 $\mu$ s . . . . .	226

C.11 Rabi map for 18 $\mu$ s . . . . .	226
C.12 Rabi map for 20 $\mu$ s . . . . .	227
C.13 Rabi map for 22 $\mu$ s . . . . .	227
C.14 Rabi map for 24 $\mu$ s . . . . .	228
C.15 Rabi map for 26 $\mu$ s . . . . .	228
C.16 Rabi map for 28 $\mu$ s . . . . .	229
C.17 Rabi map for 30 $\mu$ s . . . . .	229

# CHAPTER 1

## Introduction

This work presents the first demonstration of an AC Zeeman trap on an atom chip. In the subsequent chapters, we examine the theory, simulations, and many empirical findings surrounding this novel trap. In this chapter, I discuss the various qualitative features of the AC Zeeman effect, situating this discovery within modern atomic research, and indicating its usefulness for experiments enabled or fundamentally transformed by the addition of this AC Zeeman tool.

### 1.1 Foundation

Many modern experiments utilize atoms and ions as standard, sensitive instruments capable of remarkable precision, measuring fundamental constants [1, 2, 3, 4, 5], gravity [6, 7, 8, 9, 10, 11, 12, 13], rotation [14, 15, 16], and acceleration [17] via atom interferometry, or acting as quantum information bits [18, 19, 20, 21, 22]. A typical modern platform uses a dilute gas of alkali atoms at ultracold temperatures inside a vacuum chamber [23, 24, 25, 26, 27], where propagating lasers along with direct currents (DC) and alternating current (AC) generating magnetic fields exert control on the atoms from an external ‘shirtsleeve’ environment. Atom tempera-

tures are roughly  $1 \mu\text{K}$  above absolute zero (or lower), and atoms can be brought to Bose-Einstein Condensation (BEC) [28, 29, 30, 31] for interesting matter-wave or atom laser experiments. Our apparatus contains an ‘atom chip’ as the primary test platform [32, 33, 34, 35, 36], which is very simply a handful of parallel current-carrying conductors  $50 \mu\text{m}$  wide on an insulating substrate, affixed to the top of the vacuum chamber, facing down. A cartoon schematic of our setup is in Fig. 1.1. An atom chip’s primary role is generating steep gradients of magnetic field near the chip using controlled AC and DC currents. Close spacing of multiple chip wires allows field control with precision on the  $1 - 10 \mu\text{m}$  scale, roughly the size of chip features and smaller. In general, one should minimize the Size, Weight and Power (SWaP) of an apparatus, and the atom chip’s small size is a great benefit.

A typical atom chip micro-magnetic trap uses a local minimum of DC Zeeman energy to trap atoms in weak-field-seeking ground hyperfine electronic states. The magnetic near field from a single DC chip current is negated by an oppositely-oriented field between a pair of nearly Helmholtz electromagnetic coils. This DC field zero occurs in one location, and a restoring force from the DC Zeeman energy potential around this area can contain atoms in a magnetic ‘bottle,’ if it’s stronger than gravity [37]. By controlling current in the chip trace and coil pairs along three axes, we can shift the position, depth, or curvature of this chip-based DC Zeeman trap, and this is a standard modern technique.

## 1.2 AC Zeeman Overview

The AC Zeeman effect [38, 39, 40, 41, 42, 43, 44] is an atom-photon effect using the oscillating magnetic field near chip wires carrying radiofrequency (RF) and microwave ( $\mu\text{w}$ ) currents, with frequencies near-resonant to hyperfine atomic transitions. Atoms in select spin states have their energy shifted by the applied

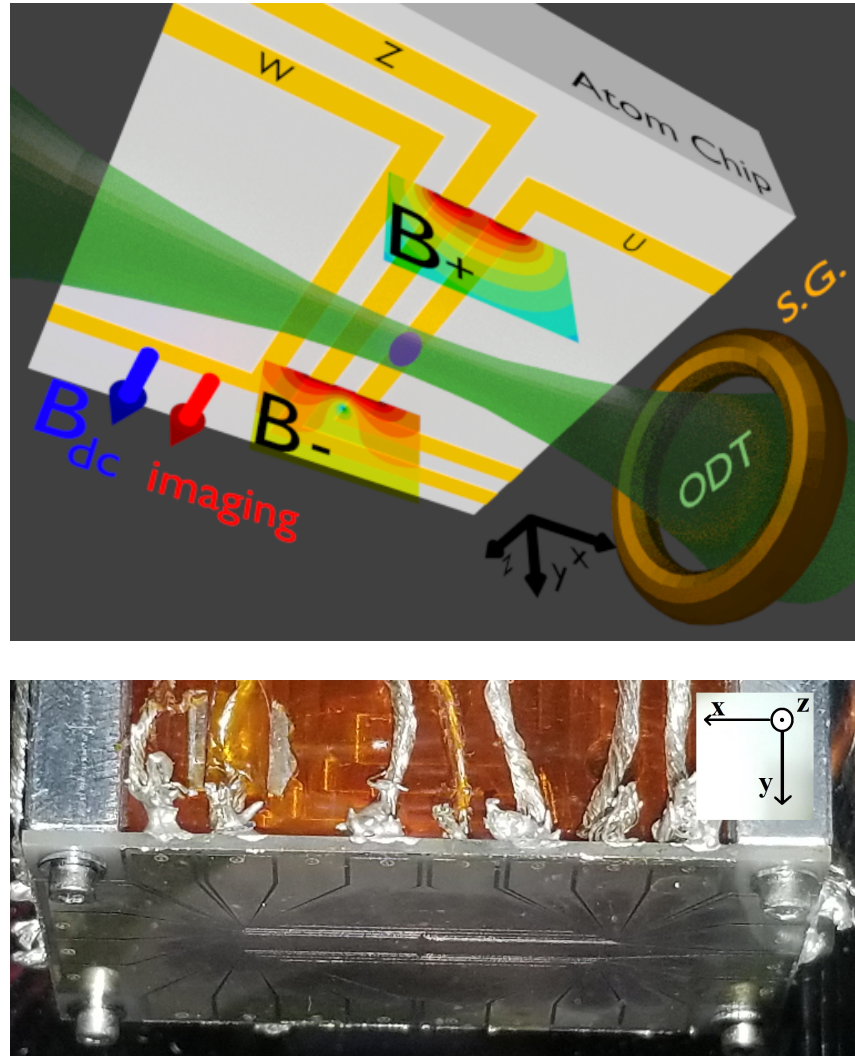


FIG. 1.1: Atom chip and basic experimental layout. Top: A cartoon of the experiment, looking up at the atom chip. Fields produced by alternating currents in chip wires generate non-uniform circular polarization components  $B_+$  and  $B_-$  fields simultaneously, trapping low-field seeking AC Zeeman states. Other experimental features are described in detail later. Middle: An image of the atom chip, viewed from the opposite direction as the cartoon. Bottom: Diagram of chip, illustrating connected traces by color.

alternating magnetic field polarization, power, and frequency. Utilizing the high  $\frac{1}{r}$  magnetic gradients when atoms are a short distance  $r$  from chip wires, we can exert a significant *spin-specific* force on atoms, and can trap targeted spin states, as demonstrated in this thesis.

Summarizing some key AC Zeeman characteristics at a glance:

- **Spin-specific:** We can target spin states with  $\mu w$  or whole hyperfine manifolds with RF, depending on polarization ( $\sigma^+, \sigma^-, \pi$ ) and resonance of the applied frequency.
- **Bipolar:** In the two-level system, we can generate high- *or* low-field-seeking states from the same atomic states.
- **Resonant:** AC Zeeman energy has its maximum on resonance and decreases with higher detuning  $\delta$ , allowing us to tune trap behavior with applied frequency.
- **Any spin state** can be targeted and trapped in the microwave case, and any  $m_F \neq 0$  in the RF case. This feature could allow experiments and Bose-Einstein condensation (BEC) in typically un-trappable states.
- **Any background DC field** can be used, as it only adjusts the atomic resonance frequency. This flexibility is particularly useful for Feshbach resonance measurements and using magnetic noise insensitive “magic”  $B_{DC}$  values.
- **Simultaneous spin-specific traps:** In some trapping schemes, multiple useful traps are generated simultaneously, using different near-field polarizations. Additionally, multiple frequencies can generate independent traps using the same wires that target different spin states. Either of these methods can be a basis for a spin-dependent matter wave interferometer.

- **Phase as a trapping parameter:** Using two (or more) AC signals at the same frequency introduces their differential phase as a tunable, useful parameter, controlling trap position.
- **No spontaneous emission:** Because the hyperfine splittings are small compared to optical transitions, the spontaneous decay rate ( $\Gamma \propto \omega^3$ ) renders states nearly immune to spontaneous emissions, and transitions receive narrow linewidths as a result.
- **Insensitive to surface roughness:** The polarization selection helps atoms ignore imperfections in current flow, lowering roughness effects by over an order of magnitude, per our simulations [45].
- **Small Features:** Even though RF wavelengths are tens of meters, we observe  $\mu\text{m}$ -level features on the scale of the atom chip's wire width and spacing.

Many experiments *already* employ RF in atom chip traces as an evaporation ‘knife,’ enabling AC Zeeman force on current machines for a ‘software’ change. Indeed, ion traps have already demonstrated single wire AC Zeeman as a spin-dependent force to probe individual ions. With some ‘hardware’ phase control on multiple lines, we can trap atoms with the AC Zeeman energy, offering a transformative technology for a rather modest addition.

### 1.3 Toward Atom Interferometry

One motivation for spin-dependent trapping is the prospect for its use in matter-wave or atom interferometry (AI) [46, 34, 47, 48, 49, 50]. In general terms, an atom interferometer measures very precisely the energy differences between two states in a superposition. These two states represent the ‘arms’ of an interferometer,

which can be spatially separated to measure a local gradient in energy, and become atomic ‘clocks’ without this separating step. Conceptually, the method is similar to a Michelson interferometer for light. Here, quantum spin operations replace the beamsplitter and mirrors, but we have a single populated input arm ( $|\uparrow\rangle$ ) and the output exhibits fringes as the relative arm ‘length’ changes. An atom interferometer is ‘read out’ by examining the ratio of atom populations in each arm state, a value that oscillates as a function of the accumulated phase difference in the arms:

$$\phi_{\uparrow} - \phi_{\downarrow} = (\omega_{\uparrow} - \omega_{\downarrow})\Delta t = (E_{\uparrow} - E_{\downarrow})\Delta t/\hbar = \Delta E \Delta t / \hbar$$

depending on population numbers  $N_{\uparrow}, N_{\downarrow}$ , using arbitrary spin up  $|\uparrow\rangle$  and spin down  $|\downarrow\rangle$  states in this toy model. A proper calculation includes the integration of energy difference over time, and must account for many small additional energy shifts than the one targeted. One benefit of using trapped atoms for interferometry is the ability to take a single measurement for an integration time  $\Delta t$  approaching the trap lifetime, rather than obeying ballistic or spontaneous emission time constraints.

We show a cartoon of three atom interferometer schemes in Fig. 1.2. In one scheme, a spin-agnostic trap maintains the primary trapping of atoms, and a spin-dependent force shifts one state in position. In the second scheme, a fully spin-dependent trap holds each of the arms, moving independently of each other. In the third, we add a longitudinal lattice formed by counter-inserted microwaves, which can shift atoms axially, allowing them to enclose an area to form a Sagnac interferometer.

This spin-dependent trapping scheme allows for better measurements, as the first spin-shifting method necessarily energy-shifts the two states and prevents inertial measurements. In fact, we must be very careful to maintain trapping frequencies in each arm, or else use noise cancellation methods like spin-echo, ‘mirroring’ the

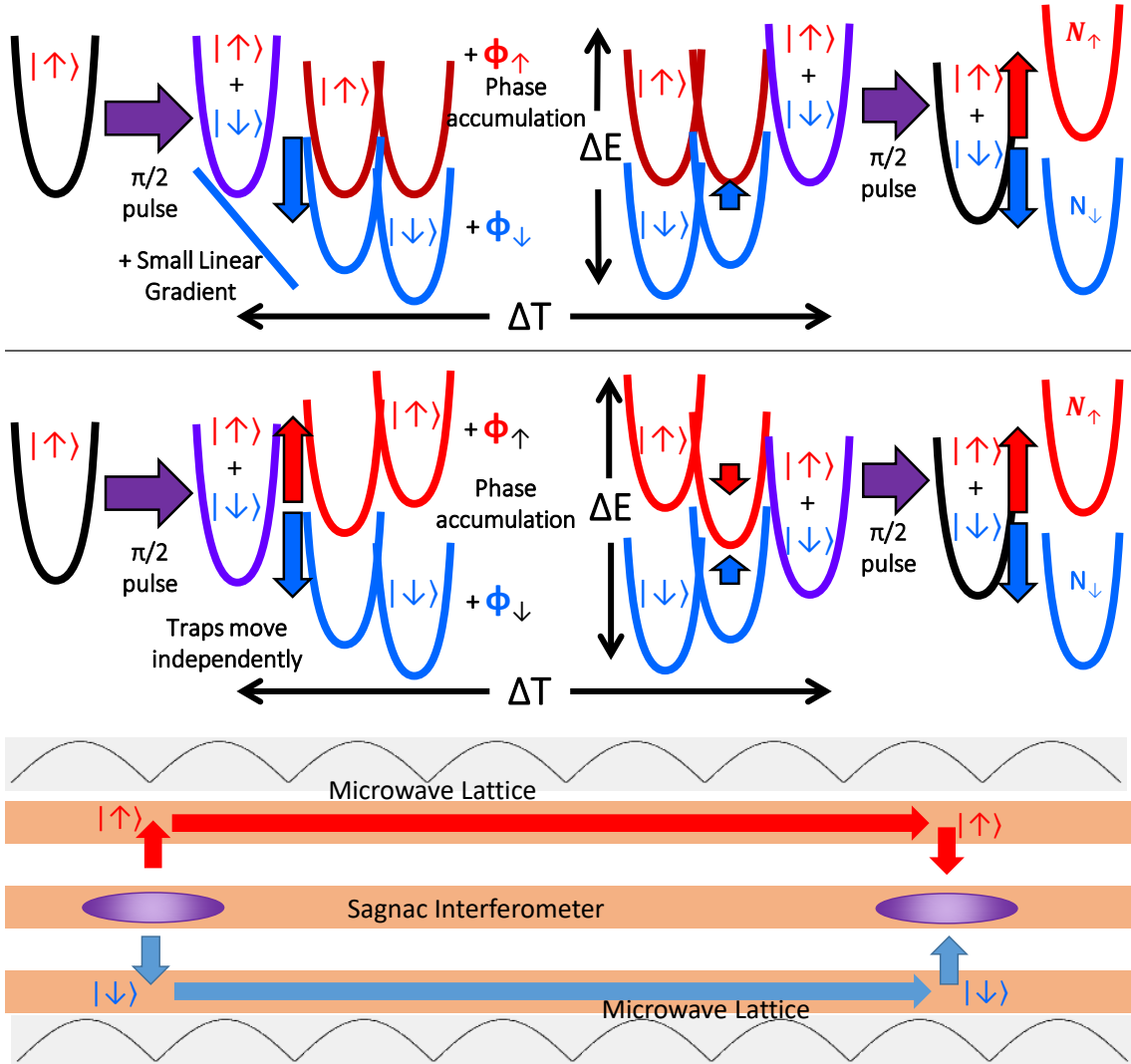


FIG. 1.2: Cartoon diagrams of atom interferometry for a single shifted state (top), a fully spin-trapping scheme (middle), and a Sagnac arrangement (bottom). Atoms are made into a two-state superposition by a  $\pi/2$  pulse. Each spin state arm then accumulates phase ( $\phi_\uparrow$  and  $\phi_\downarrow$ ) due to  $E/\hbar$  over a time  $t$ . Another  $\pi/2$  pulse recombines atoms, before spin-separating the populations in each state for read-out. In the Sagnac case, the longitudinal microwave lattice helps enclose an area for measurement.

states with a  $\pi$ -pulse, or other methods [51, 52, 53]. In addition, background energy noise is troublesome, so one can operate at ‘magic’ magnetic-insensitive frequencies, spin-squeeze the sample, or attempt other methods for noise reduction in the quantum system [54, 55]. While low temperatures typically benefit signal contrast, we elect to study thermal atoms, simulating a degenerate Fermion gas [56, 57]. While interpretation is easier for a single wave in a Bose-Einstein condensate (BEC), a thermal cloud acts as a ‘white-light’ or multi-mode interferometer, where each thermal energy level receives a ‘single-atom’ effect and participates in the full population readout at the end.

Some geometries of AC Zeeman traps (to be described in detail later) create co-located traps for different spin states, which themselves move oppositely from each other as the phase of the generating currents are adjusted. This geometry is a strong candidate for a transformative type of atom interferometer using a single frequency, although using multiple frequencies can also produce overlapping independent spin traps. Atoms generated so near to the surface of the atom chip are begging to measure near-surface gradients such as the Casimir-Polder force, probing gravity, or black body radiation using trapped atoms with test bodies  $< 1$  mm away behind the atom chip. One can imagine extra separation of interferometer arms by ‘passing’ an AC Zeeman trap across successive parallel wires, using a standing wave to move along the wires, and even combining the two techniques to enclose an area, creating a Sagnac interferometer. The whole arrangement can flip so that gravity points toward the chip, sideways, or in micro-gravity, where each case would increase trap depth for the same inserted power [58].

## 1.4 Other Applications

When generating a local minimum in AC Zeeman potential that we call a ‘trap,’ we simultaneously find a saddle point region that is broadly flat below the trap and a linear region as the point of inflection between these two curvatures. One can imagine utilizing the saddle-point to give atoms a microwave  $\pi/2$  pulse that is consistent over the size of the atom cloud, as opposed to a single-wire pulse imprinting its vertical power gradient over the cloud. One can apply a known linear gradient over an otherwise trapped cloud to shift the position or evaporate only one spin state of a trapped mixture.

In addition to slotting into other experiments as a spin-specific potential and using multiple traps simultaneously for atom interferometry, an AC Zeeman trap on its own can enable exciting physics. For one example, the AC Zeeman trap demonstrated is an elongated cigar shape, which forms a pseudo-1D potential for many-body systems. This trap’s profile can be adjusted from a linear cusp to a smooth harmonic bottom by varying RF frequency. Additionally, we have seen in simulations some more exotic trap shapes like a donut-shaped bottom (like the well of a ‘sombrero’) and a square-pyramidal linear trap bottom, given a diagonal quantizing field.

The method of generating polarization minima with phase control in multiple wires can be applied broadly on atom chips, Paul traps, atomic beam steering, perhaps macroscopic magnetic dipole control, and other applications where the polarization of field and resonance play an essential role. Even as spin-specific AC Zeeman forces today are applied to trapped ions, I believe the demonstration of an AC Zeeman trap for a small investment can have a transformative effect as a spin-targeting tool in many other experiments.

## 1.5 Layout

We begin with discussing the apparatus as our foundation in Chap. 2, then a recap of the relevant quantum mechanics and dressed atom theory in Chap. 3. In Chap. 4, we discuss the fitting of Rabi frequencies and gradients, crucial measurements in the later chapters, but not interesting enough to discuss in detail there. Then in Chap. 5, we present RF AC Zeeman force measurements, which might have been the center of this thesis if trapping was not successful. Chapter 6 contains trap pedagogy, simulations and analyzes the arbitrary position of AC Zeeman traps for two- and three-microstrip geometries in a toy model. The heart of this thesis is Chap. 7, where we demonstrate AC Zeeman trapping on an atom chip, giving empirical data and describing a few demonstrations (evaporation and a ‘throw and catch’ technique) with AC Zeeman traps. We follow with a study of the AC skin effect in lateral wires in Chap. 8 and give a summation and outlook on the future of this project in Chap. 9. The appendices include some explicit five-level dressed state math in Appx. A, a brief demonstration of a microwave lattice in Appx. B, and Rabi maps in Appx. C.

Parts of this dissertation resemble manuscripts either intended for publication as (Chaps. 5 and 7), or actually published (Chap. 8). These may contain some redundant or altered descriptions and figures with other chapters (3, 4 and 6). There is a lot of cross-referencing in this thesis, so double-check the page number before following a link to a different section.

## 1.6 Supplements

Some useful code from this project will likely be available as a .zip file Seth Aubin’s website alongside this .pdf, as well as on GitHub (as of 2021) at:

<https://github.com/drewrotunno/ThesisCode>

# CHAPTER 2

## The Apparatus

Our ultracold atom apparatus sits in a windowless basement lab in Small Hall. We use two 10'×5' optics tables: the “laser table” for preparation of lasers for potassium and rubidium that connect via optical fibers to the “science table,” which houses the vacuum chamber and much more hardware comprising ‘the apparatus.’ A view of the vacuum chamber with a schematic super-imposed is shown in Fig. 2.1. The ins and outs of this device are scattered through previous Ph.D. [59, 60, 61, 62] and undergraduate theses. Therefore, I will give only an overview of the apparatus in Sec. 2.1, a typical experimental cycle in Sec. 2.2, and focus on several new instruments, devices, and techniques that have become permanent fixtures to the apparatus in the rest of this chapter. These include modifications of the optical dipole trap in Sec. 2.3, thermal expansion mitigation in Sec. 2.4, sweeping frequency sources in Secs. 2.5 and 2.6, a modular RF amplifier in Sec. 2.7, and moving the RF evaporation signal in Sec. 2.8. We present some useful measurements of the chip traces in Sec. 2.9, and summarize in 2.10.

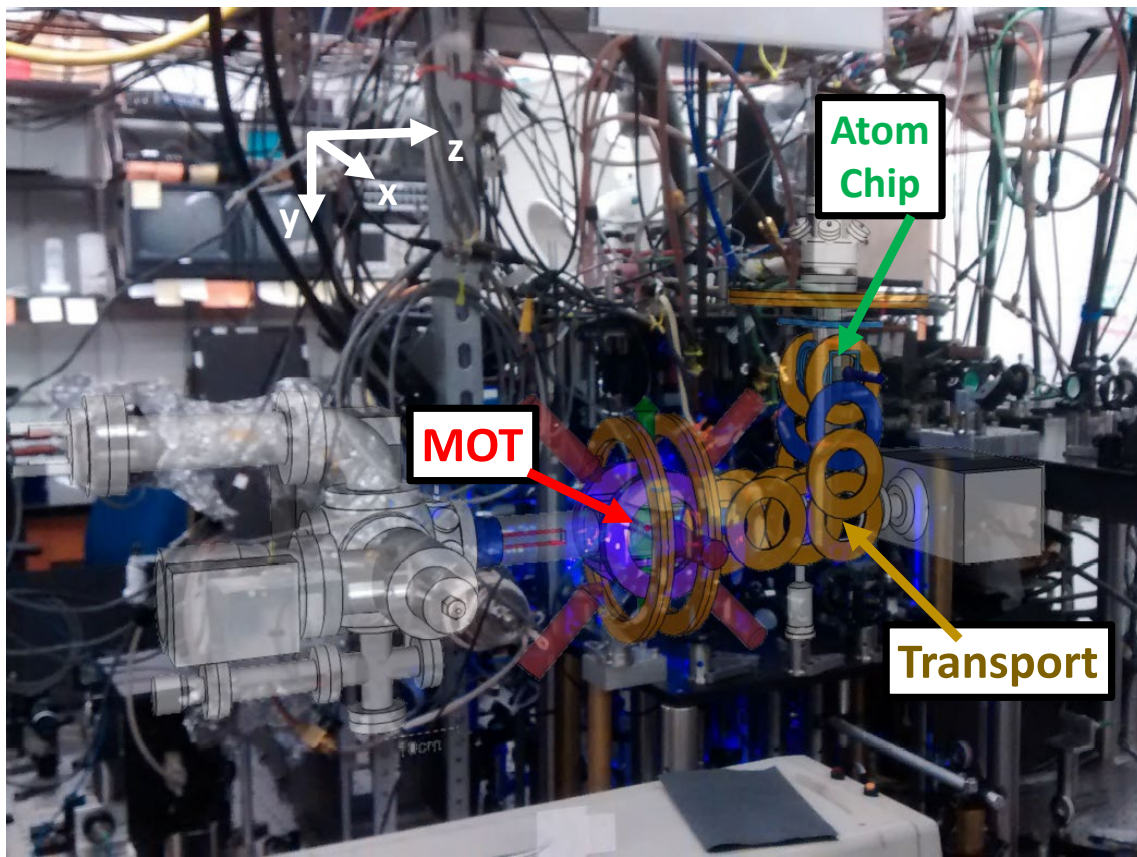


FIG. 2.1: The Apparatus on the science table with a super-imposed schematic showing coils, laser paths, and vacuum structures. Image credit: A.J. Pyle, 3-D model by Austin Ziltz.

## 2.1 General Description

The vacuum chamber in Fig. 2.1 consists primarily of two elongated square glass vacuum cells, affixed in an upright L-shape by standard steel vacuum parts. An ‘atom chip’ is inserted from above, suspended in the center of the vertical cell, with its active side pointed down. Both the side *MOT cell* and the upper *science cell* are surrounded by wire-coil electromagnets generating nominally Cartesian-oriented magnetic field components with Helmholtz-like pairs and unpaired coils, along with anti-Helmholtz pairs which form the transport traps and the ‘B-trap.’ Optical access for cameras comes from two directions at the atom chip, ‘radial’ and ‘axial’ views of a cigar-shaped cold atom cloud held beneath the chip surface. The whole system runs on a sequencer, the ADWIN, which alters analog and digital control channels on  $10 \mu\text{s}$  time steps (100 kHz), interfacing all of the hardware for the experiment from software graphical user interface (GUI) ‘panels.’

## 2.2 A Typical Cycle

This section outlines a typical 30 second apparatus cycle, along with Table 2.1.

### 2.2.1 Magneto-Optical Trap (MOT)

Atom collection begins in a Magneto-Optical Trap in the lower ‘MOT’ cell, where three counter-propagating laser pairs bathe atoms with photons near-resonant to the D2 electric dipole transition  $5S_{\frac{1}{2}} \rightarrow 5P_{\frac{3}{2}}$  at 780 nm, as drawn in Fig. 2.2.

This light Doppler cools gaseous rubidium atoms via the cycling transition:

$$|5S_{\frac{1}{2}}, \ell = 0, F = 2, m_F = -2\rangle \leftrightarrow |5P_{\frac{3}{2}}, \ell = 1, F = 3, m_F = -3\rangle$$

Description	Duration (s)	Temperature ( $\mu\text{K}$ )	Number
MOT collection	15	100	$5 \times 10^8$
Cooling, Optical pumping	< 0.1	16	$5 \times 10^8$
Magnetic transport	7	60	$3 \times 10^8$
Into Chip Trap	1	90	$2.5 \times 10^6$
Evaporation	4	1-2	$3 \times 10^5$
(Optional) to BEC	0.2	0.4	$3 \times 10^4$
Into ACZ / Dipole	0.05 / 0.5	1-2	$3 \times 10^5$
Experiment	0.001 - 2	"	"
Imaging	0.5	"	"
Total	$\approx 30$		

TABLE 2.1: Timing sequence of a typical experimental cycle. Experimental values adapted from C. Fancher's thesis.

where  $N = 5$  is the principle quantum number,  $\{S, P\}$  correspond to the orbital angular momentum  $\ell = \{0, 1\}$  and total angular momentum  $F = I + \ell + S$  combines nuclear, orbital, and electron spin respectively, with  $\hat{z}$ -projection  $m_F$ . We use two laser frequencies, the ‘trap’ and ‘repump,’ offset by nearly the ground-state hyperfine transition of 6.8 GHz. Trap light is applied with detuning  $\delta$  held slightly negative or red of the transition. ‘Fast’ or ‘hot’ atoms see this light blue-shifted back to resonance and absorb the opposing photon momentum. Additionally, an inhomogeneous local minimum in magnetic field creates a spatial detuning variation, such that atoms in the outer regions of the trap absorb a photon to move them inward, and atoms at the trap center remain ‘dark’ as they don’t absorb much light by this resonant process. The spontaneous decay rate of  $\Gamma = 2\pi \times 6$  MHz on this transition leaves atoms as cold as the Doppler limit  $T_D = \hbar\Gamma/2k_B$ , roughly 144  $\mu\text{K}$ . Repump light takes atoms that might fall ‘dark’ in  $5S_{\frac{1}{2}}, F = 1$  back into the cycling transition.

The slowed atoms congregate at the B-field zero at the center of an anti-Helmholtz coil pair, for up to 15 seconds of collection time.

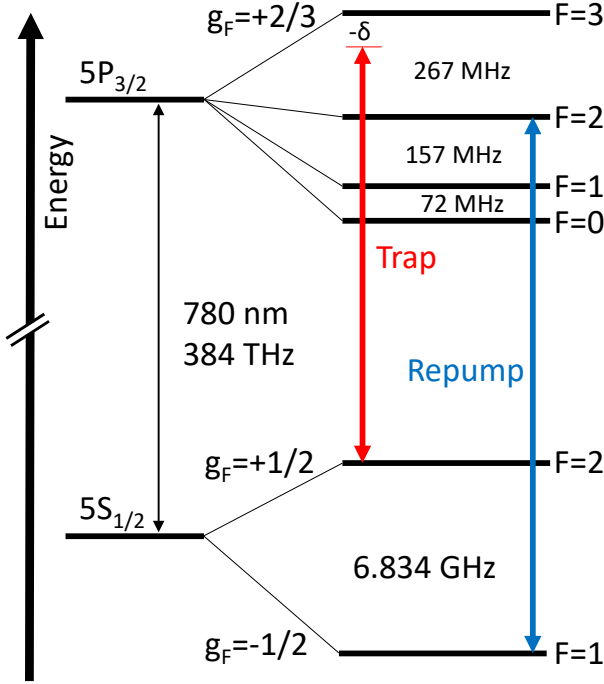


FIG. 2.2: Diagram of the  $5P_{\frac{3}{2}}$  and  $5S_{\frac{1}{2}}$  hyperfine levels and the relevant transitions for optical cooling (red, ‘Trap’) and repumping (blue, ‘Repump’) in rubidium-87 [63].

## 2.2.2 Optical Molasses and Pumping

After the collection period, atoms are slowed or cooled further using a the optical molasses technique. Briefly, by using light polarization ‘lattices,’ atoms with kinetic energy move ‘uphill’ against a gradient, before optically pumping to another state which then traverses another ‘hill’ of a polarization gradient. Colloquially, this is called ‘Sisyphus’ cooling, as atoms continue to lose kinetic energy pushing themselves ‘uphill.’ This quick process leaves the atom ensemble temperature well below the Doppler limit.

Atoms are then optically pumped using a vertically aligned  $B$ -field and a circularly-polarized beam into a single state population. We use both trap and repump light near resonance to optically ‘pump’ the atom population into the  $|5P_{\frac{3}{2}}, F = 3, m_F = 3\rangle$  state, which quickly decays to a nearly pure  $|5S_{\frac{1}{2}}, F = 2, m_F = 2\rangle$  state.

Trappable states have gyromagnetic factors  $g_F$  and  $\hat{z}$  quantum numbers  $m_F$  such that  $g_F m_F > 0$ . Specifically, we intend to trap  $|F = 2, m_F = 2\rangle$ , but get a few percent of  $|F = 2, m_F = 1\rangle$  contamination as well.

### 2.2.3 Magnetic Transport

Atoms are then caught in the ‘B-trap’ generated by the purple anti-Helmholtz coils in Fig. 2.1, as they turn on very quickly. By adjusting 100-Amp currents in multiple stationary transport coils (orange in Fig. 2.1), the field minimum moves smoothly over and up to the chip.

### 2.2.4 Atom Chip

The chip micromagnetic trap uses a single Z-shaped wire carrying direct current (DC) and a ‘hold’ field which cancels the Z’s magnetic field at one point below the chip. The Z-wire has current in the  $-\hat{z}$  direction, and the holding field points in  $-\hat{x}$ . The result is a long cigar-shaped trap along the central  $z$ -wire segment. We can control the trap’s shape and position by adjusting the generating fields, including a vertical trim field and the quantizing  $B_{DC}\hat{z}$  field aligned with the long axis of the trap. We show an illustration of the atom chip with atoms held in a crossed dipole trap in Fig. 2.3.

### 2.2.5 Radiofrequency Evaporation

We evaporate atoms in this magnetic trap as the final cooling process, using RF photons to couple the surfaces shown in Fig. 2.4. These are simulated traps with some typical experimental parameters. Evaporation sweeps from high ( $\approx 7$  MHz) to low ( $\approx 3$  MHz) frequency will move atoms in the hottest, farthest regions of the trap into anti-trapped states, where they are ejected. Atoms colder than the RF

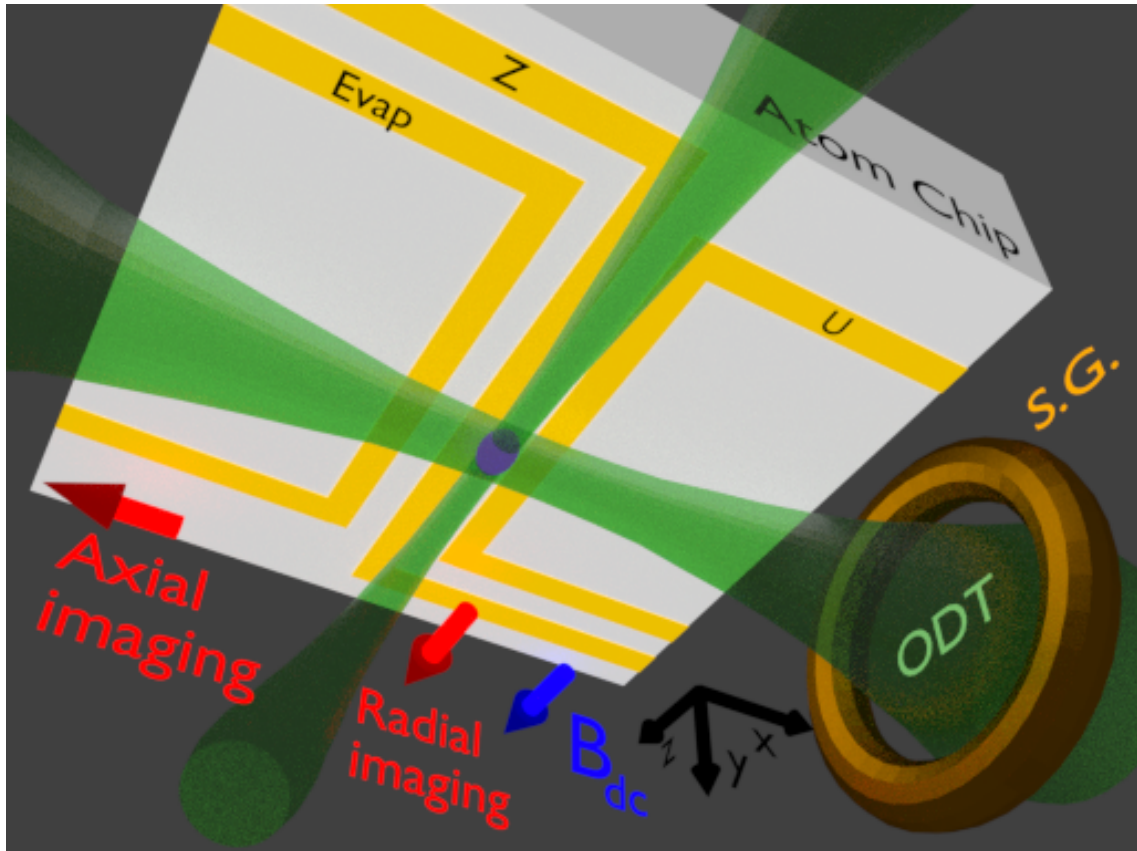


FIG. 2.3: A 3-D cartoon of the atom chip, not to scale. Illustrated in this image are the axial and radial imaging directions, the quantizing  $B_{DC}$  field direction, the atom chip U-Z-U wires, the crossed optical dipole trap (ODT), and the Stern-Gerlach (S.G.) coil.

‘knife’ frequency remain trapped, continually re-thermalizing with elastic collisions.

Atoms are prepared intentionally in a thermal atom cloud, above the critical temperature for BEC formation, but only by a few (1-2) orders of magnitude in phase-space density. Evaporation leaves roughly 200k-500k atoms at 1-2  $\mu\text{K}$  as the starting point for much of this work.

## 2.2.6 Experiment

The next item sequentially is the experiment that we want to perform after preparation. Specifics of this step will be discussed at length in Chaps. 5 and 7. It generally includes loading the atom chip trap into either the AC Zeeman trap, or the ODT, and then a sequence of RF and microwave interactions performing the experiment of interest.

## 2.2.7 DC Stern-Gerlach Separation

At the end of an experiment, when the atoms are released from a trap and are in free-fall, but before imaging, we can elect to let them fall through a horizontal ( $\hat{x}$ ) DC magnetic field gradient, which separates them by their  $m_F$  projections using the Stern-Gerlach effect. We use a single coil, noted in Figs. 2.3 and 2.5, to provide this spatially-varying field for the atoms. The Stern-Gerlach force  $F_{SG} = m_F g_F \mu_B \frac{dB}{dx}$  (variables defined in Chap. 3) makes each  $m_F \neq 0$  state into a high- or low-field seeker, who move left-and-right in  $x$  during the time-of-flight, based on the sign and magnitude of  $m_F g_F$ . This Stern-Gerlach separation method is demonstrated in later experiments, e.g. Fig. 5.8.

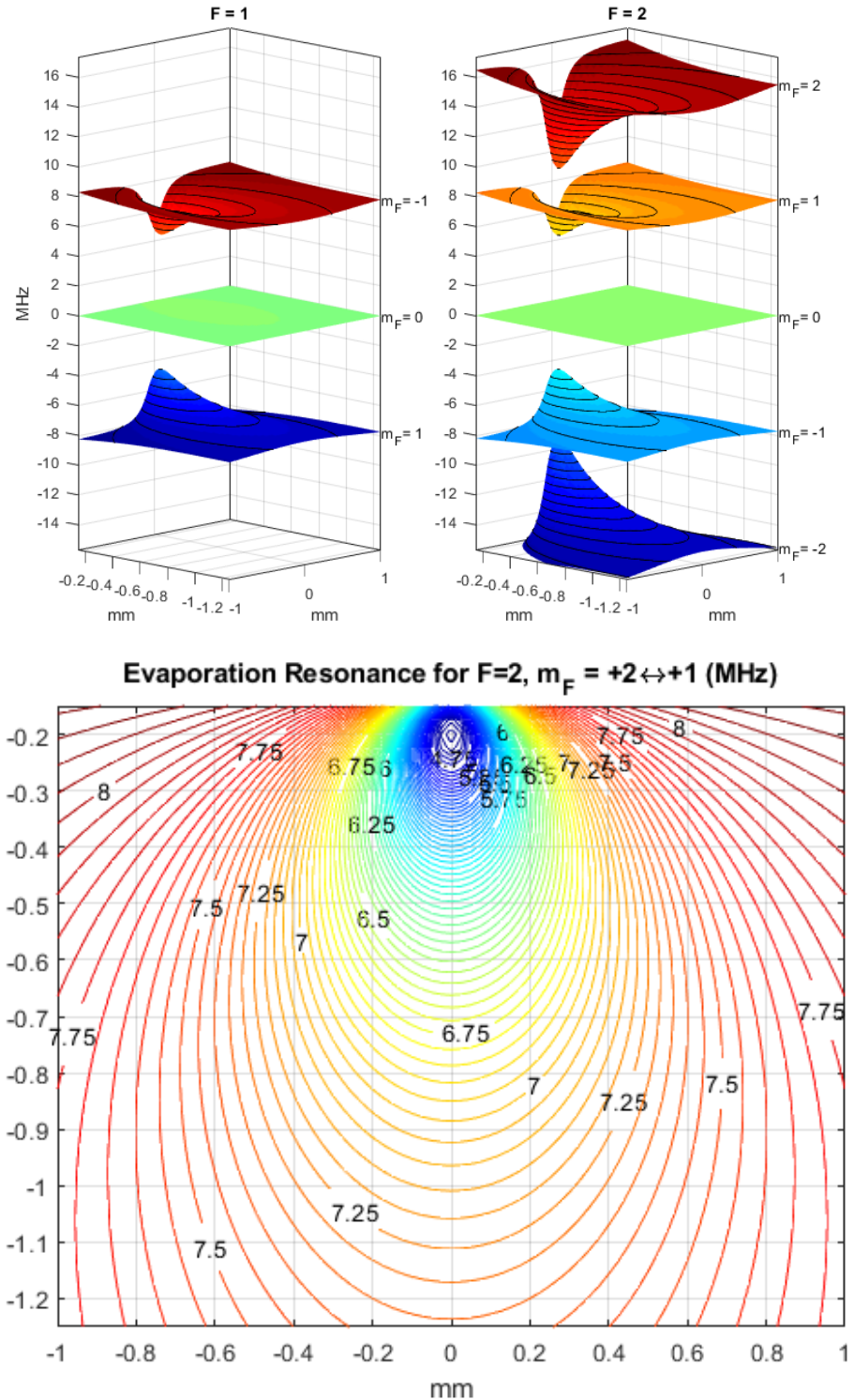


FIG. 2.4: Simulated DC chip trap. Top: Simulated trapping and anti-trapping potentials, using typical DC atom chip micro-magnetic trap parameters, shown for all 3+5 ground hyperfine levels. Bottom: Differences between trap potentials expressed in MHz, illustrating how RF can connect curves for evaporation.

## 2.2.8 Imaging

Imaging occurs as the final step of any experimental cycle to retrieve information about atom position and population after our experimental procedure. Trap light only images atoms in  $|5S_{\frac{1}{2}}, F = 2, m_F = +2\rangle$  (with the cycling transition to  $|5P_{\frac{1}{2}}, F = 3, m_F = +3\rangle$ ), so we use a 1 ms long ‘pre-pulse’ containing trap *and re-pump* light, employing the same polarized pumping scheme as before to turn all  $m_F$  states into +2.

Absorption imaging requires two images: One where atoms absorb trap light, creating a shadow in the image, and one reference of laser light intensity, *without* atoms, taken a half-second later. The optical density measures atomic column density via intensity  $I$  over the camera sensor, measured by optical depth  $O.D. = -\ln\left(\frac{I_{atoms}}{I_{laser}}\right)$ . These measurements generate high contrast false color images where red hot spots of atoms rise above blue backgrounds.

We image along two perpendicular directions indicated in Fig. 2.12: the ‘radial’ view looks down the length of the cigar ( $\hat{z}$ ), giving radial information, and the ‘axial’ view observes the long axis of the cigar ( $-\hat{x}$ ), from the side. Each camera images at a 1:1 magnification, although they have different square pixel sizes: radial (Unibrain Fire-i 530b) is coarser with  $7.4 \mu\text{m}/\text{px}$ , and axial (Unibrain Fire-i701B) is finer with  $4.65 \mu\text{m}/\text{px}$ .

Typically, we take a rectangular ‘region of interest’ (ROI), a range of pixels that contain the whole round atom cloud, and some background area around it for good fitting. Then, we sum the optical density values along one axis, projecting the 2-D area into a 1-D optical density to fit in each direction. We can fit ballistic atom clouds with a 1-D Gaussian function  $Ae^{-(\frac{x-x_0}{\sigma_x})^2}$  to resolve cloud center-of-mass position  $x_0$ , spatial size  $\sigma_x$ , and number  $A$ . Often in this thesis, only relative atom populations matter, so we can use solely  $A$  to relate multiple clouds, if they

have the same size  $\sigma_x$ , as in Rabi frequency measurements of Fig. 4.1. If fits are poor due to odd cloud shape or low number, a ‘raw’ O.D. count over the ROI can suffice. To get actual atom number for each pixel, as with population decay measurements, we can use the expression [62]:

$$N_{pixel} = -\ln \left( \frac{C_{atoms}}{C_{laser}} \right) \frac{2\pi}{3\lambda^2} \cdot A_{pixel}$$

where  $C_{atoms}, C_{laser}$  are the CCD pixel counts,  $\lambda$  is the laser wavelength and  $A_{pixel}$  is the above listed pixel size squared. This imaging technique is destructive and necessarily marks the end of an experimental run.

## 2.3 Optical Dipole Trap

We can perform experiments on atoms trapped in a focused laser beam located roughly  $100 \mu m$  below the chip, illustrated in Fig. 2.3. Transitioning to this trap was initially motivated by avoiding eddy currents when the DC trap is quickly shut off, as well as giving atoms a locally uniform  $B_{DC}$  magnitude and direction. Additionally, the electric dipole force traps *all*  $m_F$  states, a useful benefit compared to the DC trap. This optical dipole trap (ODT) is a 1064 nm laser beam pair (2 W total) that confines atoms to the intensity maximum of two crossed focal points below the U or Z wire. The power is split 80/20 into mostly the ‘main’ beam, which is focused down to nominal  $60 \mu m$  beam waist along the chip current  $\hat{z}$  direction, and less in the ‘cross’ beam at nearly a right angle, that confines atoms in the main beam axially in its focus, nominally  $120 \mu m$ . We measure the main radial trap frequency roughly  $2\pi \times 170$  Hz, and ‘cross’ beam axial confinement roughly  $2\pi \times 20$  Hz. Only the second ‘cross’ beam oriented  $-\hat{x}$  is used in the AC Zeeman trap, again for axial end-capping. We observe higher trap lifetimes in  $F = 2$  for the  $m_F = \{+2, -2\}$

stretch states  $\approx \{5.5, 7\}$  seconds, and lower lifetimes in the middle  $m_F = \{-1, 0, 1\}$  states  $\approx \{0.2, 0.5, 0.2\}$  seconds. This is likely due to inelastic spin-flipping collisions available to the non-stretch states, and affects the measurements of spin populations over time in Chap. 5.

In early 2020, we added a diagonal plate of glass on a rotation stage, translating both beams vertically for automated trap translation. This device is labeled in Fig. 2.5, and details are in Bennett Atwater’s thesis. The idea is that we can grab a high number of atoms from the end of transport into this ODT, then translate them up to the chip surface into an AC Zeeman trap, skipping the lossy DC micro-magnetic trap hand-off. The ACZ Force was measured before this addition, and the rotation stage was left in the top position for the entirety of the ACZ trap experiment.

## 2.4 Thermal Stabilization Strategies

The ODT beam was initially free-run on the table, but small air currents and thermal effects created significant movement in the trap location day-to-day. Charles Fancher, before 2016, added a fiber that helped minimized this beam wander by significantly lowering the free-travel path of the laser.

We have more recently observed movement in the ODT beams and thus atom trap position under the chip, in tandem with room temperature fluctuations of  $\sim 0.5^\circ$  C. Providing the ODT beams at the atom chip height, we have two optical breadboards sized  $18'' \times 24'' \times 2.5''$ , with tapped top and solid bottom surfaces each 3 mm thick, and a 2 inch aluminum vertical honey-comb body sit on four corner 18” stilts as shown partially in Fig. 2.5. We found that the top and bottom faces would expand differentially, cupping the top plate, tilting the edge-mounted periscope mirrors. This warping created a shifting ODT position which moved verti-

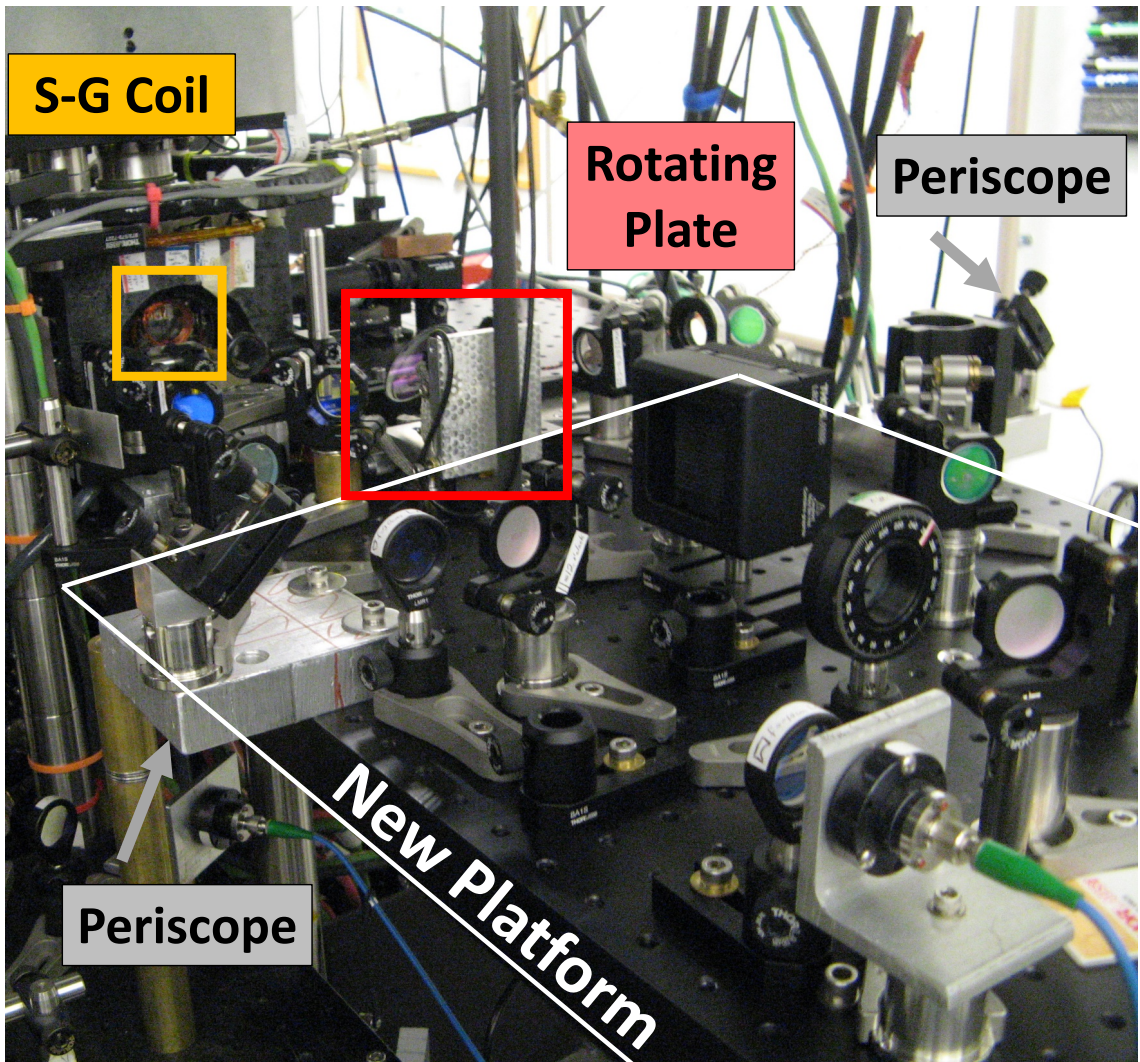


FIG. 2.5: A zoom of the platform near the atom chip, showing the new rotating plate and the platform itself, plus the Stern-Gerlach (S-G) coil, which we use in later measurements. Image credit: Bennett Atwater.

cally with room temperature and reproduced well with warming the bottom surface of the optics platform. This correlation is shown in Fig. 2.6, which shows atom height, beam height, room temperature, and table temperature over a few hours of observation. We observe sinusoidal fluctuations roughly  $10\mu\text{m}/0.3^\circ\text{ C}$ , with a nearly 90 minute cycle, due to our HVAC system, which simply turns on and off within a tight temperature interval.

The first attempt at a fix was to abate the largest heat sources near the apparatus. The driving unit for the ODT laser has a circular tube duct, which carries its excess heat away from the apparatus. Initially, this duct pointed to the room's temperature sensor, forcing colder than needed air into the space. We re-routed this duct across the lab, into the ‘theory section.’ A second heat abatement strategy was to add fans above the AOM/laser lock cabinet, which also dump hot air into the other half of the lab, so that each half's HVAC unit can share the thermal load generated by the apparatus.

As a temporary fix, we wrapped a blanket around and above half the optics table to prevent the room's HVAC from exerting too much control over the space. We affixed thick foam insulation under the platform and added thermal mass in the form of water bottles and copper mass near and on top of the optics tables to require more heat for thermal changes in the area. This brought the total position excursion in half, from around  $15\ \mu\text{m}$  to  $8\ \mu\text{m}$ .

For a permanent fix, we used replacement optics boards made from solid tapped aluminum, with six through-holes to mount onto the support columns, as well as two additional central pedestals for increased support, per thermal simulation calculations carried out by Seth Aubin. Installation and re-alignment of the ODT beams with the rotation stage was done in early 2020 and is shown in Fig. 2.1. The new tables still seem to have some minor variation of a few microns, possibly from differential thermal expansion in height between the platforms and the chip-stack

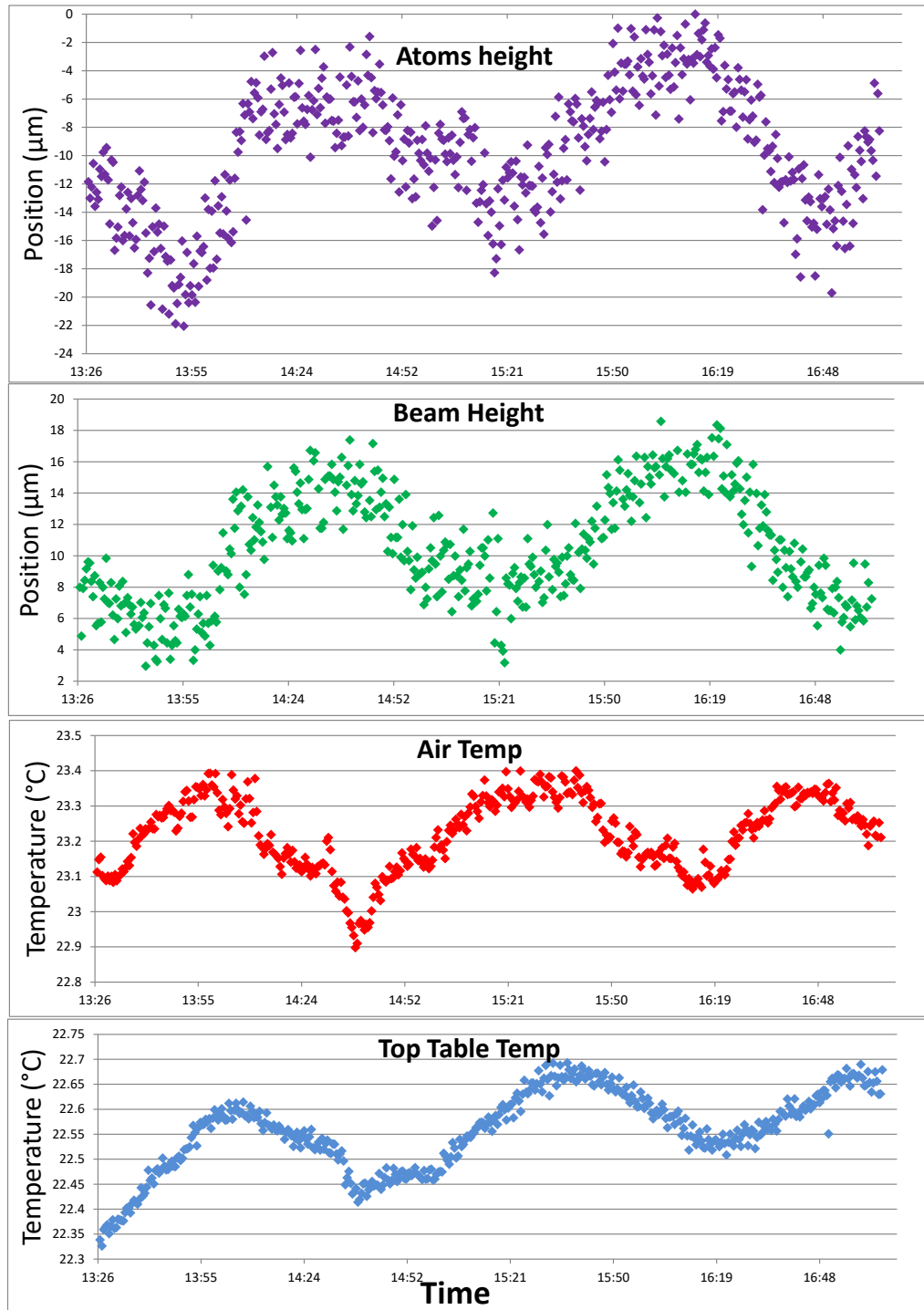


FIG. 2.6: A few hours of ODT wander, measured in relative  $\mu\text{m}$  for the top two plots, correlating with measured room temperature in Celsius in the bottom two plots. Data from May 8, 2018.

support structure. It is hard to tell whether the atoms and the chip stack are moving, if the camera's table is moving, or if the ODT beam path is tilting. We get a long-term stability of a few ( $< 5$ )  $\mu\text{m}$  in a 60  $\mu\text{m}$  waist trap, nearly our pixel resolution (4.65  $\mu\text{m}$  axial and 7.4  $\mu\text{m}$  radial).

## 2.5 Cinderella and Other RF Sweeping Sources

My first task in this lab was to fix and duplicate a direct digital synthesis (DDS) frequency sweeping signal generator using an evaluation board for the AD9910 chip. This device maintains a continuous phase as frequency sweeps, and is capable of frequency step units of  $10^9/2^{32} \approx 0.23$  Hz. The DDS changes the output voltage every 1 ns, and can alter frequency or phase parameters every 4 ns. In principle, the output frequency ranges from 0-500 MHz, but the useful range with our other RF components is more like 3-400 MHz. Controlling the DDS is an Arduino Due microcontroller with an Ethernet shield, which provides an HTML website to receive human commands, shown in Fig. 2.8. The Arduino sends translated sweep information to the AD9910, with timing given by ADWIN inputs. The initial DDS and its code were created by Harrison Cantor-Cooke, with some modifications and a new user interface by subsequent undergraduate contributors and me. Because its primary role is sweeping, I gave my box the name Cinderella, making the original the Step Mother, and we have since added Prince Charming and Glass Slipper to the roster.

When Charles Fancher was working with microwave AC Zeeman [44], we used a phase-lock-loop (PLL) frequency multiplier to convert the DDS's 107 MHz  $\times 64 \rightarrow$  6.8 GHz, and I use the same source for the microwave sweeps in Chap. 7. My first project in the lab was fixing and duplicating a direct digital synthesizer (DDS) frequency source, which provided the sweeping 107 MHz signal via a web interface.

Lots of care went into selecting filters and arranging components to reduce harmonic noise, and phase noise, where the latter aspect was significantly improved using a DDS compared to an analog source. Some signal processing extracted frequencies from an oscilloscope trace, with some representative results shown in Fig. 2.7. Analysis showed that this PLL multiplying technique led to frequency ‘overshoot’ at the end of sweeps in (c), proportional to the slope in (a). Additionally, there was some slight residuals from a linear slope in (b), and we show the reference RF signal in (d) used as the sweeping clock of the PLL system. This overshoot suggests that direct synthesis via mixing with 6.8 GHz is desirable, perhaps with IQ modulation or single-sideband mixing, rather than a feedback system.

Generating frequency ‘ramps’ or sweeps on the DDS requires just a few parameters: the frequency start and endpoints, the frequency step amount, and time step rate. Human operators often only know the total sweep time and frequency endpoints, giving the overall slope only, and we must select step sizes to fit. In cases where the desired slope is roughly one freq step/time step, slope inaccuracy will adjust timing away from the intended duration. We have to pick two integers above one as step sizes, whose ratio approximates the desired slope, and I have come up with a little algorithm to do this. We take *slope* as  $\Delta f / \Delta t$  or its inverse  $\Delta t / \Delta f$ , whichever is above 1, an improper fraction. We then invert the difference of *slope* and its nearest integer, rounding and taking the absolute value of the result:

$$multiplier = \left| \text{round} \left( \frac{1}{slope - \text{round}(slope)} \right) \right|$$

then check to see if *multiplier*  $\times$  *slope* is within acceptable error of an integer. In a trivial case, when the real slope is nearly  $slope = n + \frac{1}{q}$  for positive integers  $\{n, q\}$ ,

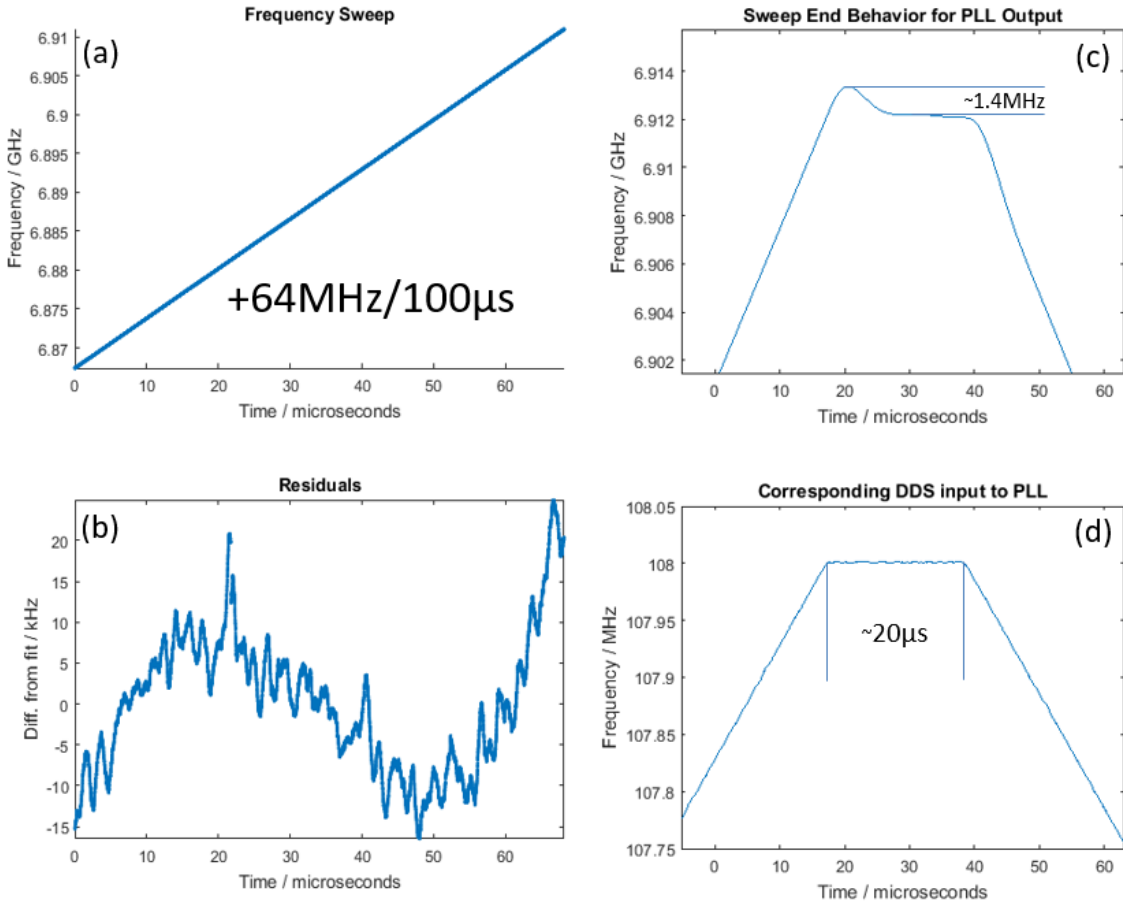


FIG. 2.7: Analysis of multiplied DDS signal, derived from an oscilloscope signal. This PLL frequency-multiplier method can make a rather linear slope as in (a) with minor frequency residuals from a linear fit in (b). However, the abrupt stop at the RF endpoint in (d) leads to an ‘overshoot’ in the multiplied signal in (c), as its feedback catches up.

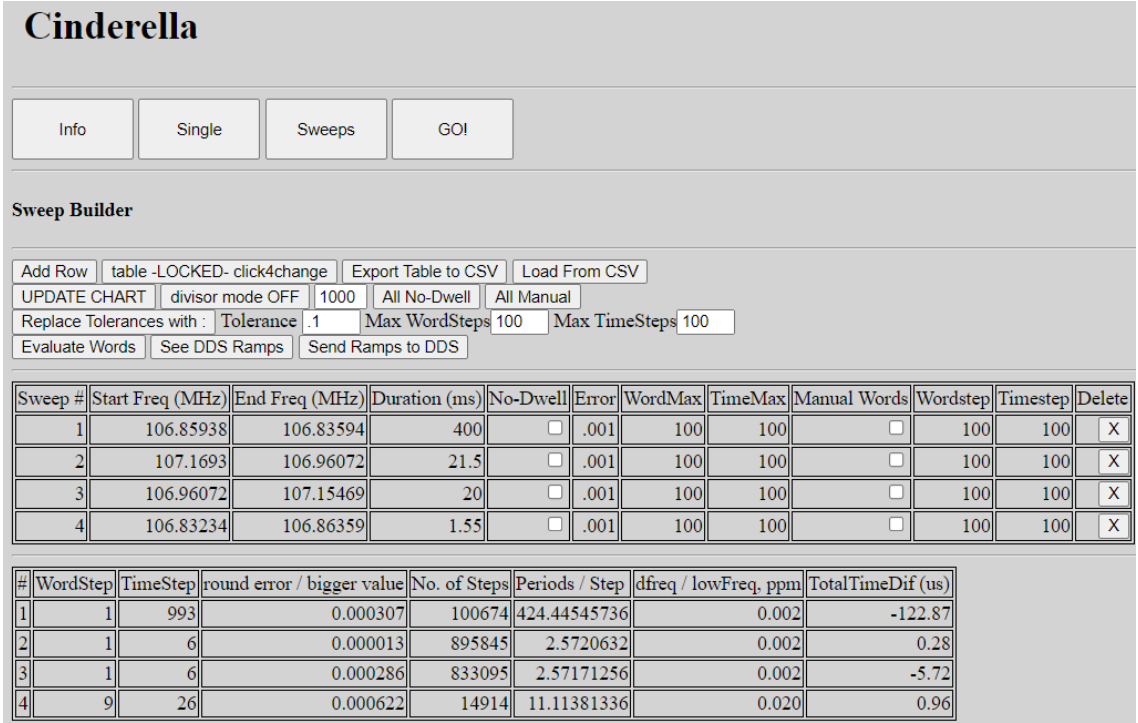


FIG. 2.8: Cinderella’s webpage interface, showing a sample experimental microwave sequence (showing frequency divided by 64). A user defines desired frequency end points and sweep times (middle table), and an algorithm determines time and frequency step sizes which minimize total time offset (bottom table).

we can see  $multiplier = q$ . Multiplying, we have

$$slope \cdot multiplier = \left(n + \frac{1}{q}\right)q = qn + 1$$

and the other integer  $multiplier = q$  as the new slope step sizes. While this quickly converges for some cases, we repeat the process of multiplying in new  $multiplier$ ’s until acceptable error is achieved, or we reach the upper step size bounds. Some considerations about step choice are given in the bottom table of Fig. 2.8, for human-defined slopes in the top table. Only the last sweep required this algorithm, yielding frequency ‘Wordstep’ = 9, and ‘Timestep’ = 26. The rest of the sweeps in this example were best suited for minimized frequency step without much timing error, shown in the last column of the bottom table.

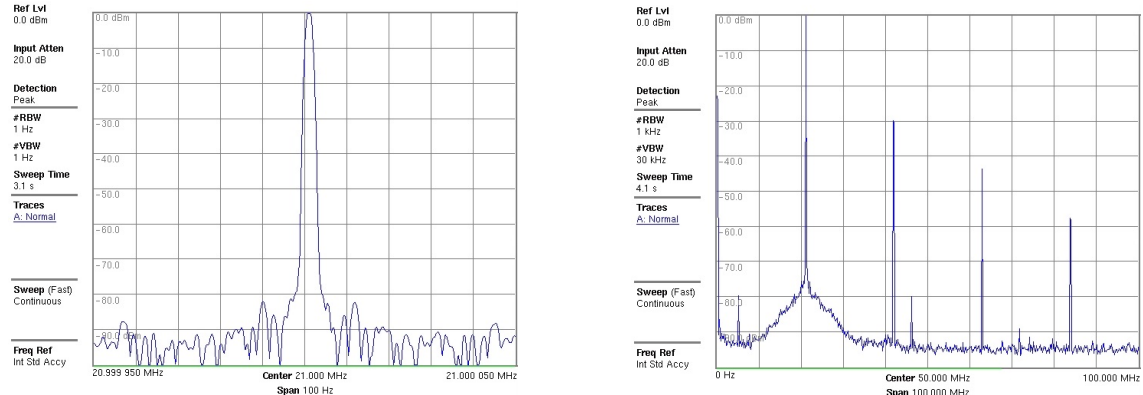


FIG. 2.9: Cinderella’s output frequency spectrum shown as dBm versus frequency, close-in on the left (100 Hz span), and broadband on the right (100 MHz span). Measured by Anritsu MS2038C spectrum analyzer.

In our use, the phase-coherence of the signal is very important, which appears as tight linewidth in the frequency spectrum. Cinderella’s output frequency spectrum is in Fig. 2.9, showing both the close-in phase noise of the carrier, as well as additional frequency components seen in the broadband range, revealing harmonics and other stray peaks which we seek to minimize. The outputs were initially used as a variable clock for phase-locked loop (PLL) frequency multiplying, converting a sweeping frequency near 107 MHz to the 6.8 GHz range. In our RF AC Zeeman work in Chap. 7, we can directly synthesize the relevant frequencies (around 20 MHz), but this creates some unwanted harmonics nearby. We often elect to frequency mix a very stable source at 100 MHz (or 6.8 GHz in future plans) to our sweeping RF sources to create the relevant frequency as their sum or difference. Mixing frequencies significantly lowers the 2<sup>nd</sup> harmonic, at the expense of higher odd harmonics (3rd, 5<sup>th</sup>, . . .), which can be suppressed more by low-pass filters. Additionally, we could lower phase noise by clocking the AD9910 directly using a good external 1 GHz clock fed by a stable 10 MHz rather than letting the on-board PLL of the DDS perform this multiplying itself.

While these DDS devices work great as single sources, we needed phase control between sources for trapping. Unfortunately, an inconsistent time delay on the

independent Arduinos prevents phase control between multiple sources. We could have split one signal and phase delayed each part, but this approach generally causes additional phase-shifts due to attenuation. Since we can control phase very precisely ( $\Delta\phi = 360^\circ/2^{16}$ ) on generation, we should make or find a DDS that has phase control on multiple lines with deterministic timing.

## 2.6 FlexDDS

We found a commercial replacement, the WieserLabs FlexDDS-NG, which utilizes multiple AD9910 chips on the same clock in expandable slot pairs. This machine has deterministic timing from internal FPGAs and an Ethernet port ready to receive teletype commands. I wrote an open-source suite of commands in MATLAB which now replaces the individual DDS's and their websites. This library is on my GitHub:

<https://github.com/drewrotunno/FlexDDS>

A bespoke GUI shown in Fig. 2.10 operates well for single-frequency mode. However, I generally found that I wanted a detailed view and explicit control over each action and trigger in a script execution, instead of ‘under the hood’ in the code of an easy-to-use GUI. In practice, I use the script version of the control program to perform the experiments of Chap. 7. Generally, instructions for an apparatus cycle are concatenated as a ‘stack,’ which is ‘flushed’ to the FlexDDS as one message per slot.

We desire phase control on two lines at the same frequency, and we elect to do that with a shared ‘rack’ TTL trigger on three signals: one frequency setting signal, which acts as the shared Local Oscillator (LO) to the mixer at  $f_{RF} + 100$  MHz, and two independent RF signals at 100 MHz with controlled differential phase. If we trigger two frequency shifting signals at slightly different times, then one signal

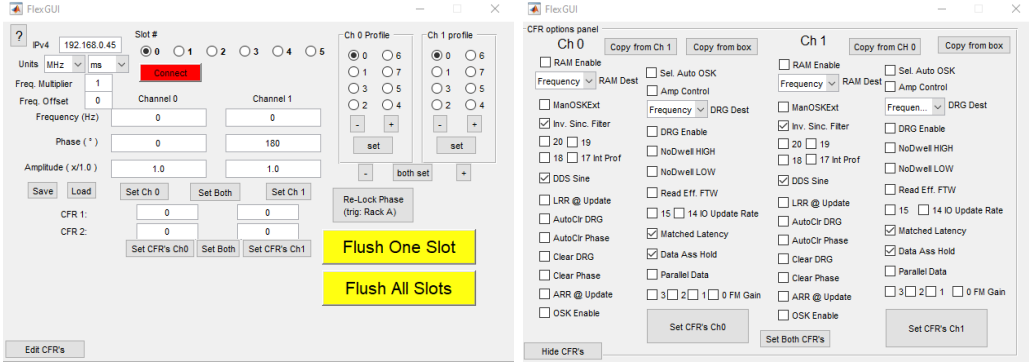


FIG. 2.10: Left: A graphical user interface (GUI) for the FlexDDDS. Right: The GUI enables control over the AD9910’s control function registers (CFR).

could phase-slip continuously with a slightly faster frequency, then un-shift at the end of the frequency sweep as the other catches up. Having one signal sweep and the others at constant frequency with tunable phase prevents this slipping and is enabled explicitly by our mixer setup.

## 2.7 Fluffy, the Three-headed Amplifier

With the frequency source in hand, we now need much more power than it produces to trap atoms. Simulations suggest 20 mW was the *very* low end of a possible trap power, and as much as 2 W would be more than enough to create near mK trap depth. We purchased some 10 W amplifiers, planning to use two for this proof-of-principle project and three in future experiments. The device ‘Fluffy’ is named after Hagrid’s three-headed dog, who guards the path to the Sorcerer’s Stone (or Philosopher’s Stone) in the first Harry Potter book.

This RF chain provides power control, frequency mixing, and signal monitoring while minimizing the harmonic contribution to the final signal. Components are tied down to an “RF breadboard” (i.e. a thin optics breadboard) and are easily re-configurable, as shown in Fig. 2.11. Two additional alterations that lowered overall harmonic representation are 1) the use of low-pass filters after the mixers

and 2) attenuating the signal before the variable voltage attenuators (VVA), which requires a compensating pre-amp afterward. We elect to attenuate before the mixers, leveraging the non-linear response for further attenuation at low power.

If too much power is sent to the chip, it can break a chip trace in any number of failure modes (e.g. melting a chip wire, having a trace separate from the substrate, connecting to a different wire, etc.), all of which are rather difficult to observe from the outside. To prevent such an irreversible failure, we have an integrated safety feedback system that will mute the signal if measured RF power (plus DC) is too high. Either of two triggers will mute the signal: 1) if the instantaneous power is  $> 0.5 \text{ W}$  or 2) the integrated power over time is  $> 1 \text{ W}\cdot\text{s}$ , with hand-set thresholds.

## 2.8 Evaporation Trace Switch

When testing higher power on atom chip wires for RF ACZ trapping (in Chap. 7), we rendered the trace formerly used for RF evaporation unusable. We know that this wire had a scratch across it from initial apparatus preparation, and this trace might have also developed small conductive connections to nearby wires over time. Applying 200 mW of RF power made the impedance of this trace jump randomly between values as the signal was applied, rather than acting as a simple resistive short as it had previously. This erratic behavior forced us to use the other U and Z wires to trap with, as we go over in Sec. 6.7. The chip's layout is shown Fig. 2.12, with the Z-wire in blue, and the lower U-wire in red used for the previous microwave experiment and ACZ trapping. We moved the evaporation signal from the top red U-wire to the purple loop in Fig. 2.12, raising the baseline evaporation power by +3 dB to achieve similar cooling as before the change.

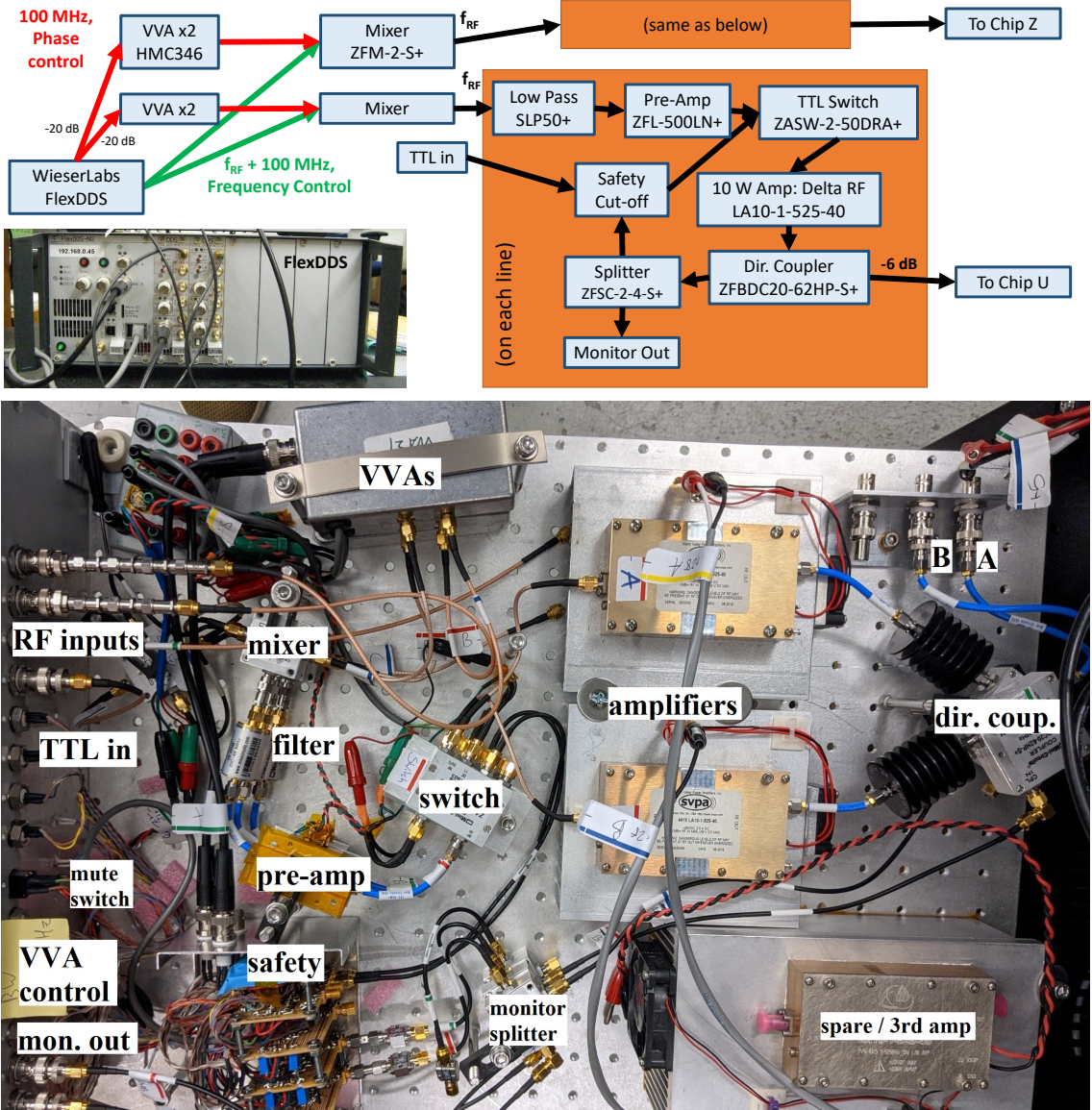


FIG. 2.11: A schematic and photos of Fluffy, the RF frequency ( $f_{RF}$ ) system. We use the FlexDDS (top left photo) as a multichannel source, and Fluffy (top: schematic, bottom: labeled photo) to mix and amplify those signals. Contents of the orange box are on each mixer output, and each connects to different chip traces, as indicated. The ‘A’ line goes to the U-wire, and the ‘B’ line goes to the Z-wire.

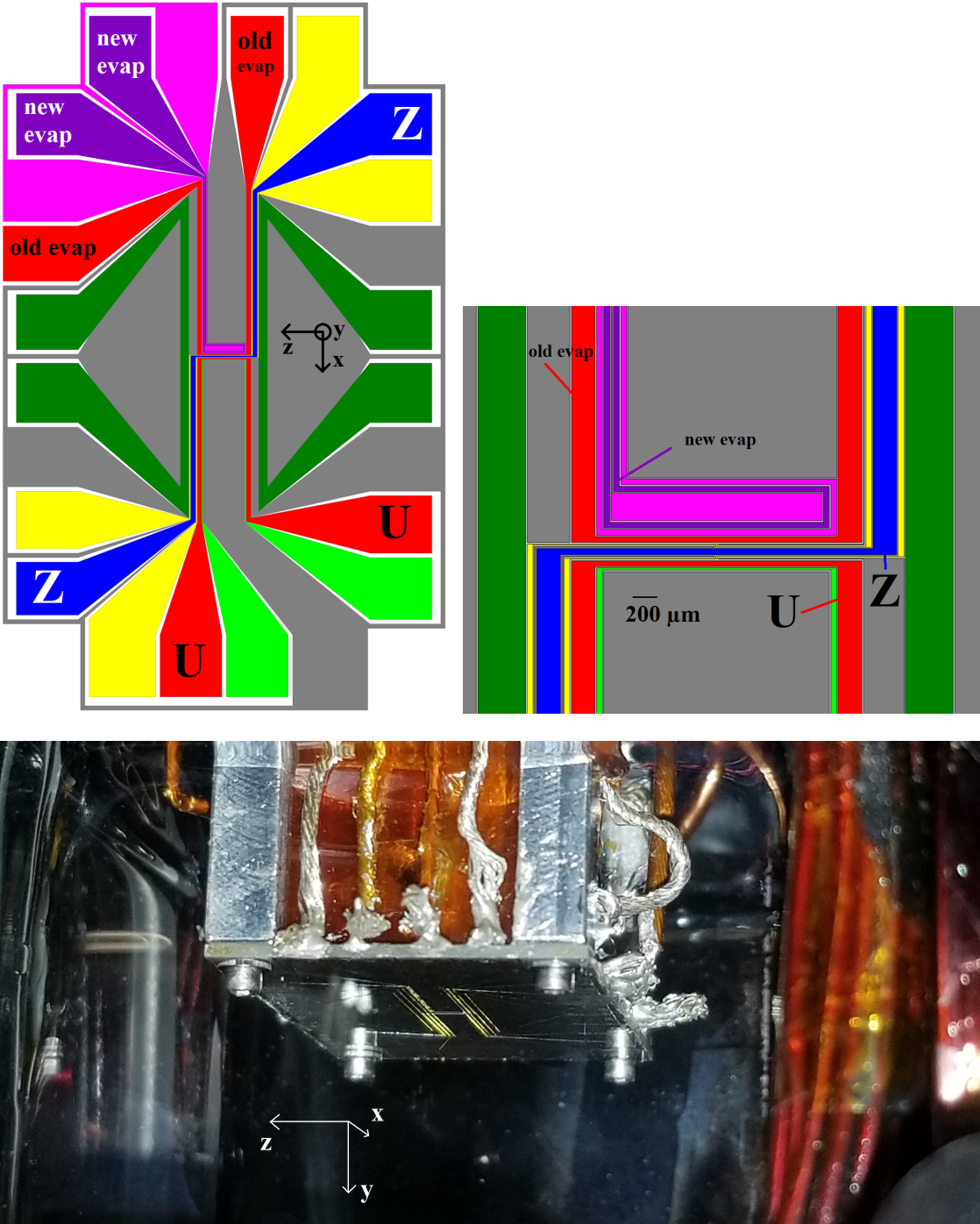


FIG. 2.12: Atom chip layout. Full schematic (top left) with a zoom-in (top right) and an image (bottom) of the chip traces. The evaporation line was moved from the left red U-wire to the purple loop. Bottom: An image of the actual atom chip, showing feed wires and the chip traces.

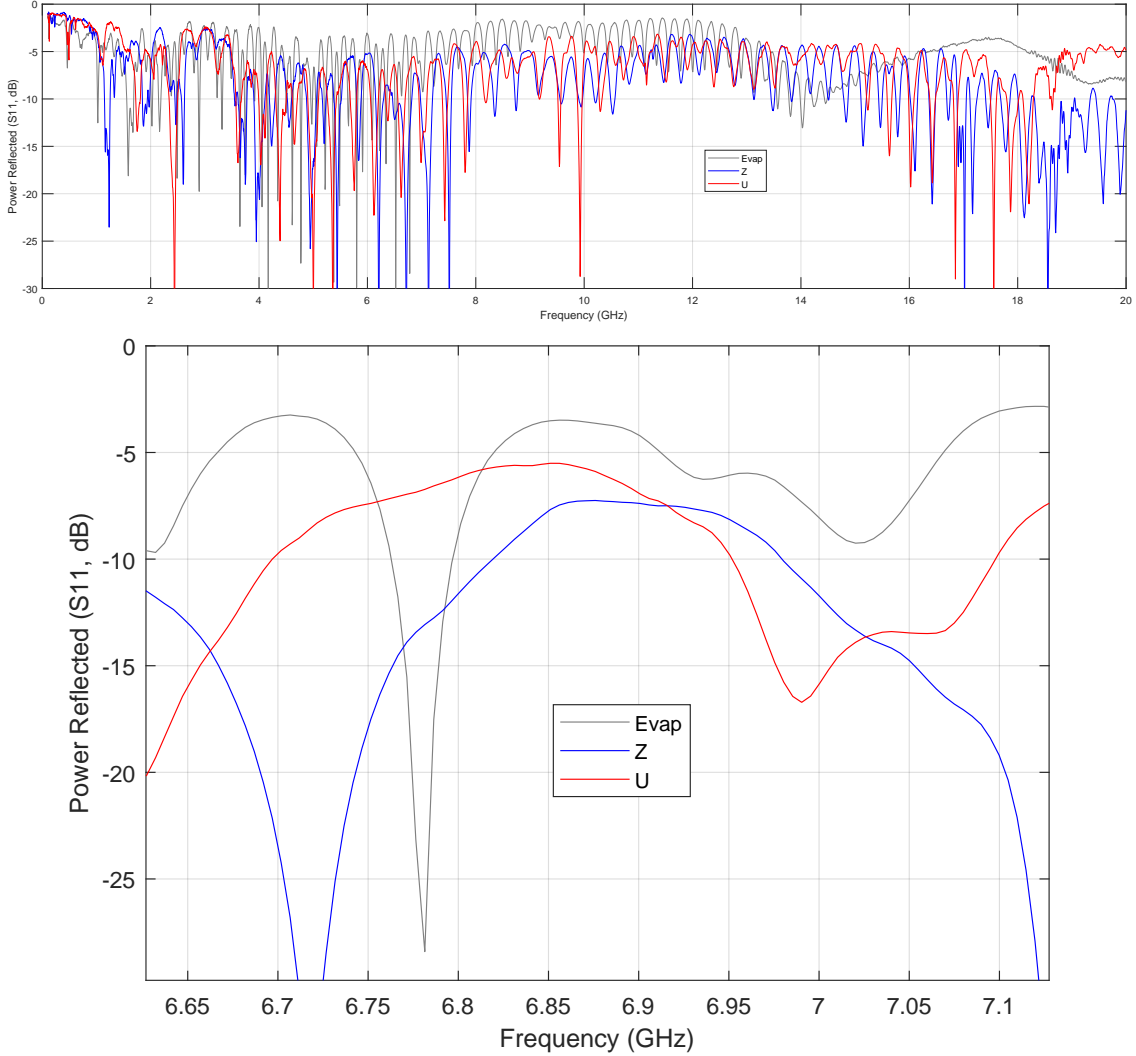


FIG. 2.13: Vector network analyzer (VNA) Bode plots of chip trace power reflection in dB vs. MHz frequency for the three center U(Evap)-Z-U wires. We show broadband 0-20 GHz data (top) and a zoom-in of the hyperfine splitting 6.8 GHz (bottom).

## 2.9 Chip VNA Measurements

A vector network analyzer (VNA, Anritsu MS2038C) is an impedance measurement tool often used in antenna testing. It sends and receives broadband (< 20 GHz) signals to a test platform, measuring return power and phase as a function of applied frequency, as shown for a broad range in Fig. 2.13 and for RF frequencies in Fig. 2.14. Measuring chip wire impedance lets us know how much inserted power is usefully applied as well as the relative phase-shifting *between* lines at different

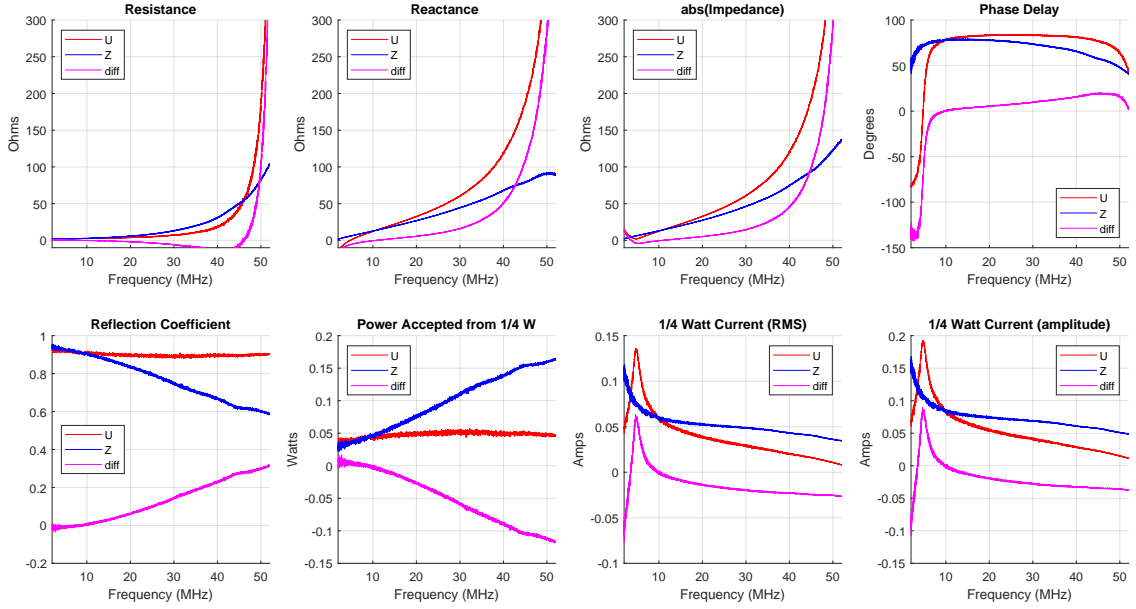


FIG. 2.14: Measurements of frequency-dependent chip behavior. Bottom: Vector network analyzer (VNA) measurements of chip trace impedance  $Z$  (and related values as labeled) on the two trapping wires and their difference across 1-51 MHz. The U-wire is relatively flat across this range, but the Z wire shows frequency dependence in power transfer and injection phase delay. This measurement motivated moving from  $\approx 8.5$  MHz to 20 MHz for trapping.

frequencies. Figure 2.13 shows a broadband measurement of all three wires, zoomed in on the hyperfine resonance and gives more detailed values for the two AC Zeeman trapping wires.

We note that the phase measurement in Fig. 2.14 shows roughly  $0.5^\circ/\text{MHz}$  slope. We will find later this frequency-dependent phase shift causes a slightly tighter trap at higher frequencies and looser traps at lower frequencies. The measured phase shift does not entirely account for the trap resonance asymmetry around both 20 MHz and 8.5 MHz, as described in Chap. 7.

## 2.10 Summary

The present apparatus [81] contains many different components: lasers, electro-magnetic coils, a vacuum system, waveform generators and so on, all of which play

a role in the eventual goal of cooling a sample of rubidium (or potassium) atoms to quantum degeneracy. While this apparatus was largely built by the time I arrived, using techniques that are common practice in modern atomic physics, I have helped maintain and modify the apparatus to our evolving needs.

We have discussed standard operation of the apparatus, as well as the RF system required for this experiment, primarily comprised of lab-built DDS's, Fluffy and the FlexDDS. Additionally, some long-term difficulties are analyzed, including thermal fluctuations in the lab and the atom chip's ability to receive broadband frequencies.

# CHAPTER 3

## Dressed Atom Theory

This chapter goes through some atomic background for the AC Zeeman effect. A good amount of the theory for this work is shared with that of so-called adiabatic traps, which use homogeneous microwave fields to generate resonant shell-shaped traps from a local inhomogeneous DC minimum [64, 65, 66]. Our case uses inhomogeneous RF field strength generated by AC currents in atom chip traces, with a single homogeneous quantizing  $B_{DC}\hat{z}$  field.

In Sec. 3.1, we decompose the hyperfine basis states  $|F, m_F\rangle$ . In Sec. 3.2, we discuss some of the spin transitions between these levels, including some numerical values for Clebsch-Gordan coefficients. In Sec. 3.3, we give some two-level driven atomic theory, which generates the AC Zeeman energy and ACZ forces in Sec. 3.4. Lastly, in Sec. 3.5, we tie these elements together to calculate the AC Zeeman energy across a range of photon frequencies for the RF transitions in both hyperfine ground state manifolds.

### 3.1 Hyperfine Basis

Often, optical transitions are used in atomic experiments, utilizing electric dipole transitions to higher electron energy levels for experimental control [46]. We use optical transitions to one of the fine-structure states  $5P^{\frac{1}{2}}$  or  $5P^{\frac{3}{2}}$  in atom preparation and imaging. The central experiment of this thesis instead uses the radio frequency and microwave magnetic transitions among the ground hyperfine states, remaining in the spherical quantum state  $5S^{\frac{1}{2}}$ , where  $\ell = 0$ . This ground state combines nuclear spin  $\mathbf{I}$ , electronic spin  $\mathbf{S}$  as the total spin  $F_{\pm} = I \pm S = \frac{3}{2} \pm \frac{1}{2}$ , yielding levels  $F_+ = 2$  and  $F_- = 1$  with a hyperfine splitting given by

$$\hat{H}_{HFS} = A_{HFS} \mathbf{I} \cdot \mathbf{S} \quad (3.1)$$

where  $A_{HFS}$  is the magnetic dipole constant determined by experiment to be  $A_{HFS} = h \cdot 3.417$  GHz for  $^{87}\text{Rb}$  [63]. We can find  $\mathbf{I} \cdot \mathbf{S}$  using

$$\mathbf{F}^2 = (\mathbf{I} + \mathbf{S})^2 = \mathbf{I}^2 + \mathbf{S}^2 + 2\mathbf{I} \cdot \mathbf{S} \quad (3.2)$$

then rearranging and taking  $\mathbf{F}^2 = \hbar^2 F(F+1)$  and likewise for all spins, we arrive at

$$\mathbf{I} \cdot \mathbf{S} = \frac{\hbar^2}{2} (F(F+1) - I(I+1) - S(S+1)) \quad (3.3)$$

With  $F=2$  or  $1$ , this equation gives values of  $+\frac{3}{4}$  and  $-\frac{5}{4}$  relative to an unperturbed  $5S$  level, yielding a total separation of  $2A_{HFS} = 6.834$  GHz between the  $F$  manifolds. This value largely comprises the ‘microwave’ transition frequency.

Each  $F_{\pm}$  manifold contains  $2F + 1$  states, that is, five in  $F_+ = 2$  and three in  $F_- = 1$ , with  $\hat{z}$ -projection  $m_F$  states spanning the integers from  $-F$  to  $+F$ . Properly, each  $|F_{\pm}, m_F\rangle$  state is a mix of  $m_S$  and  $m_I$  which sum to  $m_F$ , given for

$F_+$ :

$$\begin{aligned} |F_+ = I + S, m_F\rangle = \\ \sqrt{\frac{F_+ + m_F}{2I + 1}} |m_I = m_F - \frac{1}{2}, m_S = +\frac{1}{2}\rangle + \sqrt{\frac{F_+ - m_F}{2I + 1}} |m_I = m_F + \frac{1}{2}, m_S = -\frac{1}{2}\rangle \end{aligned} \quad (3.4)$$

and for  $F_-$ :

$$\begin{aligned} |F_- = I - S, m_F\rangle = \\ -\sqrt{\frac{F_- - m_F}{2I + 1}} |m_I = m_F - \frac{1}{2}, m_S = +\frac{1}{2}\rangle + \sqrt{\frac{F_- + m_F}{2I + 1}} |m_I = m_F + \frac{1}{2}, m_S = -\frac{1}{2}\rangle \end{aligned} \quad (3.5)$$

Notably, the stretch states  $|F = 2, m_F = \pm 2\rangle$  contain only one term with both spins co-aligned either up or down, while each  $|m_F| < 2$  state retain two possible sums. There are non-zero elements which combine between  $F_+$  and  $F_-$  (Eqs. 3.4 and 3.5), which adjust these states away from the  $|F_\pm, m_F\rangle$  basis, but  $|F = 2, \pm 2\rangle$  remain exact. These DC Zeeman / Paschen-Back energy curves are plotted in Fig. 3.1.

Consider the Zeeman energy  $H = -\vec{\mu} \cdot \vec{B}$ , where we fix  $B_{DC}$  along the  $\hat{z}$  direction, so spin operators  $F_z, S_z, I_z$  yield good quantum numbers  $m_F, m_S, m_I$ . We can break  $\vec{\mu}$  into the Bohr magneton  $\mu_B = h \cdot 1.3996 \text{ MHz/G}$ , and weights given by gyromagnetic ratios  $g_S = 2.002319$ ,  $g_I = -0.000995$ ,  $g_{F_+} = 0.501329$ ,  $g_{F_-} = -0.499338$  [63] and  $\hat{z}$ -quantum numbers:

$$H = -\vec{\mu} \cdot \vec{B} = \frac{\mu_B g_F F_z B_z}{\hbar} = \mu_B g_F m_F B_z = \frac{\mu_B (g_S S_z + g_I I_z) B_z}{\hbar} = \mu_B (g_S m_s + g_I m_I) B_z \quad (3.6)$$

where the  $m_F$  case gives a good approximation in the low- $B_{DC}$  limit, and the  $S$  and  $I$  components contribute to the exact value, but  $S$  significantly more, as  $|g_S/g_I| \gg 1$ .

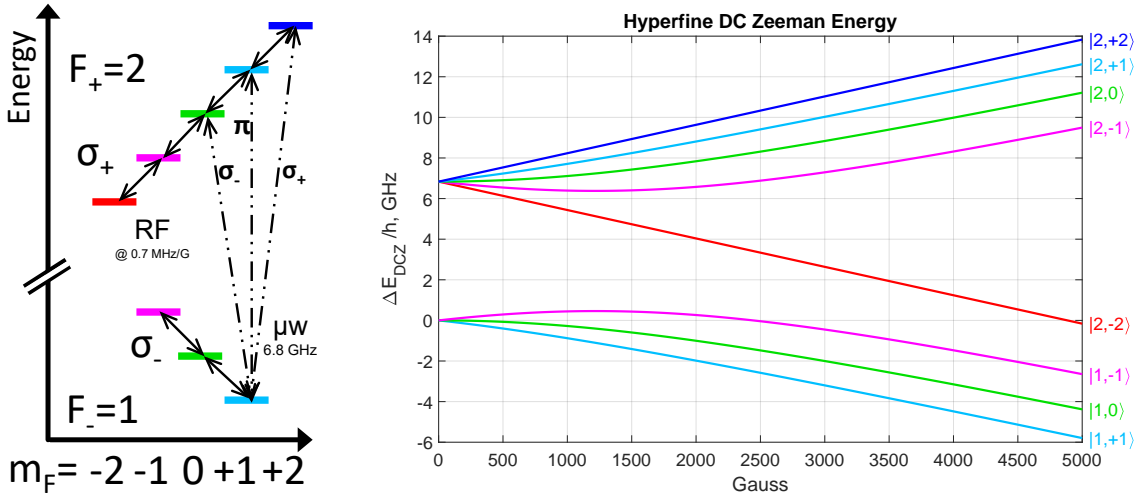


FIG. 3.1: Energies of the hyperfine ground states of  $^{87}\text{Rb}$  in a diagram (left) and as a function of applied  $B_{DC}$  (right). Energies are separated by 6.834 GHz by the hyperfine splitting. At low field,  $m_F$  are good quantum numbers, while at high field, sets of four  $m_I$  are seen for both  $m_S$  signs.

Because there exist off-diagonal elements  $\langle F = 2, m_F | F = 1, m_F \rangle$  for  $m_F = -1, 0, 1$ , these have energy adjustments when diagonalizing  $H_{HFS} + H$  across a range of  $B_{DC}$  magnitude, as shown in Fig. 3.1. We call plots like this “Breit-Rabi plots” after a well-known exact solution with  $\ell = 0$  [67]. However, we diagonalize numerically for later experiments in this work, as this approach gives both the  $|m_F\rangle$  eigenvectors and energies.

With a grip on the proper hyperfine basis states, we will continue to refer to the  $F_{\pm}$  manifolds, with  $m_F$  states as good labels at low field, although we calculate AC Zeeman energies using the diagonalized  $|I, m_I, S, m_S\rangle$ . In fact, we get all of the results from the AC Zeeman force experiment using the low- $B_{DC}$  approximations and use proper eigenvectors with higher- $B_{DC}$  in the trap experiment.

## 3.2 Transition Elements

Now we turn to the formalism that describes transitions between hyperfine states, illustrated in Fig. 3.1. We examine only single-photon transitions, where the

single unit of photon angular momentum relative to atomic quantization direction and frequency determines possible transitions. Polarizations include  $\pi$ , in which the magnetic driving field  $B_{AC}$  aligned with  $\hat{z}$  and produces no  $m_F$  change but changes the  $F$  level. The  $\sigma_{\pm}$  transitions do alter  $m_F$  by  $\pm 1$ , and can flip  $F$  between manifolds. This work focuses on the intra-manifold transitions at radio frequencies (0.7 MHz/Gauss), whereas inter-manifold transitions are at microwave frequencies ( $\approx 6.834$  GHz for  $^{87}\text{Rb}$ ). These  $\sigma_{\pm}$  transitions occur only between adjacent  $m_F$  states, and by the sign of  $g_F$  (matching  $F_{\pm}$ ), we see that only  $\sigma_+$  transitions occur in  $F_+ = 2$ , and only  $\sigma_-$  transitions occur in  $F_- = 1$ . Inspecting the level structure of Fig. 3.1, we see that when RF photon energy is added, transitions in  $F_+ = 2$  alter by  $\Delta m_F = +1$  and transitions in  $F_- = 1$  alter by  $\Delta m_F = -1$ . We will see later that this polarization dependence is crucial in tailoring AC Zeeman traps, and we will formalize the theory for now.

We turn back to  $H = -\vec{\mu} \cdot \vec{B}$ , which enabled us to find the DC Zeeman levels using self- and inter-manifold  $F_z$  terms. We look at transitions that could generate an AC Zeeman energy shift, induced by an alternating  $\vec{B}_{AC}$  field and spin ladder operators contained in  $\vec{\mu}$ . Magnetic vectors  $\vec{B}_{AC}$  (or components) that *rotate with* the DC Zeeman gyroscopes give their spins an extra ‘torque’ that does not time-average away [68]. The original name for this effect was the transverse Stern-Gerlach [38, 69], given that gradients in this rotating magnetic interaction give a spin-specific force.

We will avoid ambiguity for  $F_{\pm}$  as circular ladder operator, by using only its components, defining  $S_{\pm} = S_x \pm iS_y$  and  $I_{\pm} = I_x \pm iI_y$ , keeping  $F_{\pm}$  shorthand for 2 or 1. We can see quickly that we will have non-zero transition elements just off-diagonal for  $\langle m | \sigma_{\pm} | m \mp 1 \rangle$ . Using  $\vec{\mu} = \frac{\mu_B}{\hbar}(g_S \vec{S} + g_I \vec{I})$ ,  $S_x = (S_+ + S_-)/2$ ,  $S_y = (S_+ - S_-)/2i$

(and the same for  $B$ ) we have:

$$H = -\vec{\mu} \cdot \vec{B} = \frac{\mu_B}{\hbar} [g_S \vec{S} + g_I \vec{I}] \cdot \vec{B} \quad (3.7)$$

$$= \frac{\mu_B}{\hbar} [g_S (S_x B_x + S_y B_y + S_z B_z) + g_I (I_x B_x + I_y B_y + I_z B_z)] \quad (3.8)$$

$$= \frac{\mu_B}{\hbar} \left[ g_S \left( \frac{S_+ B_-}{2} + \frac{S_- B_+}{2} + S_z B_{RF,z} \right) + g_I \left( \frac{I_+ B_-}{2} + \frac{I_- B_+}{2} + I_z B_{RF,z} \right) \right] \quad (3.9)$$

where again, the  $S$  terms dominate  $I$  at leading order such that one can use  $\vec{\mu} = \frac{-2\mu_B}{\hbar} \vec{S}$  for 2-3 digits of accuracy.

Equation 3.9 illustrates the polarization selection of transition elements, and we should examine them further. As we can see from Fig. 3.1, the signs of  $g_F$  give a particular ladder structure to each  $F_\pm$  level, where going up in energy raises  $m_F$  by one unit in  $F_+$ , but removes  $m_F$  going up in energy in  $F_-$ . Formally, we see transition elements that look like  $\langle F_+, m'_F | S_+ | F_+, m_F \rangle$  having a non-zero value, but  $\langle F_+, m'_F | S_- | F_+, m_F \rangle = 0$  and similarly  $\langle F_-, m'_F | S_- | F_-, m_F \rangle \neq 0$  with  $\langle F_-, m'_F | S_+ | F_-, m_F \rangle = 0$ . As such, we can see that for the RF transitions within manifolds, they respect a single polarization ( $\sigma_\pm$ ), which feels only the *opposite*  $B_\mp$  field.

Fortunately, the spin ladder operators  $S_\pm$  have a simple reduction for the spin- $\frac{1}{2}$  system  $S$ :

$$S_\pm |S, m_S\rangle = \hbar \sqrt{(S \mp m_S)(S \pm m_S + 1)} |S, m_S \pm 1\rangle \quad (3.10)$$

$$S_\pm |S, m_S\rangle = \hbar \sqrt{(\frac{1}{2} + \frac{1}{2})(\frac{1}{2} - \frac{1}{2} + 1)} |S, m_S \pm 1\rangle \quad (3.11)$$

$$S_\pm |S, m_S\rangle = \hbar |S, m_S \pm 1\rangle \quad (3.12)$$

yielding just one unit of  $\hbar$ . With nuclear spin, the values depend on the value of  $I$

and  $m_I$  generally:

$$I_{\pm} |I, m_I\rangle = \hbar \sqrt{(I \mp m_I)(I \pm m_I + 1)} |I, m_I \pm 1\rangle \quad (3.13)$$

$$I_{\pm} |I, m_I\rangle = \hbar \sqrt{(\frac{3}{2} \mp m_I)(\frac{3}{2} \pm m_I + 1)} |I, m_I \pm 1\rangle \quad (3.14)$$

yielding specifically for  $I = \frac{3}{2}$  the values:

$$I_- |I, m_I = \frac{3}{2}\rangle = \hbar \sqrt{(\frac{3}{2} + \frac{3}{2})(\frac{3}{2} - \frac{3}{2} + 1)} |I, m_I = \frac{1}{2}\rangle = \sqrt{3}\hbar |I, m_I = \frac{1}{2}\rangle \quad (3.15)$$

$$I_- |I, m_I = \frac{1}{2}\rangle = \hbar \sqrt{(\frac{3}{2} + \frac{1}{2})(\frac{3}{2} - \frac{1}{2} + 1)} |I, m_I = -\frac{1}{2}\rangle = 2\hbar |I, m_I = -\frac{1}{2}\rangle \quad (3.16)$$

$$I_- |I, m_I = -\frac{1}{2}\rangle = \hbar \sqrt{(\frac{3}{2} - \frac{1}{2})(\frac{3}{2} + \frac{1}{2} + 1)} |I, m_I = -\frac{3}{2}\rangle = \sqrt{3}\hbar |I, m_I = -\frac{3}{2}\rangle \quad (3.17)$$

$$I_+ |I, m_I = \frac{1}{2}\rangle = \hbar \sqrt{(\frac{3}{2} - \frac{1}{2})(\frac{3}{2} + \frac{1}{2} + 1)} |I, m_I = \frac{3}{2}\rangle = \sqrt{3}\hbar |I, m_I = \frac{3}{2}\rangle \quad (3.18)$$

$$I_+ |I, m_I = -\frac{1}{2}\rangle = \hbar \sqrt{(\frac{3}{2} + \frac{1}{2})(\frac{3}{2} - \frac{1}{2} + 1)} |I, m_I = \frac{1}{2}\rangle = 2\hbar |I, m_I = \frac{1}{2}\rangle \quad (3.19)$$

$$I_+ |I, m_I = -\frac{3}{2}\rangle = \hbar \sqrt{(\frac{3}{2} + \frac{3}{2})(\frac{3}{2} - \frac{3}{2} + 1)} |I, m_I = -\frac{1}{2}\rangle = \sqrt{3}\hbar |I, m_I = -\frac{1}{2}\rangle \quad (3.20)$$

Sandwiching  $S_{\pm}$  and  $I_{\pm}$  between  $|F_{\pm}, m_F = m_S + m_I\rangle$  states, as decomposed in Eqs. 3.4 and 3.5, we can compute the intra-manifold transition elements within  $F_+$ :

$$\langle m'_S = \pm \frac{1}{2}, m'_I | S_{\pm} | m_S = \mp \frac{1}{2}, m_I \rangle = \hbar \frac{\sqrt{(2 \pm m'_F)(2 \mp m_F)}}{2I + 1} \delta_{m'_F, m_F \pm 1} \quad (3.21)$$

$$\langle m'_S, m'_I \pm 1 | I_{\pm} | m_S, m_I \rangle = \hbar \sqrt{(I \mp m_I)(I \pm m_I + 1)} \frac{\sqrt{(2 \pm m'_F)(2 \mp m_F)}}{2I + 1} \delta_{m'_F, m_F \pm 1} \quad (3.22)$$

and within  $F_-$ :

$$\langle m'_S = \pm \frac{1}{2}, m'_I | S_{\pm} | m_S = \mp \frac{1}{2}, m_I \rangle = -\hbar \frac{\sqrt{(2 \mp m'_F)(2 \pm m_F)}}{2I + 1} \delta_{m'_F, m_F \pm 1} \quad (3.23)$$

$$\langle m'_S, m'_I \pm 1 | I_{\pm} | m_S, m_I \rangle = -\hbar \sqrt{(I \mp m_I)(I \pm m_I + 1)} \frac{\sqrt{(2 \mp m'_F)(2 \pm m_F)}}{2I + 1} \delta_{m'_F, m_F \pm 1} \quad (3.24)$$

When calculating, I only consider the transition elements of  $S_{\pm}$  ( since  $I_{\pm}$  is heavily suppressed by  $\left| \frac{g_S}{g_I} \right|$ ), using the state's Clebsch-Gordan coefficients which include full  $|S, m_S, I, m_I\rangle$  contributions. For simple pen-and-paper analysis and to gain intuition, it is convenient to calculate using only  $S$ , ignoring  $I$ . Values of the RF transition elements are given by

$$\langle 1, 0 | S_+ | 1, -1 \rangle = \langle 1, 1 | S_+ | 1, 0 \rangle = -\hbar \frac{\sqrt{2}}{4} = -\hbar \sqrt{\frac{1}{8}} = -0.3536\hbar \quad (3.25)$$

$$\langle 2, -1 | S_+ | 2, -2 \rangle = \langle 2, 2 | S_+ | 2, 1 \rangle = \hbar \frac{\sqrt{4}}{4} = \hbar \sqrt{\frac{2}{8}} = 0.5\hbar \quad (3.26)$$

$$\langle 2, 0 | S_- | 2, -1 \rangle = \langle 2, 1 | S_- | 2, 0 \rangle = \hbar \frac{\sqrt{6}}{4} = \hbar \sqrt{\frac{3}{8}} = 0.6124\hbar \quad (3.27)$$

We can obtain exact values numerically from the eigenvector elements when diagonalizing the  $I + S$  basis at non-zero  $B_{DC}\hat{z}$  field into the basis we call  $|F, m_F\rangle$ . The following array gives numerical values of these  $\langle F', m'_F | S_{\pm}, z | F, m_F \rangle$  transition elements at 20 MHz / 28.58 Gauss, where the right vector is simply a label to the order of the  $|F, m_F\rangle$  basis states.

$$\begin{pmatrix} 0 & 0.4958 & 0 & 0 & 0 & -0.8698 & 0 & 0 \\ 0.4958 & 0 & 0.6090 & 0 & 0 & 0.8674 & -0.6168 & 0 \\ 0 & 0.6090 & 0 & 0.6108 & 0 & 0.3520 & 1.0016 & -0.3572 \\ 0 & 0 & 0.6108 & 0 & 0.5001 & 0 & 0.6114 & 0.8674 \\ 0 & 0 & 0 & 0.5001 & 0 & 0 & 0 & 0.8673 \\ -0.8698 & 0.8674 & 0.3520 & 0 & 0 & 0 & -0.3561 & 0 \\ 0 & -0.6168 & 1.0016 & 0.6114 & 0 & -0.3561 & 0 & -0.3572 \\ 0 & 0 & -0.3572 & 0.8674 & 0.8673 & 0 & -0.3572 & 0 \end{pmatrix} \begin{pmatrix} |2, +2\rangle \\ |2, +1\rangle \\ |2, 0\rangle \\ |2, -1\rangle \\ |2, -2\rangle \\ |1, +1\rangle \\ |1, 0\rangle \\ |1, -1\rangle \end{pmatrix}$$

We have RF transitions just off the main diagonal, the top-right and bottom-left corners have  $3 \times 3 = 9$  microwave transitions [60].

### 3.3 Two-Level Theory

We can view any single transition in a more general two-level approach, which allows us to write some exact expressions and generate some intuition about the atomic system. We will later expand this two-level formalism to a multi-level ladder system.

To begin our two-level discussion, we take two states, an excited state  $|e\rangle$ , and a ground state  $|g\rangle$  where the states and couplings can be hand-picked from the preceding subsections. The total atomic wavefunction is

$$\Psi_A = C_e e^{-i\hbar\omega_e t} |e\rangle + C_g e^{-i\hbar\omega_g t} |g\rangle = \begin{pmatrix} C_e e^{-i\hbar\omega_e t} \\ C_g e^{-i\hbar\omega_g t} \end{pmatrix} \quad (3.28)$$

with relative amplitude coefficients  $C_e, C_g$  and state energy  $E_e = \hbar\omega_e, E_g = \hbar\omega_g$ . At the end of an experiment, we have experimental access to the population ratios in the  $|e\rangle, |g\rangle$  basis:  $|\Psi|^2 = |C_e|^2 + |C_g|^2$ , constrained by  $|C_e|^2 + |C_g|^2 = 1$ .

Whichever pair of states we pick, they are separated by  $\Delta E_{eg} = E_e - E_g = \hbar(\omega_e - \omega_g) = \hbar\omega_{eg}$ . I will subtract a potential offset from both states, defining the excited state as the reference energy, and the ground an amount  $\hbar\omega_{eg}$  below.

$$\hat{H}_A |\Psi\rangle_A = \hbar \begin{pmatrix} 0 & 0 \\ 0 & -\omega_{eg} \end{pmatrix} \begin{pmatrix} |e\rangle \\ |g\rangle \end{pmatrix} \quad (3.29)$$

We now add a photon to the mix, or rather, a large driven AC magnetic field  $|B_{RF}|cos(\omega_{RFT})\hat{x}$ , comprised of many ( $N \simeq N + 1$ ) photons. This linearly polarized field has half strength in each circular polarization, and only one polarization is ‘felt’ by RF transitions within each of  $F_{\pm}$ . The photon’s *electric* field cannot drive transitions between hyperfine states, and can be safely ignored. We had attempted

to quantified the effect as a far off-resonant (nearly DC) AC Stark Shift, which we have found to be  $\approx 1\%$  of a resonant AC Zeeman shift.

To consider the addition of many photons, we should examine a single photon absorption, recalling that polarization couples only certain transitions. An atom will transition between  $|g\rangle$  and  $\langle e|$  by absorbing a photon, promoting the electron into a higher energy state by altering the spin state. Conversely, an atom in  $|e\rangle$  state is stimulated by a photon into  $\langle g|$ , emitting a coherent photon into the  $B_{RF}$  field. In either case, the ground state plus the photon makes the excited state, where we recall the importance of polarization. It is convenient to consider stimulated emission of the correct polarization, rather than absorbing the opposite polarization, as the reverse process to absorption. Examining the energy difference after a single-photon change in the RF magnetic field energy  $\hat{H}_\gamma$  between the states with  $N_\gamma$  and  $N_\gamma + 1$  photons,

$$\hat{H}_\gamma |\Psi\rangle_\gamma = \hbar \begin{pmatrix} 0 & 0 \\ 0 & \omega_{RF} \end{pmatrix} \begin{pmatrix} |N_\gamma\rangle \\ |N_\gamma + 1\rangle \end{pmatrix} \quad (3.30)$$

The correlation between the atom state ( $e, g$ ) and number of photons ( $N_\gamma, N_\gamma + 1$ ) prompts us to combine these into ‘dressed’ states:

$$|\Psi_D\rangle = \begin{pmatrix} |e, N_\gamma\rangle \\ |g, N_\gamma + 1\rangle \end{pmatrix} \quad (3.31)$$

Considering the energy of such a system,  $\hbar\omega_{RF}$  plus the atomic spacing ( $\hbar\omega_{eg}$ ) yields the bare state Hamiltonian

$$\hat{H}_a + \hat{H}_\gamma |\Psi_B\rangle = \hat{H}_D |\Psi_D\rangle = \hbar \begin{pmatrix} 0 & 0 \\ 0 & \omega_{RF} - \omega_{eg} \end{pmatrix} |\Psi_D\rangle = \hbar \begin{pmatrix} 0 & 0 \\ 0 & \delta \end{pmatrix} \begin{pmatrix} |e, N_\gamma\rangle \\ |g, N_\gamma + 1\rangle \end{pmatrix} \quad (3.32)$$

Here, I introduce an important parameter, the ‘detuning’  $\delta \equiv (\omega_{RF} - \omega_{eg})$ . The

detuning represents extra energy that the photon has, compared to the state separation. Positive detuning ( $\delta > 0$ , right-ward on many graphs) implies extra photon energy added to a ground state. In contrast, negative detuning ( $\delta < 0$ , left-ward on many graphs) implies insufficient photon energy added to the ground state to reach the excited state. Zero detuning ( $\delta = 0$ , typically graph center) defines the *on-resonance* condition, where the state mixing, interaction energy, ACZ force, and trap depth are all maximized. When graphing the state energies as a function of photon frequency on the  $x$ -axis, often shown in this thesis, the excited state (or my  $m_F = 0$  choice of reference state) will be a flat line, as it contains no extra photons. The ground state will have a positive slope with added photons, crossing the excited energy line at the  $\delta = 0$  point. Excited states with fewer photons will have a negative slope relative to the reference energy. This behavior is shown by the gray lines in Fig. 3.2.

Any oscillating magnetic field with the proper polarization will generate an interaction term, appearing as off-diagonal elements  $\langle e | -\vec{\mu} \cdot \vec{B}_{RF} | g \rangle$  in the Hamiltonian, as we have just examined in Sec. 3.2.

This term will govern how quickly atoms transfer between  $|e\rangle$  and  $|g\rangle$ . In the Schrödinger picture, a diagonal Hamiltonian matrix denotes energy in each of the basis vector  $|\Psi\rangle$  states. The presence of off-diagonal elements suggests that there is a better basis to read the energy of the system because the Hamiltonian acts as a time operator, and there will be population density transfer between states in the initial basis.

We are constrained by the allowed transitions  $\langle e | \leftrightarrow | g \rangle$  between these two atomic spin states, driven by a linear oscillating field perpendicular to  $\hat{z}$ , by construction:

$$\langle e | -\vec{\mu} \cdot | B_{RF} | \cos(\omega_{RF} t) \hat{x} | g \rangle \quad (3.33)$$

Spin operators  $S_{\pm}$  and  $I_{\pm}$ , contained in  $\vec{\mu}$  can transform  $|g\rangle$  into  $\langle e|$ , as we have examined in Sec. 3.2. This interaction Hamiltonian matrix has the general form:

$$\hat{H}_I |\Psi_B\rangle = \hbar \begin{pmatrix} 0 & \Omega_{eg} \cos(\omega_{RFT}) \\ \Omega_{eg}^* \cos(\omega_{RFT}) & 0 \end{pmatrix} \begin{pmatrix} |e, N_{\gamma}\rangle \\ |g, N_{\gamma} + 1\rangle \end{pmatrix} \quad (3.34)$$

The value  $\Omega_{eg} = \langle e| - \vec{\mu} \cdot \vec{B}_{RF} |g\rangle$  represents the *Rabi Frequency*, an important parameter in our investigation. Its magnitude scales with field amplitude  $|B_{RF}|$ , as well as the Clebsch-Gordan coefficients from the previous section. Ignoring the nuclear spin, the Rabi frequency is given by:

$$\hbar\Omega_{eg} = \langle e| - \mu \cdot B_{RF} |g\rangle = \frac{\mu_B g_S}{\hbar} \langle e| \frac{S_+ B_-}{2} + \frac{S_- B_+}{2} + S_z B_{RF,z} |g\rangle \quad (3.35)$$

Accounting for factors of 2 in the denominator, the one given is due to our circular definition ( $A_{\pm} = A_x \pm iA_y$  for any vector  $\vec{A}$ ) acting on  $S_x B_x$  or  $S_y B_y$ , another comes from projecting a linear field into a circular one  $|B_+| = |B_-| = |B_{RF}|/2$ , another from the rotating wave approximation (in Appx. A), and then the Clebsch-Gordan coefficients give another factor of  $\frac{\sqrt{2,4,6}}{4}$ , depending on choice of  $(e, g)$ . The value of  $g_S$  is nearly 2, so it can cancel one of the polarization factors. We can pull out a common factor that we call the ‘Rabi Strength’:

$$\Omega_0 \equiv \frac{\mu_B |B_{\pm}|}{\hbar} \quad (3.36)$$

which measures the circular field alone, either projecting from the linear  $B_{RF} \hat{x}$  or generating  $B_{\pm}$  on their own, as we discuss later. This ‘strength’ is everything in the off-diagonal of the final dressed atom Hamiltonian *but* the Clebsch-Gordan coefficient and a later  $\frac{1}{2}$  from the rotating wave approximation (RWA). The value

$\Omega_0$  lacks transition information, which is retained in the full value:

$$\Omega_{eg} = \Omega_0 \frac{\langle e | g_S S_\pm | g \rangle}{2\hbar} \quad (3.37)$$

In calculations, we typically use  $h$  instead of  $\hbar$  to work in frequency units (identified with the RF system's  $f_{RF}$  output) instead of angular frequencies ( $\omega_{RF}$ ) which are preferred when communicating physics. The values of  $\Omega_0$  reported in Chap. 4 match the typical reporting definition of  $\Omega = 2\pi \times (\text{value})$ , although due to our non-uniform circular definitions, this definition may differ from others by a factor of 2. It is a good parametric handle on ‘strength’ for the *whole* RF transition, rather than giving multiple unique numbers for each Hermitian pair.

We now add in this off-diagonal energy  $-\mu \cdot B_{RF} \cos(\omega_{RF}t) \hat{x}$  to our Hamiltonian:

$$\hat{H}_D |\Psi_D\rangle = \hbar \begin{pmatrix} 0 & \Omega_{eg}/2 \\ \Omega_{eg}^*/2 & \delta \end{pmatrix} \begin{pmatrix} |e, N_\gamma\rangle \\ |g, N_\gamma + 1\rangle \end{pmatrix} \quad (3.38)$$

where we have performed the rotating wave approximation, which we will discuss later in this chapter.

The Hermitian conjugate term  $\Omega_{eg}^*$  is a bit difficult to analyze. Simple conjugation swaps  $S_+ B_-$  and  $S_- B_+$ , but as we continue to argue and demonstrate, *only* one polarization contributes to the entire interaction. We then invoke  $\Omega_{eg}^* \equiv \Omega_{eg}$  for calculations, using the same  $S_\pm B_\mp$  combination in both elements that we know acts on the manifold. These elements are hand-selected by physical motivations rather than mathematical ones.

Finding the eigenvalues of this matrix yields the AC Zeeman energy eigenvalues for the two states:

$$E_\pm = \frac{\hbar}{2} \left( \delta \pm \sqrt{\delta^2 + \Omega_{eg}^2} \right) = \frac{\hbar}{2} (\delta \pm \Omega') \quad (3.39)$$

and we can subtract out the basis states to measure just the added AC Zeeman energy:

$$E_{ACZ\pm} = \pm \frac{\hbar}{2} \left( -|\delta| + \sqrt{\delta^2 + \Omega_{eg}^2} \right) = \pm \frac{\hbar}{2} (-|\delta| + \Omega') \quad (3.40)$$

We use the ‘Generalized Rabi Frequency’  $\Omega' = \sqrt{\delta^2 + \Omega_{eg}^2}$ . This parameter can be viewed as the hypotenuse of a right triangle with legs  $\delta\hat{z}$  and  $\Omega_{eg}\hat{x}$ , which acts as a torque on the spin orientation between basis states. This vector is the green Generalized Rabi vector on the Bloch sphere in Fig. 3.3.

We also get the eigenvectors of the interactive dressed system:

$$|+\rangle = \cos(\theta) |g, N_\gamma + 1\rangle + \sin(\theta) |e, N_\gamma\rangle \quad (3.41)$$

$$|-\rangle = -\sin(\theta) |g, N_\gamma + 1\rangle + \cos(\theta) |e, N_\gamma\rangle \quad (3.42)$$

where we use  $\cos(\theta) = \frac{\Omega_{eg}}{\sqrt{\Omega_{eg}^2 + (\Omega' - \delta)^2}}$  and  $\sin(\theta) = \frac{\Omega' - \delta}{\sqrt{\Omega_{eg}^2 + (\Omega' - \delta)^2}}$ . We plot both the two-level AC Zeeman energies and state projections in Fig. 3.2.

We observe that  $\theta$  is a population-tuning parameter, where the sign of detuning and its relation to  $\Omega_{eg}$  determine the population ratio and phase between the initial dressed states. In one sense,  $\theta$  measures the polar angle on the Bloch sphere, where pure dressed states are located at either the north or south pole ( $\pm 1\hat{z}$ ), as illustrated in Fig. 3.3. Projections far off-resonance ( $|\delta| \gg |\Omega_{eg}|$ ) will keep atoms mostly in their dressed states. In contrast, near resonance ( $|\delta| \approx |\Omega_{eg}|$ ), the dressed states necessarily mix, generating extra energy, which avoids the level crossing degeneracy.

We can leverage this behavior for a technique called Adiabatic Rapid Passage (ARP), where we sweep detuning from one side of resonance to the other, flipping the spin population between basis states as shown in Fig. 3.2. On the Bloch sphere, this looks like the green vector rotating from  $\pm\hat{z}$  to  $\mp\hat{z}$  in the  $xz$ -plane, while the pink population arrow continually rotates around the green vector, settling at the

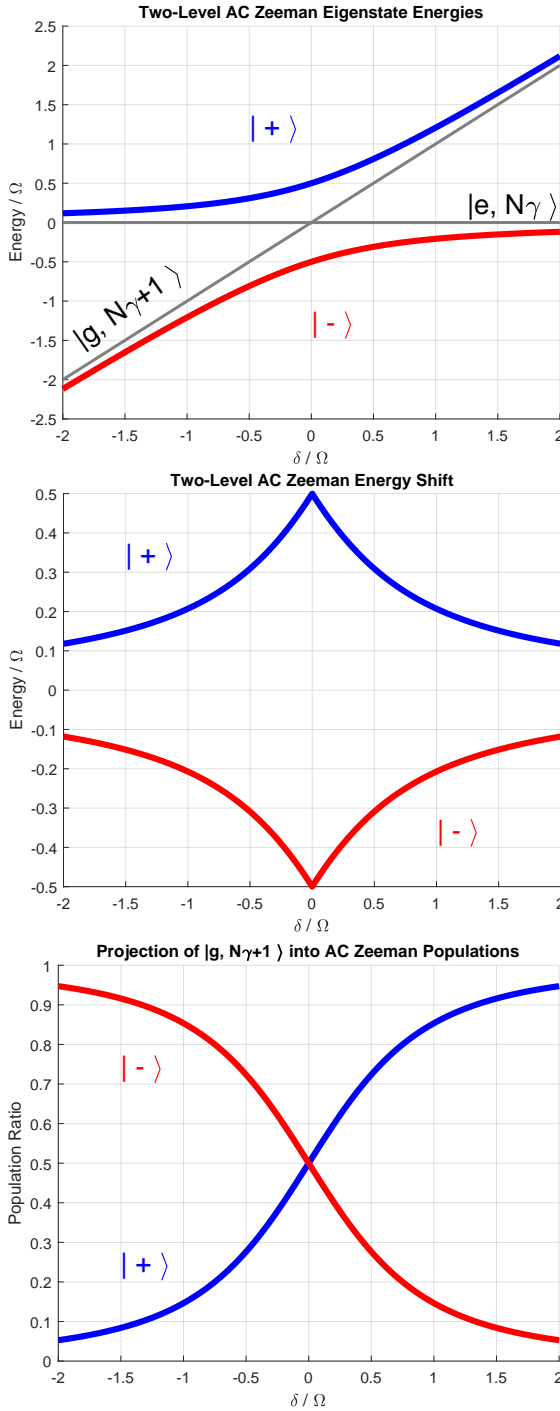


FIG. 3.2: Dressed atom theory for a two-level atom. Top: AC Zeeman eigenstate energy, normalized by  $\Omega$ . Both dressed states and AC Zeeman eigenstates are labeled, projecting to each other far off resonance. Middle: AC Zeeman energy shift of the eigenstates relative to the dressed state energies. Bottom: Two-level population curves, projecting  $|g, N_\gamma + 1\rangle$  into  $|+\rangle$  and  $|-\rangle$ . Either eigen-energy curve  $|+\rangle$  or  $|-\rangle$  has inverse components in the dressed states  $|g, N_\gamma + 1\rangle$  and  $|e, N_\gamma\rangle$ , which vary with  $\delta/\Omega$ .

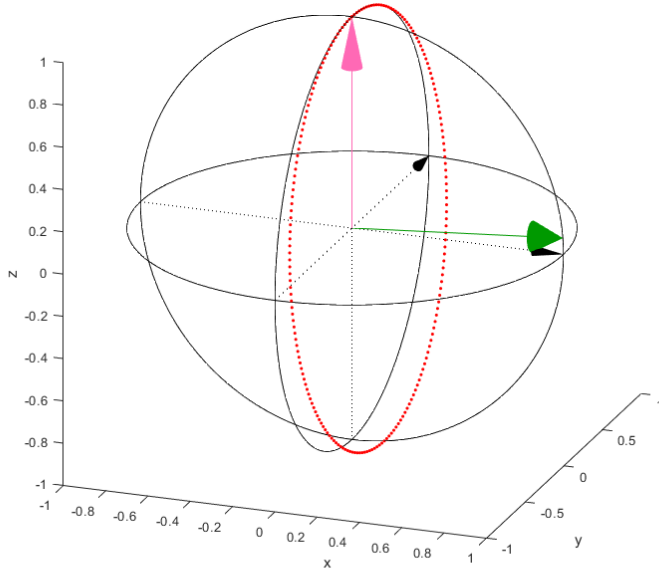


FIG. 3.3: Rotation on the Bloch sphere, one way to picture Rabi oscillations. The population vector (pink) begins at a pure population at the ‘north pole’ along  $\hat{z}$  and is rotated through one revolution around the generalized Rabi vector (green), which is held slightly above resonance ( $\delta > 0$ ). An off-resonant flop leaves the population transfer incomplete at the bottom, missing the ‘south pole’ before it rotates back up, marked by the red dots.

opposite pole from where it started, creating a complete population transfer between basis states.

I want to spend some time now with the meaning of Rabi frequency and how we measure it. First, sweeping frequencies from pure states ( $|g, N_\gamma + 1\rangle$  or  $|e, N_\gamma\rangle$ ) off-resonance can lock a population into one of the AC Zeeman curves ( $|+\rangle$  or  $|-\rangle$ ) in Fig. 3.2, and the Rabi frequency is seen to alter energy, rendering  $\Omega'$  visible via spectroscopy, relative to other states. The method we elect to use is rather direct, to simply pulse on the signal near resonance and observe how the population evolves in time. Taking this Bloch sphere picture, we could imagine observing the population at fixed time steps through the procedure, represented by the ring of red dots. The resonant condition will have  $\Omega'$  minimized to  $\Omega_{eg}$ , and fully sinusoidal transfer between the basis states with time. Off resonance (as shown in Fig. 3.3), the ‘flop’ is not complete and has a faster period, per the definition of  $\Omega'$ . In Chap. 4, we will

discuss the case of Rabi flopping for five levels, beyond the two-level case presented here.

### 3.4 AC Zeeman Force

In the case presented here, we look at a linearly polarized field  $B_{RF} \cos(\omega_{RFT})\hat{x}$  (perpendicular to the quantizing axis  $\hat{z}$ ), which generated coupling  $\Omega_{eg}$ , adjusting energy in the system by mixing states, especially on resonance. Consider a  $1/r$  gradient in this field, as there might be in the magnetic near field of a wire. We assume that the background  $B_{DC}$  field is homogeneous in amplitude and orientation, rendering  $\delta$  constant over space. Recalling our AC Zeeman energy  $E_{ACZ\pm} = \pm \frac{\hbar}{2} (-\delta + \sqrt{\delta^2 + \Omega_{eg}^2})$ , we can write the AC Zeeman two-level force

$$F_{ACZ} = -\nabla E_{\pm} = \mp \frac{\hbar}{2} \frac{\Omega_{eg}}{\Omega'} \frac{d\Omega_{eg}}{dr} \quad (3.43)$$

If our current of amplitude  $I_0$  is a current line current (in the thin wire approximation), then we have  $|B_{RF}| = \frac{\mu_0 I_0}{2\pi r}$  and  $\nabla B_{RF} = -\frac{\mu_0 I_0}{2\pi r^2}$  giving the values of  $\Omega_{eg}$ ,  $\Omega'$ , and  $\frac{d\Omega_{eg}}{dr}$  in this simple model. Later, we use models which include the spatial extent of the wires, splitting the whole current into many constituent line currents to sum over. In experiment, where we don't have an exact model of the wires, we need empirical measurements of  $\Omega_{eg}$ ,  $\frac{d}{dr}(\Omega_{eg})$ , and  $\delta$  at the atoms' location to predict an experimental force, *ab initio*.

Indeed, this concept is at the core of this work: we generate an RF magnetic field that varies in amplitude over space, leading to spatial gradients in the *coupling* components of Eq. 3.38, which affect the AC Zeeman energy when we diagonalize the couplings with the detuning, generating a spatially varying  $\Omega'_{eg}$ . If we can tailor  $B_{\pm}(r) \rightarrow \Omega_{eg}(r)$  to have a high gradient, as near an atom chip, we can have a high

impulse on atoms. If we can make a local minimum in  $B_{\pm}(x, y) \rightarrow \Omega_{eg}(x, y)$ , the upward gradient around it in all directions will provide a spatial restoring force for atoms, trapping them.

This concludes the pedagogical work using the two-level system. We will now show that we can establish a five-level dressed state Hamiltonian, giving us the AC Zeeman eigenvalues for the entire intra-manifold case after diagonalization. Much of the intuition from the two-level case still applies in a chained-two-level-ladder system, but clean expressions for  $E_{ACZ}$  and population are cumbersome when available, and there is not an easy Bloch sphere picture to help us out.

### 3.5 Five-level Eigenstate Curves

The mathematical foundation for this section is laid out in Appendix A, which derives a time-independent Hamiltonian by introducing time-dependent basis states. I elect to retain the low-field limit Clebsch-Gordan coefficients in their analytic forms, as it is instructive. The relevant result from that section is given here:

$$i\hbar \frac{d}{dt} \begin{pmatrix} \tilde{C}_{-2} \\ \tilde{C}_{-1} \\ \tilde{C}_0 \\ \tilde{C}_{+1} \\ \tilde{C}_{+2} \end{pmatrix} = \hbar \begin{pmatrix} \Delta_{-2} & \frac{\sqrt{4}}{4}\Omega_0 & 0 & 0 & 0 \\ \frac{\sqrt{4}}{4}\Omega_0^* & \Delta_{-1} & \frac{\sqrt{6}}{4}\Omega_0 & 0 & 0 \\ 0 & \frac{\sqrt{6}}{4}\Omega_0^* & \Delta_0 & \frac{\sqrt{6}}{4}\Omega_0 & 0 \\ 0 & 0 & \frac{\sqrt{6}}{4}\Omega_0^* & \Delta_{+1} & \frac{\sqrt{4}}{4}\Omega_0 \\ 0 & 0 & 0 & \frac{\sqrt{4}}{4}\Omega_0^* & \Delta_{+2} \end{pmatrix} \begin{pmatrix} \tilde{C}_{-2} \\ \tilde{C}_{-1} \\ \tilde{C}_0 \\ \tilde{C}_{+1} \\ \tilde{C}_{+2} \end{pmatrix} \quad (3.44)$$

The  $\Delta$  terms contain both the detuning and the slight non-degeneracy of atomic states, and still  $\hbar\Omega_0 = \mu_B|B_{\pm}|$ ,

We now look to diagonalize the Hamiltonian derived in Eq. 3.44, examining the eigenstates and their energies as we did in the two-level case. We do this numerically by plugging in a range of  $f_{RF}$  frequencies, with couplings  $\Omega_{eg}/2\pi$  that are state- and

$B_{DC}$ - dependent, mixing  $I$  and  $S$  into the  $|F_{\pm}, m_F\rangle$  basis, as described earlier in this chapter.

We show in Fig. 3.4 the five- and three-level ( $F_+$  and  $F_-$ ) AC Zeeman eigenstates, for a resonance held near 20 MHz ( $B_{DC} \approx 28.58$  Gauss), with  $\Omega_0/2\pi = \mu_B|B_{\pm}|/h = 500$  kHz ( $|B_{\pm}| \approx 0.36$  Gauss). We show the DC Zeeman energy levels in Fig. 3.4(a1,a2), with a dashed line indicating our resonance. These  $m_F$  states are slightly non-degenerate, seen in the gray line crossings of Fig. 3.4(b1,b2). In Fig. 3.4(b1,b2), we show the result of diagonalizing Eq. A.10 to obtain the AC Zeeman energies. The plots in Fig. 3.4(c1,c2) give just the added energy compared to the  $\Omega_0 = 0$  condition. This energy difference between bare states and the dressed eigenenergy curves defines the AC Zeeman energy in the system. We use the  $E_{ACZ}$  calculations of Fig. 3.4(c1,c2) combined with an ad-hoc gradient of  $2\pi \times 5$  kHz/ $\mu\text{m}$ , to obtain the RF AC Zeeman force curves shown in Fig. 3.4(d1,d2).

The lower half of Fig. 3.4 represents the dressed state projections of the AC Zeeman states, as a function of frequency, a more compounded version of the  $\cos^2(\theta)$  eigenvector terms from the two-level case.

We can see interesting near-resonant structure which requires this sort of advanced numeric calculation. If we were to increase  $\Omega_0$  by a large factor, this has the effect of broadening each resonance (recalling  $\delta/\Omega$  as a good handle) and ‘washing out’ some of the structure which appears at low coupling. In fact, at very low  $\Omega_0$  power, only the  $|++\rangle$  and  $|+\rangle$  curves separate at the four single-photon resonances. When  $\Omega_0$  is large enough, these real transitions broaden to affect the three connection points of  $|+\rangle$  to  $|0\rangle$ , then the two points into  $|-\rangle$ , finally to the one ‘resonance’ in  $|--\rangle$  which connects  $m_F = 2$  and  $m_F = -2$  via a composite coupling of sorts.

The sign of the force curves lets us know which states are high- or low- field seeking given a gradient, having their energy lowered by either increasing or decreasing coupling, respectively. We note that the strongest weak-field seeker is the

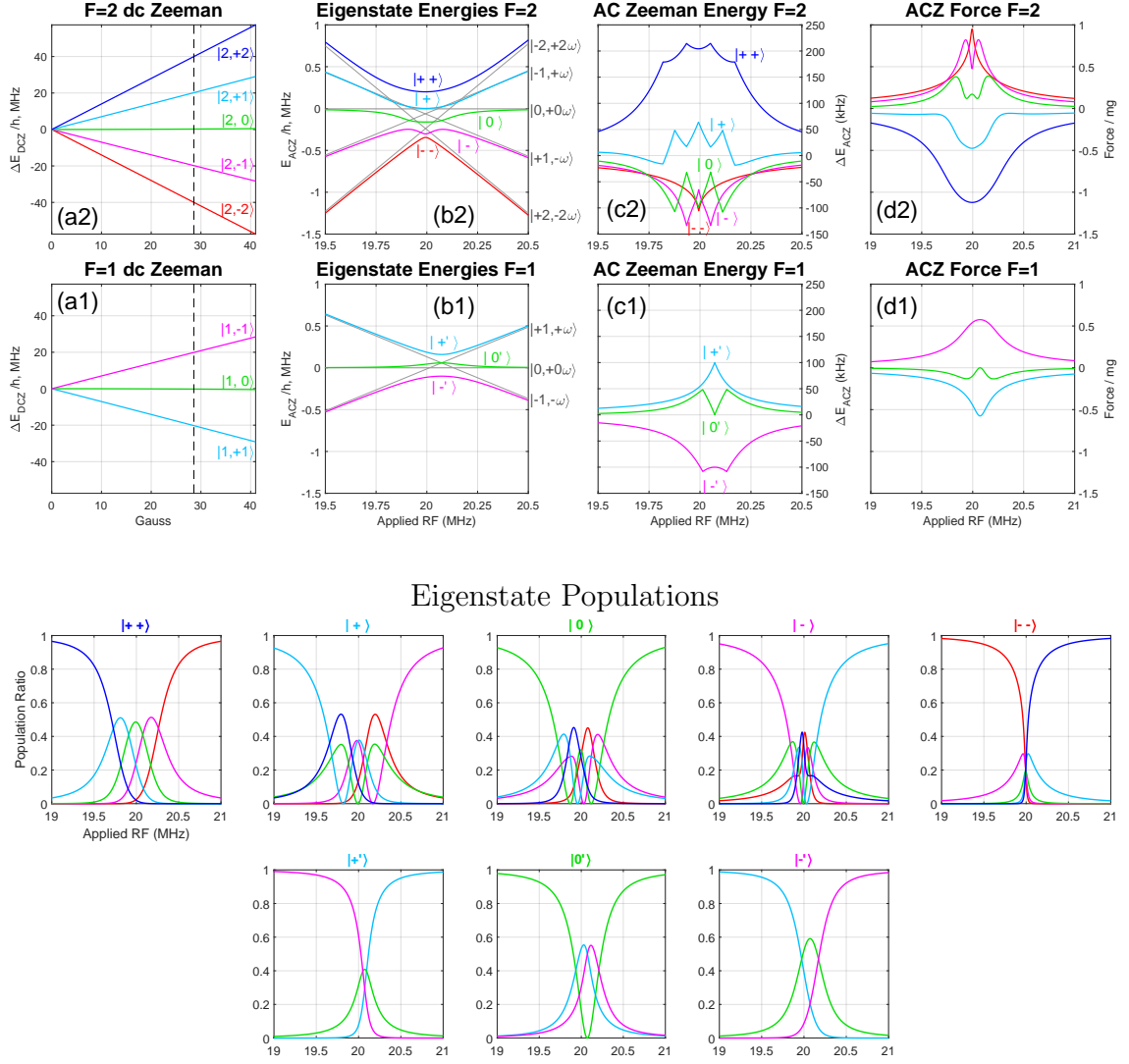


FIG. 3.4: AC Zeeman states, energies, forces, and populations. Top eight: Plots of five level and three AC Zeeman states, described in the text. In this simulation,  $\Omega_0/2\pi = 500 \text{ kHz}$ ,  $\nabla\Omega_0/2\pi = 5 \frac{\text{kHz}}{\mu\text{m}}$ . Bottom eight: Population projections from each AC Zeeman state into dressed states vs. applied frequency detuning. Each title gives the state name and matches color with (b-d), but the plotted curves match color to the dressed states  $|m_F, N \mp m_F\rangle$ , whose  $m_F$  part is given in (a).

$|++\rangle$  state, which can populate either  $|m_F = +2\rangle$  at red detuning or  $|m_F = -2\rangle$  at blue detuning. Similarly, the  $F_- = 1$  manifold's  $|+'\rangle$  state is a weak-field seeker, which can occupy either  $|m_F = -1\rangle$  at red detuning or  $|m_F = +1\rangle$  at blue detuning. While DC Zeeman  $m_F$  states are ‘locked-in’ as DC high- or low-field seekers by the sign of  $m_F g_F$ , they can all be trapped as low-field seekers in an AC Zeeman trap.

One curiosity comes from the  $F_+ = 2$ 's  $|+\rangle$  state, which is high-field seeking at low power, but low-field seeking at high power, making it a *medium*-field seeker near the four atomic resonances.

## 3.6 Summary

This covers the atomic theory behind the AC Zeeman effect, as relevant to our purposes. To summarize, applying a oscillating magnetic field that nearly matches the frequency of atomic transitions will induce absorption and emission, driving Rabi oscillations between the states, which alters their total energy. Leveraging a high gradient in this energy, we can generate a spin-specific force on atoms or trap them in a local minimum of the  $B_\pm$  field, as we will go on to demonstrate in Chaps. 5 and 7. However, we first discuss the process of measuring Rabi frequency in Chap. 4.

# CHAPTER 4

## Rabi Frequency Measurement

Rabi ‘flopping’ is the oscillation of population between atomic states that occurs when atoms are driven by a near-resonant electromagnetic wave. The spin vector of the atom precesses around an effective magnetic field, ‘flopping’ population between states, governed in time by the amplitude and frequency of the applied electromagnetic waves. On resonance, two states flop like a sine wave with an angular frequency given by the Rabi Frequency  $\Omega_{eg}$ , a definition that gets fuzzy when discussing five non-degenerate levels with unique coupling coefficients. In this chapter, we observe flopping at incremental fixed times, giving experimental population evolution over time, which we fit to get the Rabi frequency, representing the effective driving field strength for the atomic system.

Section 4.1 introduces the concepts and definitions at work in this chapter. We separate this chapter into measurements corresponding to 1) the force experiment of Chap. 5, and 2) the trap experiment of Chap. 7, although the analysis shares many details. We discuss the force setup in Sec. 4.2, moving to the actual measurement technique in Sec. 4.2.1, fitting techniques in Sec. 4.2.2, and power scaling in Sec. 4.2.3. We discuss Rabi frequency gradient measurements in Sec. 4.2.4, including

the position shifting ‘sag’ method in Sec. 4.2.5. We move on to measurements for the trap experiment in Sec. 4.3, including a ‘triangulation’ gradient measurement in Sec. 4.3.1. In Sec. 4.4, we list the fit values for Rabi frequency measurements which provide the ‘theory’ curves in later chapters. Lastly, we summarize the chapter in Sec. 4.5.

## 4.1 Introduction

In our case, Rabi ‘flopping’ will occur for the four transitions between *adjacent* states in a five-level ladder arrangement, which then flop into successive states by the same driving field. The net effect is a cyclic five-level flop in primary  $m_F$  population from  $2 \rightarrow 1 \rightarrow 0 \rightarrow -1 \rightarrow -2 \rightarrow -1 \rightarrow 0 \rightarrow 1 \rightarrow 2 \rightarrow \dots$ . We can simulate this phenomenon by directly time-evolving the dressed state population vector (nearly pure  $|F_+, m_F = +2, N_\gamma - 2\rangle$ ) with the Hamiltonian given in Eq. A.10, and watching the  $m_F$  basis vectors as they evolve in time, given a constant applied frequency and magnetic field amplitude.

Having an empirical measurement of  $\Omega_{eg}$  is a powerful analytic tool, which can generate theory curves to compare with data. We also learn about the power coupling of the signal into the atom chip (assuming  $\Omega_{eg} \propto I_0/r$ ), and knowing the power  $P_0$  sent to the chip, we can deduce for a given frequency the impedance  $Z(\omega_{RF}) = P_0/I_0^2$  for the system. We use this fact to measure Rabi frequency at low values of applied power, which we can then directly scale to much larger values of  $\Omega_{eg}$  for our experiment and the design of future high-power schemes. We see roughly the same Rabi gradient using 15 mW of 8.4 MHz RF power as for 3.3 W of 6.8 GHz of microwave power, due to power coupling differences as discussed in Sec. 2.9. In the end, direct measurements of the atoms showing the Rabi frequency are our best empirical metric on the strength of the ACZ effect, especially across space.

I want to be very explicit about how Rabi frequency and ‘strength’ are defined in this chapter since the idea is a bit different to grasp in  $N$ –level systems. We desire to algebraically pull out one value for the entire five-level system, which gets scaled by Clebsch-Gordan coefficients into the off-diagonal coupling elements. There is always  $\frac{\Omega_{eg}}{2}$  off-diagonal, motivated by the RWA, to yield a form like the two-level Hamiltonian in Eq. 3.38. What remains we seek to simplify by separating the field and the transition:  $\Omega_{eg} = \langle e | -\vec{\mu} \cdot \vec{B} | g \rangle = \Omega_0 \frac{\langle e | g_s S_{\pm} | g \rangle}{2\hbar}$ , where  $\Omega_0 = \mu_B |B_{\mp}|/\hbar$ . We used different working definitions between the force (Chap 5) and trap (Chap. 7) experiments, and I want to explain those choices now as a brief narrative for different possible representations and where we ended up. In brief, the two measurements differ by a factor of  $\sqrt{\frac{1}{8}} \approx 0.3536$ , where this factor apparently lowers the force Rabi frequency measurements compared to the trap measurements, although we report values explicitly with this factor included.

During the earlier force experiment, the analysis was sufficient using the low- $B_{DC}$  terms given in Eq. 3.25. We pull out a common  $\frac{\sqrt{2}}{2I+1} = \sqrt{\frac{1}{8}} = 0.3536\dots \approx \frac{1}{3}$  factor such that the upper manifold’s four transitions were  $\sqrt{2}$  and  $\sqrt{3}$  times it, and the lower manifold gets a  $-1$ . The value we vary in analysis is then  $\sqrt{\frac{1}{8}}\Omega_0$  for these measurements. This definition is a bit closer to a traditional definition of Rabi frequency, but is only accurate in the low- $B_{DC}$  limit. When we have significant deviations in Clebsch-Gordan coefficients at higher field (Sec. 3.1), or simply desire more accuracy, the only part that remains common is  $\Omega_0 \equiv \mu_B |B_{\pm}|/\hbar$ .

For the trapping experiment at higher  $B_{DC}$ , and armed with a proper five-level  $|I, m_I, S, m_S\rangle \rightarrow |F, m_F\rangle$  basis generating script, we take a new working variable. We leave the  $\sqrt{\frac{1}{8}}$  in the numerical Clebsch-Gordan coefficients they belong to and vary only what we define as the Rabi strength  $\Omega_0$ . To translate into a ‘proper’ Rabi frequency, one would need to reduce the stated  $\Omega_0/2\pi$  values by multiplying

numbers nearly  $\sqrt{\frac{2}{8}} = 0.5$  or  $\sqrt{\frac{3}{8}} \approx 0.6124$  for the ‘outer’ and ‘inner’  $F_+$  manifold transitions, respectively, as well as  $g_S$ .

We measure this Rabi value and gradient differently for two different systems: in the ODT (and a sagging ODT) to calibrate the ACZ Force data in Chap. 5, and for each of two trapping wires for Chap. 7 to accurately simulate trapping fields. In the ODT case, we apply the field while atoms are trapped and then drop them. In the AC Zeeman trap case, we turn off one of the two generating fields, effectively turning on a diagonal-oriented linear field at the atoms’ location.

## 4.2 Rabi Measurement with the Force Experiment

For the Rabi frequency and gradient measurements necessary for simulating the force measurement,  $I_{DC}$  in the quantizing field coils was held at 5 Amps, producing 11.98 ( $\sim 12$ ) Gauss  $B_{DC}\hat{z}$ . We picked a frequency as close to the middle of the four resonances as we could manage, 8.375 MHz, which was within a few kHz of the  $|2, -2\rangle \leftrightarrow |2, +2\rangle$  crossing in the  $|--\rangle$  state, and the  $m_F = 0$  part of the  $|++\rangle$  state. We observe noise in the  $B_{DC}$  field producing 15 kHz detuning noise, causing shot-to-shot noise in population ratios when we sweep in and drop off very close to resonance, so the best I could do was knowing it is between 8.370 and 8.380 MHz. Anywhere in this range left about the same population randomness over a few shots.

For the force Rabi measurement, RF frequency is produced by mixing 108.375 MHz single frequency from the AD9910 ‘Prince Charming’ DDS with 100 MHz from an SRS SG384 signal generator. From the mixer (an old Mini-Circuits ZAD-1), the signal passes through a variable voltage attenuator (VVA, Mini-Circuits ZX73-2500-S+) which is operated at a choice of two values of power,  $\sim 1.3$  dB apart. After the VVA, the signal goes through a TTL-controlled high isolation RF switch (Mini-Circuits ZASW-2-50DR+), which operates the time gating, and then through a

+30 dB, 2 Watt amplifier (Delta RF LA2-1-525-30 model 4360), which outputs either 11.36 dBm or 10.06 dBm, depending on VVA setting, which goes to the atom chip via a BNC cable.

Time variation of the RF uses a delay pulse generator (SRS DG535) which turns a single long TTL input from the Adwin into a short variable TTL pulse which opens the RF switch for a few  $\mu$ s at a time. The trigger also opens a switch internal to the ‘Prince-Charming’ DDS. If left open, a significant amount of RF power is still around (ballpark -60 dBm). The DDS switch reduces power before the (non-linear) mixer and is required to further suppress residual power in the RF system by 30dB or more (it falls below the spectrum analyzers noise floor at  $\sim$  -90dBm). The VVA is ‘slow,’ requiring  $> 20\mu$ s hold time for full ‘on’ condition, so the VVA is turned on 100  $\mu$ s (or more) before it is used.

It was discovered in mid-February 2019 that the turn-on time of some unknown component is non-negligible, a trait that was not observed previously. Rabi flop measurements seemed to remain at initial population ratios between 1-2  $\mu$ s before flopping, whereas previous measurements began right away. Direct measurement of the RF signal shows amplitude increasing from zero to full power over 1  $\mu$ s to about 1.75  $\mu$ s after the TTL trigger start. In the process of fitting (described later), this parameter was fit to nearly 1.25  $\mu$ s.

#### 4.2.1 Flopping Experiment

In the AC Zeeman force experiment, roughly 300,000 atoms at  $\sim$  360 nK are loaded into an optical dipole trap (ODT) directly under the ‘U’-wire, through which the RF current is driven, seen in Fig. 5.3. The RF magnetic field from this current will ‘flop’ the atoms within the F=2 hyperfine manifold between 5 different states, labeled by  $m_F$  projection (+2, +1, 0, -1, -2). We undertook one brief study which

suggested the flopping rates were equal whether we began in the +2 or -2 state, so we begin all flops in the +2 state, same as the initially prepared state.

While RF is applied, atoms evolve from almost full population in the +2 state, partially populating the  $+1 \rightarrow 0 \rightarrow -1$  states, before fully populating the -2 state and then reversing the cycle. After some time flopping with the RF on, we turn the RF off and drop the atoms from the ODT. We then apply a Stern-Gerlach gradient horizontally via a  $\sim 1$ -inch copper coil just outside of the vacuum chamber (see Figs. 2.1 or 7.4), separating the single atom cloud of mixed  $m_F$  population into five separate atom clouds by  $m_F$  population. After this horizontal Stern-Gerlach separation, and before imaging, we apply a ‘pre-pulse’ of both trap and repump light to bring all atoms to the  $|F = 2, m_F = 2\rangle$  state before taking an absorption image of the five cold atom clouds. Typical Rabi flop data is given at the top of Fig. 4.1.

To analyze the absorption images, we use MATLAB to Gaussian fit each of the five Stern-Gerlach separated clouds, using two different methods, which we refined over time. We always zoom in to a region of interest (ROI) which contains the atoms, although we parse this data two different ways. For the force Rabi measurement, we take fixed-width ( $x$ ) sections of each of the five atom clouds and fit a vertical Gaussian (over  $y$ ) for each  $m_F$  state separately. In the force measurements, atoms were observed to oscillate vertically, so we had to take elongated vertical rectangles as our region of interest. For the trap measurement, we sum vertically (over  $y$ ) and fit five horizontal (over  $x$ ) Gaussians simultaneously using the entire region containing atoms for the trap Rabi measurement, minimizing parameters by giving scaled spacing and position offsets to each cloud. This five-Gaussian fit is shown in the middle and bottom

These atom populations (from Gaussian height and width) are summed together for a total atom number. Then each  $m_F$  population is divided into the total for each

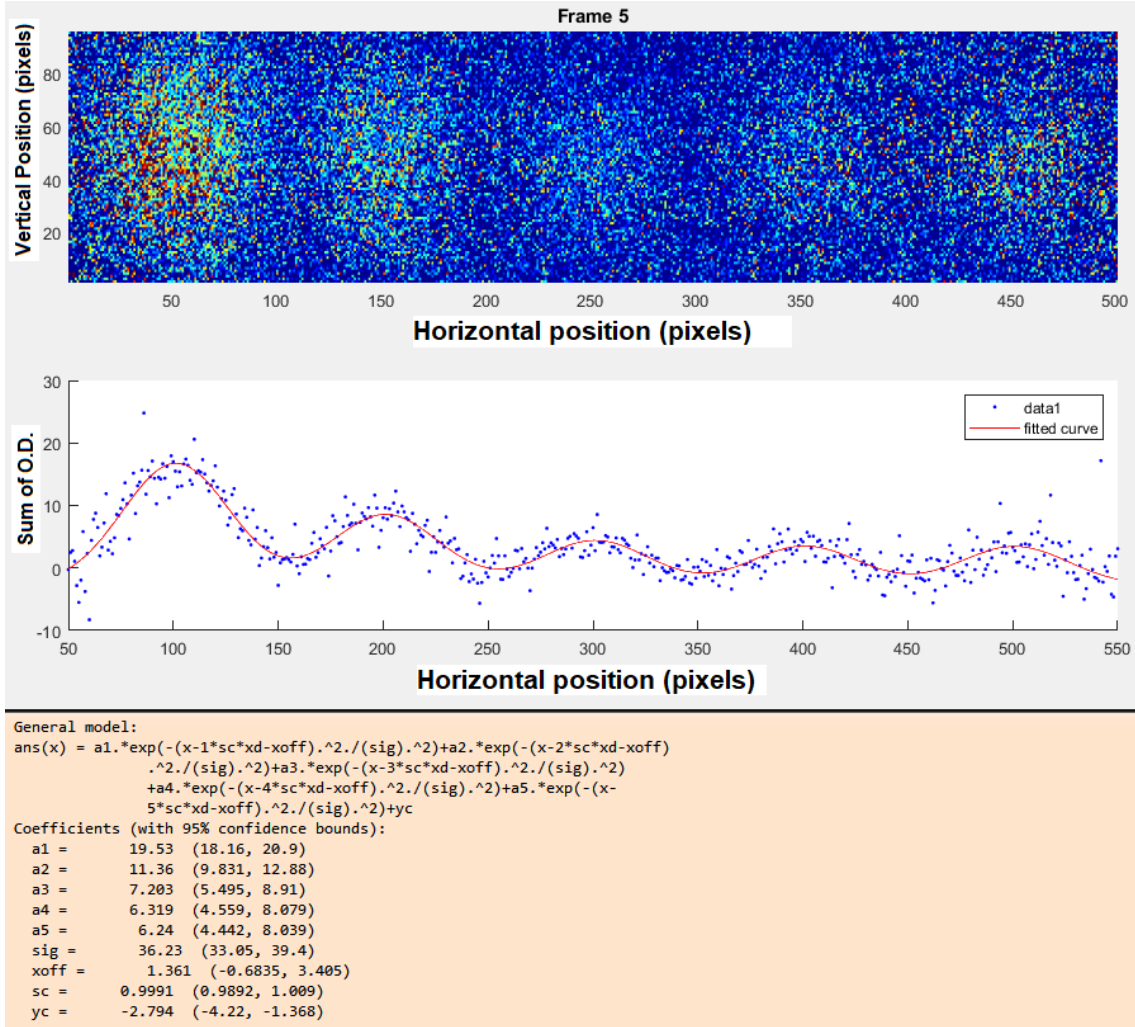


FIG. 4.1: Example of a five-Gaussian fit of Rabi oscillation data for the trap experiment. Top: False-color atom optical density measurements after an RF Rabi pulse. Middle: Data from the top image, summed vertically into the  $x$ -profile, including the five-Gaussian fits. Bottom: Fitting results from MATLAB, giving the fit function and values for this example.

state's population *ratio*.

Rabi pulses are near-square and taken in randomized duration order, stepping by 100-300 ns from  $t = 0$  up to 20  $\mu\text{s}$  depending on the set. By this end time, resolution in population ratio is below about half of the initial resolution, and going longer does not aid in Rabi frequency determination, shown in Fig. 4.2. We do not have an exact explanation for the Rabi decoherence over time, but there are a few suggestions that we can or cannot rule out:

- Rabi gradient over the cloud flops atoms at different rates spatially (backed up by vertical position shifts as flopping goes on).
- Non-degenerate detunings to each of the intra-manifold resonances (has an effect, but the theory curves also contain this information).
- Impure initial state vector (included parameter in the theory curves).
- Spin-spin inelastic collisions (possible, but the collision rate should be lower than the decoherence observed. We would love a good model for this, I had tried some ansatz's, but nothing matched well, so all were scrapped).
- Noise in background  $B_{DC}$  (likely a contribution but hard to quantify).

### 4.2.2 Fitting

The time-dependent results of experimental Rabi flopping are compared against a MATLAB-computed time-evolution of the AC Zeeman Hamiltonian for the same  $B_{DC}$  and RF frequency, shown in Fig. 4.2 for a force measurement and 4.5 for all trap measurements. We then performed reduced Chi-squared ( $\chi^2$ ) fits using population ratio values and their associated errors, shown in Fig. 4.3. Shuangli Du wrote the bulk of this fitting code.

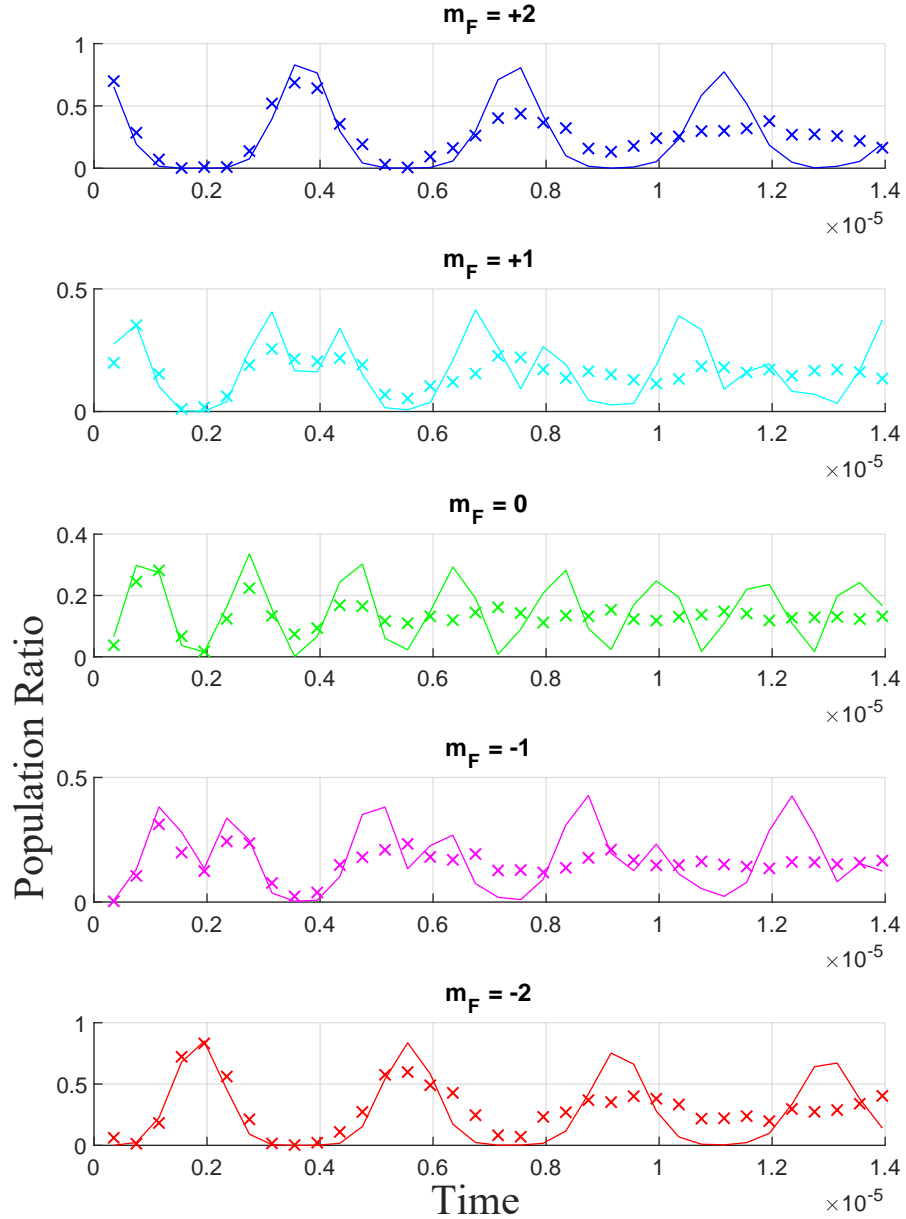


FIG. 4.2: Example of a Rabi frequency data and a MATLAB fit for each  $m_F$  state, from the force measurements. Rabi pulse times on the  $x$ -axis increment by  $0.4 \mu\text{s}$  out to  $14 \mu\text{s}$ , yielding populations ratios on each state's  $y$ -axis.

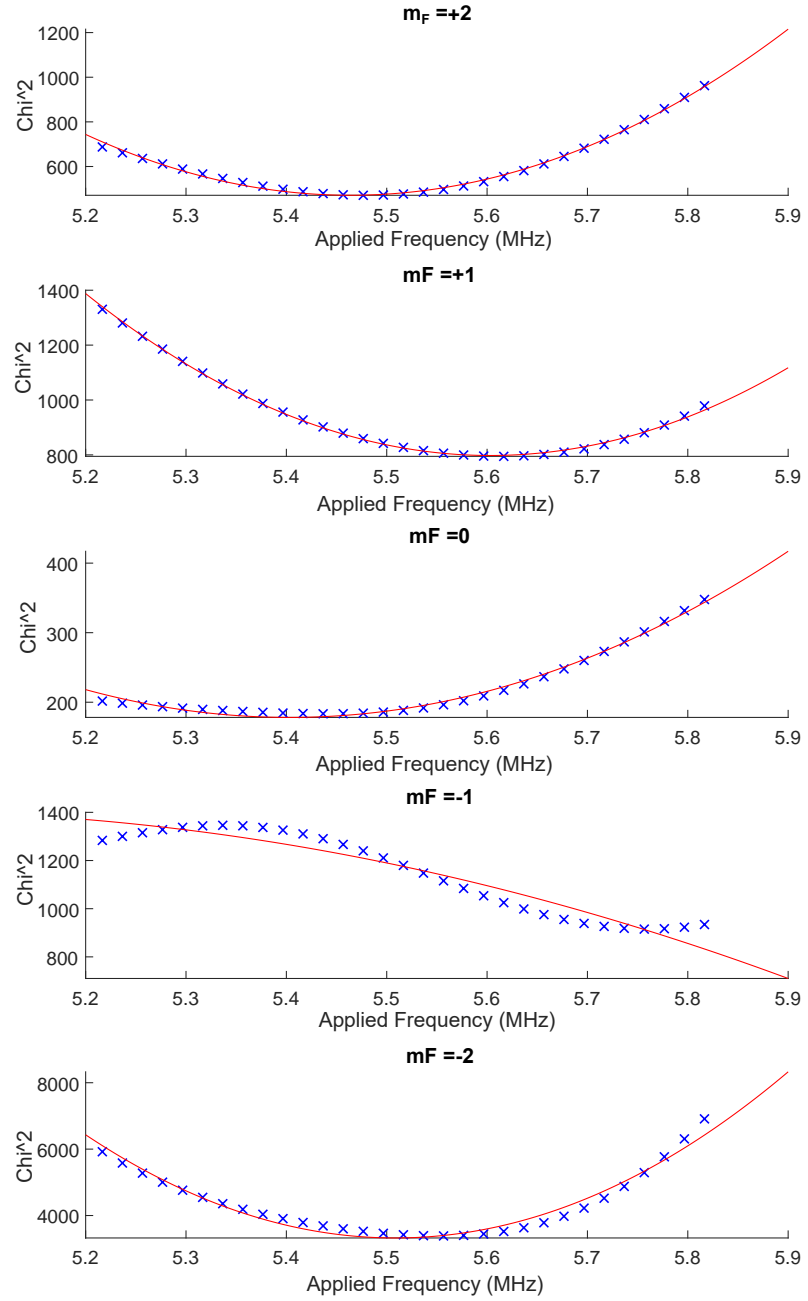


FIG. 4.3: Sample Chi-squared values across theory Rabi Frequencies, for the 20 MHz U case of Fig. 4.5. These fits illustrate why we average the  $m_F = \pm 2$  states, and neglect the possibly poor fits of the states in between.

When we go to fit, the only free parameters are the reported Rabi strength  $\Omega_0 = \mu_B|B_{\pm}|/\hbar$  ( $\sqrt{\frac{1}{8}}\Omega_0$  in the force data), the initial timing delay, and the initial population ratio (the normalized amount of  $m_F = 1$  contamination in a mostly  $m_F = 2$  sample). We vary each of these parameters independently until all sets converged to the reported values. The Rabi frequency is scanned locally over a few kHz, and a summary  $\chi^2$  is calculated as the difference between experiment and calculated population ratios, reduced by the error in measurement. That is, for population ratios  $R$ :

$$\chi^2_{m_F} = \sum_{t=0}^{t_{end}} \frac{(R_{exp}(t) - R_{calc}(t))^2}{\sigma_{exp}^2}$$

This process is carried out over a range of frequencies, altering the values in  $R_{calc}$ , and providing a  $\chi^2$  dependence on Rabi frequency for each  $m_F$  state.

Typically, only the  $|2, +2\rangle$  and  $|2, -2\rangle$  states provided the expected parabolic dependence of  $\chi^2$  on the frequency, as their top-to-bottom range was twice that of the  $m_F = \{+1, 0, -1\}$  states, as seen in Fig. 4.3. For parabolic fits of the form  $y = ax^2 + bx + c$ , the error is defined by  $\sigma = \sqrt{\frac{2}{a}}$ . We then perform a weighted arithmetic average of these two values to obtain the mean Rabi frequency for the set, reported as the Rabi strength.

### 4.2.3 Scaling

One powerful technique is the ability to measure Rabi frequency at a known low power, and scale it up and down to different power without taking new measurements. Among the six Rabi frequency gradient measurements (Fig. 4.4) are four at lower (-1.34 dB) power and two at full power. Since the Rabi frequency scales with the magnetic field  $B_{AC}$ , which scales with the RF current  $I_{AC}$ , which scales with power as  $P = I^2R$ , the Rabi frequency should scale as the square-root of power. So to scale up to ‘full’ power, we multiply the Rabi frequencies obtained at

low power by the ‘power factor’ of  $\sqrt{10^{\frac{1.34}{10}}} = \sqrt{10^{0.134}} \approx 1.167$  times. A low power Rabi frequency measurement is scaled up by this procedure and shown as the red downward triangles in Fig. 4.4, while unscaled measurements at full power are given as the blue upward triangles in Fig. 4.4.

#### 4.2.4 Rabi Gradient

If we want to know the AC Zeeman Force and not just the ACZ energy, then just as important as knowing the Rabi frequency is knowing the Rabi frequency *gradient*. Recall for the two-state system that the ACZ force is given by:

$$\vec{F}_{ACZ\pm} = \mp \vec{\nabla} \Omega_{eg}(\vec{r}) \frac{\hbar}{2} \frac{\Omega_{eg}}{\sqrt{\delta^2 + \Omega_{eg}^2}}$$

Knowledge of the spatial dependence of the ACZ energy is crucial. We assume a local linear gradient of the Rabi gradient, which is a good enough approximation far from the chip ( $\sim 100 \mu\text{m}$ ).

With good Rabi frequency measurements at two (or more) known locations, we can perform a linear fit through these data points to determine the local gradient of the Rabi strength, as shown in Fig. 4.4. Due to the ODT wander, we had to take empirical position measurements for each set.

Attempts were made on the day of taking AC Zeeman force data to determine a Rabi gradient by taking measurements at two positions set by translating the ODT beam. This translation was attempted with one turn of the vertical adjustment knob on a tilt plate holding a glass wedge, positioned after the focusing lens of the main beam. This translated atoms about  $4 \mu\text{m}$  but had a measured uncertainty just as large. Therefore, a gradient ( $\Delta\Omega_{eg}/\Delta y$ ) could not be well established by this data, although it did provide a good Rabi frequency measurement for atoms.

Measurements of ACZ force and Rabi flopping were taken with the ‘radial’

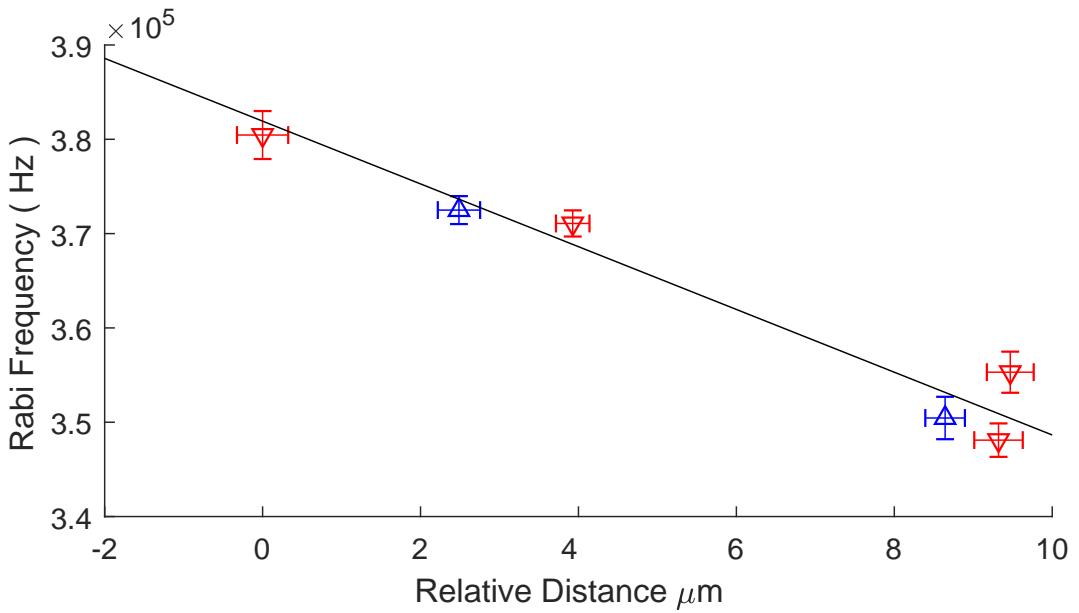


FIG. 4.4: Rabi gradient fit using measurements of  $\sqrt{\frac{1}{8}}\Omega_0$  ( $y$  axis) at different positions ( $x$  axis). Exact values are given in Tab. 4.1. Blue/upward triangles were taken at full RF power, and red/downward triangles were taken at 1.34 dB lower RF power and scaled up by  $\sqrt{10^{1.34/10}}$ . Error bars are 1- $\sigma$  error. The fit here gives  $\nabla(\sqrt{\frac{1}{8}}\Omega_0) = 3.32(55)$  kHz/ $\mu\text{m}$ . This uncertainty dominates the 1- $\sigma$  shading in Fig. 5.6 and 5.7.

camera, with pixel resolution =  $7.4 \mu\text{m}/\text{px}$ . However, the axial camera has almost double the spatial resolution, at  $4.65 \mu\text{m}$  per pixel. Therefore, this camera was used to more accurately determine the vertical position of the atoms after a very short time of flight from the ODT. The accuracy of this measurement is enhanced by measuring 10-20 frames of dropped atoms. As discussed in the Apparatus chapter 2, we observe a long-term drift in ODT position during this period, which complicates the position measurements, shown in Fig. 4.4 and Tab. 4.1.

#### 4.2.5 “Sag”

After some trial-and-error and partial realignments of the ODT, we were able to perform a different type of repeatable vertical position adjustment of the atoms in the ODT. It is preferred to manual adjustment of the ODT beam position, which cannot be guaranteed to return to the same place. This method, termed ‘trap sag,’ is achieved by lowering the total power of the ODT so that gravity ‘sags’ the trapping potential. A parabolic ( $E = ay^2$ ) trap with a linear gravitational gradient ( $E = gy$ ) will have a center ( $dE/dy$ ) at  $y_0 = \frac{-g}{2a}$ . Adjusting  $a$  has the effect of translating the trap bottom, as well as incidentally adjusting trapping frequencies.

Tuning the power of the trap is achieved by a feedback loop between a small light pick-off into a photodiode (post fiber) and the power sent to a 40 MHz acousto-optical modulator (AOM, pre-fiber) whose first order becomes the whole ODT. This system is referenced to an Adwin-supplied analog voltage, which can be adjusted. Full trapping uses -9.3 V as the reference value, with the absolute value proportional to ODT power. Atoms can remain trapped down to about a -5 V reference value, with significant loss starting at about -6 V. A rough relationship is that we get about  $3.5 \mu\text{m}$  of sag for every Volt lower in reference value. For Rabi gradient measurements, we used -7 and -9.3 V, providing 6-8  $\mu\text{m}$  of difference to measure

over, with errors of roughly 0.2-0.3  $\mu\text{m}$  in each position after averaging 11 frames each.

### 4.3 Rabi Measurement with the Trap Experiment

This measurement, like the trap experiment, uses a nominal resonance of 20 MHz at 28.58 G. For the trap Rabi frequency measurement shown in Fig. 4.5, we use the FlexDDS from Sec. 2.6, with its signal sent through Fluffy, described in Sec. 2.7 with nominal 400 mW of RF power in each trace. We took measurements by simply turning off one of the two trapping wires, and watching the atoms evolve. For atoms who were in a local zero of the trapping field, this sudden jump to high RF magnetic amplitude acts in the same way as turning on a single wire had in the force measurements. Indeed, the analysis of matching numerical solutions to empirically evolving  $m_F$  states follows the same procedure outlined above.

One difference in this measurement is that we elect to repeat it off resonance, both red of resonance at 19.5 MHz, on resonance at 20 MHz, and blue at 20.5 MHz, given at the left, middle, and right plots in Fig. 4.5, respectively. The top row of Fig. 4.5 gives U-wire measurements and the bottom row has the Z-wire's data. In a two-level case, atoms would flop faster off resonance at the generalized Rabi frequency  $\Omega' = \sqrt{\delta^2 + \Omega_0^2}$ , but an easy sine fit is not available in the five-level flopping case. The numerical comparison for fitting has this detuning information included on the diagonal, and we fit varying the off diagonal value  $\Omega_0$  (Eq. A.10). Values for Rabi frequency (as  $\Omega_0$ ) from the fits shown in Fig. 4.5 are listed in Table 4.2.

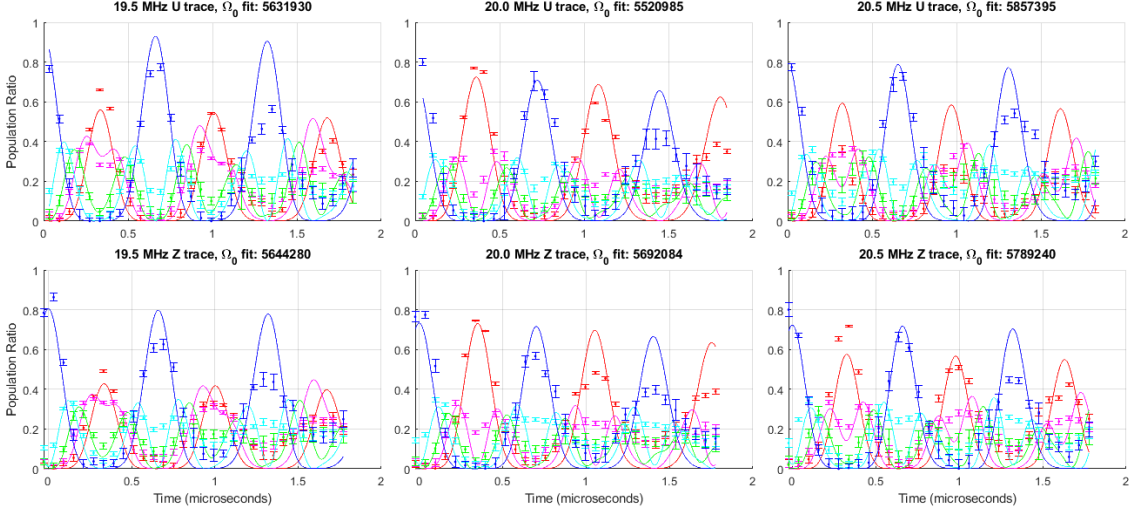


FIG. 4.5: Examples of Rabi flopping data and fits for two trap wires, U (top) and Z (bottom) at three different RF frequencies (bottom 19.5 MHz, middle 20 MHz, top 20.5 MHz). Ratio is determined by individual state population, divided by the sum of all five state populations. Colors for the  $(+2, +1, 0, -1, -2)$   $m_F$  states are (blue, cyan, green, magenta, red). While the experimental data decoheres, the theory curve does not account for this. Free parameters are the Rabi frequency, initial time delay, and initial population ratio.

### 4.3.1 Push Triangulation

When we test the AC Zeeman trap, it is not so clear where the trap location is with respect to the chip surface and its generating wires. Knowing position will help ‘back out’ values for current in the wires, but the gradient Value information is not needed in this case. We elect to leverage the gradient to give atoms a push diagonally from either wire, revealing an inclination angle for the applied force. Applying a non-sweeping pulse projects the  $|2, +2\rangle$  state into the low-field seeking  $|++\rangle$  state red of resonance, and the high-field seeking  $|--\rangle$  state blue of resonance. We compare a push, pull, and no force to generate the diagonal lines in Fig. 4.6. In a simple geometric picture, we can let each of these angles point back to the center of either wire separated by a known distance, triangulating the initial trap location. A schematic diagram for the mean case is shown in Fig. 4.6, and this uncertainty in position remains a significant source of error in our theory curves.

Since the measured Rabi frequency for the Z-wire is higher than that of the U-

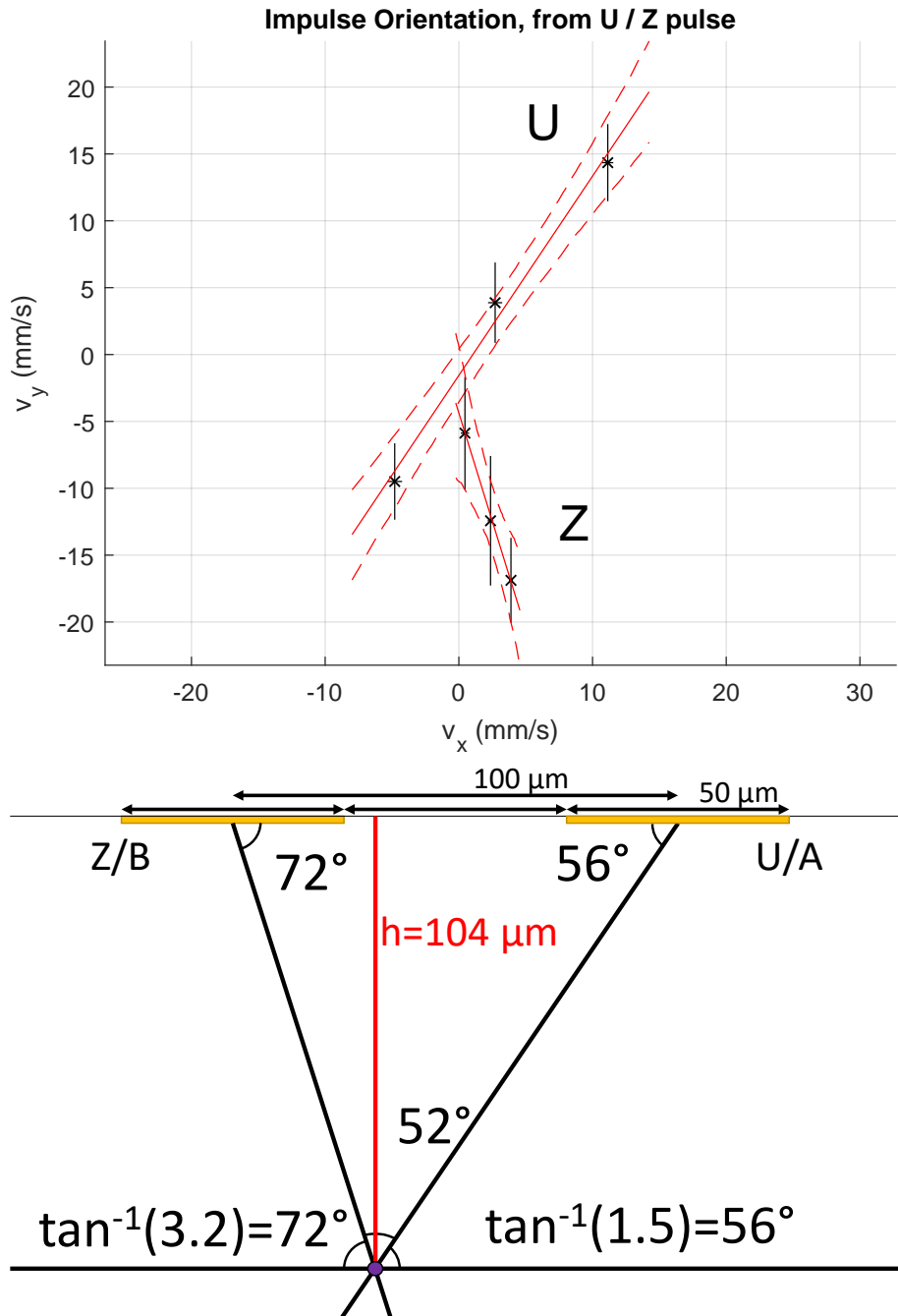


FIG. 4.6: Using Rabi gradient pushes from two wires to determine atom initial location. Top: Plot of center-of-mass velocity after a long Rabi pulse above, on, and below resonance for both U and Z wires. These fits should align spatially with wire positions. Bottom: Using the impulse fits, we can ‘triangulate’ an estimate of the trap position relative to the wire traces. Traces are also labeled by the Fluffy output that drives them: Z/B and U/A.

Position/Set	Power	$\sqrt{\frac{1}{8}}\Omega_0/2\pi$ (kHz)	error (kHz)	height ( $\mu\text{m}$ )	error ( $\mu\text{m}$ )
High	Full	372.493	1.481	2.4867	0.2680
Low	Full	350.449	2.250	8.635	0.2506
first High	Low	371.077	1.385	3.9275	0.2123
second High	Low	380.452	2.544	0	0.3245
first Low	Low	355.306	2.180	9.4685	0.2966
second Low	Low	348.101	1.771	9.3197	0.3068
Gradient	kHz/ $\mu\text{m}$ :	3.32	0.55	-	-

TABLE 4.1: Table of Rabi Frequency (as Rabi ‘strength’  $\Omega_0/2\pi$ , including  $\sqrt{\frac{1}{8}}$ , see Sec. 4) measurements for the ACZ force experiment, scaled up to full power. Data is also visualized in Fig. 5.15, yielding the local Rabi gradient, given in the last row.

Signal	Applied $f_{RF}$	$\Omega_0/2\pi$ (MHz)	Error (kHz)	Time Offset	Initial $m_F = 1$
U	19.5	5.617765	5.698	0.66709	0.03132
U	20.0	5.516618	5.002	0.65399	0.14759
U	20.5	5.857396	10.002	0.67547	0.10958
Z	19.5	5.644003	9.617	0.72806	0.10279
Z	20.0	5.691406	7.948	0.72384	0.14376
Z	20.5	5.789243	9.914	0.72241	0.15019
U	(mean)	5.597	0.148		
Z	(mean)	5.705	0.0626		

TABLE 4.2: Table of Rabi Frequency (as Rabi ‘strength’  $\Omega_0/2\pi = \mu_B|B_{\pm}|/h$ ) measurements for the ACZ trap experiment. These values are the fits in Fig. 4.5.

wire, we would have expected a trap on the lower-current side (rightward in Fig. 4.6), per arguments in Chap. 6, which is opposite the experimental finding here. This suggests a systematic error in this triangulation method when it comes to assessing the actual trap position.

## 4.4 Compiled Measurements

We have the force/gradient measurements from Fig. 4.4 in Tab. 4.1, and the measurements for the two trapping lines in Fig. 4.6 in Tab. 4.2.

## 4.5 Summary

While the formal Rabi frequency is defined well for the sinusoidal population transfer between only two states, we expand the definition a bit to be a useful parameter governing the five- and three-level behavior as well. This requires making a motivated re-definition using the Rabi strength ( $\Omega_0 = \mu_B B_{\pm}/\hbar$ ), which measures the available oscillating field, but must be de-rated to the specific transitions within the ladder-like manifold.

Rabi frequency measurements are often performed indirectly, observing spectroscopically the shift in energy levels using a weak probe field. We elect to measure it rather directly, observing the time-evolving atom population with varying RF pulse lengths. These atom number evolution data is then compared to a numerically-generated theory Rabi flop, and fit to as few variables as are justifiable: the Rabi strength, initial state impurity, and time delay. Additional parameters which govern the de-phasing or loss in signal strength can make these fits better, although we do not have a proper model at the present time.

The value of Rabi frequency (or  $\Omega_0$ ), along with  $B_{DC}$  and  $\delta$  entirely determine the energy structure of the resultant AC Zeeman potential. We prefer using the atoms as an empirical measuring tool of the Rabi frequency at the trap position (or over space, as in Appx. C), over relying on simulations, because effective coupling and wire cross-talk are unknown.

Further, measurements of Rabi *gradient* are important, especially when predicting the AC Zeeman force for Chap. 5, and for determining trap location in Chap. 7. These measurements are necessary for later theory curves, but the process of Rabi fitting is a little too pedantic for inclusion in those later experiments.

# CHAPTER 5

## RF AC Zeeman Force

As atom chips gain utility, new uses for radiofrequency (RF) and microwave ( $\mu\text{w}$ ) signals in current traces can aid in diverse fields of atom and ion chip research: trapping, selective evaporation, or population transfer between states without the need for lasers. One application for RF-controlled cold atoms is in matter-wave interferometry, which measures small energy shifts in spatially separated states. Adding a spin-specific force to a spin-independent trap can shift positions for specific states, generating interferometer arm separation, which is helpful for some measurements but cannot usefully measure inertial forces. We view the work of this chapter as a calibrating stepping-stone toward fully state-specific trapping, as demonstrate in Chap. 7, which can enable arbitrary ‘arm’ motion for useful gradiometry.

This chapter demonstrates a force-producing tool for cold atoms using an AC magnetic field. We test *intra*-manifold applications of the AC Zeeman (ACZ) effect, using RF transitions within the  $F_+ = 2$  manifold in contrast to the *inter*-manifold transition near 6.8 GHz in  $^{87}\text{Rb}$ . Sweeping frequency of the RF from either side of resonance can project each  $m_F \neq 0$  state into a high- *or* a low-field seeking state, necessarily mixing spin states near resonance, as we show.

We demonstrate the RF AC Zeeman force with background  $B_{DC}=12$  Gauss, which corresponds to RF transitions around 8.4 MHz for ultracold  $^{87}\text{Rb}$  atoms in five states within the  $5\text{S}_{1/2}$   $F=2$  hyperfine manifold. We observe almost three times the force of gravity for  $\sim 15$  mW of applied RF power at a distance of  $\sim 100 \mu\text{m}$  from the RF current. Our measurements are consistent with theoretical predictions and demonstrate the spin-state dependence of the force and its resonant and bipolar behavior. As we examine this force for use in atom trapping, we observe the time dependence of dressed state mixing as a function of detuning and power.

This chapter is organized into the following main sections: Section 5.1 outlines the theory of the AC Zeeman force for intramanifold transitions. Section 5.2 details the experimental method used and the main force measurements. Section 5.3 demonstrates a procedure we call the AC Stern-Gerlach effect. Section 5.4 analyzes the time evolution of states subject to continued AC Zeeman energy shifts. Next, we discuss two experimental calibrations required for this experiment, the Rabi frequency and gradient in Sec. 5.5 and the background  $B_{DC}$  gradient in Sec. 5.5.1. We conclude in Sec. 5.6.

## 5.1 Theory

We focus on the  $5\text{S}_{1/2}$  ground state of  $^{87}\text{Rb}$ , in the upper hyperfine manifold,  $F=2$ . A small DC magnetic field  $B_{DC}$  separates five ( $2F+1$ ) quantized  $m_F$  projections almost linearly and determines the energy separation between these states. We use the dressed atom basis, where a field of  $N$  photons at angular frequency  $\omega_{RF}$  and magnitude  $B_{AC}$  envelops the atoms, which can absorb from or emit into the RF field via M1 transition, changing  $m_F$  level by  $\pm 1$  and photon number by  $\mp 1$ . The dressed atom basis is given per atom for five near-degenerate energy levels, selecting  $m_F = 0$  as the reference. We then have:  $|m_F, N_{RF}\rangle = \{|+2, N-2\rangle, |+1, N-1\rangle,$

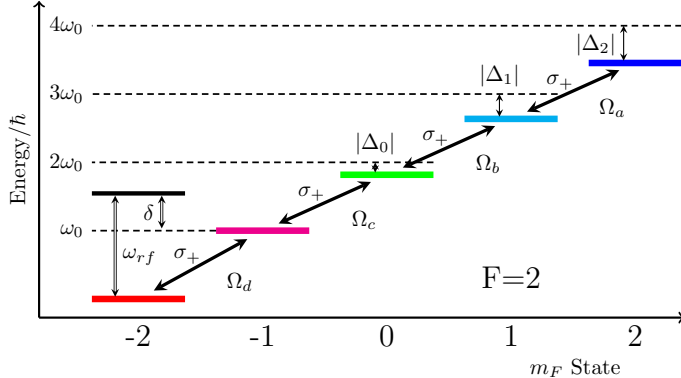


FIG. 5.1: Illustration of intramanifold hyperfine transitions within  $F_+ = 2$ . An external oscillating magnetic field at angular frequency  $\omega_{RF}$  drives transitions with Rabi frequencies  $\Omega_{[abcd]}$  between near-resonant DC Zeeman states. We label the detuning  $\delta$  between applied frequency  $\omega_{RF}$  and the lowest atomic transition  $\omega_0$ , as well as  $\Delta_{[012]}$ , the difference between multiples of  $\omega_0$  and atomic state energies (over  $\hbar$ ).

$$|0, N\rangle, |-1, N+1\rangle, |-2, N+2\rangle\}.$$

The Hamiltonian for the dressed atom system is:

$$\frac{H_{tot}}{\hbar} |\psi\rangle = \begin{pmatrix} -2\delta + \Delta_2 & \Omega_a/2 & 0 & 0 & 0 \\ \Omega_a^*/2 & -\delta + \Delta_1 & \Omega_b/2 & 0 & 0 \\ 0 & \Omega_b^*/2 & \Delta_0 & \Omega_c/2 & 0 \\ 0 & 0 & \Omega_c^*/2 & \delta & \Omega_d/2 \\ 0 & 0 & 0 & \Omega_d^*/2 & 2\delta \end{pmatrix} \begin{pmatrix} |+2, N-2\rangle \\ |+1, N-1\rangle \\ |0, N\rangle \\ |-1, N+1\rangle \\ |-2, N+2\rangle \end{pmatrix} \quad (5.1)$$

We have redefined atomic energy levels in relation to the energies of the two lowest atomic levels:  $\hbar\omega_0 \equiv E_{-1} - E_{-2} \equiv hf_0$ . The detuning is defined relative to this transition,  $\delta \equiv \omega_{RF} - \omega_0$ , and the other state energies are re-defined in relation to multiples of this value using  $\{\Delta_0 = (E_0 - E_{-2})/\hbar - 2\omega_0, \Delta_1 = (E_1 - E_{-2})/\hbar - 3\omega_0$ , and  $\Delta_2 = (E_2 - E_{-2})/\hbar - 4\omega_0\}$ , shown in Fig. 5.1. Atoms can only change one unit of angular momentum at a time, so the five-level ‘ladder’ can be viewed as a series of two-level interactions.

Since allowed transitions within this manifold are only  $\sigma_+$  polarized (that is, energy increases for an increase in angular momentum  $m_F$ ), then the Rabi frequency

given by  $\Omega_{eg} = \langle e | -\vec{\mu} \cdot \vec{B}_{AC} | g \rangle$  can be simplified into  $\Omega_{eg} = -\frac{\mu_B g_s}{2\hbar^2} \langle e | S_+ B_- | g \rangle$ , where the subscripts  $\pm$  denote circular polarization ( $B_\pm = B_x \pm iB_y$ ,  $S_\pm = S_x \pm iS_y$ ) with respect to  $B_{DC}\hat{z}$ . We define a common factor, the ‘Rabi strength’  $\Omega_0/2\pi = \mu_B |B_\pm|/\hbar$  that we report as  $\sqrt{\frac{1}{8}}\Omega_0$  in this chapter.

While the Rabi frequencies are unique from one another, we can approximate them using Clebsch-Gordan coefficients assuming a ladder-like distribution, which remains the case for low  $B_{DC}$  values. While the general case is given in Chap. 3, for  $F_+ = 2$  transitions, we have  $\langle 2, m | S_+ | 2, m' \rangle = \frac{\hbar\sqrt{(2+m)(2-m')}}{4} \delta_{m,m'+1}$  yielding values of  $\sqrt{\frac{2}{8}}\Omega_0 \approx \Omega_a \approx \Omega_d$ , and  $\sqrt{\frac{3}{8}}\Omega_0 \approx \Omega_b \approx \Omega_c$ . In this chapter, the common factor  $\sqrt{\frac{1}{8}}$  is still in the reported strength.

Diagonalizing this Hamiltonian in Eq. 5.1 across a range of photon frequencies ( $\omega_{RF}$  or  $\delta$ ) gives the frequency-dependent energy curves shown in Figs. 5.2 and 5.4, as well as the eigenvectors, which are combinations of the dressed states, illustrated in Fig. 3.4. We refer to the five resultant dressed state-comprised eigenvectors in order from highest to lowest energy as  $\{|++\rangle, |+\rangle, |0\rangle, |- \rangle, |--\rangle\}$ .

The origin of the ACZ force is a gradient in the ACZ energy:  $\vec{F}_{ACZ} = -\nabla E_{ACZ}$ . In our experiment, the force arises from the gradient of the magnetic near field from atom chip traces above the atoms. In an idealized form, a point-like wire current source above the atoms will have a circularly shaped magnetic near field which falls off like  $\frac{1}{r}$  with the distance  $r$  away from the wire. Far enough away, this field approximates to a horizontal linearly polarized alternating  $B_{AC}$  field with a vertical linear gradient, shown in Fig. 5.3. To calculate this force, we diagonalize matrix 5.1 at two different values of  $\Omega_0(\vec{r})$  with a fixed spatial separation, simulating a known gradient of  $\frac{\Delta E}{\Delta r}$ , and producing a force value that we normalize by the gravitational force  $mg$ . These calculations are shown as dashed curves with the right axes in Figs. 5.6 and 5.7. These force curves are integrated over duration including sweeps to generate the solid curves (and error) with the left axes in the same figures.

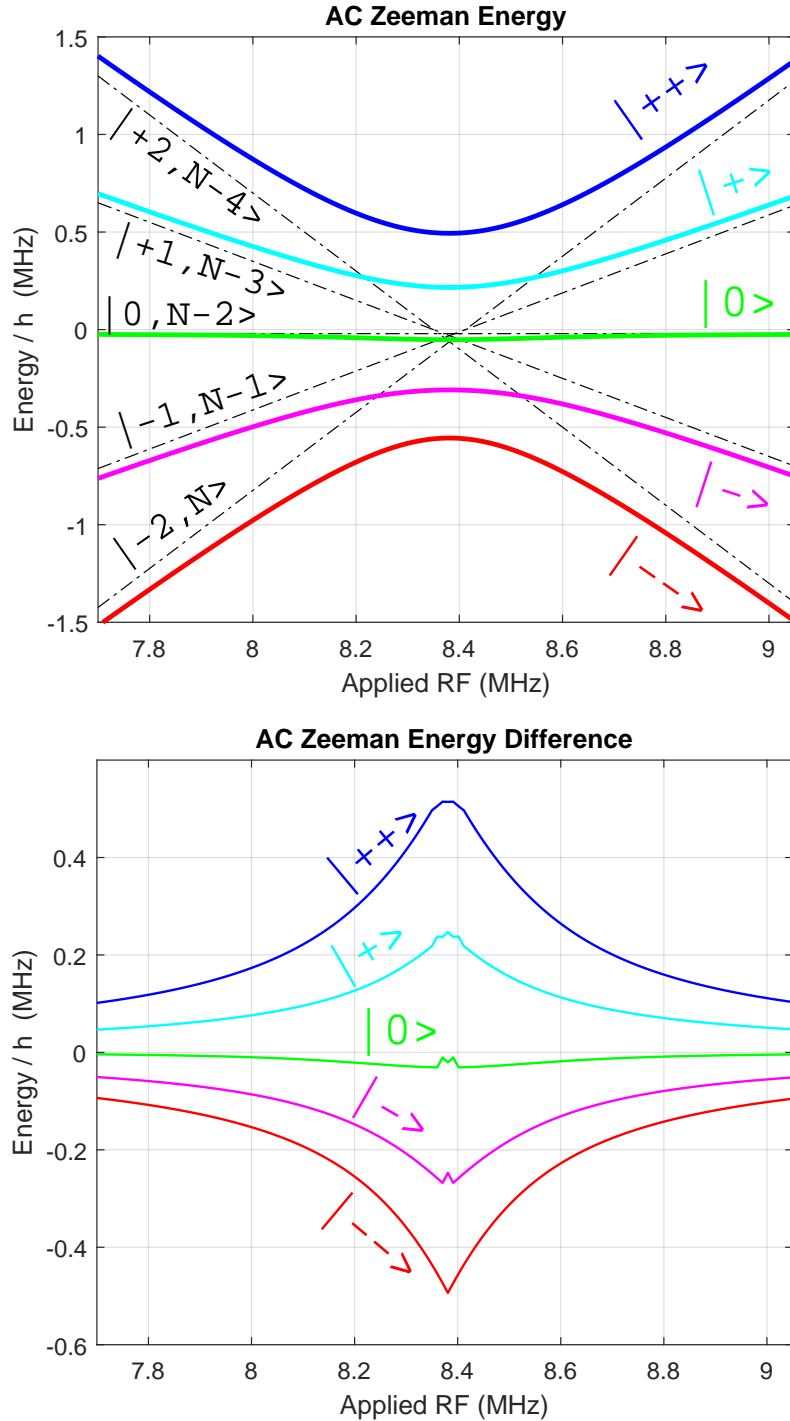


FIG. 5.2: AC Zeeman energy curves vs. applied RF frequency. Top: Eigenenergies (colored curves) and dressed states (black dot-dashed lines). Bottom: Plot of  $E_{ACZ}$  for the five eigenstates, the extra energy above zero  $B_{RF}$  field. The case given is a near-degenerate ladder matching experimental conditions, calculated with  $\sqrt{\frac{1}{8}}\Omega_0/2\pi = 3.7 \times 10^5$  Hz.

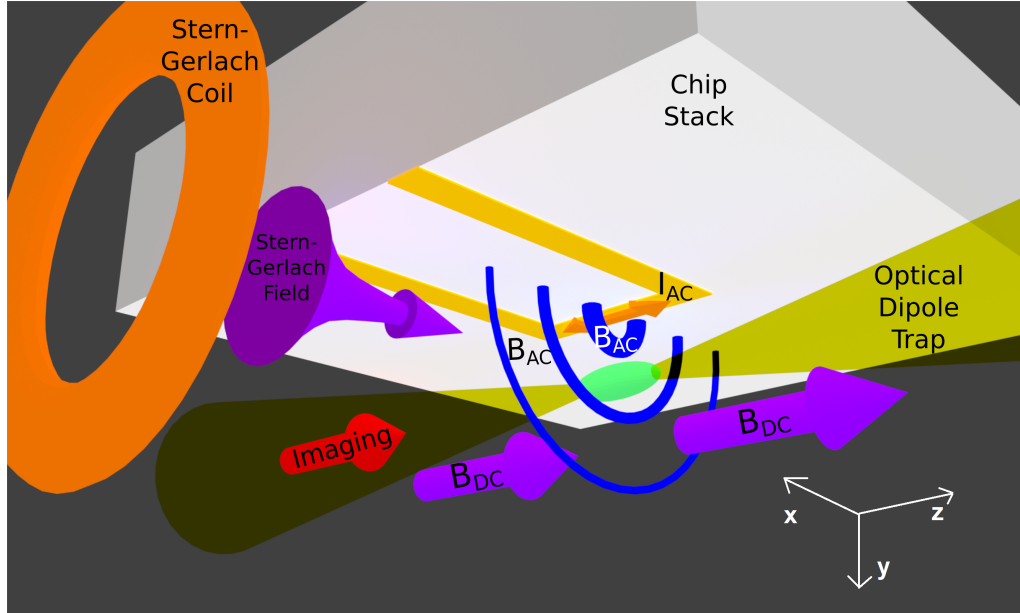


FIG. 5.3: Basic experimental setup, not to scale. Atoms are held in an optical dipole trap (a near-perpendicular  $\hat{x}$ -oriented beam is omitted for clarity) which is aligned below the atom chip trace carrying an RF current,  $I_{AC}$ .  $B_{DC}$  is oriented in the  $\hat{z}$  direction, providing a quantization axis for  $B_{AC}$ , whose field lines curl around  $I_{AC}$ . Locally, these are primarily in the  $\hat{x}$  direction, which decomposes into  $B_{AC+}$  and  $B_{AC-}$  fields. The gradient in  $B_{AC}$  creates a force in the  $\pm\hat{y}$  direction. The DC Stern-Gerlach coil is shown with its high-gradient field,  $B_{SG}$ . It separates atom states along the  $\hat{x}$  direction, just prior to imaging.

## 5.2 Experiment

Atoms are initially cooled in the  $|F_+ = 2, m_F = 2\rangle$  state of Rubidium-87 in a micromagnetic chip trap, then loaded into an optical dipole trap (ODT) with a population of about 300,000 thermal atoms at roughly 350 nK. The ODT has measured trapping frequencies of  $\omega_{(x,y,z)} = 2\pi \times (184, 164, 28)$  Hz and a calculated trap depth of 23  $\mu\text{K}$  [44]. The ODT is positioned  $\sim 100 \mu\text{m}$  below a 50  $\mu\text{m}$  wide RF current-carrying atom chip trace (see Fig. 5.3). To prepare atoms in different  $m_F$  states, we raise the current in a pair of coils with a magnetic field parallel to the primary dipole trap orientation, to  $B_{DC} = 51.75 \text{ G}$ , sufficiently breaking degenerate DC Zeeman splitting (see Fig. 5.4). A frequency sweeping RF source follows the  $|++\rangle$  state from negative detuning to perform adiabatic rapid passage (ARP) on

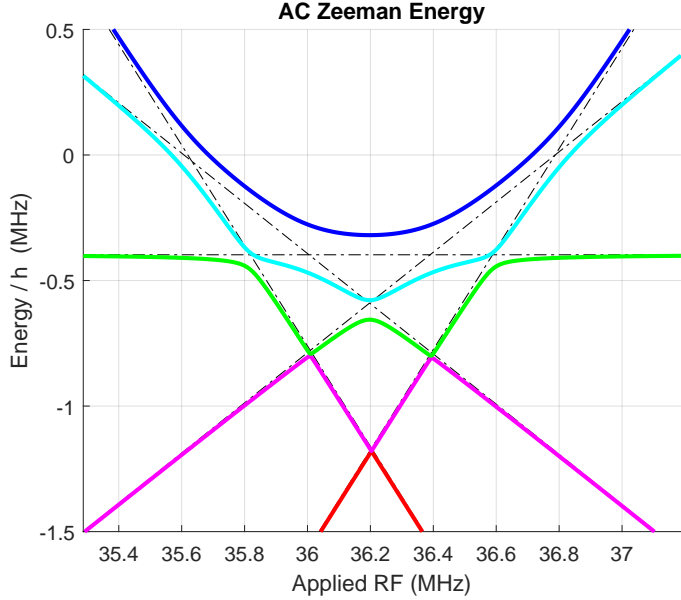


FIG. 5.4: Calculations of the AC Zeeman energy at high  $B_{DC} = 51.75$  G, calculated using  $\sqrt{\frac{1}{8}}\Omega_0/2\pi \approx 117$  kHz, matching the population ARP sweep on  $|++\rangle$  (blue) to any dressed state (black). This plot also illustrates the small and uneven energy gaps for the lower curves, and the low-field seeking of the  $|+\rangle$  state (cyan) at low field.

the atoms between the initial  $|F_+ = 2, m_F = +2\rangle$  state into any  $m_F$  states. To reach the  $(+1, 0, -1, -2)$  state, we ramp the frequency from 25 MHz to (35.8, 36.2, 36.6, 37.0) MHz, respectively, for 100 ms before ramping off the RF power and lowering  $B_{DC}$  to 11.98 G for the push/pull experiment. This sequence is illustrated in Fig. 5.5.

Crucial in this theory is the adiabatic, phase continuous sweeping (or ramping) of the RF frequency. Since sweeps through an avoided level crossing are prone to non-adiabatic [64] transitions ( i.e. Landau-Zener transitions), we must be careful regarding low power and fast sweeps, where we observe these undesired transitions. Sweeps must begin from far off-resonance, compared to the Rabi frequency, so that the bare  $m_F$  states map onto the eigenstates. AC Zeeman states near resonance employ multiple dressed states in superpositions, but we always sweep frequency back off-resonance before measurement in the  $m_F$  basis. A single triggered, fast sweeping RF source based on the AD9910 Direct Digital Synthesizer (DDS) is used

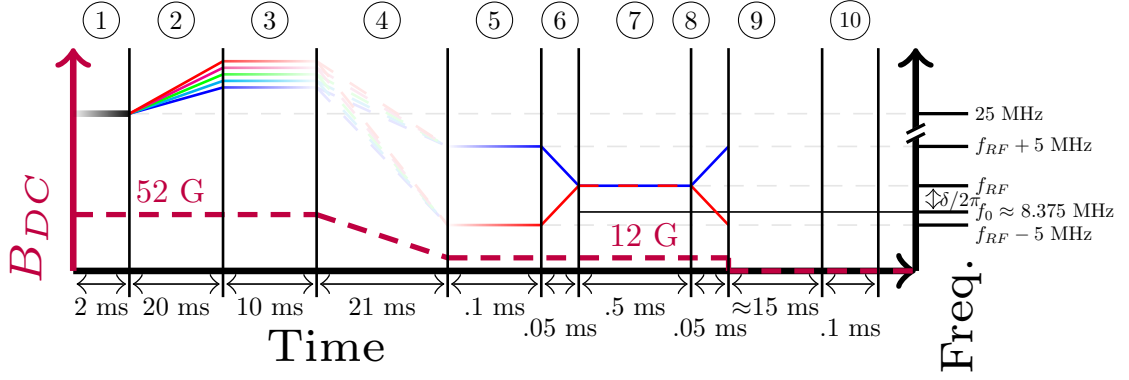


FIG. 5.5: Timing diagram for the main push/pull experiment. 1: At high  $B_{DC}$  field,  $f_{RF}$  is turned on far below resonance at 25 MHz. 2: An ARP sweep brings the population to our choice of  $m_F$  state (see Fig. 5.4). 3: Power is ramped off. 4: With power off, frequency is brought to  $f_{RF} \pm 5$  MHz, and  $B_{DC}$  is dropped to the working resonance  $f_0$ . 5: Power ramped on. 6: Sweep frequency to resonance. 7: Hold at  $f_{RF}$ . 8: Sweep frequency out from resonance. 9: Time of flight ( $t_{of}$ ) with minimized  $B_{DC}$ . 10: Imaging.

here, mixed down with a 100 MHz reference.

Early in the experimental process, we realized that sweeps beginning below half of the resonant frequency (roughly 4 MHz) would produce an enhanced force for the atoms during preliminary tests. We suspected that a harmonic of the frequency was performing a weak additive force, so we used a mixer along with a reference local oscillator at 100 MHz to mix down to the desired frequency. This mixing diminished the first harmonic by about -30 dB, rendering it negligible. We did not test it, but using constant RF frequency and an adiabatically changing  $B_{DC}$  should achieve the same effect.

The push/pull impulse measurements follow the procedure shown in Fig. 5.5, with data plotted in Figs. 5.6 and 5.7. After the population sweep, atoms in the chosen initial  $m_F$  state are held in the ODT for  $\approx 100$  ms while  $B_{DC}$  is held near 12 G. This hold lets any residual motion from changing the  $B_{DC}$  gradient (the subject of Sec. 5.5.1) to dissipate. Next, the RF power is turned on to full power far from resonance, at either  $\pm 5$  MHz from the experimental ‘hold’ frequency  $f_{RF} = \omega_{RF}/2\pi$ . The ODT power is turned off, allowing atoms to fall under gravity. As soon as this

## ACZ Force: Sweep up from ( $f_{RF}$ -5) MHz

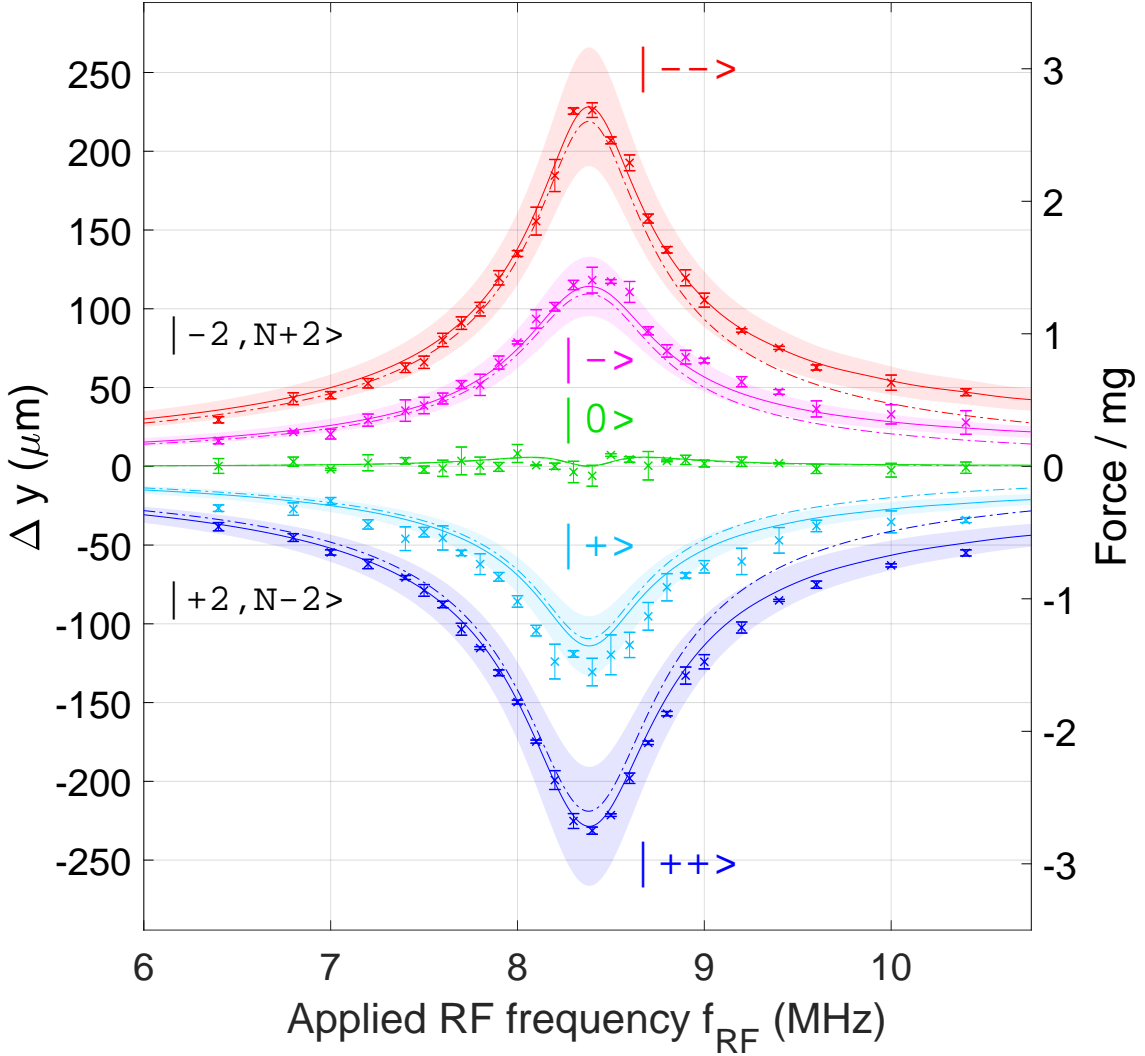


FIG. 5.6: Comparison of theory and data for the intra-manifold ACZ force, or push/pull experiment. Initial frequency is below resonance in this figure. The left axes plot data for the change in position after  $t_{of}$ , relative to baseline ‘no push’ measurements. Each color represents a different AC Zeeman state, which can be reached from either negative or positive initial detuning (here or Fig. 5.7, respectively) from a different dressed state (black). Two dressed states are labeled on the populating side by their far off-resonance projections, intermediate curves are inferred sequentially in the dressed state basis of Eq. 5.1. Error bars in the theory curves are  $1-\sigma$  deviations in measurements of  $\Omega_0$  and  $\nabla\Omega$ , dominated by the uncertainty in  $\nabla\Omega$  measurement (see Sec. 5.5). Each data point is the weighted arithmetic mean of three data points, with the standard error of the weighted mean given as the error bars.

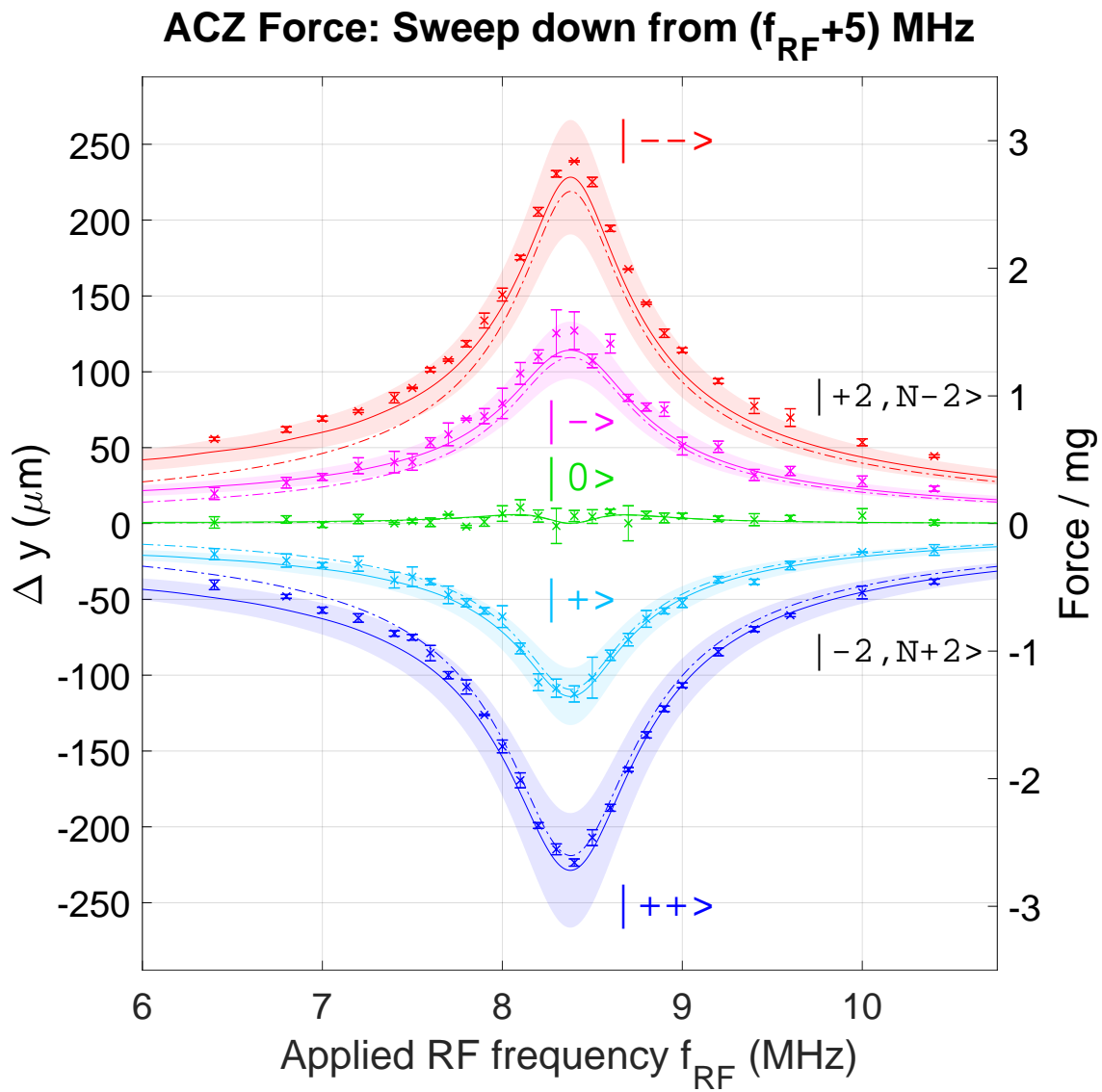


FIG. 5.7: Continuation of Fig. 5.6, separated for clarity. Initial frequency is above resonance in this figure.

happens, the frequency is swept in for  $t_{sweep} = 50 \mu\text{s}$  to the ‘hold’ frequency ( $f_{RF}$ ), held for  $t_{hold} = 500 \mu\text{s}$ , then swept back to  $f_{RF} \pm 5 \text{ MHz}$  for  $t_{sweep} = 50 \mu\text{s}$  to project back into initial  $m_F$  population. This force impulse during the ‘hold’ time changes the momentum of the atom cloud, to first order as  $\vec{F}_{ACZ} \cdot t_{hold} = \Delta\vec{p}$ , where the magnitude of the force depends on detuning, RF power, and initial state.

Atoms with altered momentum fall for  $t_{of} = 16.55 \text{ ms}$  during a time-of-flight drop, and are compared to the same atom state which did not receive an ACZ impulse. The experimental height displacement data are shown on the left axis of Figs. 5.6 and 5.7.<sup>1</sup>

The theory curves to compare against are two-fold. One set, the five dot-dashed lines, represents the simple ACZ force impulse height displacement:

$$\Delta y = \frac{\Delta\vec{p}}{m} \cdot t_{of} = \frac{\vec{F}_{ACZ}}{m} \cdot t_{hold} \cdot t_{of} \quad (5.2)$$

These curves are measured on the right axis in terms of  $mg$ , the force due to gravity. The solid lines and corresponding  $1-\sigma$  error in position on the left axis are integrated over the non-zero momentum during the initial and final sweeps, as well as the less than 1% contribution from variations in RF power as a function of time, frequency, and height drop during the impulse. These integrated force curves are plotted on the left axis as the difference between the final measured position and the non-impulse case. Some entire data sets appear offset vertically from the theory curves, possibly due to systematic errors in reference position measurement corresponding to the set, although an estimate of this systematic error is included in the error bars.

We measured all five AC Zeeman curves, populating from either detuning side

---

<sup>1</sup>Reference ‘no push’ position values were taken before each experimental set, except for the  $m_F = -1$  sets from above and below, the  $m_F = 0$  from below, and one of three  $m_F = 0$  from above sets. We had mistakenly run the wrong experimental sequence for these reference images. These positions were linearly interpolated from the complete set of reference positions for the other  $m_F$  states and are calculated with the fit error added.

in Figs. 5.6 and 5.7. We see that  $m_F \neq 0$  states are weak-field or high-field seeking depending on the initial detuning, and the  $m_F = 0$  remains largely unperturbed but slightly high-field seeking.

We observe forces approaching  $3 mg$  for  $11.36 \text{ dBm} \approx 13.6 \text{ mW}$  of power sent to the atom chip. This result is a significant improvement over a previous experiment, which achieved about the same magnitude of force using  $3.3 \text{ W}$  of  $6.8 \text{ GHz}$  power on the *intermanifold* ( $F_+ = 2$  to  $F_- = 1$ ) transition [44]. We attribute this mainly to the impedance characteristics of the atom chip. Since the current amplitude generates force, and  $P = I^2Z$ , then the frequency dependence of the impedance,  $Z(f)$  between a few MHz and a few GHz, determines the effectiveness of the force to power ratio. Optimization of GHz power transfer via microstrips, co-planar waveguides, and other techniques is key to the advancement of this technology as a neutral atom trapping mechanism.

### 5.3 AC Stern-Gerlach

To demonstrate simply the power of this technique to turn spin states into high- *or* low-field seekers, we separate  $m_F$  states vertically using the ACZ force, and horizontally with a traditional DC Stern-Gerlach magnetic gradient. The result is shown in Fig. 5.8, and the process is illustrated with a timing diagram in Fig. 5.9. To populate all five states, we perform a resonant Rabi pulse for much longer (1 ms) than the coherence time (about  $10 \mu\text{s}$ ). Low trap lifetimes for the  $m_F = \pm 1$  and 0 states leave them with a lower population number than the  $m_F = \pm 2$  states. With all  $m_F$  states populated (unevenly), we perform the sweeping push/pull procedure from  $f_0 + 5$  or  $f_0 - 5 \text{ MHz}$  into resonance at  $f_0 = 8.375 \text{ MHz}$ , to maximize the ACZ force. Sweeping frequency allows the  $m_F$  states to transform into the ACZ eigenstates, each seeking high- or low-field, to varying degrees. An atom whose

energy is raised with the ACZ effect will seek the lower field away from the atom chip, while atoms whose energy is lowered by the ACZ effect will seek a higher field toward the atom chip. During the hold time impulse, the momentum of atoms changes, turning into a position displacement after a time of flight. Ramping frequency from higher or lower initial frequency, the direction of this impulse changes (except for the  $|0\rangle$  state). Sweeping back off-resonance projects ACZ states back into pure  $m_F$  states. In essence, we repeat the central point at  $f_{RF} = 8.375$  MHz from the plot in Figs. 5.6 and 5.7 for five states simultaneously.

After this impulse, we apply a horizontal DC Stern-Gerlach pulse, comprised of a DC magnetic field gradient induced by the current in a single coil. Atoms in  $F_+ = 2$  with positive (negative)  $m_F$  numbers seek lower (higher) field at low  $B_{DC}$  values, thus always react the same to a  $B_{DC}$  gradient.

As shown in Fig. 5.8, non-zero  $m_F$  atom states are pushed or pulled by the AC Zeeman effect depending on the ACZ state and the sign of initial frequency detuning (here, -5 and +5 MHz), where they are pushed or pulled by the DC Stern-Gerlach effect depending only on their  $m_F$  state. We call this use of the AC Zeeman force to separate atoms by spin state the ‘AC Stern-Gerlach’ effect, although it was initially called the ‘transverse Stern-Gerlach’ in the literature [38]. Separation of spin state by this effect has been demonstrated on a number of different quantum platforms [69].

## 5.4 Time Evolution of States

Since the intra-manifold AC Zeeman effect requires interaction between multiple dressed states (in our case, five) at near-degenerate energies, we explore the tendency of these states to mix over time. Ideally, we would see no mixing between states for long hold times at the force peaks for when trapping, although we will find this is not

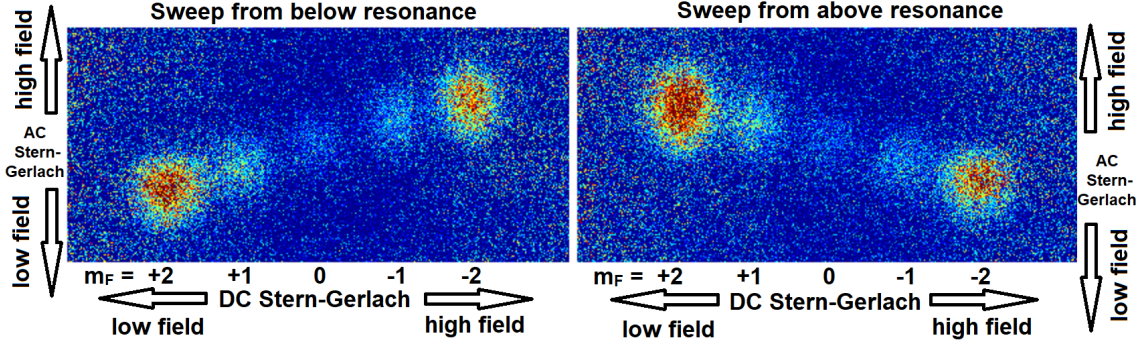


FIG. 5.8: An example of sequential AC and DC Stern-Gerlach separation. All five  $m_F$  projections are populated with atoms, which are pushed and pulled vertically by the spin-dependent ACZ force, then separated horizontally by the DC Stern-Gerlach effect. False color optical density plots here are composite sums of more than a dozen experimental images each.

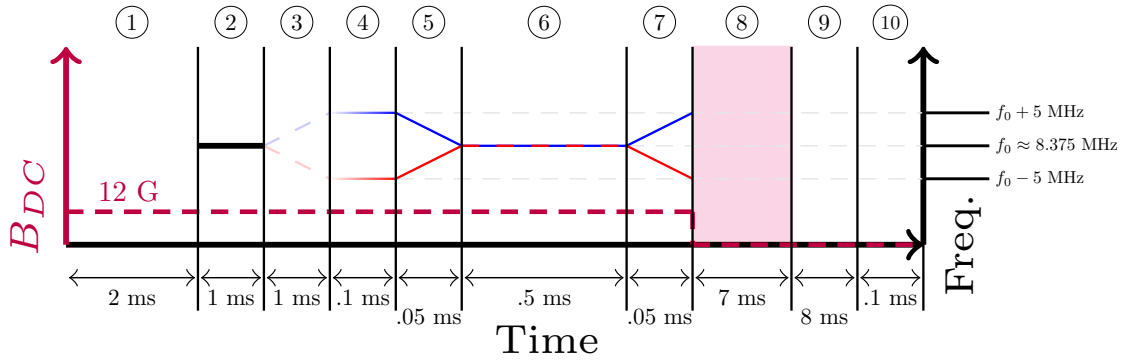


FIG. 5.9: Timing diagram for the AC Stern-Gerlach experiment. 1: A long resonant Rabi pulse scrambles population into each  $m_F$  state. 2: With power off,  $f_{RF}$  is moved red or blue of resonance. 3: RF power ramped on. 4: Frequency sweeps in to resonance, from 5 MHz red or blue. 5: Frequency held on resonance. 6: Frequency sweeps out from resonance, to 5 MHz red or blue. 7: Atoms fall with DC Stern-Gerlach on, and  $B_{DC}$  minimized. 8: Atoms fall without DC Stern-Gerlach. 9: Imaging. 10: Experiment ends.

the case. To test this state mixing, we populate either ACZ state  $|++\rangle$  or  $|--\rangle$ , by beginning at positive or negative detuning using one of the  $m_F = \pm 2$  states. While holding atoms in the ODT, we then sweep to near resonance, hold for some time, and sweep the frequency away from resonance to count atoms projected back into bare  $m_F$  states. Increasing populations in states other than the initial one indicate mixing, shown in some sample mixing data in Fig. 5.10. The RF power used in this section is significantly lower ( $\approx -10$  dB) than used for the force measurements.

Since this behavior is not strictly exponential or linear, our measure of choice here is  $T_{cross}$ , the time when population in the initial state  $P_{start}$  equals the summed population in all other states:  $P_{other} = \sum_{i \neq start} P_i$ . Equivalently,  $T_{cross}$  is the time it takes for the initial state to make up only half the total population. We should note that the hold time in the ODT is not equal for all states. The  $m_F = +2$  and  $-2$  states have an  $e^{-1}$  time constant of roughly 7 and 5 seconds respectively, while the  $m_F = 1, 0, -1$  states have time constants just below 1 second, likely due to the ability of non-stretch states to have inelastic collisions. Since the primary contribution to the total  $P_{other}$  is the adjacent state ( $m_F = \pm 1$ ), the non-stretch states' relatively short lifetimes will diminish the population more in  $P_{other}$  than in  $P_{start}$ . The difference in state lifetimes will artificially increase  $T_{cross}$  compared to its value with full retention of the *other* states.

A sample of the time dependence of state population data is given in Fig. 5.10. Total atom number decreases exponentially over this test, measurements are always of population ratios, and precision decreases with low total population number. We perform a fit of  $P_{start}$  and  $P_{other}$  over a hand-picked range around the crossing point, which gives  $T_{cross}$  and its error. Fits are linear in population ratio and  $\log(\text{time})$ , implying this delayed decay is exponential.

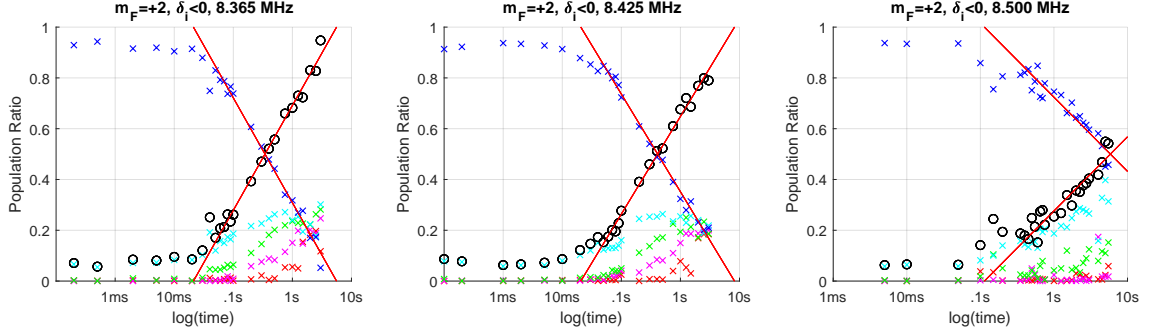


FIG. 5.10: Three examples of the time dependence of fractional population data, including fits for determining  $T_{cross}$ , using 0.66 mW (-1.83 dBm). Selected data is slight negative detuning (left), slight positive detuning (middle), and farther positive detuning (left), and correspond to three points in Fig. 5.12. Each color ( $\times$ ) represents a different  $m_F$  state, and black ( $\circ$ ) represents the sum of all non-initial population ratios. Fits used to obtain  $T_{cross}$  values are shown in red.

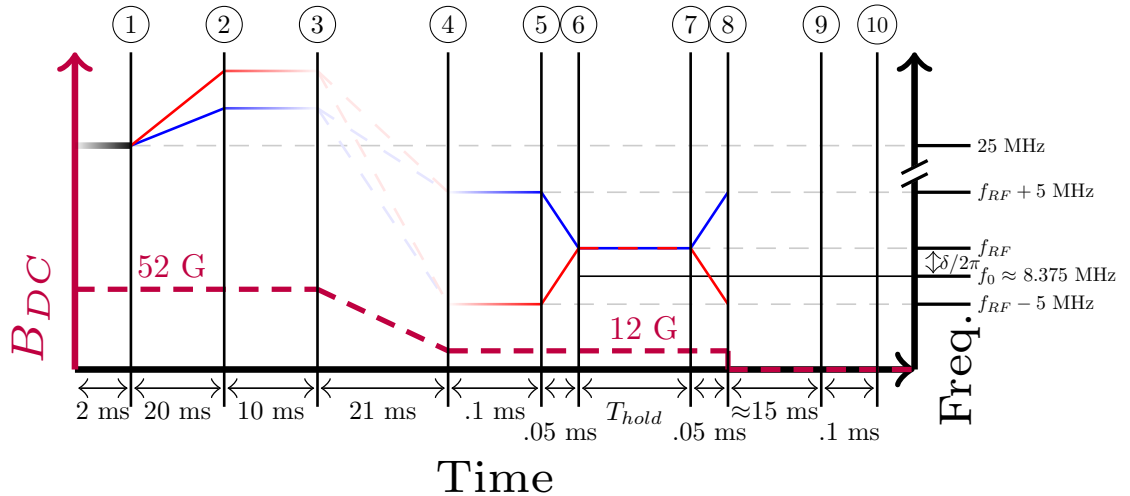


FIG. 5.11: Timing diagram for the time dependence of state population experiment. 1: A frequency sweep populates either  $m_F = \pm 2$  from  $|++\rangle$  at the 52 G resonance. 2: The ARP sweep power ramps off. 3: Frequency and  $B_{DC}$  both drop to the 12 G resonance. 4: RF power ramps back on. 5: Frequency sweep to the hold frequency from either red or blue detuning. 6: A variable hold time, while atoms remain trapped in the ODT. 7: Frequency sweep back off-resonance to project AC Zeeman states to  $m_F$  states. 8: Atoms fall and separate due to DC Stern-Gerlach field. 9: Imaging.

### 5.4.1 Detuning Effects

We find that the detuning of the applied RF has a major effect on state mixing. Operating far from resonance will result in longer times to mix states ( $T_{cross}$ ). The shortest  $T_{cross}$  times are found very close to atomic resonances, where the highest force is found, so creating a strong AC Zeeman trap without significant state mixing requires balancing these two factors via selection of detuning. We suspect that resonant losses are due in part to inelastic collisions of population components in the non-stretch states ( $m_F = -1, 0, 1$ ), similar to the ODT's various lifetimes for the  $m_F$  states.

Additionally, we argue that one contribution to dressed state mixing could be akin to the Landau-Zener effect, but with periodic or noisy non-adiabatic energy sweeping, rather than a linear in time sweep. The current source providing the tunable  $B_{DC}$  field has a few mA of noise at 60 Hz, which maps to roughly 15 kHz RMS jitter in the resonant frequency of the atoms. By holding frequency constant but moving the atomic resonance, the atoms can “jump curves” and transition between states. We can see the relevant atomic transitions clearly in Fig. 5.4, whereas Fig. 5.2 represents the correct resonance and non-degeneracy matching the experiment. At roughly  $\sqrt{\frac{1}{8}}\Omega_0 = 83$  kHz, comparing the  $|--\rangle$  state, which has only one level crossing, with the  $|++\rangle$  state, with four crossings, at most 60 kHz apart, we see a much wider central low  $T_{cross}$  region where crossings are spread roughly 60 kHz more than the single-resonance  $|--\rangle$  case. This spread is shown in Fig. 5.12, suggesting that the proximity to bare level crossings (low detuning) is a major contributing factor to state mixing times whether or not Landau-Zener transitions are the reason. When  $|\delta|/2\pi > 100$  kHz,  $T_{cross}$  for both the  $|++\rangle$  and  $|--\rangle$  states is observed greater than 3 seconds, the longest time we measured.

We expect the Rabi gradient, which was helpful for forces, to flop atoms at a

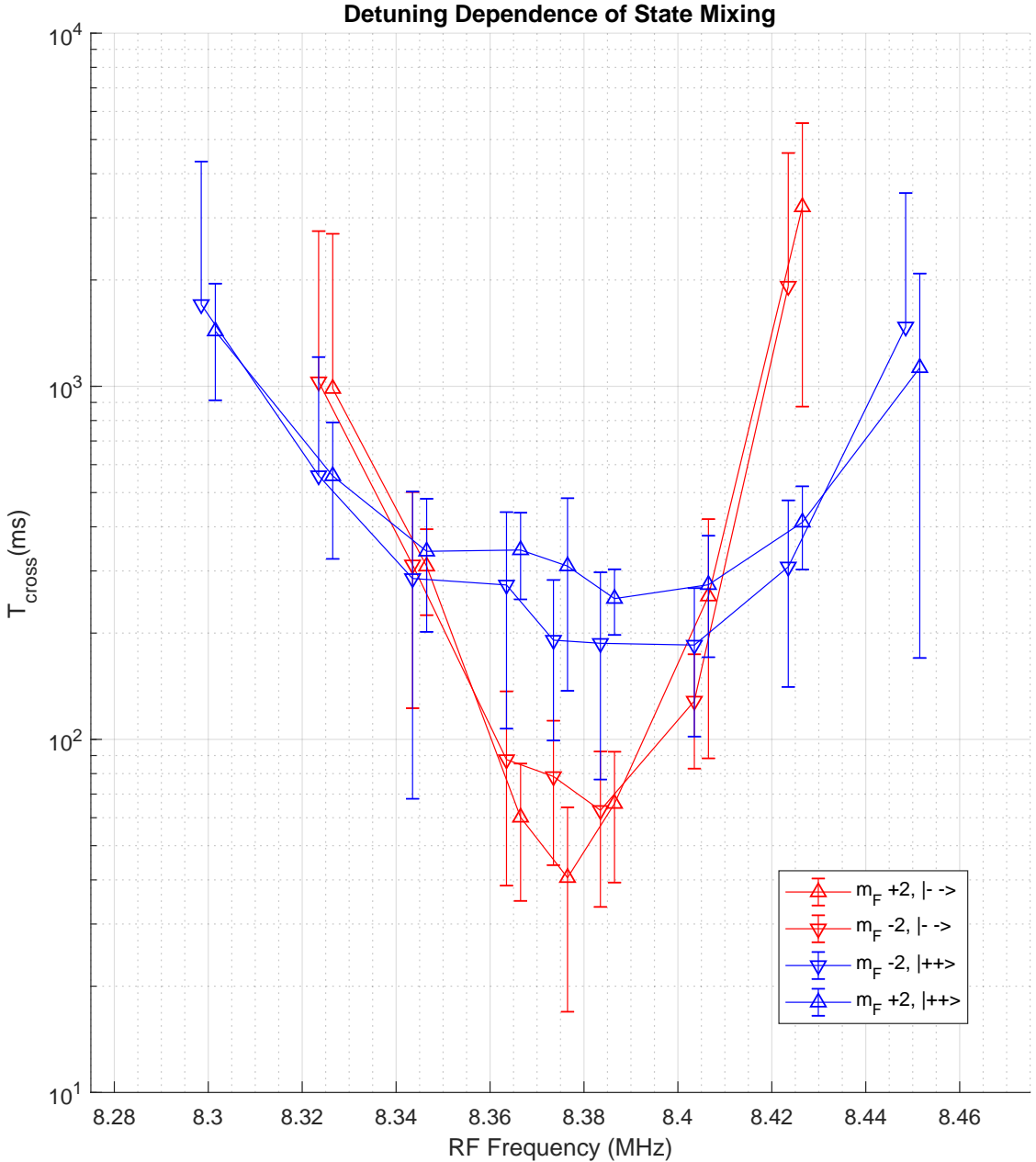


FIG. 5.12: Detuning dependence of  $T_{cross}$  using 0.66 mW (-1.83 dBm). Pink and blue curves represent  $|-\rangle$  and  $|+\rangle$  states respectively, where up/down triangles indicate initial state,  $\pm 2$ . Both initial states from both detuning directions are shown. Data points are slightly offset right and left of the measured value for clarity. Actual detunings shown are  $[(-75), -50, -30, -10, 0, 10, 30, 50, (75)]$  kHz, from 8.375 MHz. Data further detuned have times longer than the 3 seconds reliably measured. Large error bars which reach negative values are omitted.

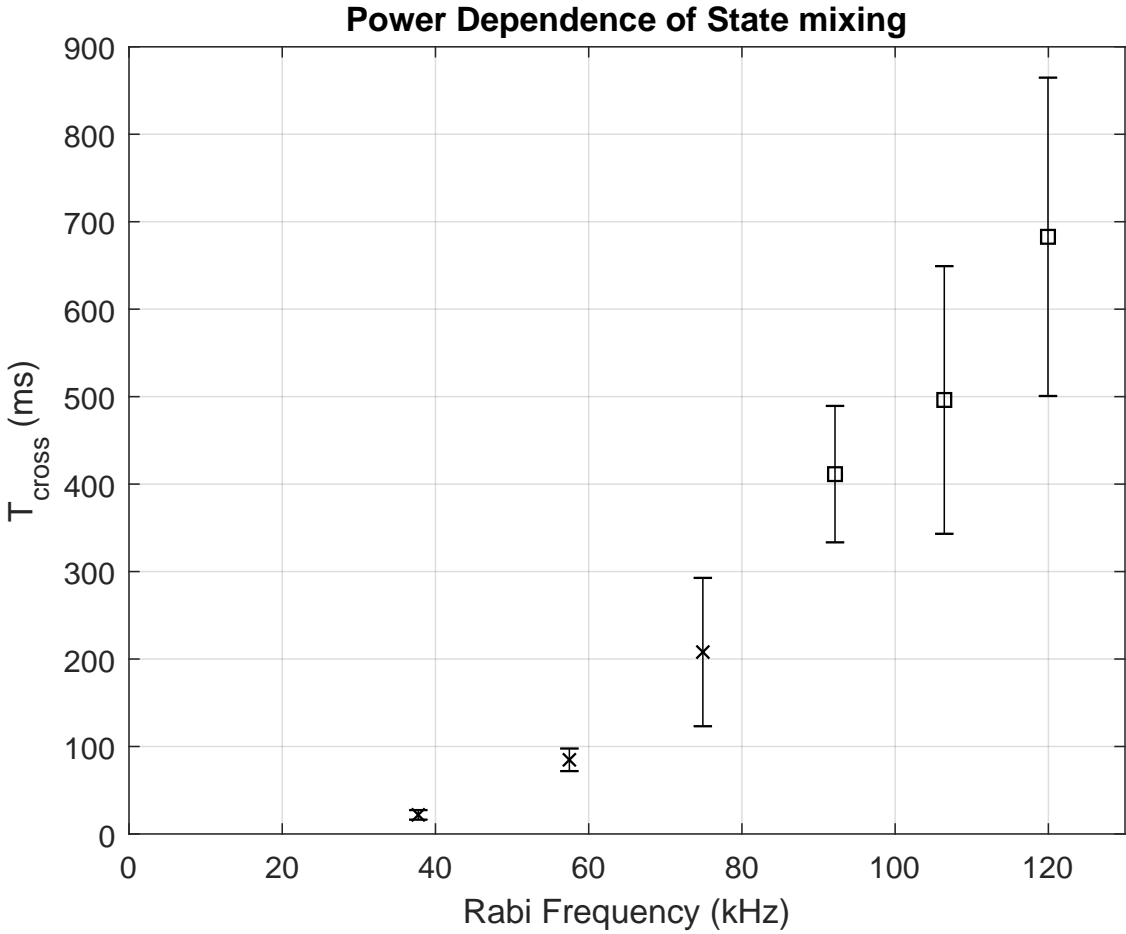


FIG. 5.13:  $T_{cross}$  (ms) vs. scaled values of  $\sqrt{\frac{1}{8}}\Omega_0$  in kHz. All points come from  $T_{cross}$  fits for resonant holds of  $|++\rangle$ , and errors in  $\times$  symbols come from these fits. Errors in  $\square$  points are hand-picked as bounds on  $P_{other} >$  or  $< P_{start}$  from viewing the data, which had a good fit but a large error given a small time sample.

different rate over the vertical extent of the cloud, maximizing at resonance. This gradient can cause decoherence as atoms sample the spatial extent of the cloud over long hold times, population flopping with larger amplitudes near resonance, and rates dependent on position. A colder atomic population should sample less of the field, mitigating this effect. We did not simulate this pathway, but it is a likely cause for some of unfortunate state mixing observed in the system.

### 5.4.2 Power Effects

Another major contributing factor to the mixing rate of dressed states is their energy separation. On resonance, the energy separation is proportional to the Rabi frequency, which depends on applied power. With more power and thus more energy separation, atoms are less prone to state transitions. We study the on-resonance behavior of the low-field seeking  $|++\rangle$  state, a prime candidate for trapping, at six powers spanning 10 dB. We calculate the Rabi frequency for measured powers using square-root power scaling from measured quantities.

We find that higher powers provide longer times remaining in the initial state, and low powers are more prone to mixing. For the power scales tested on resonance, a rule of thumb is that for each 10 kHz gain in Rabi frequency, one gains 83 ms of time before  $T_{cross}$ .

### 5.4.3 Beyond Landau-Zener

If the state mixing were purely from the Landau-Zener non-adiabatic crossing effect, we suspect the time behavior of the population ratios would be different from that observed. Both the current-generated field and environmental field exhibit 60 Hz noise in  $B_{DC}$  from US utility power, one might expect changes in population to occur in  $\frac{1}{60Hz} \approx 16.7$  ms steps (depending also on relative experimental timing), or to in general have a constant rate not dependent on population over long times. The behavior observed is that atoms remain in the initial state for some time (typically 20-200 ms depending on parameters) before transitioning into an exponential decay, populating successive adjacent states, approaching an equal population in all states (on resonance case). We do not have a theoretical model for the cause of this behavior. However, the initial plateau and exponential change agree with aspects observed previously on state mixing in inter-manifold AC Zeeman state mixing [44].

One potential difference is the observed approach to equal population, where the inter-manifold mixing approached different ratio plateaus, depending on detuning. We cannot claim that the ratios always approach equal values since the time to reach static populations off-resonance are much longer than the  $m_F = \{-1/0/1\}$  trap lifetimes, so we cannot measure this expectation accurately.

#### 5.4.4 Outlook for Trapping

These mixing experiments were performed at significantly lower power than the push-pull experiment (roughly -10dB or 30% of  $\Omega_0$ ). For experimental conditions akin to ours, one can expect at least hundreds of milliseconds before state mixing takes effect on resonance at full power. Additionally, one could move, say 100 kHz away from resonance, still retaining more than half the force, but perform significantly better with state mixing, allowing state fidelity times better than a few seconds in theory. This behavior allows a wide range of parameters for state-specific trapping, for which state mixing and trap depth both favor increased power.

### 5.5 Rabi and Rabi Gradient

In order to predict the ACZ force magnitude and detuning dependence in Figs. 5.6 and 5.7, we require an accurate measure of both the Rabi frequency  $\Omega_0$  and its local gradient  $\nabla\Omega_0$ . This section briefly recaps relevant material from Chap. 4. We measure  $\Omega_0$  using resonant RF (8.375 MHz, nominal 12 G  $B_{DC}$ ) applied to atoms held in the ODT. The Rabi broadening of  $\approx 400$  kHz covers the slight spread of resonances ( $\approx 60$  kHz), but our numerical fitting model includes the detuning of each particular transition. Atoms initially in the  $m_F = +2$  state flop sequentially through partial populations in the  $m_F = \{+1, 0, -1\}$  states before fully populating the  $m_F = -2$  state, then the order reverses and repeats. The decoherence

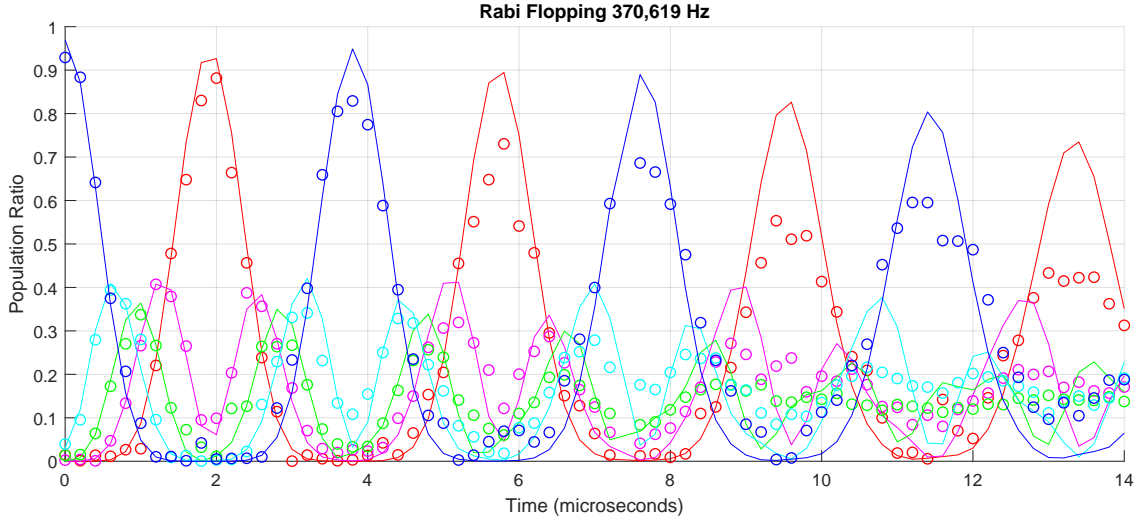


FIG. 5.14: An example of Rabi flopping data, where the title gives the  $\sqrt{\frac{1}{8}}\Omega_0$  fit value. The ratio is determined by individual state population, divided by the sum of all five state populations. Colors for the  $(+2, +1, 0, -1, -2)$   $m_F$  states are (blue, cyan, green, magenta, red). While the experimental data decoheres, the theory curve does not account for this. Free parameters are the Rabi frequency, initial time delay, and initial population ratio. Atoms had an initial wave function of (85, 15)% in the  $(+2, +1)$   $m_F$  state.

of states means that only 4-6 flopping periods are observable. Images are taken in randomized order for every  $0.1 \mu\text{s}$  out to  $14 \mu\text{s}$ . After the Rabi pulse, atoms are dropped by turning off the ODT and then separated by  $m_F$  state horizontally by a 9 ms Stern-Gerlach pulse in a single current coil. Atoms in each  $m_F$  are counted, and the collected data is a least-squares fit to a time-evolved Hamiltonian. Since the  $m_F = \pm 2$  states give the clearest signal, we average only these two fits to resolve a Rabi frequency for each set.

To measure at different positions, the power in the ODT is lowered to about 60%, letting the atoms sag roughly  $\Delta y = 7 \mu\text{m}$  under gravity while remaining in the trap. Measuring the Rabi frequency allows for a linear fit between two points (or multiple readings at each point) to get the local  $\nabla\Omega_0$ , shown in Fig. 5.15 and detailed in Sec. 4.2.4. In theory, Rabi field has a spatial  $\frac{1}{r}$  character (distance  $r$  from a thin wire), and its gradient has a  $-\frac{1}{r^2}$  character, which are useful for envelope calculations of effective chip current from measurements of  $\Omega_0$ . In practice, only a local linear

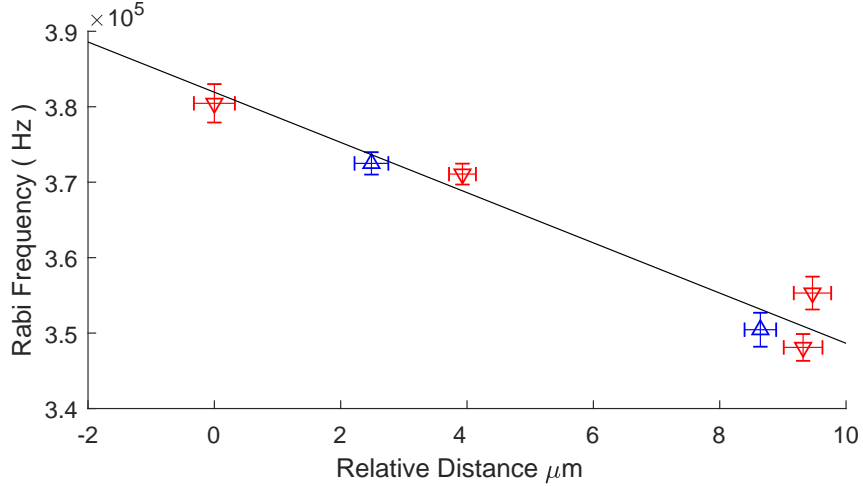


FIG. 5.15: Rabi gradient fit using measurements of  $\sqrt{\frac{1}{8}}\Omega_0$  ( $y$  axis) at different positions ( $x$  axis). Exact values are given in Tab. 4.1. Blue/upward triangles were taken at full RF power, and red/downward triangles were taken at 1.34 dB lower RF power and scaled up by  $\sqrt{10^{1.34/10}}$ . Error bars are  $1-\sigma$  error. The fit here gives  $\nabla\left(\sqrt{\frac{1}{8}}\Omega_0\right) = 3.32(55)$  kHz/ $\mu\text{m}$ . This uncertainty dominates the  $1-\sigma$  shading in Fig. 5.6 and 5.7.

approximation is necessary.

Rabi gradient measurements were taken concurrently with the push/pull data sets but did not give precise results. After refining the gradient measuring process to the one described above, accurate  $\nabla\Omega$  measurements were scaled to the  $\Omega_0$  measurements taken alongside the push/pull data. For the same RF power, the value of  $\frac{\nabla\Omega}{\Omega}$  should be constant, so we can scale the later  $\Omega_l$  to the original  $\Omega_0$  via  $\nabla\Omega_0 = \frac{\Omega_0}{\Omega_l}\nabla\Omega_l$ .

### 5.5.1 Background $B_{DC}$ Gradient

When testing the AC Zeeman force, we measure atom cloud displacement after a known impulse and time-of-flight. Initial results showed some vertical displacement effect based on  $m_F$  level in the *absence* of an AC Zeeman force as if some vertical Stern-Gerlach gradient was affecting the free fall. I performed a study of this in August 2018, comparing observed ballistic falls in  $m_F = 2, 0, -2$  levels, at different nominal values of background  $B_{DC}$  field, compared to expected gravitational falls.

This effect would interfere with AC Zeeman force measurements, which are based on vertical displacements of each  $m_F$  state. We find a vertical gradient per applied  $B_{DC}$  field value of 53.34 (mG/cm)/G, or 141.5 (mG/cm)/Amp in the generating coils. This gradient moves  $m_F = -2$  atoms up against gravity, pushing  $m_F = +2$  down with gravity, and more in that direction for a stronger field. This gradient suggests a radial minimum from the generating coils centered below the atom chip. To accommodate this, we measure displacements with respect to the same  $m_F$ 's position in unforced free fall and lower the field as much as possible during the time of flight while maintaining a weak quantization axis for imaging.

Additionally, we see an *axial* minimum in this  $B_{DC}$  field play a role in end-capping the AC Zeeman trap in Chap. 7 and the ‘main’ ODT trap. A spatially-varying  $B_{DC}$  would alter atomic resonance as well, but this is a minor effect compared to the DC Zeeman gradient/Stern-Gerlach force.

## 5.6 Conclusion

We have demonstrated the ability to generate a force for neutral atoms using RF near field gradients at frequencies near intra-hyperfine manifold energy splittings. Force measurements agree with theoretical predictions based on the avoided level crossings of quantum spin states dressed with near-resonant photons. All non-zero  $m_F$  states can become a high- or low- field seeker, depending on initial frequency detuning. Since the intra-manifold transitions are exclusively sensitive to  $\sigma_+$  or  $\sigma_-$ , using multiple wires at different phases should allow for a local minimum in  $B_+$  or  $B_-$  field, and thus the ACZ energy, allowing for spin-specific trapping of neutral atoms using this force. Looking toward trapping, we find that the time until states mix depends strongly on power and detuning, where a slight detuning and high power should allow atoms to remain longer in the initial state.

# CHAPTER 6

## Trap Theory

In the previous chapter, we demonstrated that atoms could be made into high- or low-field-seeking states with respect to a single-wire AC Zeeman potential, a monotonic vertical gradient capable of holding atoms against gravity with  $F_{ACZ} > mg$ . However, Earnshaw's theorem states that we cannot construct a local static magnetic maximum in free space, which also applies to our AC near fields, so we seek to generate a local minimum that can trap low-field-seeking AC Zeeman states. We restrict ourselves to parallel RF currents in the  $\hat{z}$ -direction, as on our atom chip, to generate  $B_{\pm}(x, y)$  fields which have a local minimum, e.g., where the field from two different wires cancel each other in a particular way. Having RF signals on multiple wires introduces the relative phase  $\phi$  as a crucial parameter for controlling the generated field.

In this chapter, we give a pedagogical explanation in Sec. 6.1, of our trapping approach using a simple two-wire case. We show some simulations in Secs. 6.2 and investigate a local linear region in Sec. 6.2.1. We briefly discuss the effect of detuning on trap profile and population in Sec. 6.3. We discuss the location of a trap in Sec. 6.4, focusing on the two-wire and two-microstrip cases in Sec. 6.4.1 and 6.4.2,

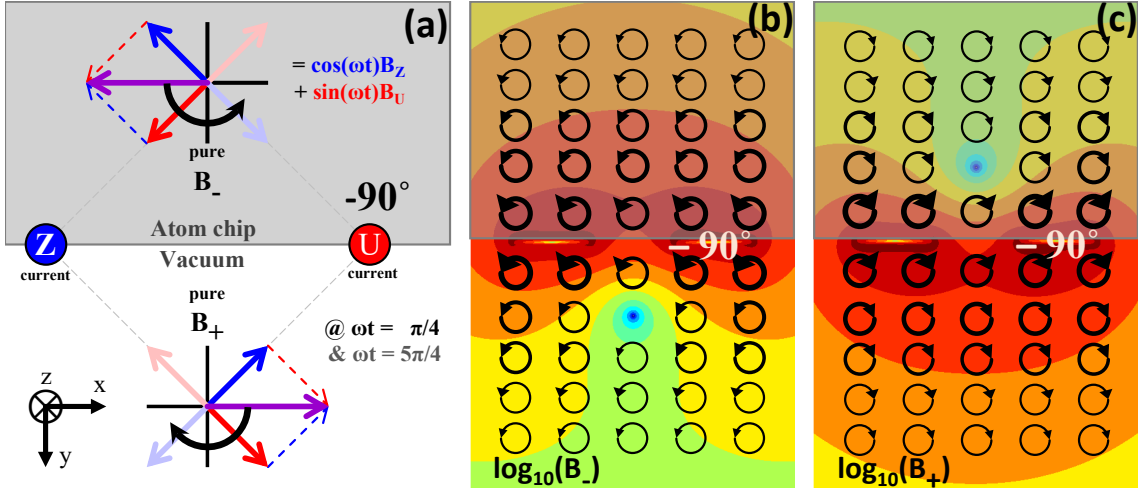


FIG. 6.1: Pedagogical two-wire trap illustration. (a) A pedagogical explanation of the circular polarization of the magnetic near field when the right-hand wire is phase-delayed by  $90^\circ = \pi/2$ . Two locations are seen to have pure circular polarization, where the *opposite* polarization component has a minimum. (b,c) Simulated contours of  $\log_{10}(B_\pm)$  with finite-sized wires matching the experiment. The  $B_-$  field in (b) exhibits a local minimum below the chip surface, which can trap atoms in the  $F_+ = 2$  manifold.

respectively. The ‘microstrip’ version includes a ground plane and image currents, which fundamentally changes trap behavior. In Sec. 6.4.3 and 6.4.4 we discuss location of a trap in the three-wire and three-microstrip cases. Then, we move on to discuss a few exotic traps which have appeared in our simulations: a ‘donut’ trap for the medium-field seeking  $|+\rangle$  state in Sec. 6.5, and a pyramidal trap with a diagonal quantizing field in Sec. 6.6. We end with a summary in Sec. 6.8

## 6.1 Pedagogical Explanation

Using the schematic diagram of Fig. 6.1(a), I will describe a two-wire trap, the same one as we demonstrate in Chap. 7, and analyzed more generally in Sec. 6.4.1. By construction, we have two thin wires (identified with actual chip wires, called ‘U’ and ‘Z’) separated by a distance  $2d = 100 \mu\text{m}$  center-to-center. Each wire carries equal current amplitude and RF frequency, but the two currents have a relative phase difference, defined as the amount the right ( $x > 0$ ) U-wire current precedes

the Z-wire  $\phi_{UZ} = \phi_U - \phi_Z$ . We set  $\phi_{UZ} = -90^\circ$ , so that the Z wire precedes by a quarter phase, as  $\cos(\omega_{RFT})$  to  $\sin(\omega_{RFT})$ , shown in Fig. 6.1. If we look at each wire's right-hand-rule contribution to the local magnetic field at positions  $y = \pm d, x = 0$  (or generally,  $y = \pm \tan(\phi_{UZ}/2)$ ), we find pure circular components as the local magnetic  $B$  vector evolves in time. As indicated on the axes, the purple vector rotates over a cycle from blue→red→anti-blue→anti-red, and so on. This rotating vector is purely  $B_+$  at  $y = -d$ , and purely  $B_-$  at  $y = d$ , notably *different circular directions* at either location. This pure circular polarization in either  $B_\pm$  implies *no* component in the opposite  $B_\mp$  field at that specific location. This behavior generates the local minimum we were seeking: Moving away from this position generally gives elliptical polarization containing both polarizations, but atoms only respond to *one* of these polarizations, as discussed in Chap. 3. An equivalent statement about the zeros in  $B_\pm$  is that at these locations the local magnetic oscillations along  $\hat{x}$  and  $\hat{y}$  have phase difference  $\Delta\phi_{xy} = \phi_x - \phi_y$  equal to  $\pm\pi/2$  and their amplitudes are equal:  $|B_x| = |B_y|$ .

A more realistic description using finite-sized wires is shown in Fig. 6.1(b,c) which shows the logarithmic ( $\log_{10}$ ) contour maps of the  $B_\pm$  field strength near the wires. In Fig. 6.1(b) there is a local minimum in  $B_-$  below the chip, and in Fig. 6.1(c) there is a minimum in  $B_+$  within the chip substrate.

## 6.2 AC Zeeman Trap Simulation

In order to calculate the  $B_\pm$  near fields and the resultant AC Zeeman potential, we conduct numerical simulations across a finite square grid of sample points in the manner described in this section. We invoke our currents (thin wires or finite-sized), then calculate over an area of  $(x, y)$  the quasi-static (Biot-Savart law)  $B_x$  and  $B_y$  components that those currents generate, including the complex phase information

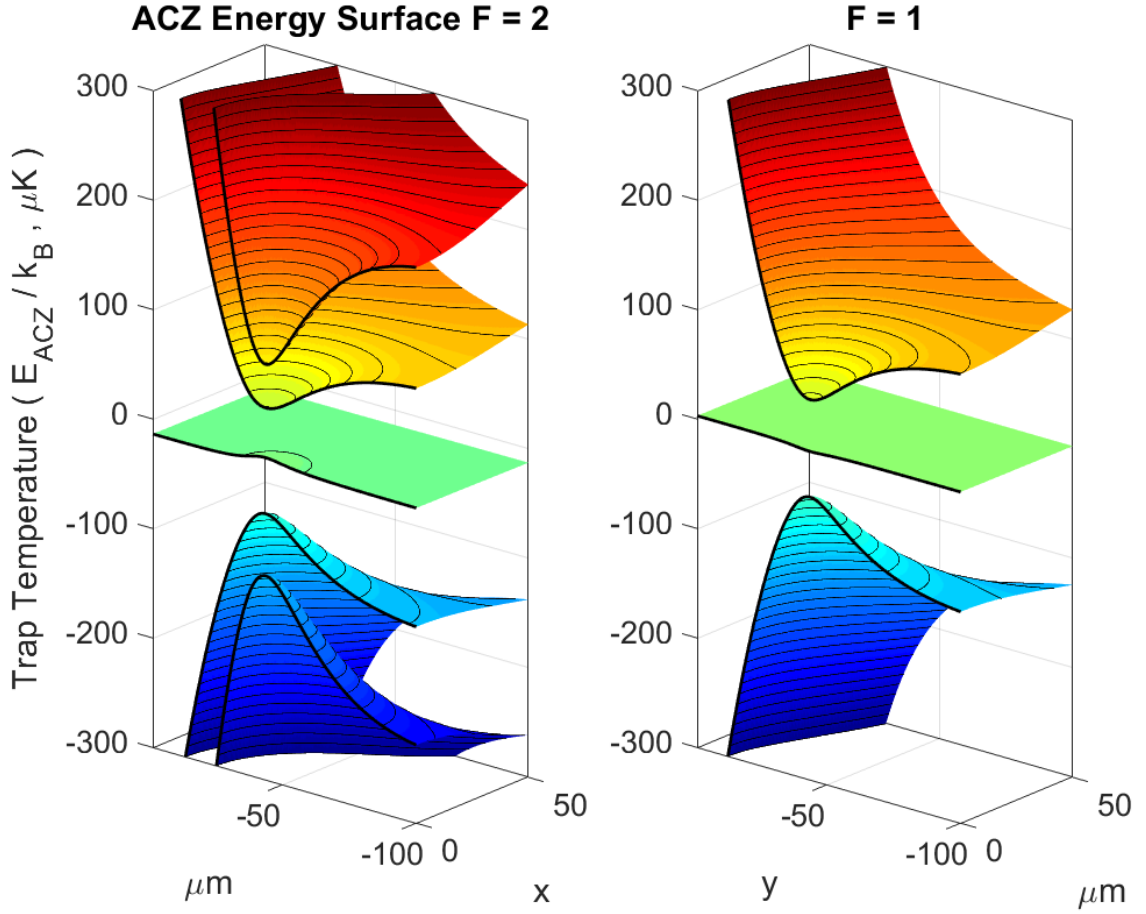


FIG. 6.2: Simulated trapping and anti-trapping energy surfaces for all RF AC Zeeman states, using  $\phi_{UZ} = +90^\circ$  for  $F_+ = 2$  (left) and  $-90^\circ$  for  $F_- = 1$  (right). Simulations use  $I_A = I_B = 500$  mA amplitude in two  $50 \mu\text{m} \times 4 \mu\text{m}$  wires using the Silvester simulation method (Chap. 8), separated  $100 \mu\text{m}$  center-to-center. Applied frequency  $f_{RF}$  in this simulation is 21 MHz ( $\delta \approx 1$  MHz) for  $B_{DC} = 28.58$ , leading to nearly 1 MHz separation of potential surfaces at the  $B_\pm$  field zero. Black contour lines mark each  $10 \mu\text{K}$ .

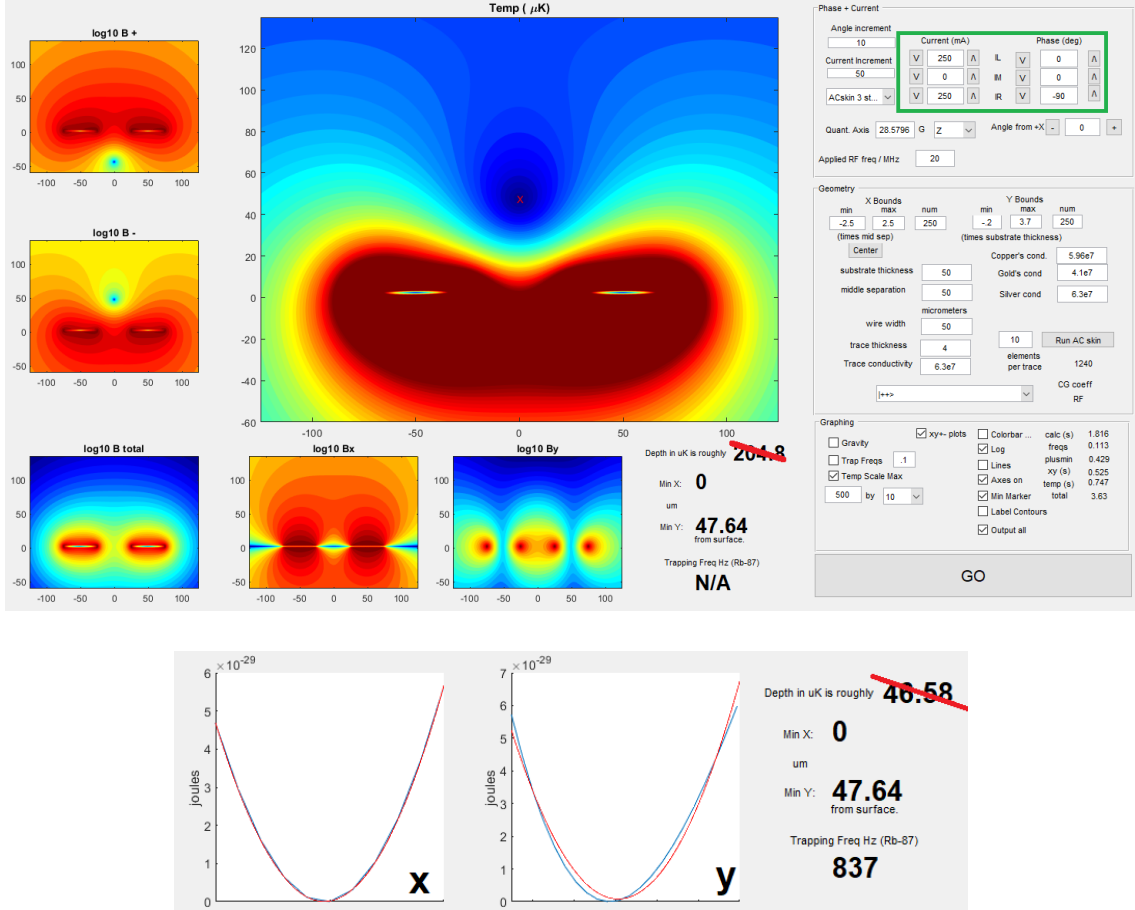


FIG. 6.3: Top: Screenshot of an AC Zeeman trap simulation GUI, matching the pedagogical example but reversing vertical orientation, so that the chip is at the bottom of this simulation ( $y$  still measures distance to the chip surface). The  $E_{ACZ}$  trapping potential for  $|++\rangle$  is shown on the largest ( $x, y$ ) axes over real space  $\mu\text{m}$ , with value plotted by color, converted to temperature using  $T = E_{ACZ}/k_B$ , with 10  $\mu\text{K}$  color grades and a cutoff at 500  $\mu\text{K}$ . Current settings in the top right corner (green box) generate  $B_x, B_y$ , plotted in two bottom middle graphs. Their quadrature total is shown in the bottom left corner, and the fields of interest,  $B_{\pm} = B_x \pm iB_y$  are two plots in the top left corner. Geometry and AC skin settings are entered with the right middle panel, and plotting options in the bottom right panel. Bottom: The GUI can also fit trap bottom curvature to get average trap frequencies, shown for a slight detuning  $\delta \approx 1$  MHz. Accurate trap depths require calculating the saddle-point beyond the trap (top of this figure), simulations which are zoomed in on the trap or measure inside false trace minima are incorrect, and this value is crossed out.

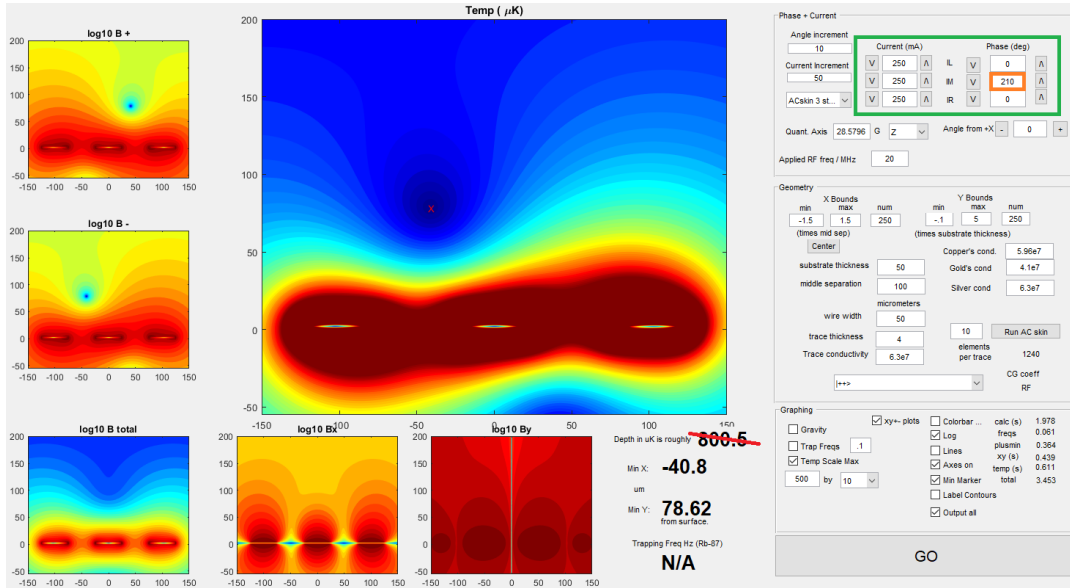
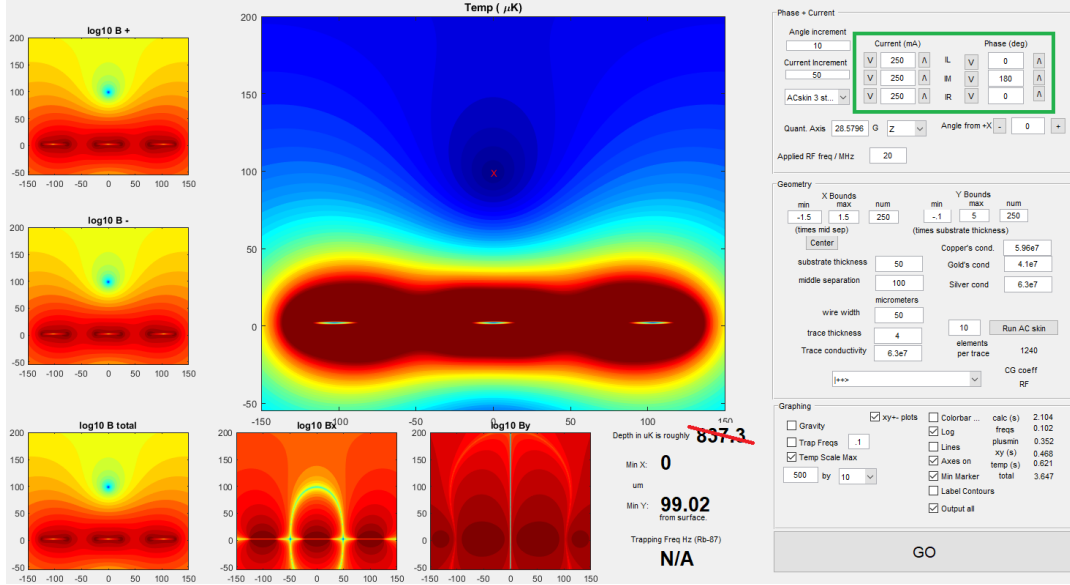


FIG. 6.4: Simulations of  $|++\rangle$  in a three-trace trap, where the middle wire is  $180^\circ$  out-of-phase on the top image, and  $210^\circ$  for the bottom image. Note for the top case, the total  $B$  field also has its minimum at the ACZ trap location. In the bottom case, the  $B_\pm$  move differentially sideways, as indicated later, but only one contributes to the RF AC Zeeman energy.

from the currents. Next, we calculate  $B_{\pm} = B_x \pm iB_y$ , which generates  $\Omega_0 = \mu_B|B_{\pm}|/\hbar$ , and we calculate the AC Zeeman energy over each point in space, from the  $\Omega_0(x, y)$  coupling at each point, but with uniform detuning  $\delta$  and quantizing field  $B_{DC}$ . Sample trapping (and anti-trapping) potential surfaces are shown in Fig. 6.2, with 1 MHz detuning. At the trap bottom where  $\Omega_0 = 0$ , the detuning ( $1 \text{ MHz} \times \frac{\hbar}{k_B} \approx 48 \text{ } \mu\text{K}$ ) represents the primary energy separations in AC Zeeman energy. Note that the generating phase is flipped by  $\pi$  between the two simulations ( $F_+ = 2$  on the left,  $F_- = 1$  on the right) so the minima of  $B_{\pm}$  are in the same location below the chip.

I have made a graphical user interface (GUI) in MATLAB, where a user can input various currents, phases, and geometries to rapidly test different trapping ideas, gauge power requirements, and look for different methods of trapping by playing around with the software. This GUI performs the procedure just described: Current traces with accurate AC skin current distributions from Chap. 8 (but not proximity effect) generate  $B_x(x, y)$  and  $B_y(x, y)$ , which make  $B_{\pm}(x, y)$  (which are different but not independent), which then generate AC Zeeman potentials, given a selected state or transition.

We show an example of this GUI at work with a standard two-trace trap (a phase-shift away from the trap demonstrated in Chap. 7) with an optional parabolic trap bottom fit, shown in Fig. 6.3. We show a three-wire trap in Fig. 6.4, along with a slightly phase-modified version illustrating a case given in Sec. 6.4.3. The caption of Fig. 6.3 gives a breakdown of the user-side information and layout of the GUI.

This GUI is contained in the GitHub repository,<sup>1</sup> including AC skin calculation and AC Zeeman Hamiltonian diagonalization.

---

<sup>1</sup><https://github.com/drewrotunno/ThesisCode>

### 6.2.1 Finding Linear Gradients

After generating the AC Zeeman potential via simulation, we can examine its outputs for other useful features. One such feature is a linear region between upward and downward curvature, illustrated in Fig. 6.5 using a microwave two wire trap, with 250 mA amplitude in each wire,  $-100^\circ$  phase difference, and  $\approx +1$  MHz detuning from the  $|2, 2\rangle \leftrightarrow |1, 1\rangle$  transition. While the vertical potential is locally linear, the horizontal retains parabolic local curvature here. The location of this linear region moves farther away from the chip as detuning increases.

While a simple gradient can shift states differentially, it would generally imprint its curvature on to the atom cloud. Using a linear gradient has the effect of simple uniform translation of a parabolic trap, a useful feature for interferometer arm separation. A larger region would allow farther separation, and we would like this to be larger than the trapped atom cloud size as well. We see a rather linear region only over a few  $\mu\text{m}$ , shown in Fig. 6.5.

## 6.3 Effect of Detuning

While the strength of the  $B_\pm$  field generates the off-diagonal  $\Omega$  coupling in the Hamiltonian (Eq. A.10), the detuning remains on the diagonal, comprising the entire energy separation where  $B_\pm = 0$ . We illustrate detuning as a moderating effect on  $E_{ACZ}$  in Fig. 6.6 for a microwave interaction, where  $\delta$  is well-defined. Traps with zero detuning have a linear gradient, which flattens to parabolas as the detuning increases. Increased detuning also decreases trap depth, seen as the energy maximum on the right of Fig. 6.6.

Detuning, as analyzed in Chap. 3 and Fig. 3.4, also controls the  $m_F$  basis population of the trapped  $|++\rangle$  cloud. This state selection by detuning allows an

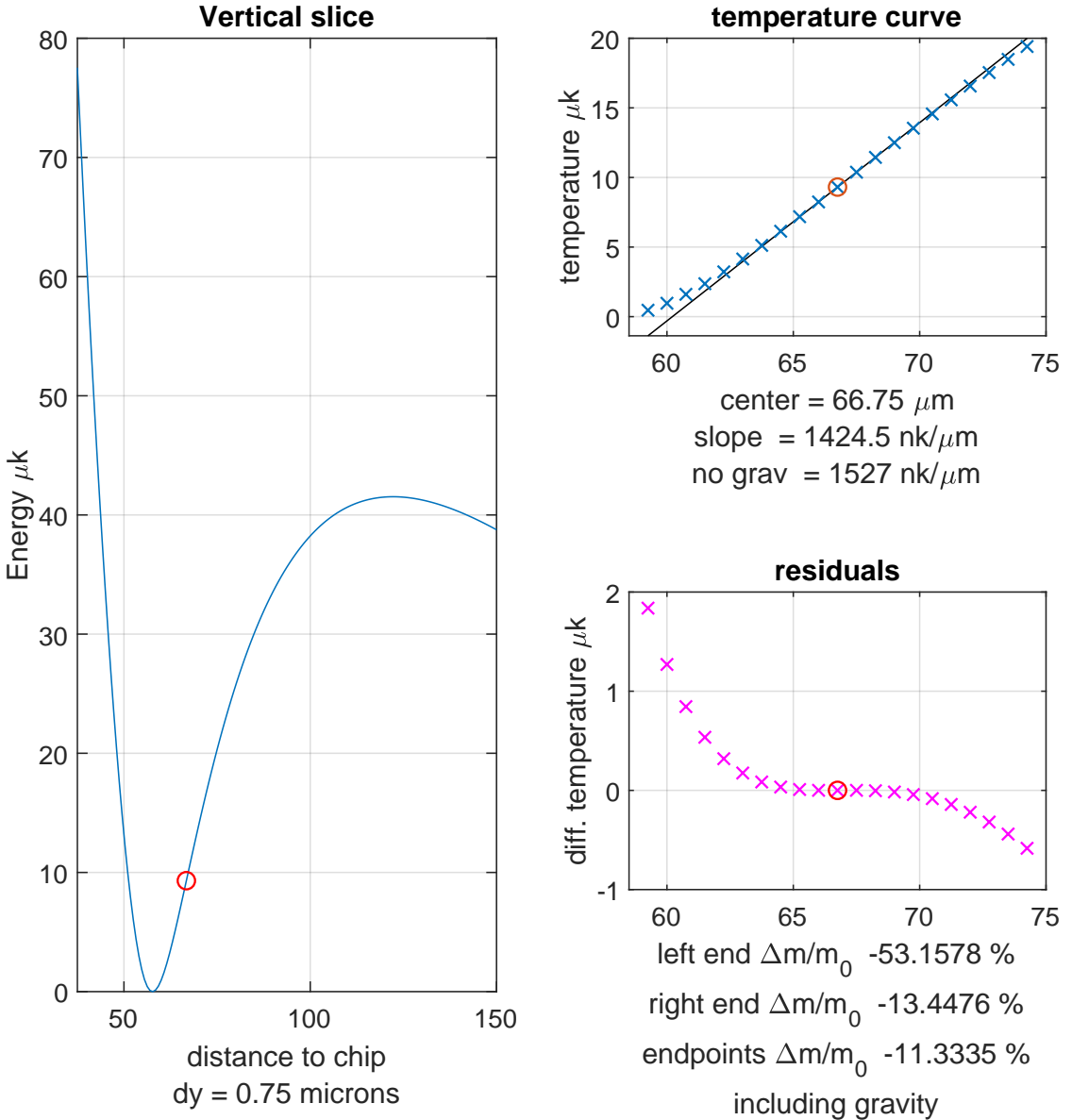


FIG. 6.5: Examination of a local linear profile near the trap. Left: A vertical cross-section of AC Zeeman potential (two wire trap, 250 mA,  $\phi_{UZ} = -100^\circ$ , 1 MHz detuning from the  $|2, 2\rangle \leftrightarrow |1, 1\rangle$  transition). Top right: comparison of the local linear gradient (red circle, black line) with the local curvature (blue  $\times$ ) over  $15 \mu\text{m}$ . Bottom right: Residuals from the fit above. We also give the normalized gradient difference  $\Delta m/m_0$  where  $m_0$  is the center slope, and  $\Delta m$  is the slope of the leftmost or rightmost two points in the range given, as well as the slope across the whole range.

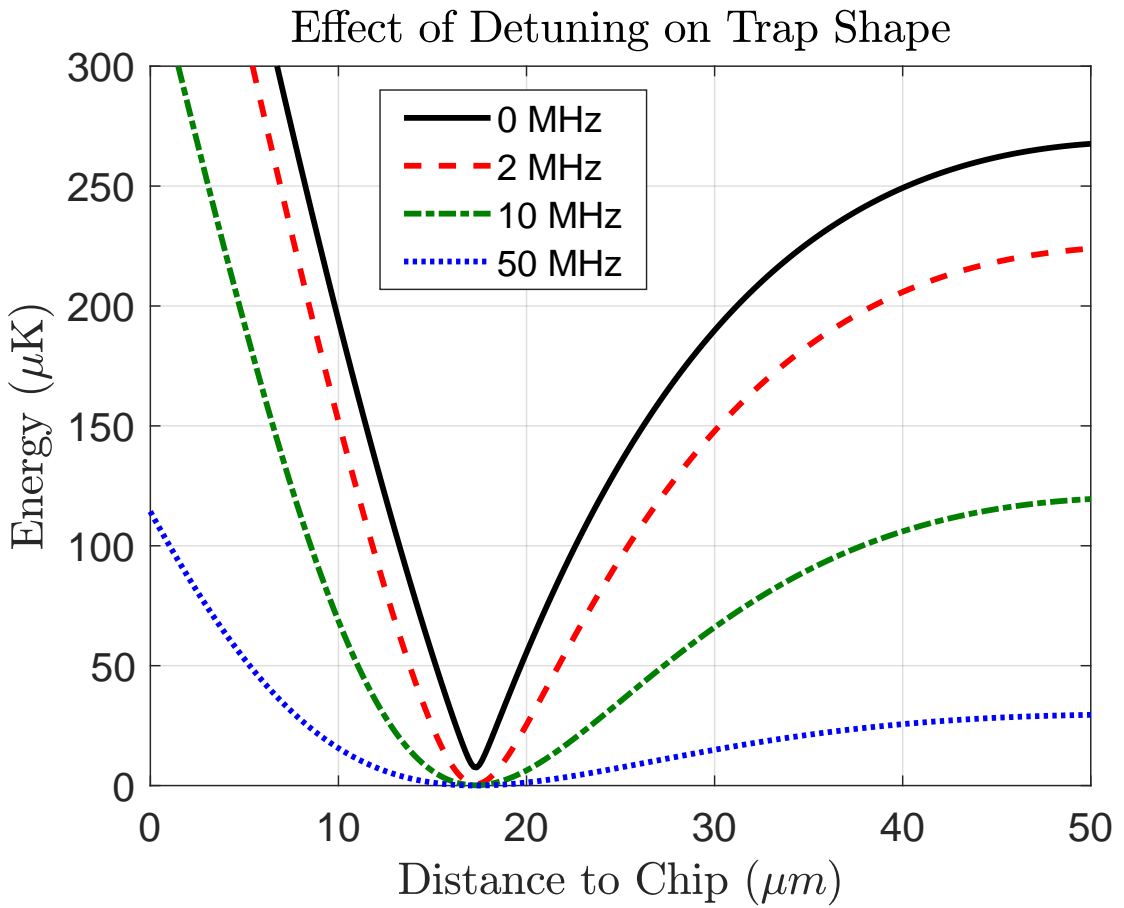


FIG. 6.6: An illustration of detuning's effect on trap frequency and depth. The trap profile is nearly linear on resonance, flattening to harmonic bottoms with lower trap depth with large detuning  $\delta$ . The simulation uses a microwave  $\langle 2, 2 | S_+ | 1, 1 \rangle$  trap generated by 0.5A in two in-phase wires in the two-microstrip configuration, separated by 100  $\mu m$  with substrate thickness 50  $\mu m$ .

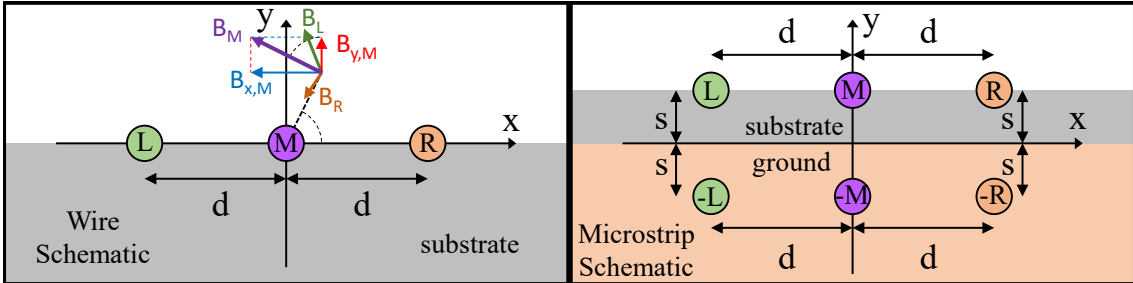


FIG. 6.7: Schematic diagrams of (left) the multiple-wire configuration and the (right) microstrip structure, with an added ground plane and image currents.

experimenter to trap ‘any’ spin state as the primary population of  $|++\rangle$ , using RF. Detuning also provides transition selection in the microwave case, allowing two-level bipolar action, actually targeting any single hyperfine state.

## 6.4 Trap Location Theory

In this section, we investigate the trap position’s dependence on relative phases and currents by mapping the zeros of the circularly polarized  $B_{\pm}$  fields using a toy model for the atom chip. We can write simple, pedagogical expressions for the trap position when using simplifications like long, thin, parallel wires aligned to the background  $B_{DC}$ ,  $B \propto 1/r$  spatial scaling, and perfect image currents. Effects that appear experimentally such as inductive couplings between wires, the AC skin effect, and image proximity effects are excluded here, but are discussed in Chapter 8.

Calculations here are performed quasi-statically, where a current  $I = |I|e^{i\omega t+i\phi}$  in the  $\hat{z}$  direction encodes its complex angle  $\phi$  and its amplitude  $|I|$  into the generated magnetic field vectors  $(B_x, B_y)$ . The layout of the wire and microstrip configurations is given in Fig. 6.7. The current  $I$  at  $(x_0, y_0)$  will generate magnetic field components at location  $(x, y)$  given by  $B_x = -I \frac{\mu_0}{2\pi} \frac{(y-y_0)}{r_0^2}$  and  $B_y = I \frac{\mu_0}{2\pi} \frac{(x-x_0)}{r_0^2}$ , where  $r_0 = \sqrt{(x-x_0)^2 + (y-y_0)^2} = \sqrt{(\Delta x)^2 + (\Delta y)^2}$ . These carry  $1/r_0$  spatial scaling, the complex  $I$ ’s phase, and  $\hat{\theta}$  vector orientation from  $\cos(\theta) = \frac{\Delta x}{r_0}$  and  $\sin(\theta) = \frac{\Delta y}{r_0}$ ,

with  $\theta$  is the polar angle around the  $z$ -axis wire, starting from  $+\hat{x}$ . We sum over active currents (replacing  $I$  at  $(x_0, y_0)$ ) at horizontal distances  $d$  to the midline: left ( $I_L$  at  $x_0 = -d$ ), middle ( $I_M$  at  $x_0 = 0$ ), and right ( $I_R$  at  $x_0 = +d$ ), all at  $y_0 = 0$  for the “wire” cases. For microstrips, we add a ground plane at  $y = 0$  by moving the currents to  $y_0 = +s$ , the substrate thickness above the ground plane. To satisfy the boundary conditions at the ground plane equal and opposite image currents are added at  $y_0 = -s$ .

Having calculated the complex values of  $B_x$  and  $B_y$  in all  $xy$ -plane positions, we generate the circular polarized fields via  $B_{\pm} = B_x \pm iB_y$ . Searching for zeroes in  $B_{\pm}$ , we can locate the trap in terms of a few geometric and phase parameters. An equivalent analytic expression for finding pure or zero  $B_{\pm}$  is where the local magnetic phase relationship is given by  $\phi_x - \phi_y = \pm\frac{\pi}{2}$ , with  $|B_x| = |B_y|$  [64]. In the subsections below we analyze traps produced by two- and three-wire and microstrip geometries.

#### 6.4.1 Two-wire Trap

First, we consider the two-wire trap, which does not contain the microstrip ground plane needed for good microwave power coupling, but represents an instructive case for understanding trap behavior. Additionally, a RF trap based on this design if demonstrated in Chap 7. In the general case, two wires are separated horizontally by  $2d$ , and the right wire precedes by some phase  $\phi_{RL} \equiv \phi_R - \phi_L$ , with real positive magnitude ratio to the left current,  $r_{RL} \equiv \left| \frac{I_R}{I_L} \right|$ . We find that the general solution for zeroes in  $B_{\pm}$  is:

$$y \pm ix = \pm id \cdot \frac{1 - r_{RL}e^{i\phi_{RL}}}{1 + r_{RL}e^{i\phi_{RL}}} \quad (6.1)$$

where the imaginary and real parts of the right-hand expression are identified as the trap coordinates  $(x, y)$ , and both signs match to select for  $\pm$  polarization. Solutions to  $B_{\pm} = 0$  are seen to be negative complex conjugates of one another, tracing the same paths in opposite directions, with phase  $\phi_{RL}$ . The two-wire trap position in Equation 6.1 is plotted as “iso- $r$ ” curves for a cycle of phase delay  $\phi_{RL}$  at various values of current ratio  $r_{RL}$  in Fig. 6.8. Paths that maintain phase (“iso-phase”) at  $\pm 90^\circ$  and vary  $r_{RL}$  are seen to trace out the dashed circle of radius  $d$ .

In the case of equal currents ( $r_{RL} = 1$ ), the trap is located at  $x = 0$ , with  $y$  controlled by phase  $\phi_{RL}$  as:

$$y_{\pm} = \pm d \tan(\phi_{RL}/2) \quad (6.2)$$

We plot Equation 6.2 in Fig. 6.9(a), for each  $B_{\pm}$  field across a cycle of phase. As phase  $\phi_{RL}$  shifts away from zero, the  $B_+$  and  $B_-$  minima move vertically in opposite directions away from  $x = 0$ . Perturbations are linear near  $\phi_{RL} = 0^\circ$  (i.e.  $y = 0$ ), although this is not experimentally useful due to the chip’s surface. When currents are  $180^\circ$  out-of-phase ( $I_R = -I_L, \phi_{RL} = \pi, r_{RL} = 1$ ), the traps are asymptotically far away. The single trap is seen to return to its original position after moving through a single cycle ( $2\pi$ ) of phase delay.

An instructive and useful special case is  $\phi_{RL} = \pm 90^\circ$  and  $r_{RL} = 1$ , which yields  $y_{\pm} = \pm d$  for the  $B_{\pm}$  field. This arrangement gives one polarization-specific trap in a useful location  $y_+ = +d$  above the chip, but leaves the other  $-d$  below the chip surface.

When  $r \neq 1$ , the trap crosses the  $x$ -axis outside of  $d$  for  $\phi_{RL} = \pi$  rather than asymptoting to  $y \rightarrow \infty$ , as well as crossing the  $x$ -axis between the wires for  $\phi_{RL} = 0$ . Plugging  $\phi_{RL} = \{0, \pi\}$  into Equation 6.1 we see the  $x$ -axis crossings occur at  $x = d \cdot \frac{1 \pm r_{RL}}{1 \mp r_{RL}}$ .

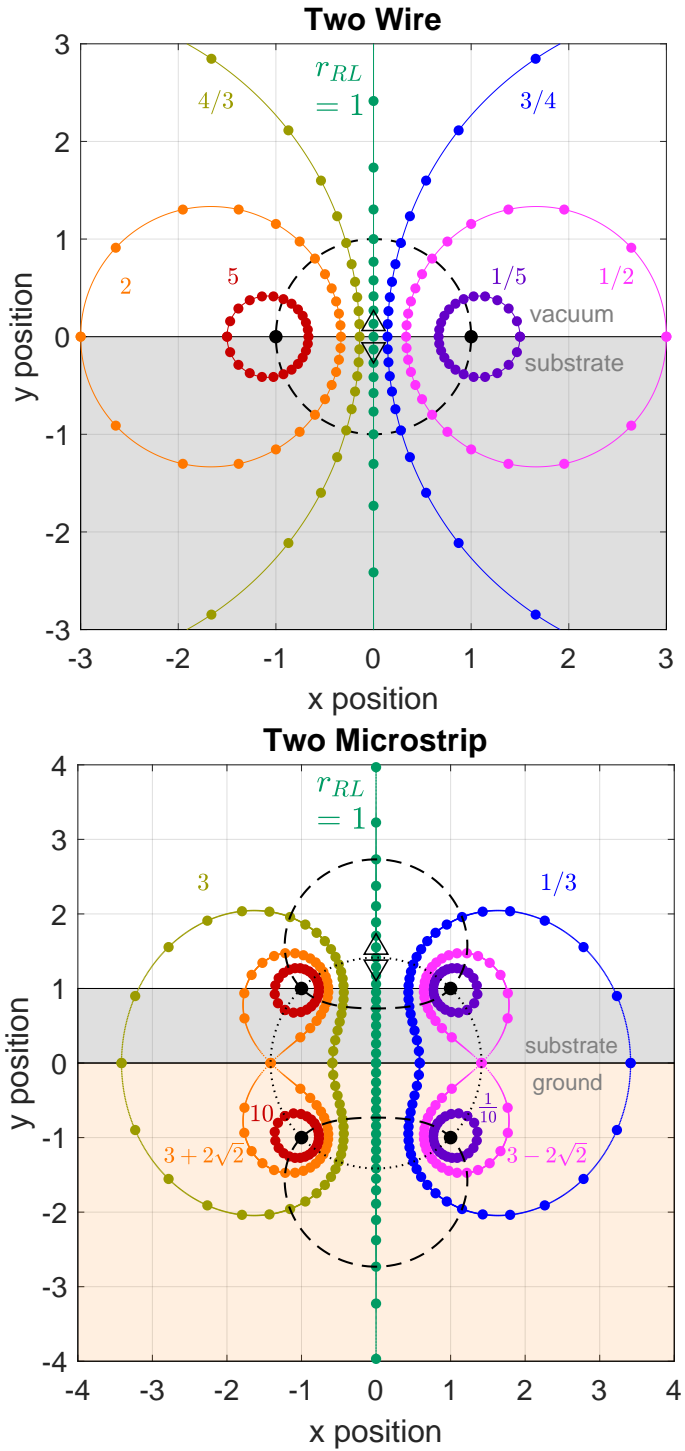


FIG. 6.8: Trap minima locations in the two-wire (left) and two-microstrip (right) models, for  $d = s = 1$ . Currents are marked by black dots. We plot various values of  $r_{RL}$  (labeled connected curves) across a cycle of phase  $\phi_{RL}$ , given in  $15^\circ$  increments with large dots. The dashed curves map out trap position for  $\phi_{RL} = \pm\pi/2$  while varying the current balance  $r_{RL}$ . Similarly, dotted lines map  $\phi_{RL} = 0, \pi$ . Locations of a  $B_+$  and  $B_-$  trap at  $\phi_{RL} = 15^\circ$  are marked with a  $\triangle$  and  $\nabla$ , respectively.

### 6.4.2 Two-Microstrip Trap

Adding a ground plane to the two-wire case moves the in-phase trap out of the chip substrate, usefully co-locating both  $B_{\pm}$  minima outside of the chip. In this new geometry, the single wires become microstrip transmission lines for efficient microwave transmission, modeled using two mirror image currents, as seen in Fig. 6.7(right). Additionally, more traps are formed with now four complex currents (at  $x_0 = \pm d$  and  $y_0 = \pm s$ ), causing the field to cancel in two places for both  $B_+$  and  $B_-$ . We find the general expression for the  $(x, y)$  location of the trap minima for both  $B_{\pm}$

$$y \pm ix = \pm i \cdot \frac{d(1 - r_{RL}e^{i\phi_{RL}}) \pm \sqrt{4d^2r_{RL}e^{i\phi_{RL}} + s^2(1 + r_{RL}e^{i\phi_{RL}})^2}}{1 + r_{RL}e^{i\phi_{RL}}} \quad (6.3)$$

where the left-hand side  $\pm$  sign matches the leading right-hand side  $\pm$  sign referring to  $B_{\pm}$ , while the third  $\pm$  sign inside the numerator gives both solutions per field polarization component. We plot this function in the same manner as before in Fig. 6.8(right). By counting  $15^\circ$  dots in Fig. 6.8, or counting curves for the case  $r_{RL} = 1$  in Fig. 6.9(b), each phase  $\phi_{RL}$  now gives four trap locations simultaneously. Further, the two traps of each polarization ( $B_{\pm}$ ) travel in opposite directions with phase shifts. Each trap is located at  $y > 0$  over one  $2\pi$  cycle, and at  $y < 0$  for another  $2\pi$  cycle, crossing over at  $y = 0$  and  $y \rightarrow \infty$  (for  $\phi = \pm\pi$ ). After a cycle of  $2\pi$ , the field returns to the same initial state, but if we label the two traps and track their motion, we see that each of the two traps moves to the other's location in  $2\pi$ , returning to their initial locations over two full cycles, i.e.  $4\pi$ .

Extreme values of  $r_{RL}$  restrict paths to just around the wires, cycling each  $2\pi$ . As before in Fig. 6.8(right), black dashed curves mark iso-phase for  $\phi_{RL} = \pm\pi/2$ , now in two locations each. Dotted lines give the iso-phase circle marking  $\phi_{RL} = \{0, \pi\}$ , the in- and out-of-phase conditions, for  $s = d = 1$ .

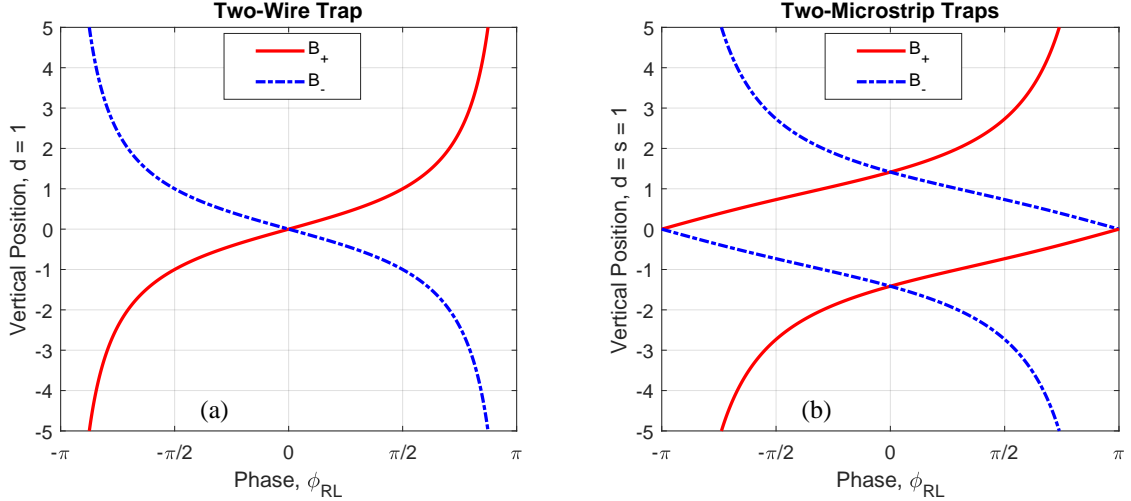


FIG. 6.9: The  $y$ -position of trap minima in the two-wire (a) and two-microstrip (b) cases, for equal currents ( $r_{RL} = 1$ ) in units of  $d = s = 1$ .

Again, equal currents ( $r_{RL} = 1$ ) restrict the trap location to  $x = 0$ , and the general vertical position as a function of phase difference  $\phi_{RL}$  is

$$y_{\pm} = \pm d \tan(\phi_{RL}/2) \pm \sqrt{s^2 + d^2 + d^2 \tan^2(\phi_{RL}/2)} \quad (6.4)$$

where again the leading sign matches  $B_{\pm}$ , and the inner sign gives two solutions. We plot these microstrip curves for in Fig. 6.9(b), for  $r_{RL} = d = s = 1$ .

Perturbing phase around  $0^\circ$  with  $I_L = I_R$ , one can separate opposite polarization traps vertically from co-location, but trap frequencies will differ, and must be compensated for in an interferometer scheme. Additionally, this phase control scheme can co-locate one polarization's minimum with a linear gradient or saddle-point regions from the opposite polarization's field.

### 6.4.3 Three-Wire Trap

Considering the case of three currents (adding  $I_M$  at  $x_0 = 0$  to  $I_R$  and  $I_L$  at  $x = \pm d$  from Section 6.4.1, no images currents), we observe left-right separation of spin polarization for phase shifts near  $0^\circ$ , fundamentally changing behavior from

the two-wire case. We restrict ourselves to the case of equal left and right currents, in magnitude and phase, whereas we vary each of those parameters in the middle wire, with respect to the outer wires. We use:  $\{|I_L|e^{i\phi_L}, |I_M|e^{i\phi_M}, |I_R|e^{i\phi_R}\} = \{1, r_M e^{i\phi_M}, 1\}$ , with  $r_M = |I_M|/|I_L| = |I_M|/|I_R| = |I_M|$ , and  $\phi_L = \phi_R = 0$ . The positions of the zeroes of  $B_{\pm}$  for three co-planar wires are given by:

$$y \pm ix = \pm id \frac{\sqrt{r_M e^{i\phi_M}}}{\sqrt{2 + r_M e^{i\phi_M}}} \quad (6.5)$$

where each  $B_{\pm}$  field (identified by the left-hand  $\pm$  sign) has two solutions, distinguished by the  $\pm$  sign on the right-hand side. The trap minima are plotted for various  $r_M$  values, for a cycle of  $0 \leq \phi_M \leq 4\pi$ , with  $d = 1$  in Fig. 6.10. Again, as in the two-microstrip case in Section 6.4.2, the solutions in Equation 6.5 are  $2\pi$  periodic in  $\phi_M$ . However, if atoms are in a given trap and the phase  $\phi_M$  is varied continuously, then the atoms will return to their original location after a  $4\pi$  cycle of  $\phi_M$ , although the field looks identical over each  $2\pi$  cycle.

For  $r_M < 2$ , the trap positions form closed loops around the middle wire, convex for  $0 < r_M < 1$ , growing to bulging bowling-pin shaped loops for  $1 < r_M < 2$ , as shown in Fig. 6.10(left). At  $r_M = 2$ , i.e. the standard co-planar waveguide (CPW) configuration, a trap cannot form directly above the center trace (i.e.  $x = 0$ ). Furthermore, the trapping positions do not form a closed loop but instead demarcate diagonal asymptotes as  $\phi_M \rightarrow \pi$ , limiting the CPW as a useful ACZ trapping platform. When  $r_M > 2$ , the trap positions form two loops around the outer wires. As the phase  $\phi_M$  is varied, the loops cross the  $x$ -axis once between the wires, and once outside, at  $x = \pm d \frac{\sqrt{\pm r_M}}{\sqrt{2 \pm r_M}}$ .

An instructive case is  $I_L = -I_M = I_R$ , using  $r_M = 1, \phi_M = \pi$ , where a trap is formed at  $y = d$  above the middle wire, and a quick mental sketch shows the vector-wise  $B$ -field cancellation. Perturbations around  $\phi_M = \pi$  introduce imaginary

components, shifting  $B_{\pm}$  zeros left-and-right differentially (see  $\Delta$  and  $\nabla$  in Fig. 6.10), making this scheme an interferometric spin separation candidate for use with a single frequency.

#### 6.4.4 Three-Microstrip Trap

We convert the three-wire scheme from Section 6.4.3 to a three-microstrip layout by adding a ground plane and the three associated image currents. This arrangement of currents produces four zeroes for both  $B_+$  and  $B_-$  field polarizations. The general expression for the trap position ( $|B_{\pm}| = 0$ ) as a function of the center current's relative amplitude  $r_M$  and phase  $\phi_M$  is given by:

$$y \pm ix = \pm \sqrt{\frac{d^2(1 - r_M e^{i\phi_M}) + s^2(2 + r_M e^{i\phi_M}) \pm id\sqrt{d^2(4r_M e^{i\phi_M} - 1) + (2s)^2 r_M e^{i\phi_M}(2 + r_M e^{i\phi_M})}}{2 + r_M e^{i\phi_M}}} \quad (6.6)$$

where the two  $\pm$  signs on the right-hand side give four solutions, and the left-hand side  $\pm$  sign identifies the  $B_{\pm}$  polarization. The four expressions are plotted in Fig. 6.10 with the same formatting as Fig. 6.8. The fields in Equation 6.6 still repeat when  $\phi_M$  is advanced by  $2\pi$ , but similar to the two-microstrip and three-wire schemes, the phase must be advanced by multiples of  $2\pi$  for trapped atoms to return to their original locations. For different ranges of  $r_M$ , it takes a  $2\pi$ ,  $4\pi$ , or  $8\pi$  advance in the phase to make a “total” cycle, depending on  $r_M$ 's magnitude, shown in Fig. 6.10(right). Crossovers between these regions of 4, 2, 1, 2, or 4 connected trap curves (shown by color or  $r_M$  in Fig. 6.10(right)) are found to be simple expressions for  $r_M$ , only for a simple case like  $s = d = 1$ .

We can find topological boundary values of  $r_M$  between the number of connected

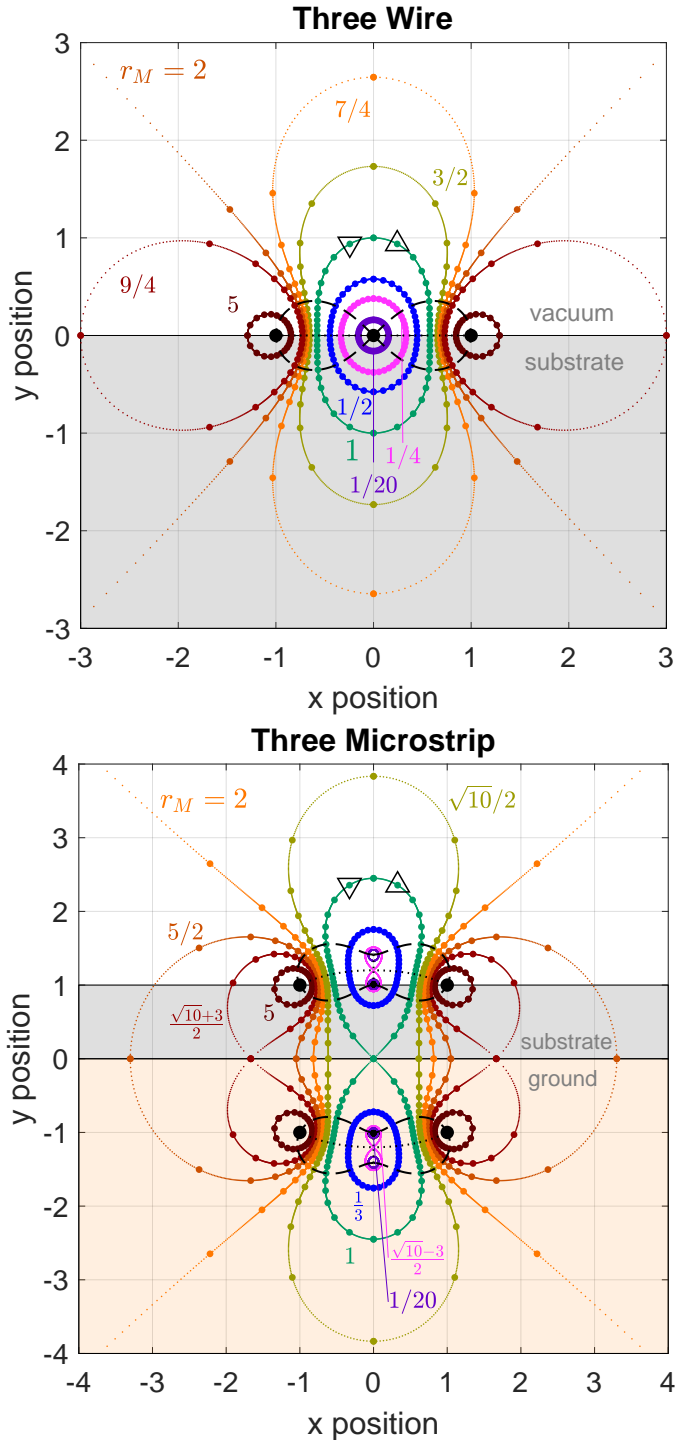


FIG. 6.10: Trap minima locations in the three-wire (left) and three-microstrip (right) models, for  $d = s = 1$ . Currents are marked by black dots. We plot various values of  $r_M$  (labeled curves), across  $2\pi$  of phase  $\phi_M$  given in  $15^\circ$  increments with large dots and milliradians in small dots. The black dashed figure-eight curve maps constant  $\phi_M = \pm\pi/2$  for a range of  $r_M$ . Similarly, black dotted lines map  $\phi_M = 0, \pi$ . Locations of  $B_+$  and  $B_-$  traps at  $\phi_M = 195^\circ$  are marked with a  $\triangle$  and  $\nabla$ , respectively.

curves by locating curves that contain a ‘crossing’ like the  $r_M = \left\{ \frac{\sqrt{10}-3}{2}, 1, \frac{\sqrt{10}+3}{2} \right\}$  curves in Fig. 6.8 , which can split into more curves, or merge into fewer curves with perturbations in  $r_M$ . Mathematically, these values of  $r_M$  mark the zeroes and 1/0 poles under square roots in Equation 6.6, marking transitions between real and imaginary total values (trading  $x$  and  $y$ ). Values of  $r_M$  will depend generally on the eccentricity  $s/d$  of the design.

## 6.5 Middle-field Seekers

One interesting detail that appeared in our course of trap simulation is that the  $|+\rangle$  trap appears as a donut ( $\circledcirc$ ) shape for specific frequencies, shown in Fig. 6.11. Considering the energy diagrams of Fig. 6.12, for low-power perturbations (given at  $\Omega_0 = 50$  kHz), the  $|+\rangle$  state is perturbed *down* in energy near the four atomic resonances, before the Rabi broadens resonances to push against the  $|0\rangle$  state to bring  $|+\rangle$  *up* in energy, as in the 1 MHz case also given in Fig. 6.12. This behavior makes the  $|+\rangle$  state a *medium*-field seeker, pushed high given low fields, and pushed low in high fields, around the four  $\Delta m_F = \pm 1$  crossings shared with  $|++\rangle$ .

Given a resonant radial linear trap, the low point in  $B_-$  at trap center pokes up in  $E_{ACZ}$ , creating a donut well mapping the medium field around the trap bottom. Under gravity, this donut sags into more of a croissant ( $\mathbb{U}$ ) shape. We show GUI simulations for these cases in Fig. 6.11, where gravity points downwards, in typical atom chip orientation. We did not attempt to observe atoms in the donut specifically, but this odd feature may hinder population observation in this trap, discussed in Sec. 7.4.2.

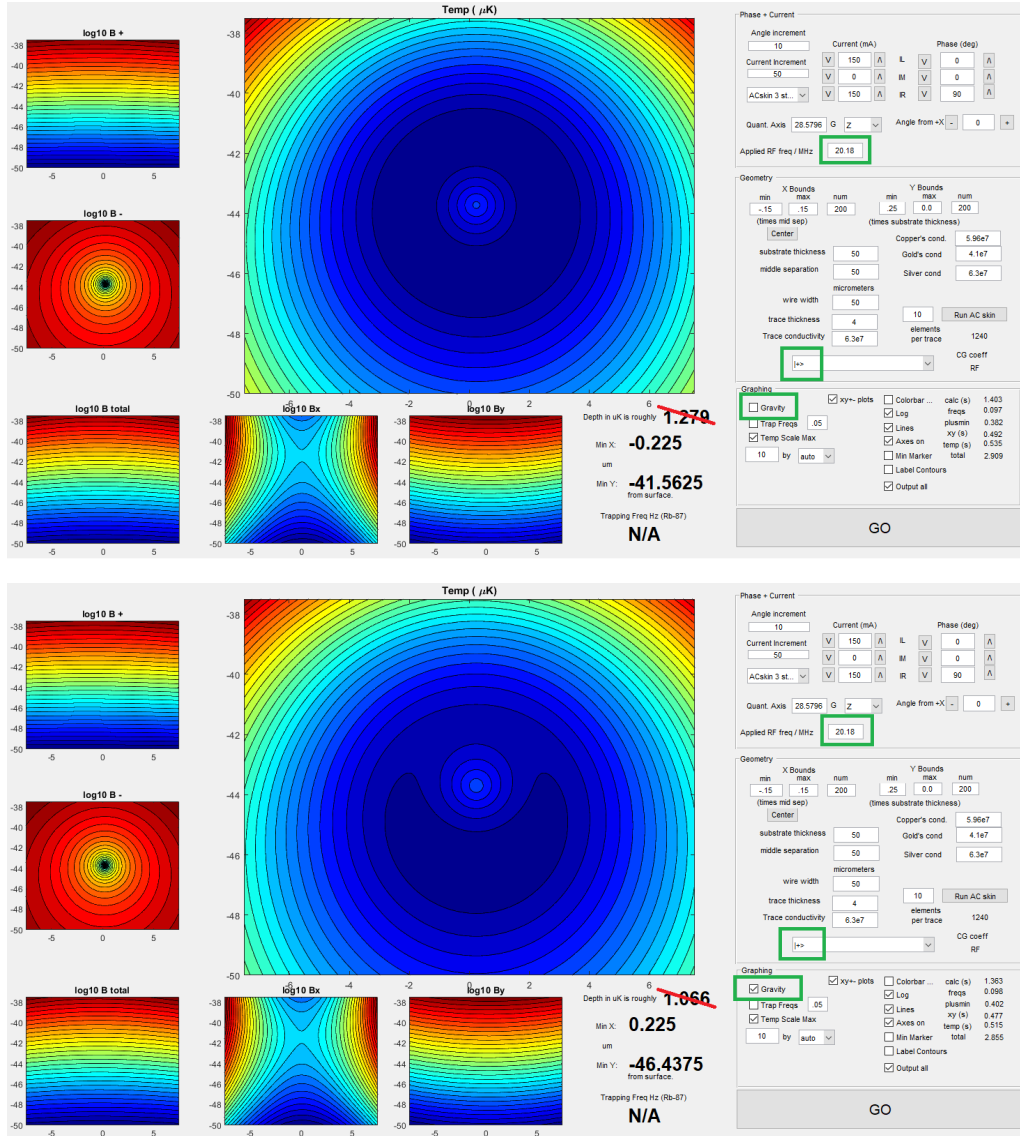


FIG. 6.11: Simulations showing the  $|+\rangle$  state in a *medium-field seeking trap*, which appears as a donut (top) in ACZ energy alone, and a croissant under gravitational sag. Highlighted values are the applied frequency 20.18 MHz, the selected state  $|+\rangle$ , and the gravity checkbox.

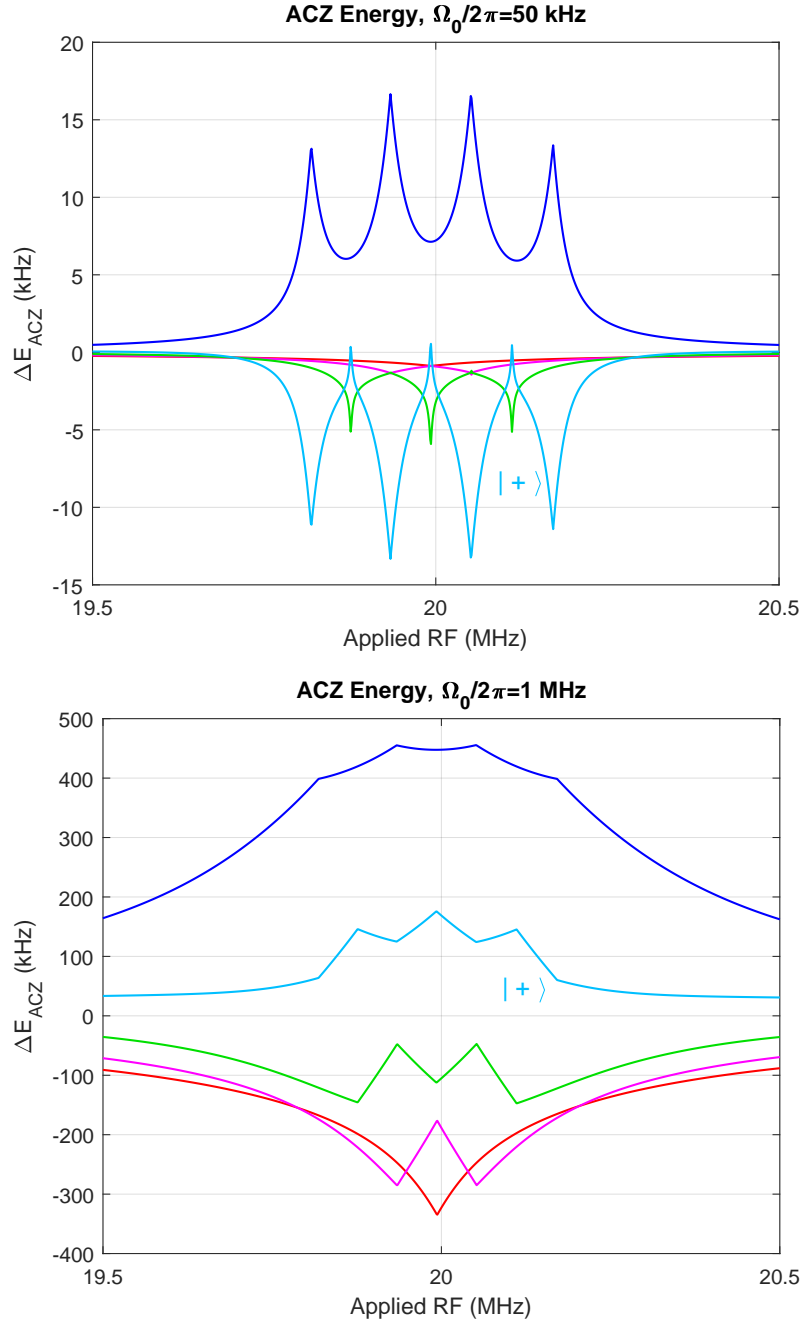


FIG. 6.12: Calculations showing the  $|+\rangle$  state's AC Zeeman energy at low and high driving  $\Omega_0$ , using  $\Omega_0 = 50$  kHz (top) and 1 MHz (bottom). This is evidence that the  $|+\rangle$  state, for certain frequencies, behaves as a medium-field seeker.

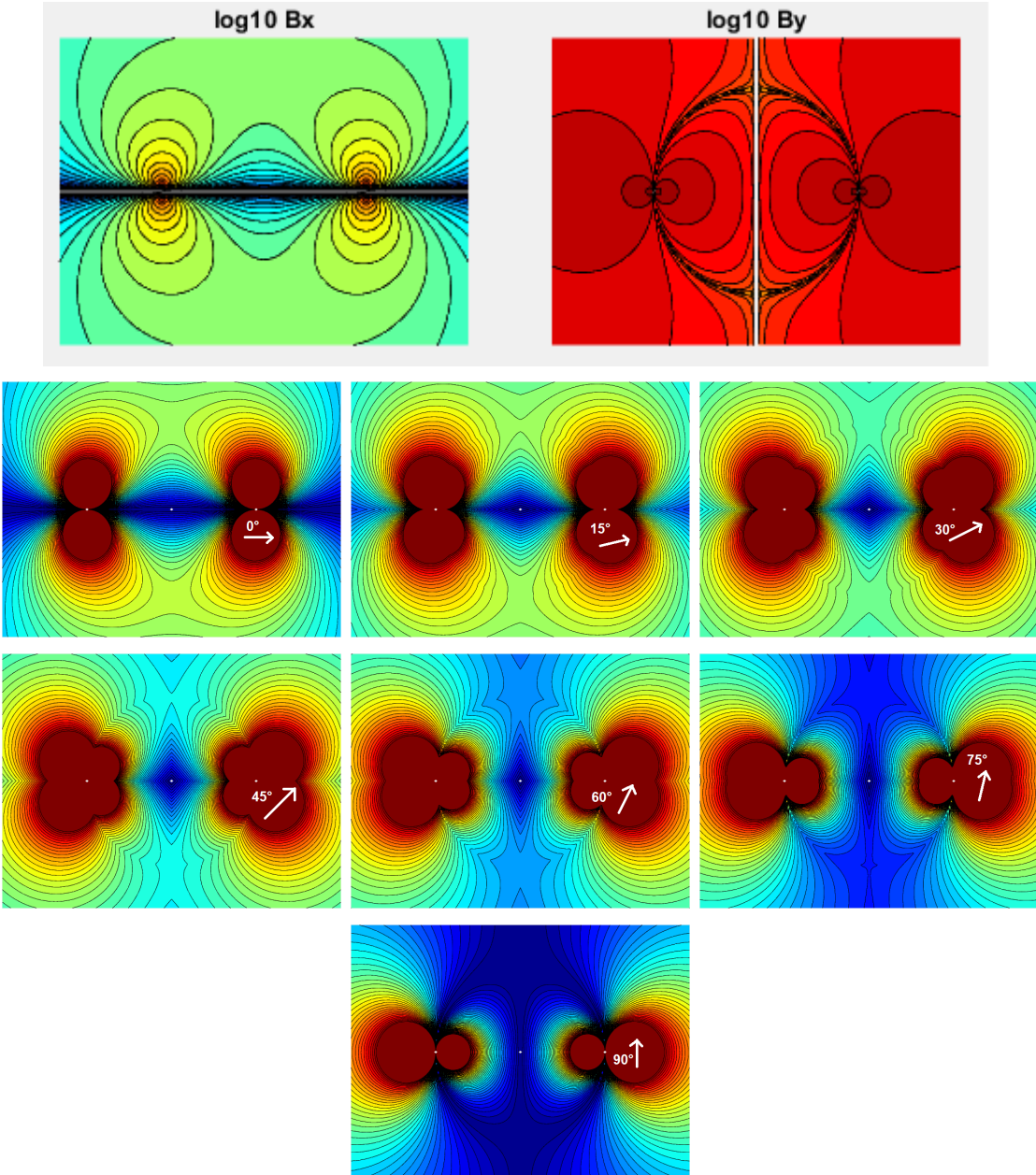


FIG. 6.13: Example of a ‘pyramid’ trap, generally a kite shape, using the  $\pi$  transition  $\langle 2, 0 | \leftrightarrow | 1, 0 \rangle$  and point-wire currents, where the quantizing axis  $B_{DC}$  is not out of the page, as in the rest of this work, but diagonal in the  $xy$ -plane, as labeled. Top two: The  $B_x$  and  $B_y$  fields felt by the  $\pi$  polarization in varying amounts as  $B_{DC}$  moves. Bottom seven: The AC Zeeman energy potential shapes vary with  $B_{DC}$  orientation, given as polar angle from  $\hat{x}$  to  $\hat{y}$  on each plot.

## 6.6 Pyramidal Trap

While playing around in the GUI, I found a trap with a square/diamond/kite shape in the  $xy$ -plane with in-phase signals. By changing quantizing field from the  $\hat{z}$  direction, in-and-out of the page, to a direction in the  $xy$  plane of the page, we can use the  $B_x$  and  $b_y$  fields around the wires to drive  $\pi$  transitions.<sup>2</sup> With quantization direction along  $\hat{x}$  or  $\hat{y}$ , the AC Zeeman will only be affected by the  $B_x$  and  $B_y$  fields, respectively, which are shown at the top of Fig. 6.13. With diagonal direction, both affect AC Zeeman energy and thus the trapping potential, shown in the rest of Fig. 6.13, where each  $B_{DC}$  angle is written near the right wire. A local minimum line of  $B_x$  and  $B_y$  run along the  $\hat{x}$  and  $\hat{y}$  axes, respectively, and using both allows us to trap at their intersection. This trap makes an inverted pyramid shape in AC Zeeman energy, with  $1/r$  gradients roughly linear at trap bottom. In that case, the angle will mix the alternating  $B_x$  and  $B_y$  components, which each have a zero-value line along their axis.

This square-shaped trap with a near-linear bottom produces the (inverted) pyramidal-shaped trap, and a pyramidal energy spike for high-field seekers. Moving off resonance dulls the energy/depth gradient of the pyramid ‘tip’ but maintains the sharp kite corners. This simulation uses a ‘wire’ model, not finite traces, so the effect has sharper edges. The apparent symmetry of the  $30^\circ$  case suggests a local gradient ratio of nearly 1:2 between the two directions, and perhaps an examination of the analytic expressions can give explicit descriptions of the trap, as in Sec. 6.4.

Letting the quantization axis circle or oscillate locally around the  $xy$ -plane, this trap has an  $x - y$  ‘breathing’ or ‘fortune teller’ operation, named after the origami piece that opens in either of two directions. Regarding applications, one could look at condensate superfluidity [73, 74] in a container with sharp edges, exciting spin-

---

<sup>2</sup>This arbitrary  $B_{DC}$  direction was in an old version of the GUI, the modern one assumes  $B_{DC}\hat{z}$ .

oscillation coupling modes [75] in a separately trapped cloud, or just observing the novelty of a pyramidal trap.

## 6.7 Trap Schemes Using the Existing Atom Chip

We consider two unique wire configurations that could trap using the existing U-Z-U setup on our atom chip (as in Fig. 7.4). The first configuration is a three-wire trap, with equal current amplitude in each wire but reversed phase on the middle one. The second trap geometry uses only two wires, with a phase difference near 90°. Either method creates a local minimum in the  $B_{\pm}$  field, which holds low-field seeking AC Zeeman states.

In each case, we must consider multiple parameters at once. A primary concern is the trap depth in  $\mu\text{K}$  of temperature ( $T = \frac{E}{k_B}$ ). This quantity is defined as the energy difference from the bottom of the trap (redefined 0 potential) to the saddle point directly below the trap, comprised of ACZ energy and a linear gravity gradient pulling away from the chip. Atoms hotter than the trap depth will find their way out of a trap, setting a ceiling on allowed temperature, and a good rule of thumb is to have a trap depth nearly  $10\times$  the thermal cloud temperature. The two parameters that control the trap depth are current magnitude in wires and RF frequency detuning.

A secondary concern is the trap's position, generally measured away from the surface of the substrate. Whether we load from an ODT (as near as 100-150  $\mu\text{m}$  from the chip before occlusion) or a micro-magnetic chip trap (10-200  $\mu\text{m}$ , depending on parameters), control over and knowledge of trap position is very helpful.

A third dependent parameter is the curvature of the trap bottom, measured by trap frequency (if harmonic), and more specifically, *how* harmonic the trap is at the bottom. This parameter adjusts many experimental properties such as average

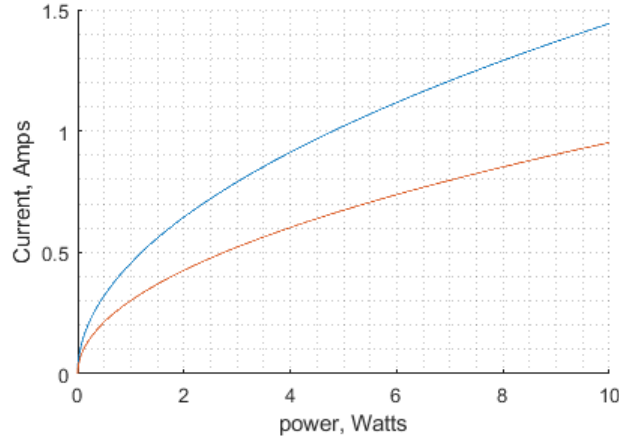


FIG. 6.14: High ( $4.8 \Omega$ , blue) and low ( $11 \Omega$ , red) estimates for the power-current curves.

temperature, collision rate, and energy separation of trapping modes.

The wire current is often measured by proxy using the known power sent to the vacuum-chip system, measured in watts or dBm. We estimated the effective resistance of the chip system using measurements of RF Rabi frequency ( $\Omega_0 \propto |B_{RF}| \propto I/r$ )<sup>3</sup> and estimating the distance from the chip to be 100-150  $\mu\text{m}$ . These measurements of inserted power and estimated current give an effective resistance range of  $R_{eff} \approx 5 - 11 \Omega$  (illustrated in Fig. 6.14.), and we take a convenient number  $8 \Omega$  as  $R_{eff}$  around 8.5 MHz. Using the equations  $P = I_{RMS}^2 R_{eff}$  and  $I_{RMS} = \sqrt{P/R_{eff}}$  we can convert between the two units, e.g. 2 W  $\rightarrow$  500 mA RMS, or 0.5 W  $\rightarrow$  250 mA RMS. A recent result [44] using 6.8 GHz showed that using 3.3 W of  $\mu\text{w}$  power caused  $\approx 37$  mA RMS in the wires (backed out from Rabi frequency measurements), giving an effective microwave impedance of 2400  $\Omega$ .

The trap designs of this section are limited to the current atom chip wire layout. Designs that optimize microwave frequencies or make use of extra chip wires were studied in Sec. 6.4. The center of the U-Z-U arrangement has three parallel conductive strips, primarily silver with gold plating, each 50  $\mu\text{m}$  wide and 4  $\mu\text{m}$

---

<sup>3</sup>Simulations use current *amplitude*, implied here, but power calculations relate to *RMS* values of the current, which are lower by  $1/\sqrt{2}$

tall. These are separated center-to-center by  $100 \mu\text{m}$ , and other unconnected parallel traces exist between and beyond these three (see Fig. 2.12). Each U-wire middle section meets wider traces which lead to contacts on the side of the atom chip. The Z-wire has similar leads, which go either way, giving it a ‘Z’ shape.

### 6.7.1 Three-Wire Scheme

Again, a three-wire trap is formed by three equal amplitude currents, where the outer wires are in sync, and the middle is opposite those. The result is a trap that sits above the central wire as far as the side wires are from the middle, a fixed value. This atom-chip distance can be adjusted by altering the current in the middle wire relative to the outer wires, and horizontal adjustments to the  $B_{\pm}$  minima can be made with phase changes in the middle wire. Often, attenuation of signals *causes* a phase shift.

We consider reasonable ranges of parameter space here. A few watts of power, intending to use commercial 10 W amplifiers, and a detuning as far as a few MHz, and a working  $f_{RF}$  roughly 5-50 MHz. More power makes a deeper trap, but we must be careful not to break the chip or the amplifier at large powers and long hold times. A low detuning makes for a deeper trap but a faster state mixing rate and higher loss. A large detuning mitigates these things but lowers trap depth for this resonant process.

Plotted in figure 6.15 are trap depths for chip current and detuning parameters. Each connected curve represents a different applied current in each wire. A very high microwave power (above 40 W, causing 134 mA) is added as a comparison, to exclude any reasonable microwave trapping experiment on our chip.<sup>4</sup> We investigate a handful of round numbers in nominal power, and calculations use various values

---

<sup>4</sup>This arbitrary number is an artifact of faulty envelope math using 20 W, but still represents a system with very poor current generation with applied  $\mu\text{w}$  power.

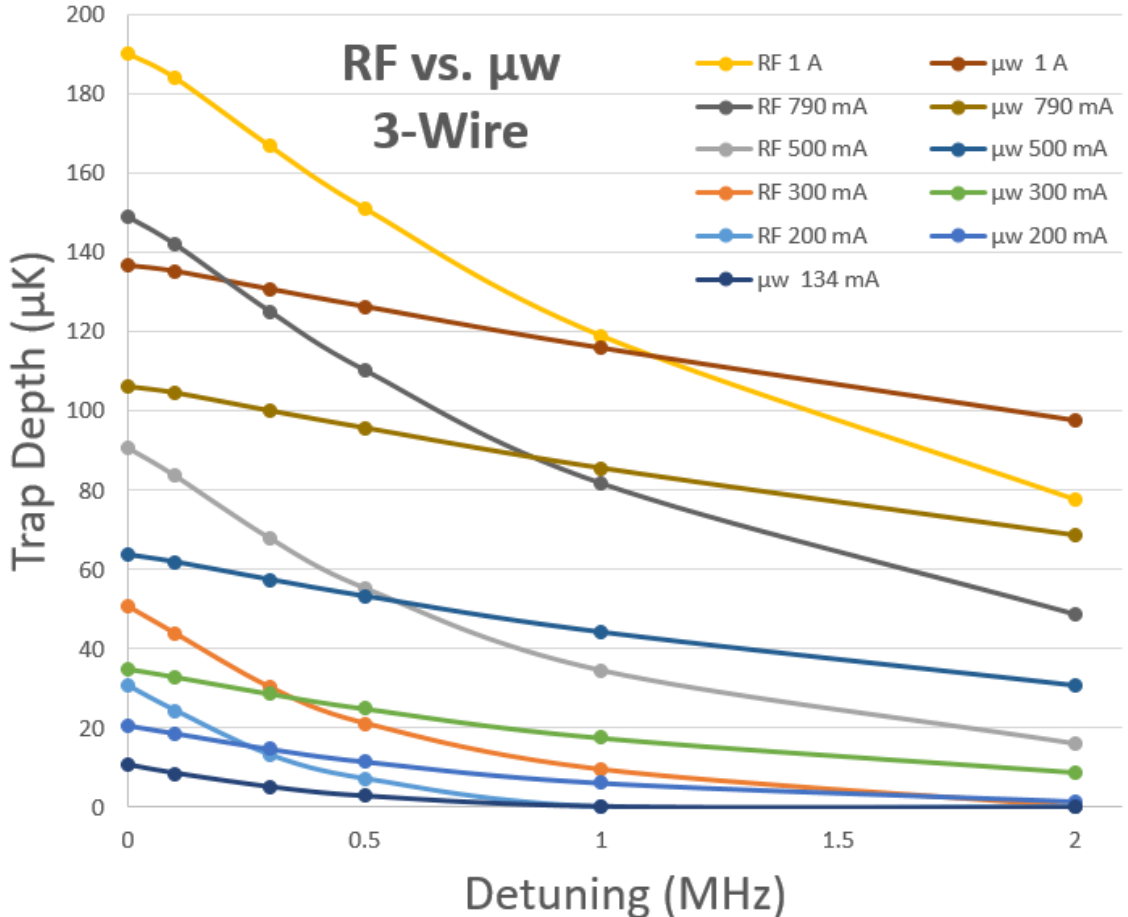


FIG. 6.15: A comparison of trap depth in the three-wire scheme as a function of detuning for different current values in the RF and  $\mu w$ , as labeled. We compare five RF power values and use the same total current with the ‘good’ AC skin effect in the microwave data. It can be seen that the RF beats the microwave on resonance, but vice versa at larger detunings.

of current amplitudes, as labeled.

### 6.7.2 Radiofrequency vs. Microwave Comparison

We expect the effectiveness of RF and  $\mu w$  traps to differ on two fronts: Atomic physics differences in the ACZ effect between intra- and inter-manifold hyperfine transitions and the atom chip’s engineering ability to carry a 6.8 GHz signal, rather than a few MHz one. We show in Fig. 6.15 a comparison between RF  $|++\rangle$  state’s and the microwave  $|2, 2\rangle \leftrightarrow |1, 1\rangle$  transition if we could get equal currents, each over

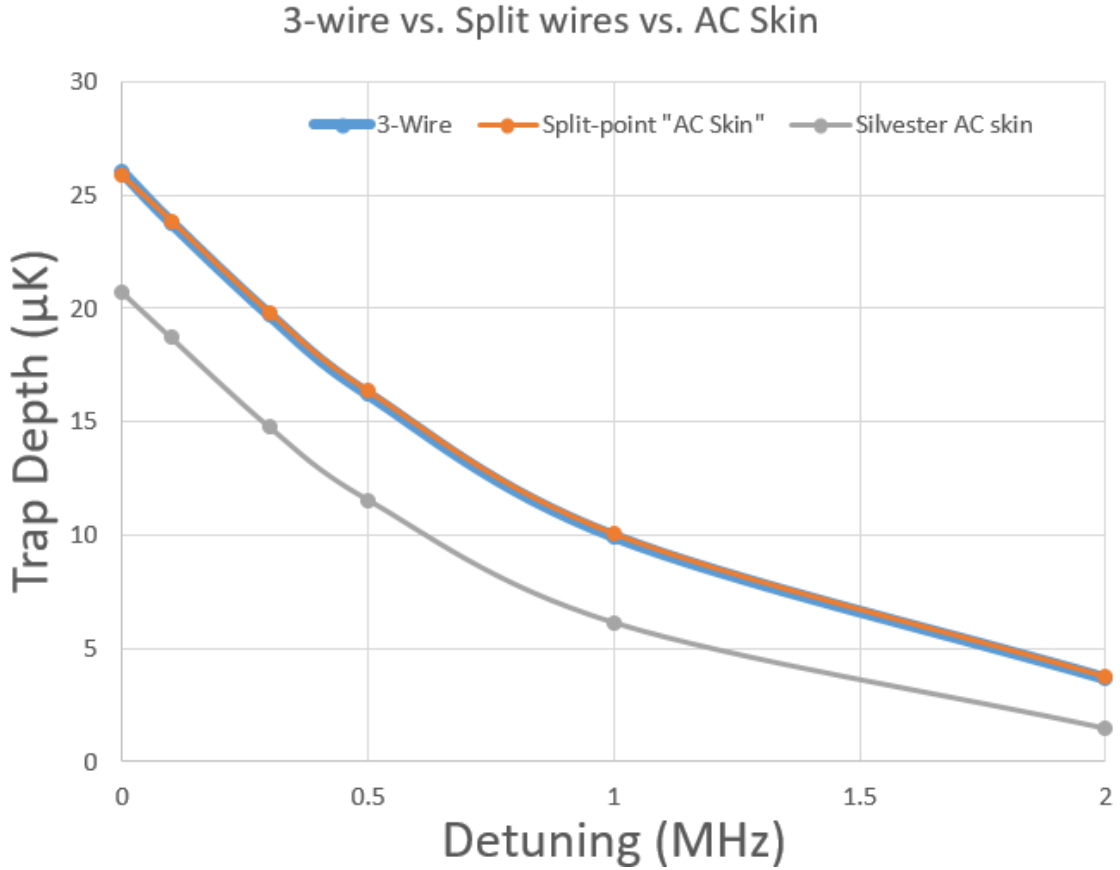


FIG. 6.16: Result of the AC Skin effect altering trace currents in the three-wire model. The best AC Skin model shows much lower trap depth than either single-wire models or a low frequency near-uniform current density model. Simulations use 134 mA for the  $|2, 2\rangle \leftrightarrow |1, 1\rangle$  transition in the 3-wire model

a range of detuning.

On the physics side, it is worth noting that the total AC Zeeman energy splitting for the intra-manifold RF transition is stronger than a single inter-manifold microwave transition on resonance ( $\delta=0$ ), but the  $\mu_w$  is better far off-resonance. Although the individual couplings are weaker in the RF compared to  $\mu_w$  (from Sec. 3.2), the  $|++\rangle$  state experiences four near-resonant two-level transitions simultaneously. The inter-manifold  $\mu_w$  transition is more powerful at high detuning, indicated by the difference in  $\frac{\delta}{\Omega}$  fall-off.

### 6.7.3 AC Skin Effects in Modeling

Another important consideration is the current distribution in broad wires at high frequencies. The AC skin effect must be considered, both in the phase and amplitude changes it induces in the wire trace.

In the simplest case, no extension is given to the wire and it is treated as an infinitely small point in the transverse plane. This thin wire case is shown in blue in Fig. 6.16. While useful for pedagogy and analytic expressions, this case lacks the geometric nuance contained in a finite-sized model.

In a slightly naïve approximation, one can assume in the high frequency limit that the current splits itself to maximum current density the two extreme ends of the wide trace. This turns out to be unphysical, and not as good a model as some spatial analytical expressions in Sec. 8.7.1. This ‘bad’ AC skin model is shown in orange in Fig. 6.16. It closely matches the expected trap depths using the thin-wire method.

We must also consider that the high frequency will draw a large portion of the current to the edge of the strip while adjusting the phase over space via the AC skin effect, as analyzed in Chap. 8. We use our ‘Silvester2D’ method with  $\approx 10^3$  current elements. The skin effect severely decreases the available  $B_{\pm}$  in the trapping field and decreases trap depth to roughly 80% of the un-adjusted value, shown in gray in Fig. 6.16. We can expect that this slipping of phase contributes to the diminished values for ‘clean’  $B_{\pm}$  fields in an accurate simulation.

Furthermore, the proximity effect between traces could substantially change the aforementioned  $B_{\pm}$  calculations, specifically lifting the zero to a finite value and shifting the effective phase difference between the wires. I believe there is some ‘artificial’ cancellation when we use the same current patterns in nearby traces, compared to ones which have additional phase and amplitude adjustments that

is unique in each trace. I suspect that this proximity case may not fully cancel to produce a  $B_{\pm}$  field zero, with the affected phases and amplitudes leaving both polarizations everywhere. Certainly, it would still be a field minimum in roughly the same location, but it might not be as deep in reality as the idealized simulation.

It would seem that on the physics side, microwaves are a better choice since they are stronger off-resonance, where we would prefer to operate. Additionally, using microwaves with sufficient level splitting can target a single transitions via detuning, allowing bipolar control of any hyperfine state. However, taking into account the poor coupling setting a pretty low ceiling for expected current values, as well as the AC skin effect, we decided to use much lower frequencies with the intra-manifold RF transitions for our first attempts at AC Zeeman trapping.

#### 6.7.4 Two Wire Trap: U-U / U-Z comparison

A two-wire trap is formed using two equal amplitude and frequency currents in two parallel wire traces, where the differential phase between the two signals is controlled. If the differential phase is zero, the local minimum in the  $B_{\pm}$  field is exactly between the wires. However, as the differential phase is introduced, the  $B_+$  and  $B_-$  minima move vertically in opposite directions. A phase shift of  $90^\circ$  places the trap as far above the chip surface as the wires are separated. In our analysis here, the U-Z case has trace centers separated by  $100 \mu\text{m}$ , and the U-U case has  $200 \mu\text{m}$  between the traces. Using closer wires increases trap depth significantly for the same power and detuning, as shown in Fig. 6.17, due to the  $1/r$  falloff of the magnetic field.

The height-to-phase relationship ( $y = -d \tan(\phi_{UZ}/2)$ ) can be affected by the gravity gradient for very shallow traps. This relationship is shown for the U-U and U-Z traps at two different detunings in figure 6.18. It is worth noting that

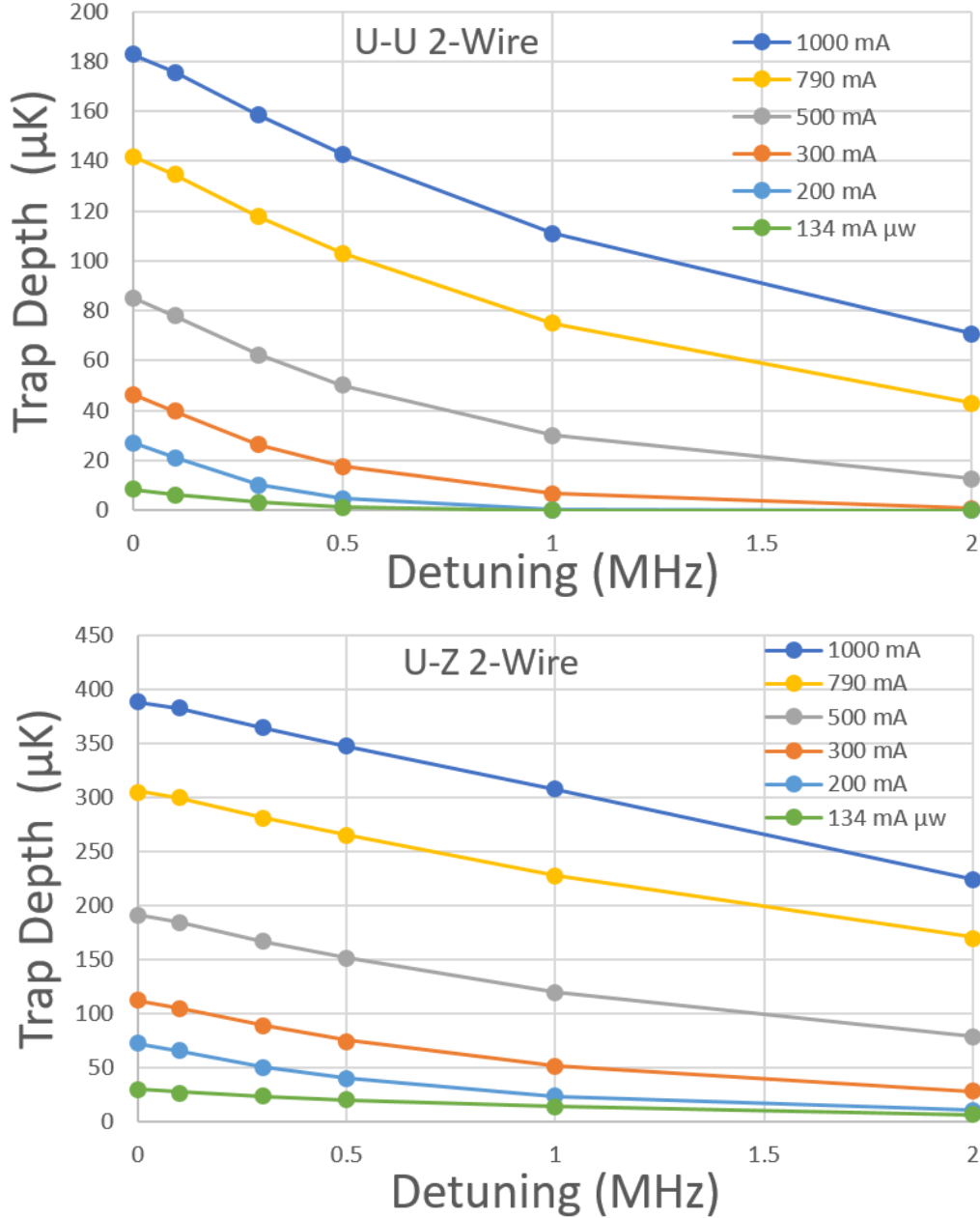


FIG. 6.17: Comparison of U-U ( $2d = 200 \mu\text{m}$ ) and U-Z ( $2d = 100 \mu\text{m}$ ) AC Zeeman trap simulations using the  $90^\circ$  case, across the same range of current and detuning. The U-Z trap is much deeper (note the  $y$ -axis scaling) as it sits closer to each generating wire than the U-U case.

one parameter, the phase difference, almost entirely determines the vertical trap position.

The two-wire U-Z and U-U cases differ only by the separation distance of the wires, although the trace impedance might differ in the experiment. In our calculations, we look at 500 mA of current at only two detunings (100 kHz and 1 MHz), and primarily look at the effect of phase on trap depth and trap position. In Fig. 6.18, we show the depth vs. phase curves for two pairs of cases. We can see that the U-U case (orange and blue) shows much lower trap depths, owing to the increased distance between the two traces, while the U-Z case (yellow and purple) shows the much greater trap depths allowed by closer traces.

Since we might expect to load this RF ACZ trap from an ODT located 100-150  $\mu\text{m}$  away from the chip surface, we would prefer the deepest trap in this region. If we load from the DC chip trap, we can be significantly closer to the chip. In figure 6.18, we plot the depth as a function of trap distance from the chip. We find that the U-U configuration with further wires can make a deeper trap at larger distances than two closer wires with a larger phase difference. While the U-Z is generally deeper for the same power, the depth loses to the U-U case at larger distances.

### 6.7.5 Decision

We have run simulations across a variety of trap geometries and parameters, revealing pathways toward making a proof-of-principle RF ACZ trap for atoms about 100-150  $\mu\text{m}$  from the chip surface, using the present chip geometry. Comparing microwave and RF transitions, the microwave looks to be a preferable option *ab initio*, but the poor chip coupling precludes this without high power. Comparing the three-wire and two-wire setups, the two-wire has less complexity with only one differential phase to control and gives inherent vertical positional control. Trap

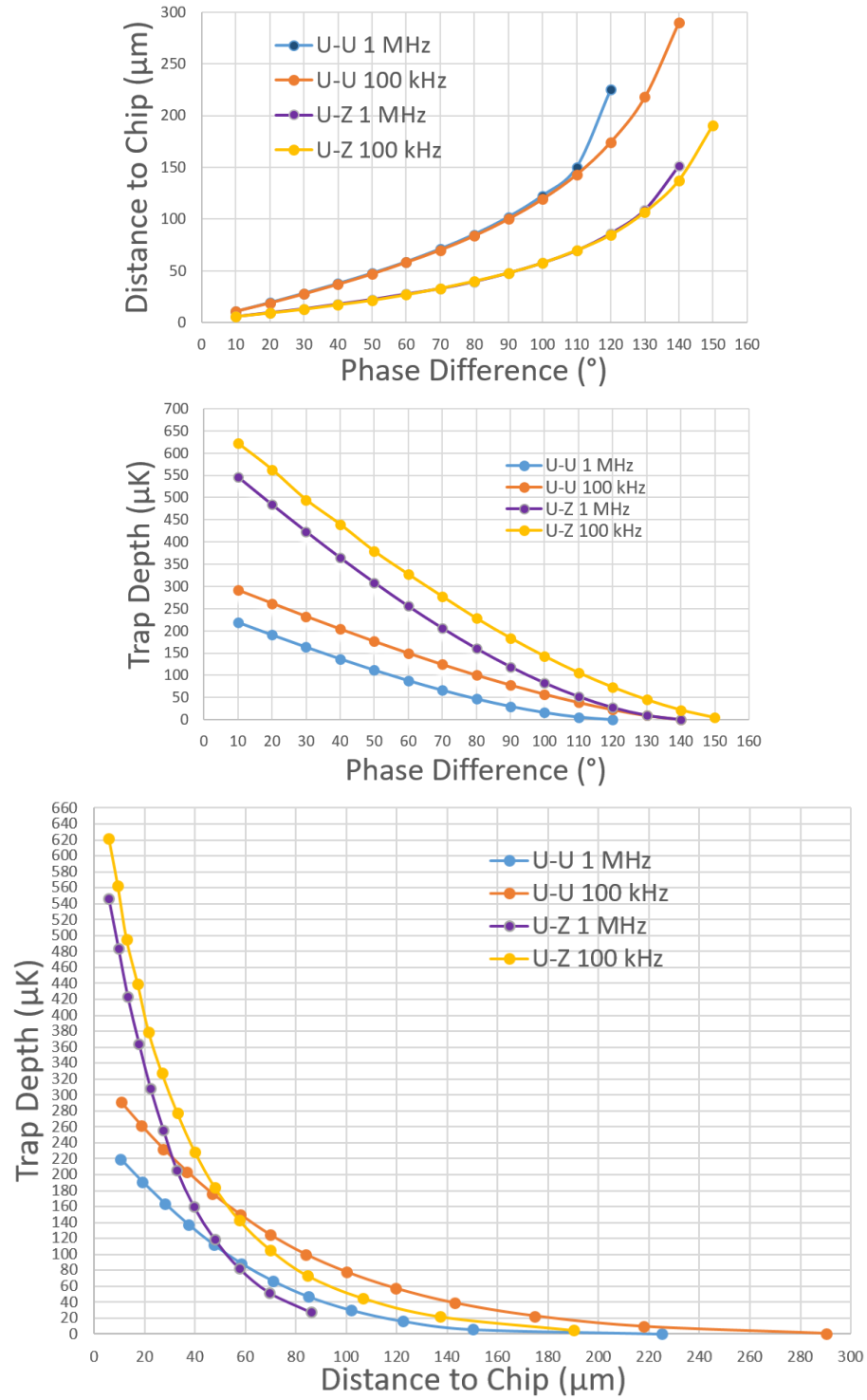


FIG. 6.18: Simulated comparison of the U-U and U-Z two-wire trap schemes for two detunings (0.1, 1 MHz), across a range of phase. The top graph shows trap position as a function of phase, and the middle shows trap depth as a function of phase. We plot these two values against each other in the lower graph, showing depth as a function of distance to chip, for different trapping schemes.

depths for the two configurations are almost equal at  $100 \mu\text{m}$ , for the same power and detuning.

Comparing the choice of U-Z or U-U wires shows that a deeper trap, very close to the chip, could be formed using the U-Z, but at  $100 \mu\text{m}$  and beyond, the U-U wires make a deeper trap. For 2 W of RF power on both U-wires in the current atom chip in a two-trace design, we expect roughly  $30 \mu\text{K}$  of trap depth with  $\delta = 2\pi \times 1 \text{ MHz}$  at  $100 \mu\text{m}$ , although we expect to see trapping at lower power as well.

When testing whether we could use higher powers in August 2020, we rendered one U-wire (the ‘old evap’ trace) unusable. It did not fail open or short, instead its impedance became unstable at any power, jumping back and forth between values as monitored by reflected power, as if temporarily making and breaking connections to other wires or itself. This variability in impedance causes unknown fluctuations in Rabi frequency and the RF evaporation knife on this line, so we elect to use the remaining stable wires, U and Z, in a two-wire configuration, which is the topic of the next chapter.

## 6.8 Summary

This chapter covered five main topics, all to do with theoretical AC Zeeman traps. First we used a pedagogical example, explaining how multiple phase-controlled currents can generate a field that rotates in time, and is spatially inhomogeneous. Second, we showed the GUI, which simulates AC Zeeman potentials and useful trap parameters from given currents and trapping states. Third, we examined a more general approach towards trapping, enabled by simplifying wires down to points. We are able to write in relatively simple expressions the trap location across a range of phase and power ratio, and plotted many such curves. Fourth, we take a look at two relatively exotic AC Zeeman traps: the Donut and Pyramidal

traps. Lastly, we take a look at applying this theory to two wires on the existing chip, weighing the relative merits of a U-Z and a U-U trap, as well as using the microwave transitions and looking forward to a three-wire trap.

# CHAPTER 7

## RF AC Zeeman Trap

### Demonstration

This chapter contains the core result of this thesis, the AC Zeeman two-wire trap demonstration. We repeat some figures and equations from earlier chapters, to help this chapter stand alone. The date of our first AC Zeeman trap was September 23<sup>rd</sup>, 2020, and all data was taken by December 23<sup>rd</sup>, 2020.

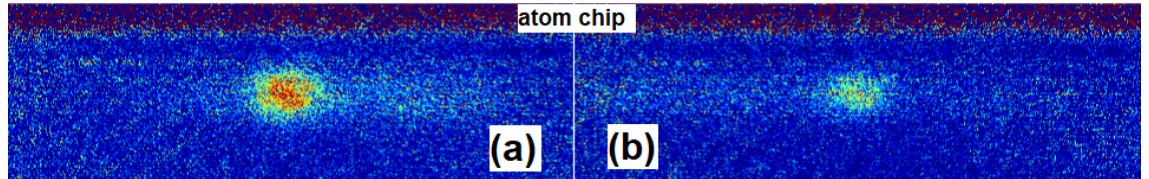
We begin with an introduction in Sec. 7.1, then take a look at hyperfine DC and AC Zeeman energy calculation in Sec. 7.2, moving to chip geometry and numerical simulations in Sec. 7.2.3. We discuss the experimental setup in Sec. 7.3 and present measurements of trap frequency with theory estimates and empirical lifetime measurements in Sec. 7.4. We demonstrate three forms of evaporation in Sec. 7.4.3, and Sec. 7.5 demonstrates position changes with power and phase. We provide some supplemental low-frequency data in Sec. 7.6, and discuss phase shifting effects in Sec. 7.7. We conclude in Sec. 7.8.

## 7.1 Introduction

Ultracold atoms and ions are commonly trapped by static electromagnetic field gradients, far off-resonant optical dipole traps (ODTs), or RF Paul and Penning traps, which contain an atom ensemble in vacuum through cooling and experimentation. Traps often leverage internal quantum mechanical properties, such as electronic spin state, to manipulate the ensemble's externally observable position and thermal properties. Spin-specific traps using RF magnetic near fields instead of propagating optical photons are a valuable tool for chip-based atom interferometry (AI) and quantum information. Further, trapped atoms have the potential advantage of long phase integration times and localization for AI measurement.

In this chapter, I present the first demonstration of a polarization-specific radiofrequency (RF) magnetic trap on an atom chip based on AC Zeeman (ACZ) [38, 39, 40, 41, 42, 43, 44] potentials. Local minima in the  $B_{\pm}$  circular polarization components near chip wire currents become traps in AC Zeeman energy ( $E_{ACZ}$ ), depending on the power, frequency, and relative phase of the chip currents. Notably, trap features are on the chip trace scale ( $10 - 100 \mu\text{m}$ ), significantly smaller than the wavelengths used ( $\approx 10 \text{ m}$ ). Additionally, this method allows trapping at an arbitrary background magnetic field  $B_{DC}$ , beneficial for clock state and Feshbach resonance applications [76, 77]. While we use solely *intra*-manifold hyperfine transitions to trap in this work, with  $\approx 20 \text{ MHz}$  radiofrequency resonance (set by the DC bias magnetic field), this technique should be applicable to two-state *inter*-manifold hyperfine transitions using microwave frequencies near 6.8 GHz in  $^{87}\text{Rb}$ , and in fact microwave operation allows two-level bipolar targeting of any hyperfine state.

We show our qualitative ‘figure of merit’ in Fig. 7.1, which plainly shows atoms dropped from AC Zeeman traps after a short time-of-flight. One remarkable feature of an AC Zeeman trap is its ability to trap spin states that are typically



## AC Zeeman trapped states

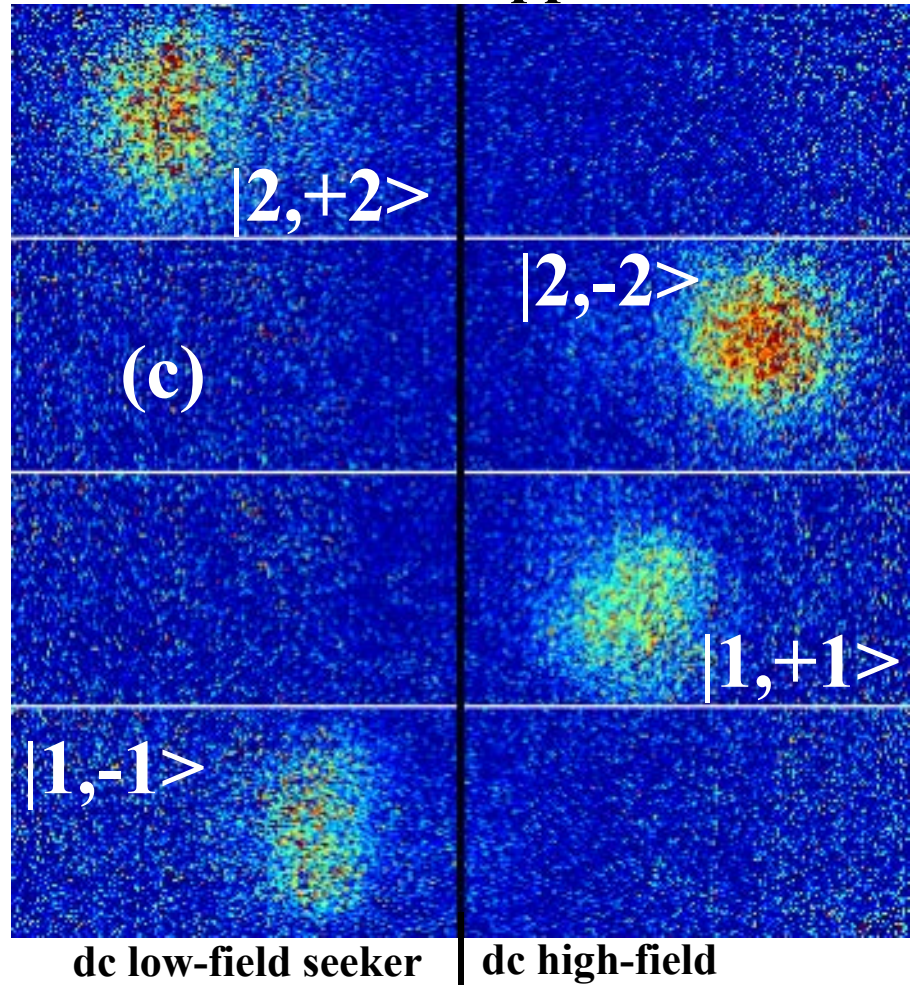


FIG. 7.1: Atoms released from AC Zeeman traps. (a,b) Side-view showing the axial end-capping provided by the ODT for atoms in  $m_F = +2$  and  $-2$ , respectively. (c) Front view along trap, imaged after a  $\approx 15$  s time of flight. We separate  $m_F$  states horizontally via Stern-Gerlach pulse after they have been dropped from their respective ACZ trap. These images demonstrate that we have trapped both high- and low-field seeking DC states.

untrappable with the traditional DC Zeeman energy, e.g. the high-field seeking  $|F = 2, m_F = -2\rangle$  or  $|F = 1, m_F = +1\rangle$  states. We demonstrate trapping of opposite signed  $m_F$  spin states in Fig. 7.1, each in a different AC Zeeman trap. The two images in Fig. 7.1(a,b) show a side-view ( $-\hat{x}$ ) of the cigar-shaped AC Zeeman trap, where the confinement from the ODT is evident in the horizontal direction. Atoms in Fig. 7.1(a) are held at red detuning, populating primarily the  $|2, +2\rangle$  state, while atoms in Fig. 7.1(b) are held at blue detuning, populating primarily the  $|2, -2\rangle$  state. Each atom cloud is imaged after a short ( $\approx 5$  ms) time of flight with a ‘prepulse’ from Sec. 2.2.8.

In the rest of Fig. 7.1(c), we show a view along the cigar trap ( $\hat{z}$ ) after a short time-of-flight, where a DC Stern-Gerlach field separates high- and low-field seeking  $m_F$  states, as indicated. The hold detuning selects the sign of  $m_F$ , and a phase difference of nearly  $180^\circ$  separates the traps for  $F_+ = 2$  and  $F_- = 1$ . This result starkly demonstrates the ability of an AC Zeeman trap to contain DC high-field seeking states.

## 7.2 Theory

Predicting properties such as trap shape, position, oscillation frequency, trap depth, etc. depends on calculating two components explained here: In Sec. 7.2.1 and Fig. 7.2, we explicitly calculate AC Zeeman eigenenergies and eigenstates of atoms in an RF magnetic field. In Sec. 7.2.2, the circular-polarized  $B_\pm$  magnetic field components are calculated and plotted from known currents and geometries, as in Chap. 6. The RF magnetic field maps are converted into trapping potentials in Sec. 7.2.3 and Fig. 7.3.

Our AC Zeeman trapping method shares atomic theory with another hyperfine chip confinement method called adiabatic trapping [78, 64, 65], but they differ in

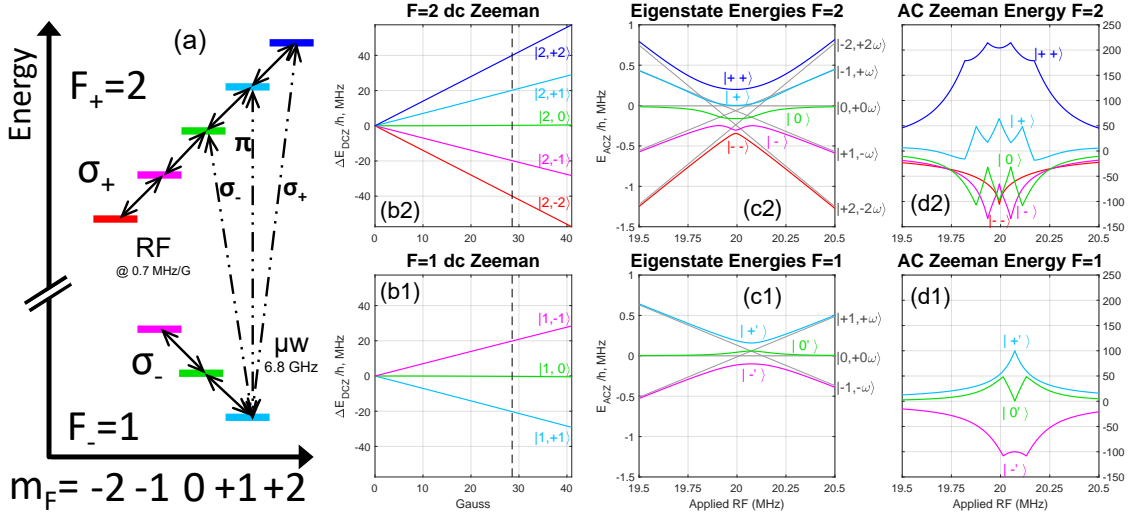


FIG. 7.2: DC and AC Zeeman atomic states and energies, each plot (b-d) also labeled for  $F_+ = 2$  (top), and  $F_- = 1$  (bottom). (a): Rb-87 5S hyperfine sub-state diagram, with RF transition polarizations labeled. (b1,b2):  $B_{DC}$ -dependent DC Zeeman energy, with resonance used in this chapter denoted by a dashed line. (c1,c2): AC Zeeman eigenstate energies vs. bare states, plotted for  $\Omega_0/2\pi = 500$  kHz, labeled by  $E_{ACZ}$  state, matching color with red  $m_F$  projection. In gray labels, we denote  $|m_F \pm N\omega_{RF}\rangle$  projection at far blue detuning. (d1,d2): Only the additional energy in each curve in (c) from its low-power limit. Population curves are given in Fig. 3.4.

the core method of trapping. In adiabatic traps, inhomogeneous DC magnetic fields perform trapping (and anti-trapping), with an RF or  $\mu$ w field providing adiabatic passages between high- and low-field seeking  $m_F$  states, confining atoms to a shell potential. In our case, the RF  $B_{\pm}$  near field generates the trapping field, with a single homogeneous  $B_{DC}\hat{z}$  magnetic field providing the quantization axis.

One phenomenon to recall here is the DC Zeeman effect, where an atom's spin projection into a quantizing DC magnetic field  $B_{DC}$  breaks the degeneracy and gives atomic hyperfine  $m_F$  sub-states distinct energies. At low  $B_{DC}$  field we have the expression for the DC Zeeman energy shift  $\Delta E_{DCZ} = \mu_B g_F m_F B_{DC} \simeq \pm h \cdot 0.7 \text{ MHz/G}$  (28.58 G → 20 MHz). Figure 7.2(a,b1,b2), shows the DC Zeeman energy shifts for the ground hyperfine states of  $^{87}\text{Rb}$ .

### 7.2.1 AC Zeeman Energy

The energies of ultracold atoms can be adjusted by microwave and radio-frequency photons of energy  $\hbar\omega_{RF}$  via the AC Zeeman interaction originating from the Zeeman Hamiltonian  $\hat{H} = -\vec{\mu} \cdot \vec{B}$ . Here,  $\vec{\mu}$  is the atom's magnetic moment and  $\vec{B}$  is the magnetic field, with both AC and DC components. The AC Zeeman energy acts as an avoided level crossing in frequency space, where energy levels are rendered non-degenerate via the added AC Zeeman energy  $E_{ACZ}$ . In one picture, the AC magnetic field has components that are *rotating with* the precessing DC Zeeman magnetic moment “gyroscope,” producing a continuous force, when the applied frequency nearly matches atomic energy gaps.

Analysis typically considers a ‘dressed atom,’ that is a ‘bare’ atomic state in the  $|F, m_F\rangle$  basis ‘dressed’ with multiple photons  $|m_F, (N \mp m_F)\hbar\omega_{RF}\rangle$  (for  $F_\pm = \frac{3}{2} \pm \frac{1}{2} = 2$  or  $1$ ), so that all states are nearly degenerate. These are the grey lines in Fig. 7.2(b). The total Hamiltonian is the sum of the DC Zeeman atomic energies, photon field (both diagonal by construction in the dressed basis), and their off-diagonal interaction energy  $H_{tot} = H_{atom} + H_\omega + H_{int}$ .

Choice of transition polarization selects out a part of the total Rabi frequency definition:

$$\hbar\Omega_{m'm} \equiv \langle F', m' | -\mu \cdot B | F, m \rangle = \frac{gs\mu_B}{2\hbar} \langle F', m' | \sigma_+ B_- + \sigma_- B_+ + 2S_z B_{ac\hat{z}} | F, m \rangle \quad (7.1)$$

which inter-mixes  $m_F$  states, using circular definitions  $S_\pm = S_x \pm iS_y$  and  $B_\pm = B_x \pm iB_y$ . Inter-manifold transitions can access all available polarizations, but within each manifold, only one polarization gives non-zero transition elements. Interactions in the intra-manifold RF case used here are seen strictly between adjacent states so that  $\Delta m_F = +1$  ( $-1$ ), forming a near-degenerate ladder with four (two) Rabi frequencies in  $F_+ = 2$  ( $F_- = 1$ ).

Diagonalization reveals eigen-energies for the the AC Zeeman states from high to low energy:  $|++\rangle$ ,  $|+\rangle$ ,  $|0\rangle$ ,  $|-\rangle$ ,  $|--\rangle$  for  $F_+ = 2$ , and  $|+' \rangle$ ,  $|0' \rangle$ ,  $|-' \rangle$  for  $F_- = 1$ . Eigenstates with ‘+’ are trappable low-field seekers, and states with ‘-’ are high-field seekers and cannot be trapped with this method. These AC Zeeman dressed atom energies are represented in Fig. 7.2(c), with each state’s AC Zeeman energy alone plotted in Fig. 7.2(d). The would-be degeneracy near resonance when  $\omega_0 \approx \omega_{RF}$  (i.e. low detuning  $\delta \equiv \omega_{RF} - \omega_0 \approx 0$ ) is avoided via the added interaction energy. As the  $\Omega$  coupling varies over space with  $|B_\pm|$ , states that have positive  $E_{ACZ}$  are trappable as low-field-seekers, while states with negative  $E_{ACZ}$  are high-field-seeking, as either case lowers the total energy.

A helpful experimental technique that is interwoven with this framework is performing adiabatic rapid passage (ARP) between spin states, using a frequency-sweeping source. ARPing can populate a choice of  $m_F$  state (vis-à-vis Fig. 7.2 (e2) ) from the initial state  $|2, +2\rangle$  along  $|++\rangle$  by sweeping from below resonance at significant power and  $B_{DC}$  to between transitions, then lowering power to fully populate that selected  $m_F$  state (e.g.  $\rightarrow \{|2, +1\rangle, |2, 0\rangle, |2, -1\rangle, |2, -2\rangle\}$ ). Notably, the region near trap bottom has near-zero Rabi frequency, minimizing state mixing, making a nearly pure frequency-dependent arbitrary trapped  $m_F$  state available when the population is very cold.

### 7.2.2 RF Magnetic Near Field

Here we consider a simple pedagogical example to illustrate the relationship between the relative signal phase and the location of the magnetic polarization minima. We analyzed arbitrary  $B_\pm$  minima for four trap designs in Chap. 6.

Consider the case illustrated in Fig. 7.3(a), a cross-section of two parallel line-like equal currents (Z and U) separated by distance  $2d$ , which are in phase,  $\phi_{UZ} \equiv$

$\phi_U - \phi_z = 0$ . Then, a point-like field cancellation occurs at the midpoint between the currents for each of  $B_x$ ,  $B_y$ , and thus  $B_{\pm}$ . Shifting the phase difference by  $\phi_{UZ} = -90^\circ = -\pi/2$  (right lags), as in Fig. 7.3(a), then results in a point in space at  $y = \pm d$  (the right angle of a  $45^\circ/45^\circ/90^\circ$  triangle with the currents) where the field moves purely right-circularly (or left circularly, at the opposite  $y = \mp d$  position), as both currents oscillate through a cycle. At such a location, where one circular polarization is pure, the other circular polarization component has an amplitude zero. These minima in  $B_{\pm}$  move equal and opposite to each other with phase shifts, and are located at (for equal currents):

$$y_{\pm} = \pm d \cdot \tan(\phi_{UZ}/2) \quad (7.2)$$

When the two currents are precisely out of phase  $\phi_{UZ} = \pm\pi$ , the fields cancel asymptotically far away at  $y \rightarrow \pm\infty$ . Given power imbalances, the trap circles back outside the wires on the  $x$ -axis for  $\phi_{UZ} = \pi$ , and inside the wires when  $\phi_{UZ} = 0$ , both nearer the lower magnitude wire.

We can determine an arbitrary function for the position of  $B_{\pm}$  minima in the case of point-like AC currents  $I_U$  at  $x = d$  and  $I_Z$  at  $x = -d$ , with current ratio  $r_{UZ} = \frac{I_U}{I_Z}$  and phase difference  $\phi_{UZ}$ . The expression

$$y \pm ix = \pm id \cdot \frac{1 - r_{UZ}e^{i\phi_{UZ}}}{1 + r_{UZ}e^{i\phi_{UZ}}} \quad (7.3)$$

gives the  $x$  and  $y$  coordinates as the real and imaginary parts of the right side of Eq. 7.3, scaled by geometry as  $d$ , with sign matching the  $B_{\pm}$  polarization component. When  $r_{UZ} = 1$ , traps remain on the  $x = 0$  line, and  $y$  simplifies to the tangent expression Eq. 7.2, moving vertically with phase. Varying current ratio at constant  $\phi_{UZ} = \pm 90^\circ (e^{i\phi_{UZ}} = \pm i)$  traces a circle around the origin (as shown in Fig. 6.8).

To predict the trapping potential from a current source with the spatial extent of our chip traces, we simulate a 2-D plane of the  $B(x, y, z_0)$ -field numerically, due to complex RF current cross-sections  $\tilde{I}_U(x, y)\hat{z}$  and  $\tilde{I}_Z(x, y)\hat{z}$ . Both the currents evolve at the driving frequency  $\omega_{RF} = 2\pi f_{RF}$ , with some insertion phase difference  $\phi_{UZ} = \phi_U - \phi_Z \pmod{2\pi}$  by which U precedes Z. We can write  $I_Z = \tilde{I}_Z(x, y)e^{i\omega_{RF}t}\hat{z}$ , and  $I_U = \tilde{I}_U(x, y)e^{i(\omega_{RF}t+\phi_{UZ})}\hat{z}$  as the complex, spatial currents. In this simulation, wires have no cross-talk or proximity effects on each other, which does adjust experimental current distribution and phase, as discussed in Sec. 7.7. These simulated currents induce complex magnetic fields perpendicularly in  $B_x$  and  $B_y$  via the Biot-Savart law. We integrate over the finite-sized conductors with further complex information from a skin-effect computation on each wire separately (as in Chap. 8 and [79]). This complex quasi-static approach maps the current phase information into complex B-fields. The  $B_x$  and  $B_y$  fields are then converted into their circular parts:  $B_{\pm}(x, y) = B_x(x, y) \pm iB_y(x, y)$ . Note that this conversion is not customary or unitary but dovetails nicely in our Rabi definitions.

### 7.2.3 Trap Simulation

Combining these elements, we calculate a diagonalized five- and three-level Hamiltonian over the Rabi map  $\Omega(x, y)$  generated by  $B_{\pm}(x, y)$  using Eq. 7.1, shown in Fig. 7.3. These results reveal multiple trapping and anti-trapping surfaces of AC Zeeman states, depending on both the amplitude of fields (as  $\Omega$ ) and the frequency detuning of the field (as  $\delta$ ). Increased detuning lowers  $E_{ACZ}$  from the full resonant value, thus lowering both trap depth and trap frequency. Trap bottom shape changes from a linear cusp on resonance, smoothing to a harmonic shape at higher detuning, akin to the effect of the quantizing field value in a DC chip micromagnetic trap. AC Zeeman states can be populated from a pure  $m_F$  state via a frequency sweep from

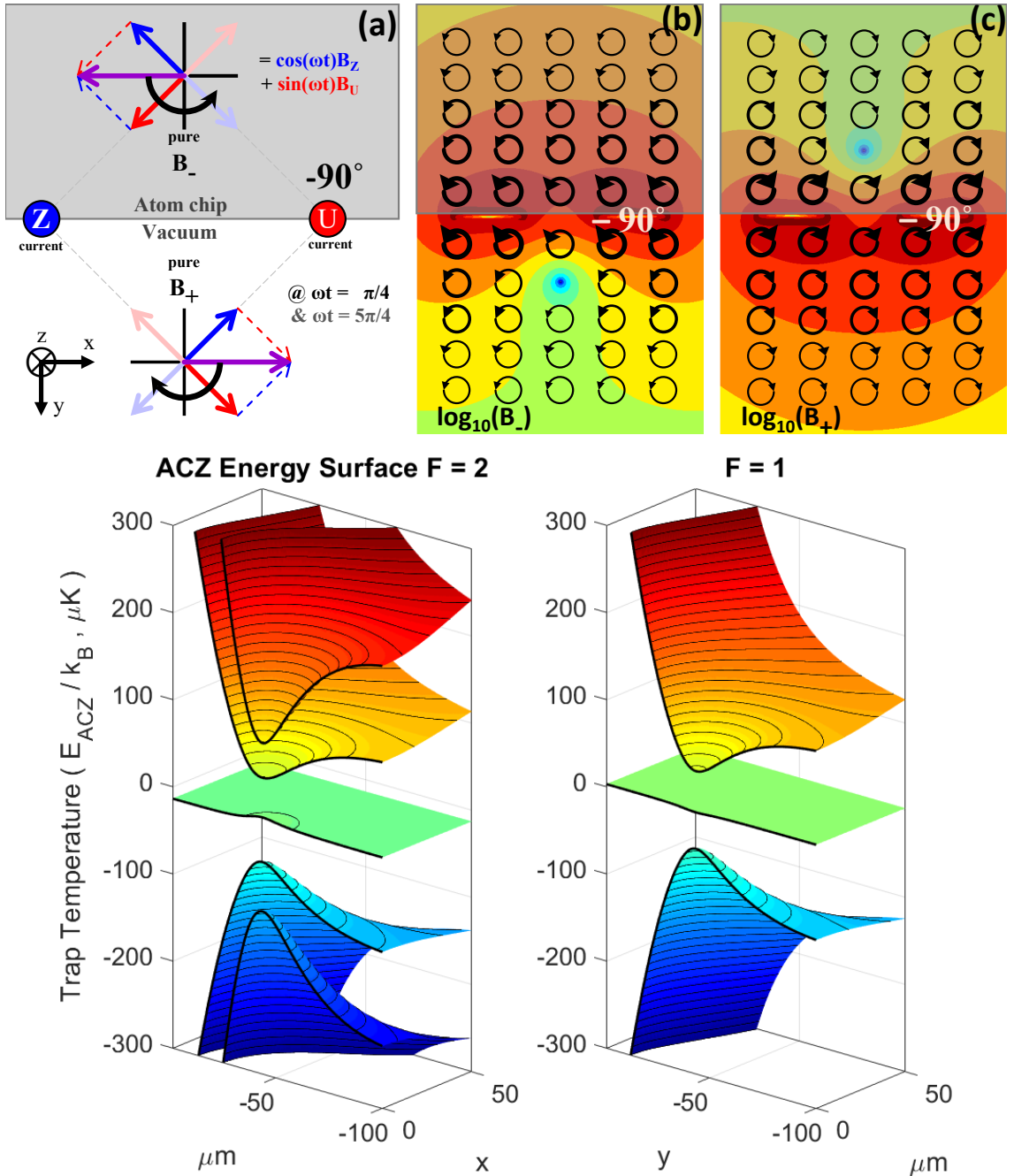


FIG. 7.3: Pedagogical trap explanation and sample AC Zeeman trapping potentials. (a) A pedagogical explanation of the polarization parity when the right-hand wire is phase-delayed by  $90^\circ = \pi/2$ . Two locations are seen to have pure circular polarization, where the *opposite* parity has a minimum. (b,c) Simulated contours of  $\log_{10}(B_\pm)$  with finite-sized wires matching the experiment. Bottom: Simulated trapping and anti-trapping energy surfaces for all RF AC Zeeman states, using  $\phi_{UZ} = +90^\circ$  for  $F_+ = 2$  (left) and  $-90^\circ$  for  $F_- = 1$  (right). Simulations use  $|I_A| = |I_B| = 500$  mA in two  $50 \mu\text{m} \times 4 \mu\text{m}$  wires, separated  $100 \mu\text{m}$ , center-to-center. Applied frequency  $f_{RF}$  in this simulation is 21 MHz for  $B_{DC} = 28.58$ , leading to nearly 1 MHz separation of trap bottoms. Black contour lines mark each  $10 \mu\text{K}$ .

far detuning, beginning in the appropriate state, as indicated in Fig. 7.2 (c). In this work, we only populate the curves  $|++\rangle$  from  $|2,+2\rangle$  and  $|+\rangle$  from  $|1,+1\rangle$ .

While the skin effect and finite-size simulation are a step beyond point-like currents in a 2-D simulation, we find that inductive coupling with the proximity effect between the chip wires has a significant impact on trap location, as it adjusts the power and phase in each of the participating wires. A high-frequency finite element electromagnetic 3-D simulation software (e.g. FEKO) can be used to simulate atom chips in order to iterate designs with more accurate feedback than the 2-D analytic models used in this work. We cover this material separately [80], but a significant finding is that each wire has a proximity effect on the other, causing an adjustment in power and phase along each wire, beyond the inserted parameters, whose strength depends on the phase difference. In practice, we tune insertion parameters empirically to accommodate these changes, using measurements of atoms as feedback.

### 7.3 Experiment

This experiment uses just two horizontal microchip wire segments, nominally  $50 \mu\text{m} \times 4 \mu\text{m} \times \approx 2 \text{ mm}$ , at the center of the atom chip. Three suitable wires, in a U-Z-U arrangement (, as in Fig. 7.4) were used: both U-wires ( $200 \mu\text{m}$  center-to-center) for low-power Rabi map work (Fig. 7.5), and the Z-wire and one U-wire ( $100 \mu\text{m}$  center-to-center) for the high-power trapping and Fig. 7.6. The Z-wire is used for the DC trap and the diagonal DC push/pull in Fig. 7.7.

The RF system uses a multi-channel direct digital synthesizer (DDS), a phase-controlled, frequency sweeping RF (1 GS/s, 400 MHz) source (the WeiserLabs

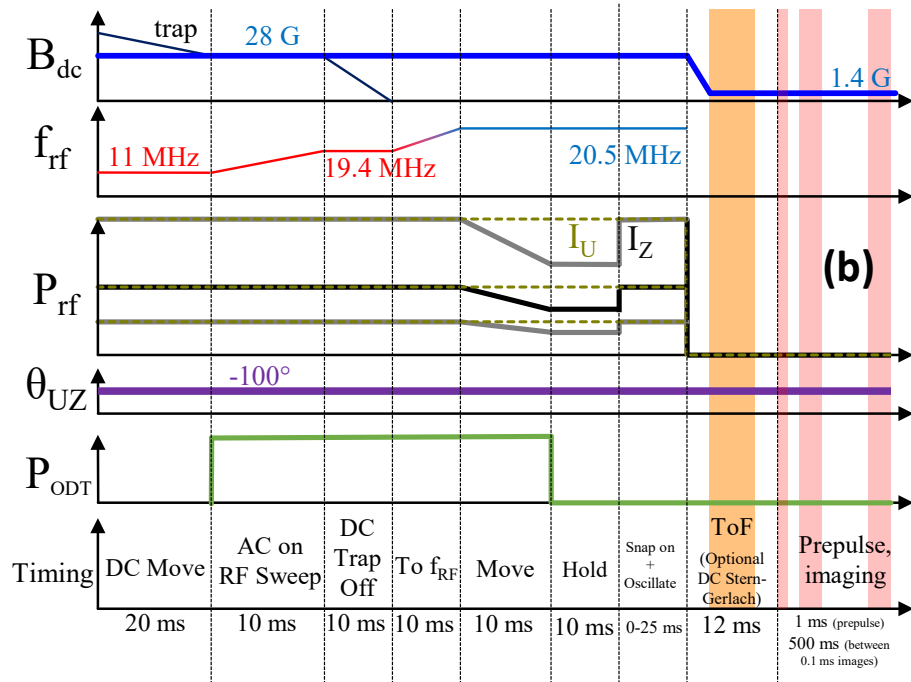
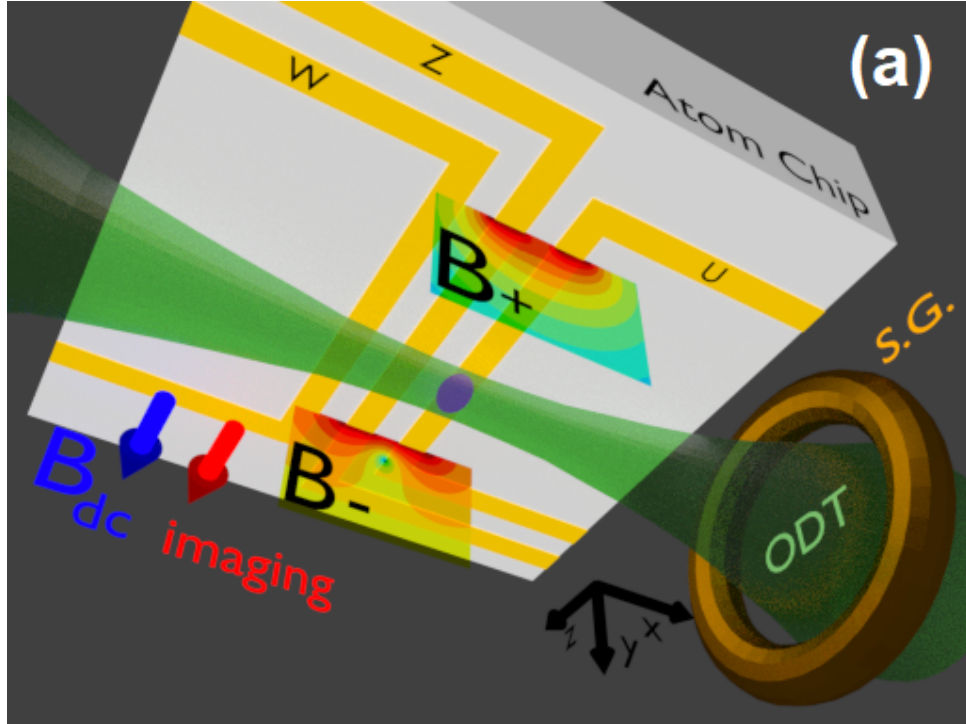


FIG. 7.4: Setup and a sample timing diagram for the AC Zeeman trapping experiment. Top: Cartoon schematic diagram looking up at the atom chip. Three atom chip traces (W, Z, U) carry AC currents, generating an inhomogeneous  $B_{\pm}$  field. Each center segment is 50  $\mu\text{m}$  wide, separated 100  $\mu\text{m}$  center-to-center, and roughly 2 mm long. We display these near-fields as  $\log_{10}(B_{\pm})$ . for  $\phi_{UZ}=115^\circ$  A near-uniform  $B_{DC}$  field provides the quantizing  $\vec{z}$ -axis. An ODT holds atoms axially, and a single-coil provides the  $B_{SG}$  field. Bottom: A sample timing diagram (not to scale), here for the inset of Fig. 7.8.

FlexDDS-NG<sup>1</sup>), with a MATLAB library<sup>2</sup> to send experimental command packets over local Ethernet. The DDS's sequential commands are TTL triggered by the main apparatus sequencer. The RF outputs are sent through an RF preparation chain (described in Sec. 2.7), and then through vacuum ports to the chip traces (shown in Fig. 2.12).

Atoms are initially prepared in a DC micromagnetic chip trap [81] containing roughly  $2 \times 10^5$  atoms at 1-2  $\mu\text{K}$ . We adjust DC trapping fields to bring the trap location closer to the chip, roughly centered between the U and Z wires, and relax the trapping potential, as indicated in the timing diagram of Fig. 7.4(b). We also turn on additional axial confinement along the  $\hat{z}$ -axis from the ODT during this DC trap movement, as shown in Fig. 7.4(a). With the DC trap in place, we send in RF power into the U and Z wires and sweep  $f_{RF}$  from far red (but above  $f_{RF}/2 = 10$  MHz to avoid the second harmonic) to near red ( $\delta = -1$  to  $-0.5$  MHz) at full power, maintaining the population in the DC trapped state,  $|2, +2\rangle$ . We then ramp off the DC trapping fields except for  $B_{DC}\hat{z}$ , leaving atoms only in an AC Zeeman trap with hold frequency  $f_{RF}$ . The relative RF phase  $\phi_{UZ}$  is kept constant,<sup>3</sup> throughout the loading process. All subsequent experiments begin with this DC chip trap to AC Zeeman trap loading process. We measured free-fall thermal expansion of atom clouds and find temperatures in the range 0.5-2.5  $\mu\text{K}$ , although this number depends heavily on the chosen trap parameters: detuning, phase, and power.

As this work represents a proof-of-principle AC Zeeman trap, we did not spend much effort in globally optimizing procedures of trap loading, movement, evaporation, and so on. Broadly, some working parameters were found and locally optimized, though we would expect some improvements from more careful loading and movement of the trap, when precision or a colder sample is needed.

---

<sup>1</sup><https://www.wieserlabs.com/products/radio-frequency-generators/WL-FlexDDS-NG>

<sup>2</sup><https://github.com/drewrotunno/FlexDDS>

<sup>3</sup>Although a small sweep can account for the frequency-dependent phase from Sec. 2.9

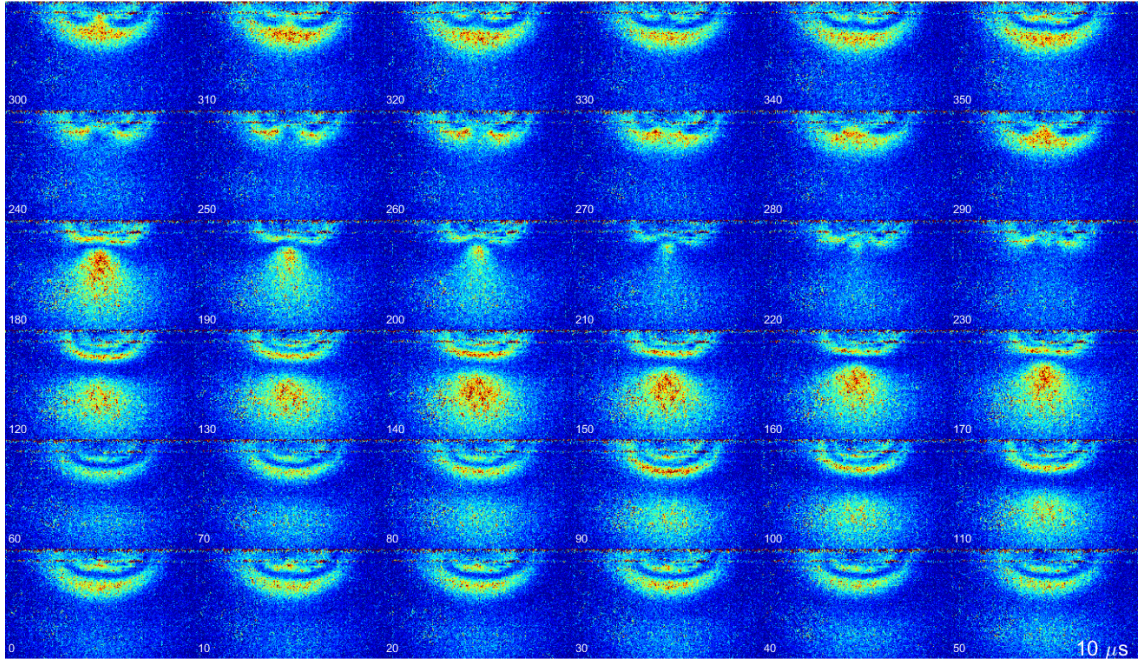


FIG. 7.5: Two-Wire U-U Rabi maps for a full cycle of phase delays, at  $10^\circ$  increments between each cell, beginning left to right in the bottom row, then up rows each  $60^\circ$ . Nominal power in each wire is 20 mW, for a  $10 \mu\text{s}$  pulse using 8.5 MHz and  $B_{DC} \approx 12.3$  G. More information about this imaging technique is found in Appx. C.

### 7.3.1 Low-Power Field Mapping

One method used in preparation for high-power trapping was low-power field mapping, using snapshots of a wide-spread atom cloud after a brief RF pulse (few  $\mu\text{s}$ ) with a spatially-varying Rabi frequency [82], which we call a ‘Rabi map,’ shown in Fig. 7.5. Rabi maps are illustrated with more time steps and a more detailed explanation in Appx. C, and an animation is included in the online materials. Atoms oscillate fully out of their state and back for a resonant applied field, with a rate dependent on the amplitude of the local  $B_\pm$  field (vis-à-vis Fig. 7.3). Images produced with this method appear as bright and dark bands mapping contours of iso- $\Omega_0$  as  $B_-$  acts on the  $F_+ = 2$  state as the field shape changes across a cycle of phase in Fig. 7.5. Evident in this figure across the third row is the local ‘trap’ minimum, which doesn’t flop as fast as the atoms around it, moving toward the chip as phase approaches  $360^\circ = -100^\circ$ . Additionally, this

imaging method helps illustrate the ‘saddle-point’ area of flat field below the trap, as in the  $290^\circ$  cell of Fig. 7.5.

In Fig. 7.6, we use Rabi maps to demonstrate the polarization selection between  $F_+ = 2$  and  $F_- = 1$ , using opposite phases (top and bottom) for each hyperfine manifold (left and right).<sup>4</sup> Notably, the same generating conditions form a useful trap under the atom chip for only one manifold at a time, while the other gets a monotonic gradient away from the wires. When we perform microwave evaporation in a later section, it is roughly these surfaces that we evaporate to. Examining this Rabi map data over space and time can extract  $\Omega_0(x, y)$  information [82], but we did not analyze it in this manner. Generating and observing Rabi maps is useful when coarsely tuning relative current and phase relationships, testing unknown chip impedance behavior with a low risk of frying the chip at high power.

Another field probing method is to pulse on the trapping field for a significant amount of time (few ms) and look for forces from gradients acting on the atoms, like the ACZ force experiment of Chap. 5. Applying such an impulse can shift a cold cloud’s center of mass, or act on a large spatial extent of atoms, producing clumping or spreading of atoms spatially after some time-of-flight due to gradients from trap-like curvature.

The third method for imaging RF field strength using atoms is to perform a medium-to-low power ARP sweep. Atoms in strong  $\Omega_0$  regions will fully pass to the final state, whereas regions with low or no  $\Omega_0$  power will leave atoms in their initial state. This process yields a single contour line at a time, set by  $d\omega_{RF}/dt \sim \Omega_0(x, y)$  and the Landau-Zener transition approximation [64].

---

<sup>4</sup>We ARP atoms from  $|2, 2\rangle$  to  $|1, 1\rangle$  via a  $100 \mu s$  sweep in a hand-made dipole antenna  $\approx 10$  cm from the atoms.

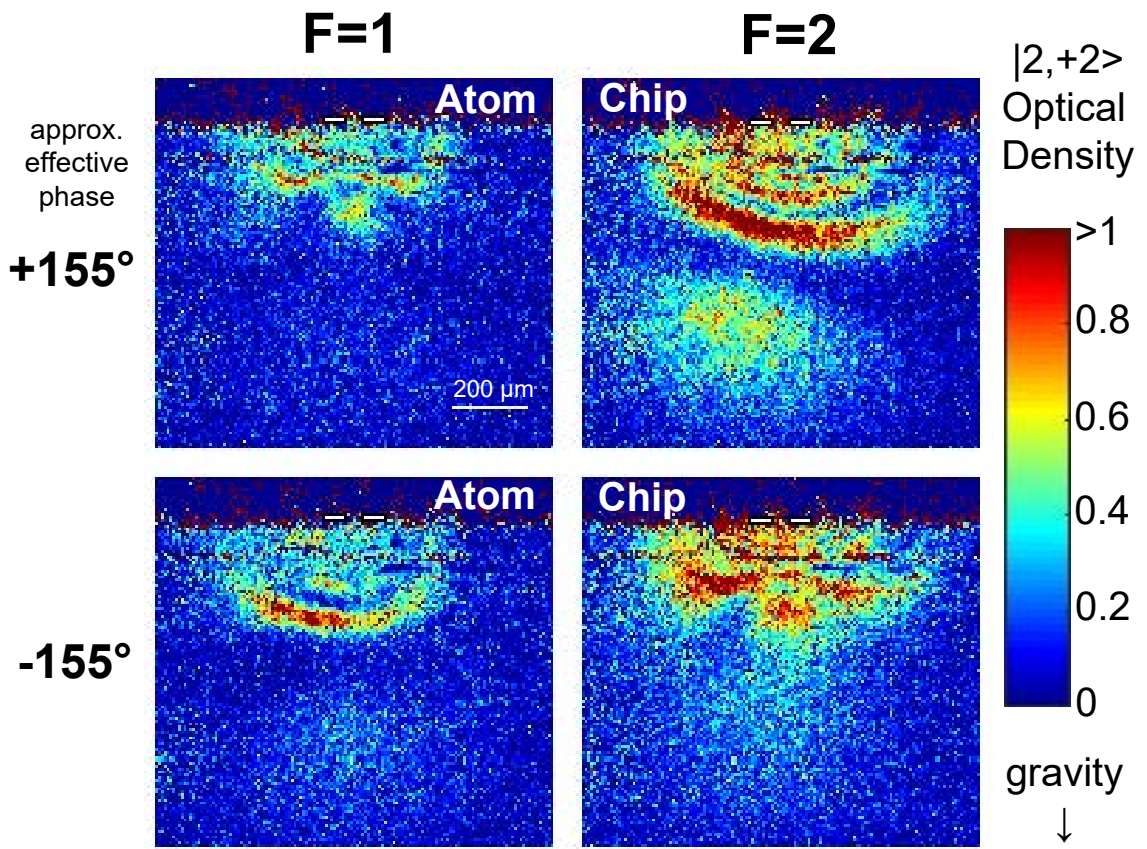


FIG. 7.6: Two-wire U-Z Rabi map images demonstrating the difference between hyperfine manifolds (left and right) with respect to field polarization (top and bottom). Hyperfine states are imaged only the initial state  $|2, +2\rangle$ , after a  $\approx 2 \mu\text{s}$  RF pulse with  $\approx 20 \text{ mW}$ . Atoms are sent to and returned from  $|F = 1, m_F = +1\rangle$  via microwave ARP sweeps before and after the RF pulse. Atoms in the  $F=1$  state map the  $B_+$  field, while  $F=2$  atoms map the  $B_-$  field. Approximate chip trace sizes are drawn in. More information about this imaging technique is found in Appx. C.

### 7.3.2 Dipole and Ioffe End-capping

The 2-D AC Zeeman trap described here provides a restoring force in only two dimensions ( $x$  and  $y$ ) and alone makes an open-ended cannoli shape, leaking atoms axially along the  $\hat{z}$ -axis. We elect to use a transverse  $-\hat{x}$ -oriented optical dipole beam to provide end-capping (in  $\hat{z}$ , plus modest  $\hat{y}$  confinement), in the form of a 1064 nm laser with roughly 0.6 W of power focused to a beam waist of 120  $\mu\text{m}$ . By design, the ODT is not sufficient to hold atoms against gravity, but provides axial end-capping and localizes atoms, with estimated trap frequency  $\omega_z/2\pi = 22$  Hz. The optical dipole end-capping was almost always utilized in our experimental trap setup for consistency, atomic density, and lifetime benefits.

We observe the axially confined atoms in opposite  $m_F$  states in Fig. 7.1(a,b). Without the ODT, we observe slight axial confinement for  $m_F=+2$  (red-detuned  $|++\rangle$ ) and spreading of  $m_F = -2$  (blue-detuned  $|+\rangle$ ) from the axial minimum between the two  $B_{DC}$ -generating coils. Atoms in  $|2, -2\rangle$  appear to hit ‘walls’ of unknown origin as they spread axially, not leaking out the ends as we had suspected, remaining confined on the chip but much less dense, covering a larger spatial extent. Effects from perpendicular trace segments and conductor roughness appear to contribute partially to end-capping or localizing the atoms along the trace in this case. We had expected surface roughness effects to diminish significantly using AC, but there is clumping structure observed in atom density over a large axial atom cloud, possibly due to roughness.

### 7.3.3 Throw from F=2 and Catch in F=1

While an initial red detuned ACZ trap can confine  $|2, +2\rangle$  atoms directly from a DC chip trap, the  $|1, +1\rangle$  state, which can be reached with a single microwave ARP sweep, is anti-trapped ( $|-\rangle$ ) for red detuning. To trap  $|1, +1\rangle$ , we need to

start from initial blue detuning, with a phase flip in  $\phi_{UZ}$  with respect to the  $F_+ = 2$  trap, to trap  $|+\rangle$ . If we simply drop atoms, make a population-changing microwave pulse, then catch them again in a new RF ACZ trap, they would be farther from the chip due to gravity, in a weaker trap, with downward velocity.

Instead, we elect to shift the atoms toward the chip while moving red with detuning and off in power, releasing the atoms in a slight upward trajectory in  $m_F = +2$ . When the RF power is off, the frequency is brought to far blue detuning with an opposite phase, while a hand-made dipole antenna  $\approx 10$  cm away emits a  $\approx 6.894$  GHz microwave ARP sweep (1 MHz / 100  $\mu$ s) to transfer the  $|2, 2\rangle$  population to  $|1, 1\rangle$ .

We observe that this microwave antenna field couples into chip wires, inducing local gradients in microwave power. Surprisingly, a fixed local minimum in this field is observed, an accidental low-power AC Zeeman trapping field, fixed in phase by the unknown coupling into multiple chip wires. However, the microwave field fully transfers atoms in this throw-catch application.

Atoms now in the ballistic  $|1, 1\rangle$  state are ‘caught’ by the RF trapping field sweeping in from above resonance at high power. The timing of each “throw and catch” RF/ $\phi$  sweep is on the order of 2 ms, adjusting interval timing and phase empirically, optimizing for high population with minimal heating. This throw and catch process precedes measurements of the trapped  $F_- = 1$  states in Figs. 7.1(c) and 7.7.

## 7.4 Results

The primary result is that we have demonstrated trapping using a two-trace AC Zeeman atom chip trap, as evidenced by trap oscillation frequency measurements in Fig. 7.8, and hold lifetime measurements in Fig. 7.9. Further, we trap atoms in states that are untrappable in a DC trap, as demonstrated in Figs. 7.1 and 7.7.

Motivated by using the ACZ as a general-purpose trap, we test forced evaporation in this trap using conventional and unconventional methods.

We measure trap frequencies for a range of detuning and power, comparing these values to numerical AC Zeeman potential surface fitting in Sec. 7.4.1. We observe a few hundred Hz of trap frequency, decreasing off resonance, using nominal measured power 200 mW (23 dBm) of RF power sent to each the U and Z wire traces. We compare these trap frequency measurements with simulations which use only independent measurements of  $\Omega_0$  and position, per Sec. 4.3. Resonant traps are linear at the trap bottom, and more detuning can round the trap bottom into a harmonic trap of decreasing frequency. Lifetime measurements as a function of hold frequency are presented as observed in Sec. 7.4.2, without a model to explain their values. Long lifetimes are found at significant detuning, at the cost of a lower effective  $E_{ACZ}$ .

We also demonstrate that the trap position is controllable with both the phase and relative RF power sent to the U and Z wires, which we discuss in Sec. 7.5. Phase-delay and power loss effects on-chip after insertion play an important role, but these become tractable problems to plan around with detailed simulation and in current experiments with experimental compensation.

One major unexplained finding is the resonance asymmetry in lifetime and trap frequency, where we cannot trap more than 1 MHz red detuned but retain a trap more than 20 MHz blue detuned in our setup. This behavior held at 8.5 MHz and 20 MHz and is only partially explained by the phase-delay in wire coupling ( $\approx \frac{1}{2}^\circ/\text{MHz}$ ). We see that the second harmonic play a significant role, killing the cloud when we sweep from below  $f_{RF} \approx f_0/2$ , and we must remain aware of the RWA approximation, where it might not hold that  $f_0 + f_{RF} \gg f_0 - f_{RF}$ , or even  $f_0 \gg \Omega/2\pi$ . Additionally, we expect to observe spin-mixing of  $|++\rangle$  into the also-trapped  $|+\rangle$  state, as we have saw in Sec. 5.4 with a long ACZ gradient pulse on

atoms fully retained in an ODT. However, we did not observe this spin mixing in this experiment when we tried to induce it near resonance.

### 7.4.1 Trap Frequencies

Trap frequencies are one of the primary properties of harmonic traps, relating potential energy curvature (as simulated) with the oscillation frequency of confined atoms (as observed). Experimental data employs some perturbation on atom position, then we drop and observe position evolution (measuring momentum at release via fixed time-of-flight) with increasing hold time, as shown in Fig. 7.7. These positions in  $x$  and  $y$  are fit to a exponentially damped sine curve to give the trap frequency.

In the example of Fig. 7.7, we perturb opposite  $m_F$  stretch states in each manifold using a DC current in the Z-wire to generate a diagonal Stern-Gerlach force, pushing  $|2, 2\rangle$  and  $|1, -1\rangle$  states while pulling  $|2, -2\rangle$  and  $|1, 1\rangle$  states. This demonstration was devised by ShuangLi Du as a method to prove atoms remain high- and low-field DC seeking, while ACZ low-field seekers in  $|++\rangle$  and  $|+' \rangle$  states. We see this impulse gives atoms opposite initial direction and roughly  $1:\sqrt{2}$  ratio for  $F = 1$  or  $2$  trap frequency.

Detuning plays a significant role in trap profile as examined in Sec. 6.3, creating linear-bottomed traps near resonance, perturbing into shallower, more harmonic traps off-resonance, plotted for 1 MHz detuning in Fig. 7.3. We continue to plot harmonic fits to these sharp potential curves, and heavily damped position oscillation fits.

In Fig. 7.8, we plot measurements of trap oscillation frequency versus detuning, and compare these with fits of ACZ trap bottoms from simulations using an independent measurement of  $\Omega_0$  (from Sec. 4.3). We observe trap frequencies ap-

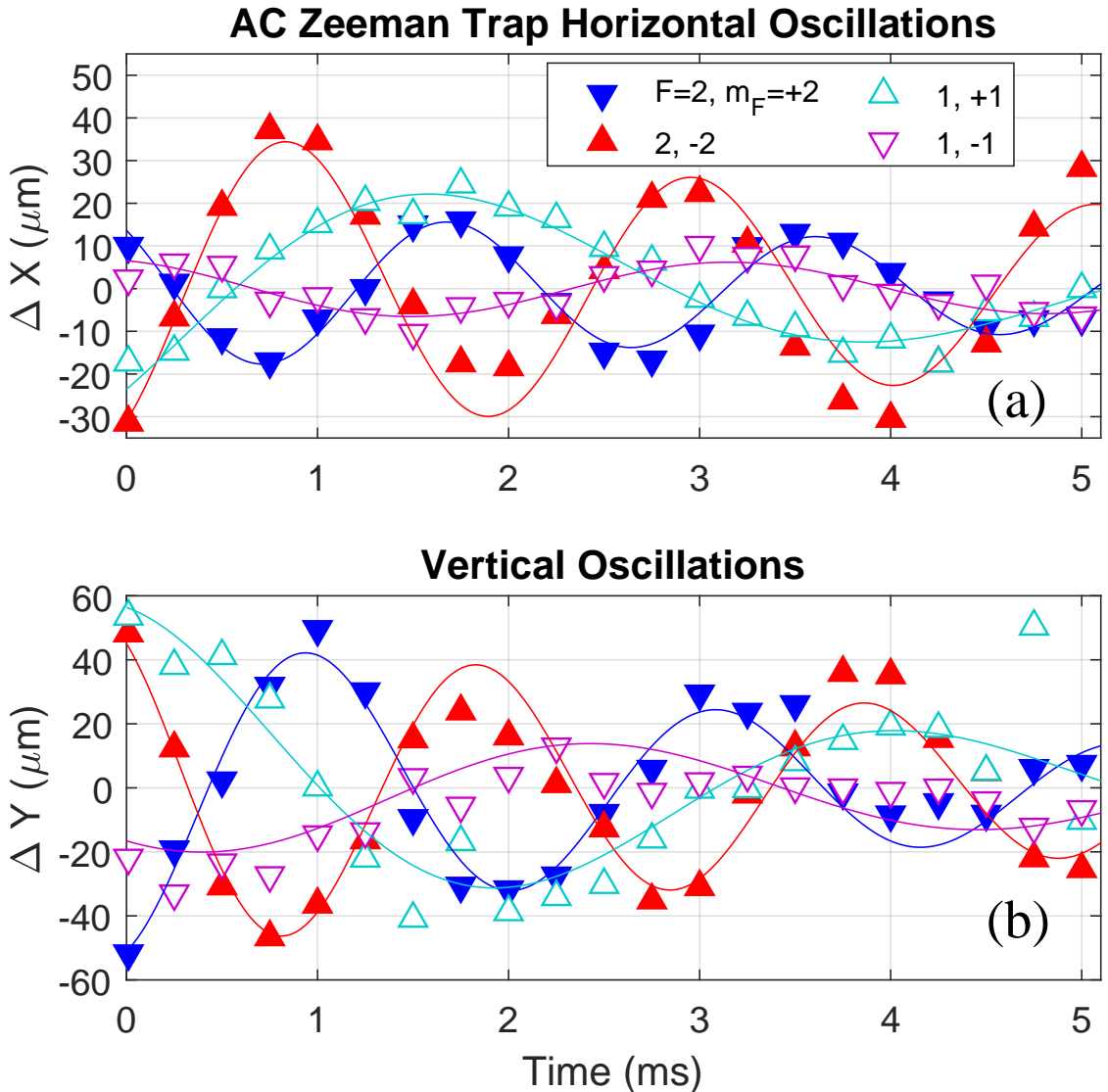


FIG. 7.7: Atoms released from AC Zeeman traps. We show observed trap oscillations ( $x$  in (a) and  $y$  in (b)) for atoms perturbed in-trap by a diagonal DC Stern-Gerlach pulse, held in traps (nominally 400 mW) slightly below and above resonance, 19.5 MHz and 21.5 MHz, respectively, with  $B_{DC} = 28.58$  G, and nearly 180° out-of-phase for  $F_- = 1$  and  $F_+ = 2$ .

proaching 1 kHz on resonance in the  $|++\rangle$  state, using 200 mW of power into each trace. These measurements also reveal significant asymmetry between the vertical and horizontal oscillation frequencies, even though simulations suggest symmetric trap bottoms. With balanced currents, the horizontal direction ( $x$ ) should be symmetric, while the vertical ( $y$ ) will always have a high field above and the gravity-fighting hump below it. Hot atoms in deep traps will sample this non-harmonic field, thus one would expect a harmonic potential and symmetric frequencies only for the coldest samples. This suggests that the deepest traps on resonance will have more-symmetric  $x$  and  $y$  trap frequencies, as we observe. Inset in Fig. 7.8, we give data on trap frequencies as a function of applied power. We observe square-root scaling, as  $\Omega_0 \propto |B_{\pm}| \propto I \propto \sqrt{P}$ . Specifically, over the range measured, we quadruple power and see only double trap frequency.

While a trap hold frequency off-resonance can project atoms into single states impelled by a Z-wire Stern-Gerlach field as in Fig. 7.1, atoms in mixtures near resonance do not lend themselves to this technique. When attempted, eigenstate components in  $m_F = +1$  and  $m_F = -1$  stretch the cloud diagonally and cannot be analyzed by cloud position alone. Therefore to obtain diagonal oscillations, we require a process shown in the timing diagram of Fig. 7.4. We lower the Z-wire's RF power linearly over  $\sim 10$  ms, then quickly snap it back to its full value. This procedure creates the oscillations measured in Fig. 7.8. The ODT is turned off when the Z wire's RF power is snapped back on so that measured frequencies are due to the ACZ potential alone.

### 7.4.2 Trap Lifetimes

We measure the  $|++\rangle$  trap lifetime with a conventional  $e^{-t/\tau}$  fit over a variable hold time  $t$  of Gaussian atom number fits after a few ms times-of-flight. Experi-

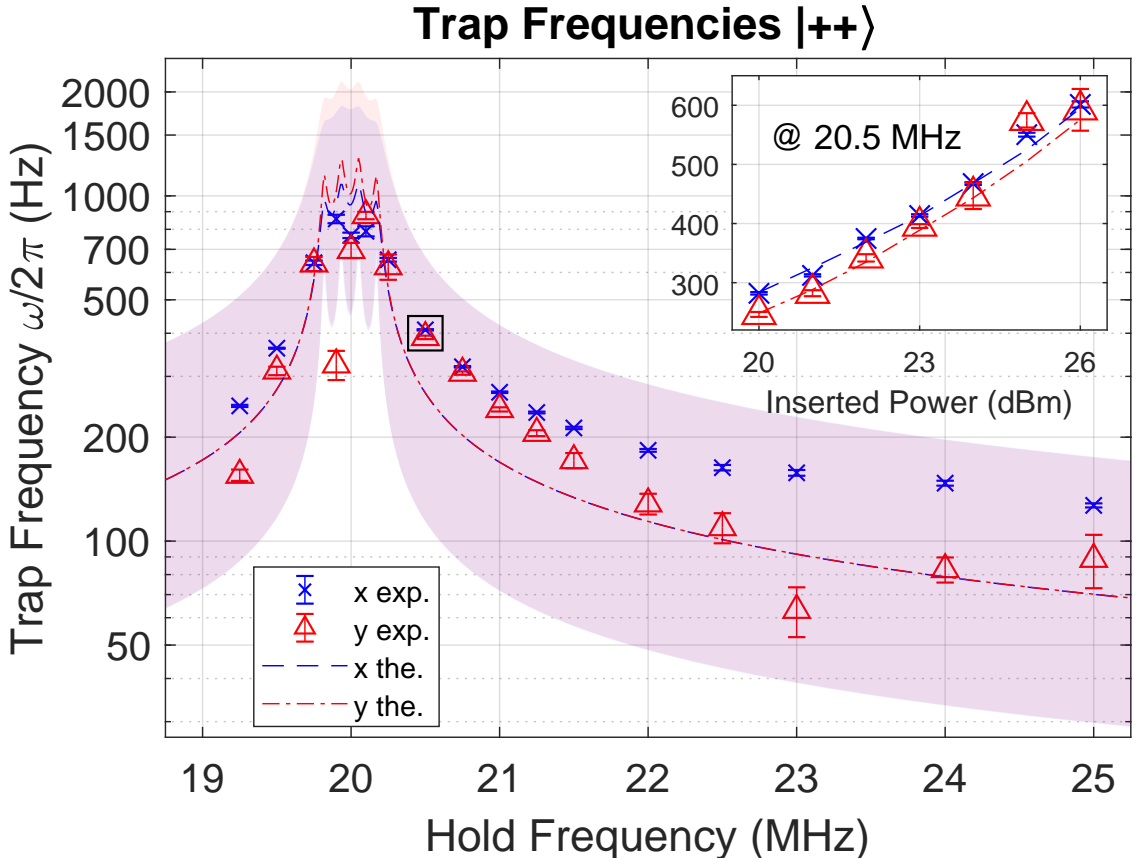


FIG. 7.8: Measurements of  $x$  (blue  $\times$ ) and  $y$  (red  $\triangle$ ) trap oscillation frequencies vs. RF frequency  $f_{RF}$  on the main axis, and over a range of power inset. Each set maintained  $B_{DC} \approx 28.58$  G, effective nominal phase  $\phi_{UZ} = -100^\circ$  from experimental insertion phase  $73^\circ$ , and power nominally 200 mW or 23 dBm in each wire. Theory curves (and 1- $\sigma$  shading) use independent measurements of Rabi frequency and trap position to infer total trace current and effective phase for simulated potential fits. Theory values with 1- $\sigma$  uncertainties used:  $[I_U \text{ (mA)}, I_Z \text{ (mA)}, \phi_{UZ}(\text{)}]$  mean: [225, 250, 130], low: [174, 184, 139], high: [275, 306, 115]. Inset: Trap oscillation frequencies for a range of input powers, above and below the 23 dBm at constant frequency 20.5 MHz, with hand-picked phase  $\phi_{UZ} = 121^\circ$ . Linear fits of this data gives  $\approx 53(6)$  Hz/dB.

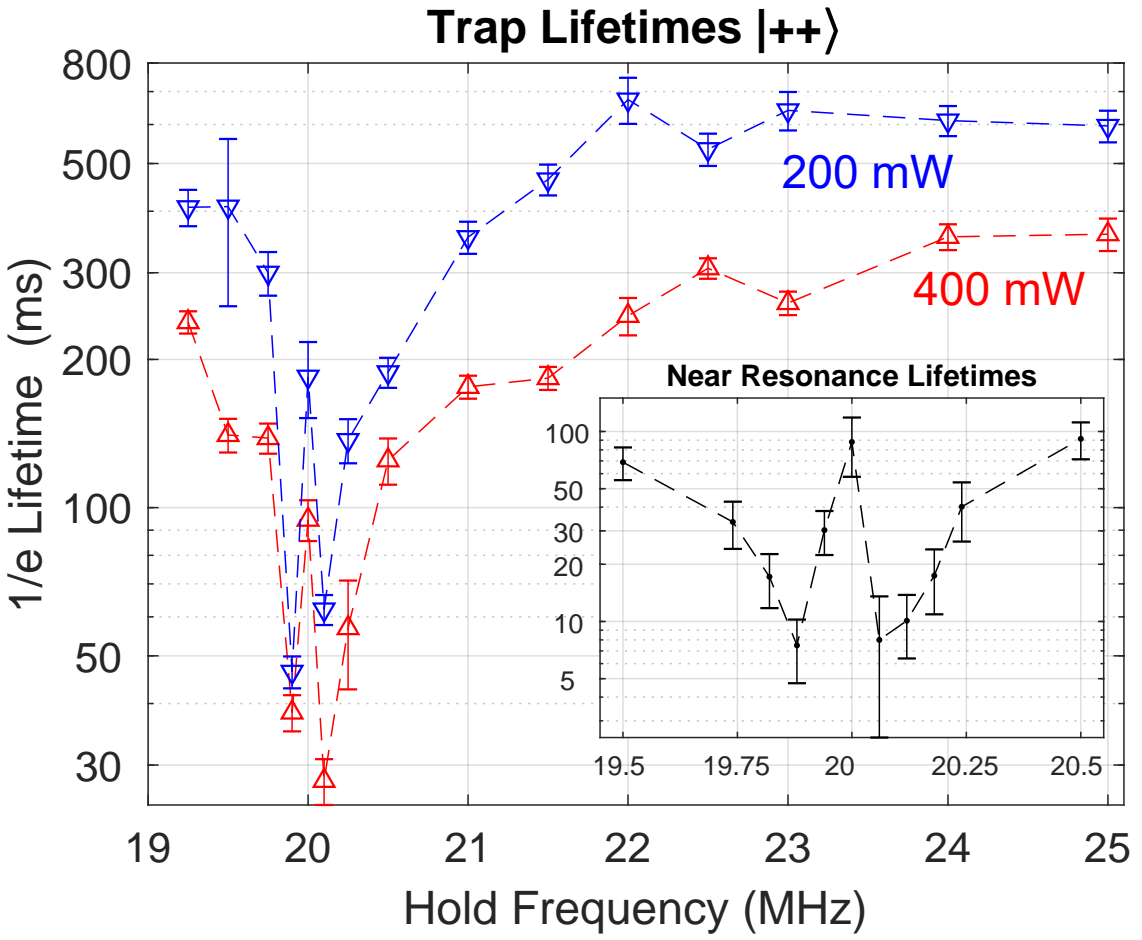


FIG. 7.9: Empirical  $1/e$  lifetime measurements at different trap hold frequencies  $\omega_{RF}/2\pi$ , with  $1-\sigma$  fit error. Full: Lifetimes were taken at two powers, nominally 200 mW (blue  $\nabla$ ) and 400 mW (red  $\Delta$ ) sent to the chip. Inset: A separate set of near-resonance lifetimes, using 400 mW, demonstrating the close-in structure near RF resonances. Dashed lines connect points in each set as a guide to the eye.

tal sets generally include 32 equal spaced, randomly ordered points covering nearly  $2\tau$  of hold time, using the ODT as described in Sec. 7.3.2. We present data for a range of hold frequencies  $f_{RF}$ , at two different powers (nominally 200 mW and 400 mW per wire) Fig. 7.9.

The longer lifetimes belong to the lower power, with its lower trap frequencies and shallower trap depth. We offer no theoretical fit for this data, but we suspect thermal losses as a major loss mechanism, as the sample appears colder for longer hold times and the lack of observable transition from  $|++\rangle$  into the  $|+\rangle$  state. Further, a linear trap shape has a different distribution of trap kinetic energy levels than the equal-spaced harmonic case.

An inset plot shows trap lifetime data close in to the resonances of the system. We had selected points both on, between, and outside of each of the four resonances, and had expected every other point to have some stability in a relatively pure  $m_F$  state, but only the  $m_F = 0$  had a longer lifetime than holds near level crossings.

The number loss appears to be evaporative, as we see the spatial cloud sizes shrink with hold time and number loss, by roughly 5-10% over a  $\tau$  lifetime. We posit that this effect can either happen ‘over’ the potential, with trap depth not much greater than sample temperature, or ‘under’ the potential when atoms pass through the central  $\Omega = 0$  location before re-projecting into untrapped states like DC Majorana losses. We do not attempt a model for either of these, but tracking down this mechanism can make AC Zeeman trapping a more valuable experimental tool.

We looked for atoms that might flip from the  $|++\rangle$  state to the also-trapped  $|+\rangle$  state by blue-projecting back into bare  $m_F$  states and Stern-Gerlach separating the final population. We purify the spin sample, removing any of the initial  $|+\rangle$  population by sweeping far blue to 40 MHz, where  $|++\rangle$  remains trapped, but gravity takes the  $|+\rangle$  trap population. We then sweep to and hold near resonance,

where we did not observe any significant subsequent population in the  $|+\rangle$  (i.e.  $|2, -1\rangle$ ) state after long hold times, when we sweep back to high detuning. We had expected this result from previous spin-mixing results (Sec. 5.4) examining atoms subject to long AC Zeeman field gradient in the ODT, which suggests they would mix after some time, faster with low detuning and low power.

### 7.4.3 Methods of Evaporation

We demonstrate evaporative atom cooling from an AC Zeeman trap using two conventional methods (RF and microwave ‘knife’) and an unconventional method, shifting the phase to move the trap near the chip surface, where the hottest atoms collide with the surface and leave the trap. We plot our results in Fig. 7.10 and 7.11. Traps used for the [RF,  $\mu\text{W}$ , Phase] evaporation employed different trap compression values, holding  $f_{RF} = [19.4, 19.7, 19.7]$  MHz with nominal power 200 mW for each (note the RF evaporation was from a more relaxed trap than the other two).

For temperature calculation, we use radial trap frequencies  $\omega_{xy}/2\pi = [282, 577, 577]$  Hz, interpolated and averaged from Fig. 7.8, while the ODT’s  $\omega_z/2\pi = 22$  Hz is derived from prior experiments [44]. Atom temperature is inferred from cloud size after a known time-of-flight using these values. Trapped atom collision rates are estimated to be [6,150,130] collisions per atom per second for the [RF,  $\mu\text{W}$ , Phase] evaporation, respectively. Atoms are already evaporated significantly before the AC Zeeman load, although decent collision rates can still be achieved through selection of trap parameters. With larger populations, and tighter or linear [83] traps, we might be able to cool more effectively.

All three methods reduce the ensemble temperature at the expense of atom number, although phase space density improvements were minor for the employed parameters, shown in Fig. 7.11. The ability to cool atoms in an AC Zeeman trap

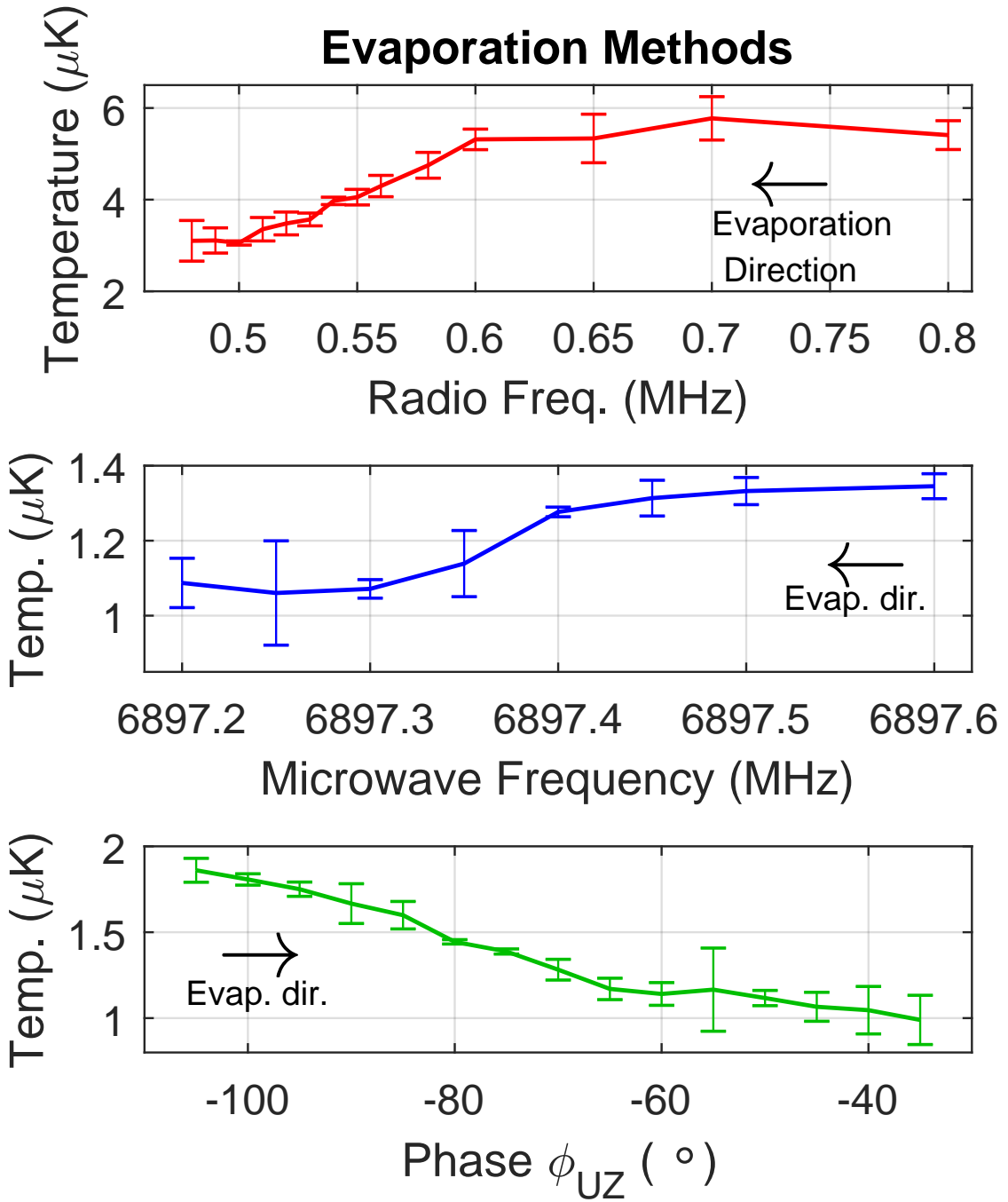


FIG. 7.10: Three evaporation methods: Top: using a traditional RF knife, Middle: using the microwave transition  $|2, 2\rangle \leftrightarrow |1, 1\rangle$ , and Bottom: using phase and the chip surface. Error bars give the standard deviation of three experimental values for each point. All methods reduce temperature as they evaporate as indicated by arrows. Phase space density for this data is given in Fig. 7.11. Specific trap parameters values are given in the text.

suggests that one may be able to produce a Bose-Einstein condensate (or a degenerate Fermi gas, in other species) in any of the  $m_F$  states contained in  $|++\rangle$  (or *any* via microwave) and at any sufficiently degeneracy-breaking background magnetic field.

Intra-manifold RF forced evaporation is nearly the same conceptual process as standard DC chip evaporation into anti-trapped states (in Sec. 2.2), while the  $\mu w$  coupling  $|2,+2\rangle \rightarrow |1,+1\rangle$  moves atoms to a broad  $\sim \frac{1}{y}$  gradient in the  $B_+$  field, as in Fig. 7.3(c). Notably, the choice of RF frequency (as detuning) can raise the trap bottom from zero to the detuning ‘floor,’ and this choice determines the evaporation knife endpoint. For example, the RF knife approaches this value at nearly 0.5 MHz, and the microwave evaporation goes to  $6,834 + 3 \times 20 + 3 \times 0.3 \approx 6895$  MHz (considering the hyperfine splitting, the  $B_{DC}$  resonance, plus the detuning, respectively, between the states  $|2,+2\rangle$  and  $|1,+1\rangle$  who have  $\Delta m_{Fg_F} = 3$ ).

Detuning also simultaneously controls trap density, depth, and collision rate, enabling dynamic trap control with  $f_{RF}$ . In our simple proof of evaporation, each parameter was ramped linearly from a fixed start frequency over 100 ms to a different endpoint, in sequential order. Points and error bars are mean and standard deviation of three measurements, assuming a known trap frequency (as given earlier) for each set.

The fact of using RF and microwave as an evaporation technique also suggests its use in something like DC/RF adiabatic trapping [64, 65, 66], that might be called RF/RF or  $\mu w$ /RF adiabatic trapping. Rather than sweeping from high to low frequency to connect potential curves to evaporate at the edges of the trap, we can sweep from low to high frequency to raise the center of the potential, generating ‘ring’ or ‘shell’ potentials from the combination of AC Zeeman potentials, by further dressing the surfaces given in Fig. 7.3.

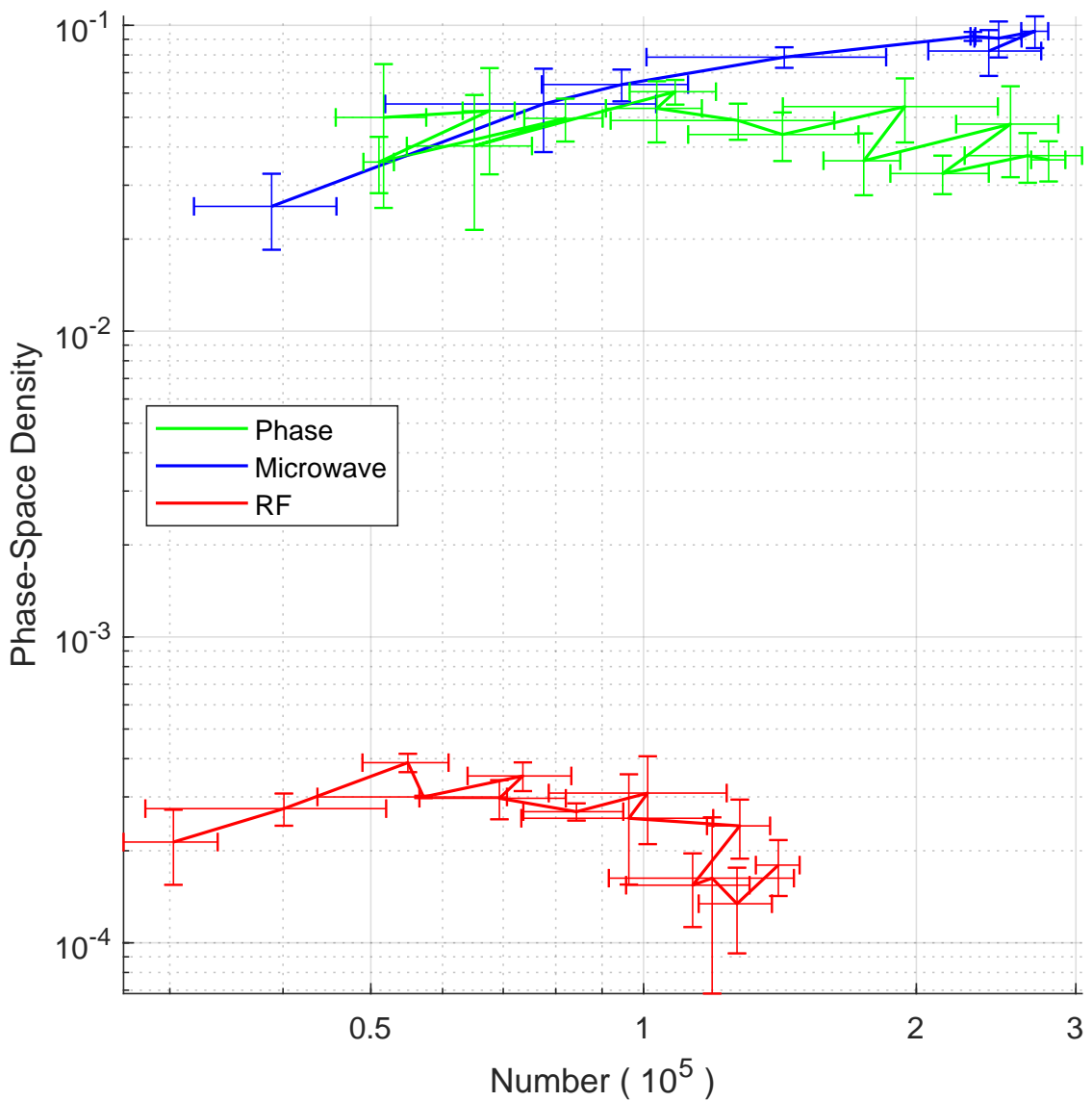


FIG. 7.11: Phase-space density paths for the evaporation examples given in Fig. 7.10. No method significantly raises phase-space density in this proof-of-principle test. Specific trap parameters values are given in the text.

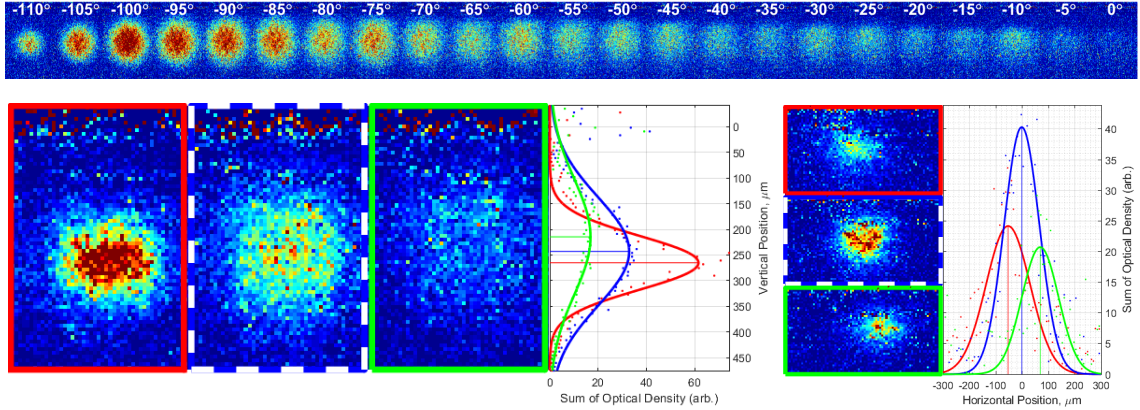


FIG. 7.12: Position control of trapped atoms via phase (top, left) and power (right). Each pixel is  $7.4 \mu\text{m}$ . Estimated effective phases shown on the left are  $\{-110^\circ, -100^\circ, -75^\circ\}$ , and power was adjusted -3 dB lower on either side.

## 7.5 Trap Position Control

We demonstrate control of trapped atom position (vis-á-vis Eq. 7.3) in a rather direct manner in Fig. 7.12. In all cases, we initialize atoms as described in Sec. 7.3, then adjust phase or power linearly over  $\approx 20$  ms, then do a hard cutoff of RF power at a constant frequency, imaging after a short 2-8 ms time of flight. For modest phase adjustments, released atoms are seen to have drastically different temperatures. Atoms released from the high-phase ( $|\phi_{RL}|$ ), weaker trap maintain their small size and high density at a lower position, whereas atoms released from a lower-phase, tighter trap are higher after the same time of flight, but much wider in momentum spread, due to the tighter trap it is released from. As phase approaches  $0^\circ$ , the trap moves vertically approaching the chip, eventually losing atoms to collisions with the room-temperature surface. Partial clouds appear as ‘cut’ Gaussian curves, containing atoms with downward momentum, as observed in the time of flight image in Fig. 7.12(top).

Adjusting the current ratio moves the trap in a left-right arc, closer to the lower current amplitude wire. Trap depth is necessarily lower as we turn down either wire to roughly half power, giving lower atom densities for the clouds moved roughly 50

$\mu\text{m}$  off-center, from between to above each participating wire in Fig. 7.12.

## 7.6 Lower Resonance Data

We measured trap frequencies and lifetimes initially near 8.5 MHz / 12.3 G and present them in Fig. 7.13 for supplementary comparison to the main findings. Similarities include the red/blue disparity, losing trapping just red ( $\delta \sim -1$  MHz) of the transition while trapping far blue of the resonance. The near-degeneracy of this case masks some of the non-degenerate structure seen in the 20 MHz data. We had initially intended to repeat this trapping experiment using a the 8.5 MHz range, matching the force experiment of Chap. 5, but VNA measurements of the chip (in Sec. 2.9) motivated moving the working frequency to a much flatter phase-response range.

## 7.7 Extra Phase Effects

Just as an alternating current in a finite-sized conductor will re-distribute density and phase within itself via the ‘skin effect’ (the focus of Chap. 8), driven currents in nearby wires will also re-distribute each other, which we refer to as the ‘proximity effect.’ This type of behavior was observed in our system, and required compensation from experimental insertion power and phase. Specifically, Fig. 7.6 uses the U-Z wires and required power re-balancing by about 1 dB to center the trap at the two different phases. However, Fig. 8.10 uses the two U-wires at low power and does not have any obvious left-right movement with phase, remaining balanced. For proper modeling, we must go beyond the finite-sized individual wire skin effect model used here, including proximity interactions and longitudinal effects.

In addition to this active proximity effect, a passive phase change comes from

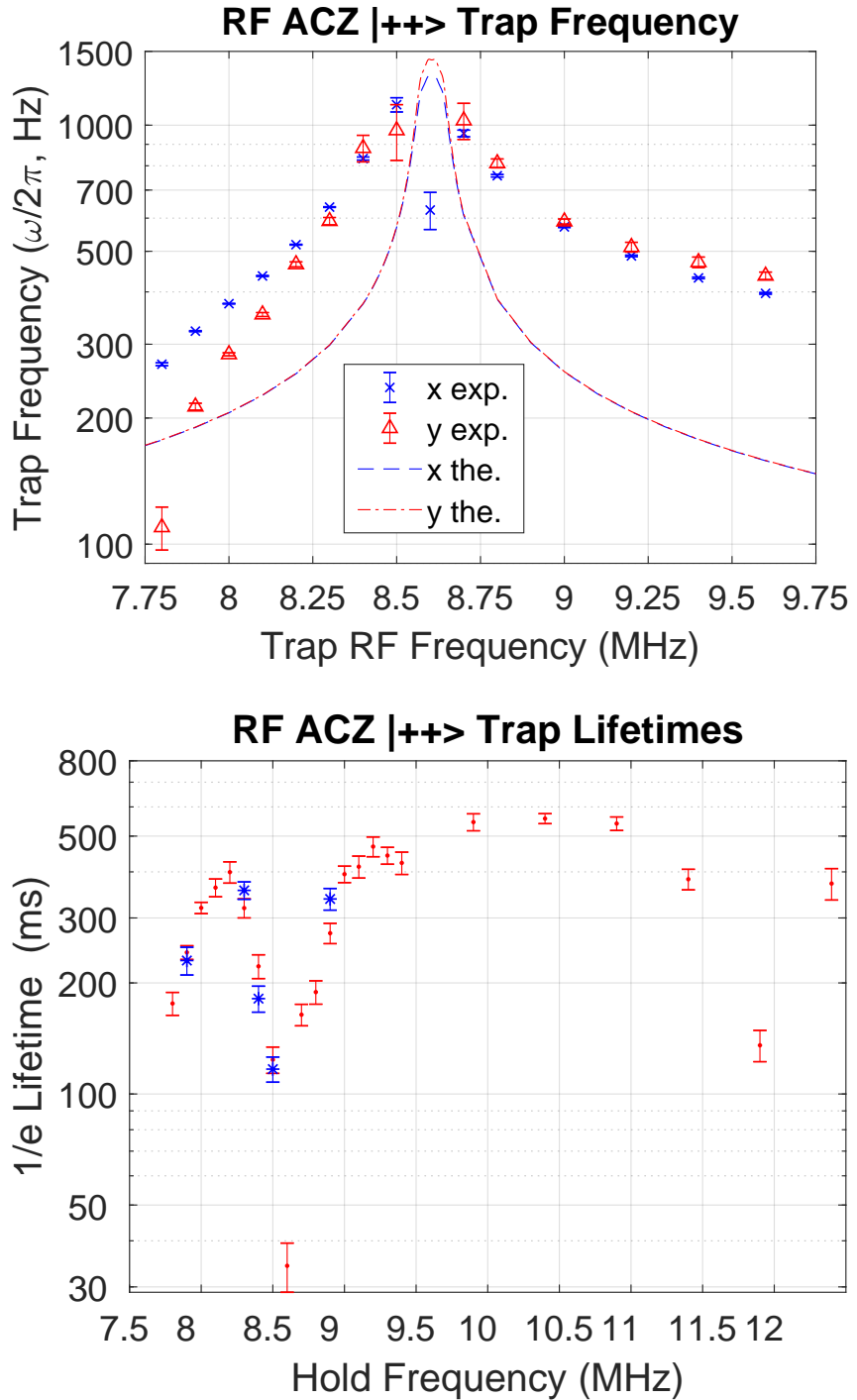


FIG. 7.13: AC Zeeman trap frequency (top) and lifetime (bottom) measurements, using 12.3 G, 8.5 MHz resonance. The theory curve matches mean parameters in Fig. 7.8, although based on the frequency-dependent acceptance measurements in Fig. 2.14, we would expect higher current in each wire at 8.5 MHz compared to 20 MHz for the same power. Data taken for 400 mW power and unknown phase near  $-100^\circ$ . For the lifetime data, we also measure lifetimes for a significantly ( $2\times$ ) colder loading temperature (blue \*), which did not significantly alter measured lifetime.

a line impedance mismatch. Insertion from a  $50 \Omega$  feed line to an unbalanced ( $Z = R + iX \neq 50\Omega$ ) chip trace will cause a power loss and a phase delay for each line independently. Vector network analysis of each line suggest a fixed  $\approx 5^\circ$  difference, where the Z-wire has slightly more delay than the U-wire. In our system, we believe the signals are attached in opposite directions on the chip, providing an extra  $180^\circ$  of phase adjustment. Useful traps were formed using insertion phases near  $75^\circ$  and  $275^\circ$  for the  $F_+ = 2$  and  $F_- = 1$  traps, which produce effective phases nearly  $-100^\circ$  and  $+100^\circ$ , respectively, making  $175^\circ$  inserted into the effective  $0^\circ$  in our chip.

Additionally, across the 20 MHz range, there is a nearly linear impedance adjustment of  $-\frac{1}{2}^\circ/\text{MHz}$  in the Z wire with a mostly flat U response. We suspect this contributes to the red-blue asymmetry in trap frequencies measured in Figs. 7.1, 7.8 and 7.13. Namely, this extra phase adjustment brings the trap closer to the chip when blue of detuning, enhancing trapping, while for red detuning it moves away from the chip, weakening the trap. According to simulations, this few-degree phase effect is only a modest adjustment, but the proximity effect may amplify phase offsets, and other unknown atomic and experimental effects may contribute to this asymmetry.

Again, this uncertainty and frequency-shifting of phase does not prevent trapping, but makes it difficult to predict actual experimental parameters without empirical measurements and simulation. These effects were easily compensated for with injected phase and power control.

## 7.8 Conclusion

This chapter presented the primary findings of this thesis, demonstration of an AC Zeeman trap. We began with a brief review of the AC Zeeman physics from

Chap. 3, and trap generation from Chap. 6. We discussed the experimental details, and performed some low-power field observations as a preliminary step. We then measure trap frequencies, which we can compare against theory curves, as well as trap lifetimes, which we do not have a good model for currently. Each of these results displays a significant asymmetry, as we can trap atoms at very far positive detuning, but cannot hold atoms at a modest negative detuning. We also demonstrated three forms of evaporation (although phase-space-density improvements were modest), as well as a ‘throw-and-catch’ technique to trap the  $F_- = 1$  state. For completeness, we provide some low-frequency data, which also displays the detuning asymmetry, and end with a discussion of a partial cause of this issue, from phase insertion effects when using multiple traces.

# CHAPTER 8

## AC Skin Effect

This chapter reproduces a publication of ours [79]<sup>1</sup>, which was motivated by a desire to understand the magnetic near fields generated by a wide ‘lateral’ wire, knowing an alternating current will redistribute itself in amplitude and phase, and to see whether we could trust our electromagnetic simulation software, both commercial and hand-coded. In this chapter,  $\delta$  is not detuning, rather it represents the skin depth, a parameter that characterizes current curvature in planar and cylindrical cases.

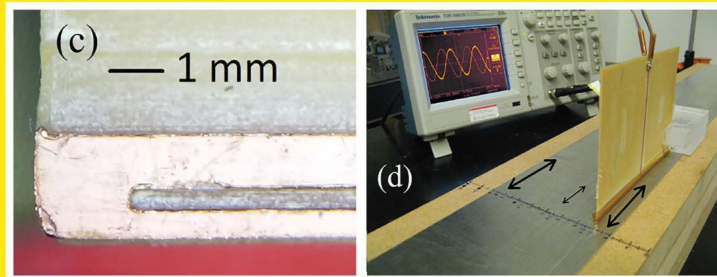
This project springs from one of Seth’s ideas, that one could probe the magnetic field just above a wide conductor as a proxy for the current just beneath the surface, a feature not afforded by round wires. This experiment became an undergraduate project by Anne Blackwell, who created the sensor and performed the experiment, and I was responsible for the computation, analysis, some data taking, and most of the text. We have used the ‘Silvester method’ [84] to generate the currents in every trap MATLAB simulation, unless explicitly using point currents. I am especially proud of the deep dive required for finding a numerical approximation

---

<sup>1</sup>Blackwell, A. E., Rotunno, A. P., & Aubin, S. (2020). Demonstration of the lateral AC skin effect using a pickup coil. American Journal of Physics, 88(8), 676-684.

# AMERICAN JOURNAL *of PHYSICS*

Volume 88, No. 8, August 2020



A PUBLICATION OF THE AMERICAN ASSOCIATION OF PHYSICS TEACHERS  
Available online—visit <http://aapt.org/ajp>

FIG. 8.1: The cover of the August 2020 issue of American Journal of Physics, featuring our submission.

for the counterflow effect threshold (Sec. 8.7.2). I wanted to call this behavior the Batman effect because of how Fig. 8.8 looks, and now those words are in print.

A major conceptual result of this work is that the principle of similitude allows us to directly relate our table-top size and kHz frequencies into the atom chip version at microwave frequencies. We also emphasize the altering of phase across the wire, due to its effect on our particular application.

One comment I want to make related to this, but beyond the paper's scope is about calculating proximity effects between multiple arbitrary wires. I believe we can get really good simulations of multiple parallel wires when the currents are in-phase, or out-of-phase as with the image, but I am hesitant as to apply this same technique to arbitrary phases between wires. We have observed experimentally and in FEKO that there is some insertion phase-dependent power and further phase adjustments, which we term the 'proximity effect.' In general, the signal which leads goes on to lead further in phase while losing effective current, and the lagging signal lags further while gaining current. Additionally, this phase slip effect appears to vary longitudinally, meaning a 2-D simulation might be incapable of capturing the full effect.

When attempting to calculate the proximity effect with the Silvester method, a simple complex rotation on the setup might do the trick, although whether that should be expressed in the voltage, or the resistance, is not clear to me. I have toyed around with it, and it might be that simple, but it would be great to know definitively the proper method of encoding arbitrary phases, augmenting Silvester's approach to create a convenient general solution for N wires and their images.

Here is our publication on the AC skin effect, which made the cover of that month's American Journal of Physics, shown in Fig. 8.1.

## 8.1 Abstract

We present a simple demonstration of the skin effect by observing the current distribution in a wide rectangular strip conductor driven at frequencies in the 0.25-5 kHz range. We measure the amplitude and phase of the current distribution as a function of transverse position and find that they agree well with numerical simulations: The current hugs the edges of the strip conductor with a significant variation in phase across the width. The experimental setup is simple, uses standard undergraduate physics teaching laboratory equipment, and is easy to implement as a short in-class demonstration. Our study is motivated by modeling AC magnetic near fields in the vicinity of an atom chip wire.

## 8.2 Introduction

While direct current (DC) flows uniformly through a conductor, a time-varying or alternating current (AC) travels preferentially along the skin of a conductor. Interactions between the alternating current, the associated magnetic field, and the induced electric field create transverse spatial variations in both the current's amplitude and phase. This behavior defines the skin effect, which has been known since the late 19<sup>th</sup> century [85, 86, 87, 88, 89, 90, 91, 92], and the current distribution has been characterized for various wire profiles. However, with the exception of a cylindrical conductor of circular cross section (i.e. round wire), numerical approaches [93, 94, 95, 96, 97, 98, 99, 100, 101, 102, 103, 104, 105] and approximations [106, 107, 108, 109, 110, 111] are required to determine the current distribution.

Primary interest in the skin effect concerns the increase in AC resistance due to the effective decrease in wire cross sectional area. For example, a 1 mm diameter copper wire with a 1 GHz AC current increases its resistance to about 2.6  $\Omega/\text{m}$ ,

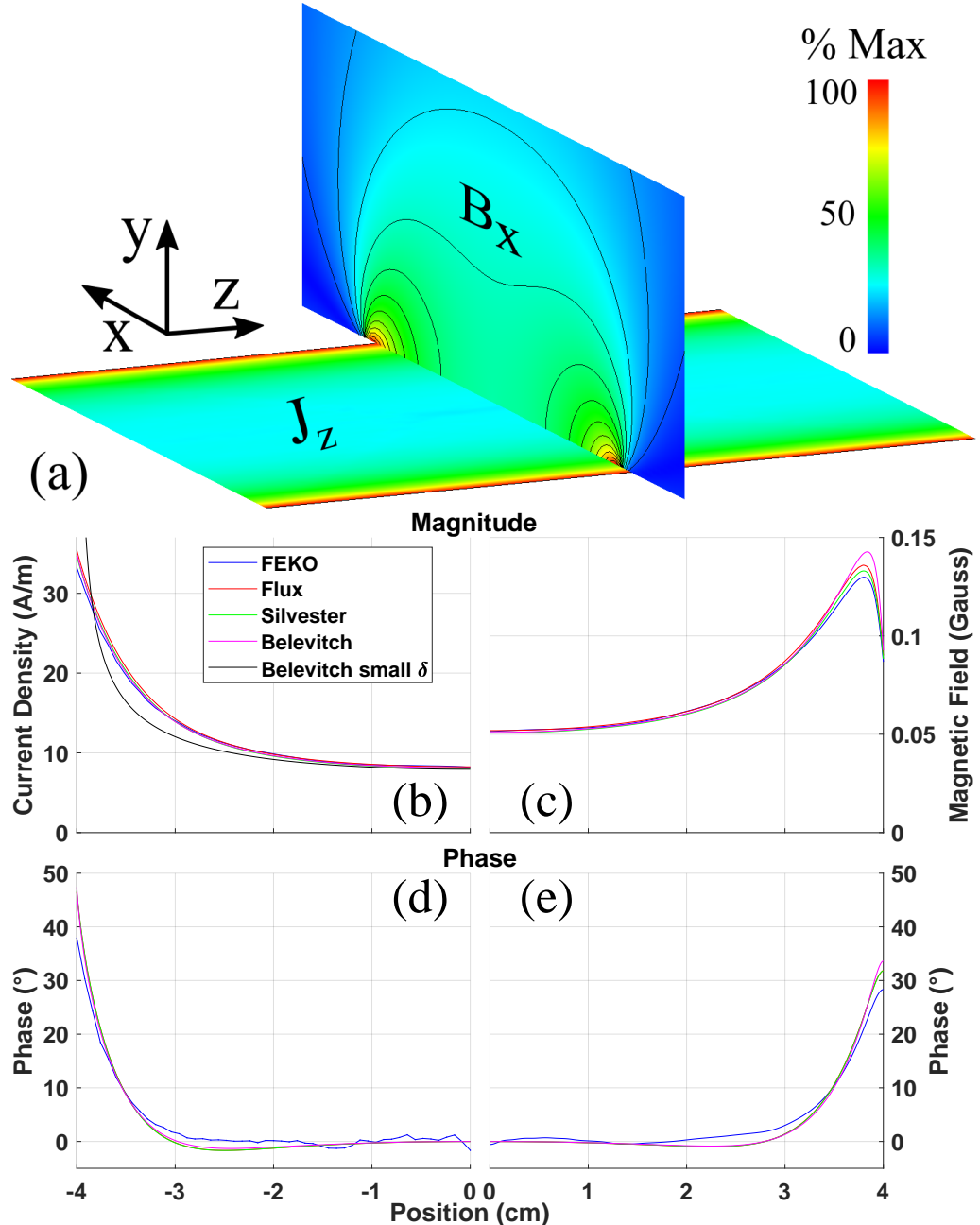


FIG. 8.2: Skin effect simulations for a 5 kHz AC current of 1 A magnitude in our strip conductor (80.1 mm wide, 0.63 mm thick, and conductivity  $\sigma = 2.50 \times 10^7 (\Omega \cdot m)^{-1}$ ). (a) False color maps of the current density  $J$  in the strip and magnetic field component  $B_x$  above it (FEKO simulation). (b) Plots of current density magnitude  $|J|$  versus position from edge to middle of the strip for four simulation methods (see Sec. 8.3.2). The black curve is an analytic prediction in the 1D limit at high frequency. (c) Plots of magnetic field magnitude  $|B_x|$  versus position at a height of 0.8 mm for three simulation methods. (d,e) Plots of relative phases versus position for  $J$  and  $B_x$ .

a factor of 120 compared to DC, while decreasing the self-inductance by a similar factor.<sup>2</sup> At high frequencies, braided and Litz wire can help mitigate the skin effect, and printed circuit board designs must account for this effect. To this end, much of the research on this topic predicts and measures bulk observables, such as AC resistance as a function of frequency [94, 97, 105] or wave penetration depth [113].

In contrast, our interest in the skin effect concerns the associated AC magnetic field in the vicinity of a ribbon-like wire. In our research on AC Zeeman forces, we manipulate ultracold atoms with radio-frequency (RF) magnetic near fields generated by currents in the microfabricated 100  $\mu\text{m}$  wide traces of an atom chip [44, 81]. While probing such  $\mu\text{m}$ -scale RF fields is challenging [114], basic near field predictions involving the skin effect can be tested experimentally with lower frequencies at the mm-scale.

In a ribbon-like conductor, with a rectangular cross section that is much wider than its thickness, the skin effect tends to concentrate the current along the two edges of the ribbon (see Fig. 8.2(a)) and is referred to as the *lateral skin effect*. Notably, the current density does not hug the edges of the ribbon as tightly as in a bulk conductor (the traditional skin depth), and does not vary appreciably over the thickness of the ribbon.

In this paper, we present a simple method for probing the current distribution and phase due to the skin effect in a ribbon-like conductor. An amplified pickup coil detects the current distribution in the conductor by measuring the amplitude and phase of the AC magnetic near field just above the conductor. Our experimental scheme requires only standard lab equipment and is sufficiently simple for implementation as a classroom demonstration or as an undergraduate lab exercise. Also, we compare our measurements with predictions from several numerical models

---

<sup>2</sup>This calculation was done using formulas from the paper of G.S. Smith [112]. The formulas are the following (they are approximations for the high frequency limit, i.e. wire radius  $\gg$  skin depth):  $\frac{R_{AC}}{R_{DC}} = \frac{1}{2} \frac{r}{\delta}$ ,  $\frac{L_{AC}}{L_{DC}} = 1/(0.5 * \frac{r}{\delta})$ , with  $\delta = \sqrt{2/\sigma\mu\omega}$ .

of varying complexity and dimensionality. Fig. 8.2 shows the current density and magnetic near field predictions for four models, which largely agree with each other.

Our experimental method works best for ribbon-like conductors, which generate a one-dimensional spatial variation of the current density, so long as the skin depth is larger than the conductor thickness. Our ribbon conductor dimensions fall in this lateral skin effect regime for all of the frequencies that we consider. Our method is reminiscent of the one developed by Tsuboi and Kunisue [115] for analyzing magnetic fields produced by large AC currents in thin conducting plates.<sup>3</sup> Recent work has measured the skin effect in a stripline transmission line [116] and in a rectangular conductor at high current [117, 118]. In contrast, Ampère’s law and cylindrical symmetry guarantee that for a round wire the external magnetic field is unaffected by the radial current distribution within it. In this case, direct measurements of the current density redistribution due to the skin effect must use an internal probe, such as neutrons [119], NMR [120], a liquid [121] or a segmented [113] conductor, to name a few.

This paper is structured as follows: In section 8.3, we present the relevant electromagnetic theory and numerical approaches, followed by details of the experimental method in section 8.4. We present and compare our measurements of the current and magnetic field distributions with simulations in section 8.5 and conclude in section 8.6. The appendices provide additional details on the calibration procedure and also review analytic expressions for the skin effect and its phase distribution.

---

<sup>3</sup>We learned of this work after submission of the manuscript.

## 8.3 Theory

A straightforward classroom exercise is to take the curl of Faraday's law, combined with Ampère's law and Ohm's law, to arrive at

$$\nabla^2 \vec{J} = \sigma\mu \frac{d\vec{J}}{dt} = i\sigma\mu\omega \vec{J} = \frac{2i}{\delta^2} \vec{J} \quad (8.1)$$

where  $\vec{J} = J(x, y)e^{i\omega t}\hat{z}$  is the longitudinally directed complex current density at angular frequency  $\omega$ , in a conductor of conductivity  $\sigma$  and magnetic permeability  $\mu$ . The equation can be written in terms of a single constant, the skin depth  $\delta = \sqrt{2/\sigma\mu\omega}$ , which sets a natural length scale for variations in current density. The diffusion relation in Eq. 8.1 gives two gifts: First, it directly shows that faster changes in the driven current create stronger spatial curvature of this current over distances of order  $\delta$ . Second, the sole dependence of Eq. 8.1 on the skin depth  $\delta$  gives rise to the principle of similitude [105, 122], which states that the current distribution in two different wires will be the same if they have the same dimensions in units of  $\delta$ . This allows for scaling of solutions to different sizes and frequencies. For example, an 8 cm wide pure aluminum strip ( $\sigma = 3.77 \times 10^7 (\Omega \cdot \text{m})^{-1}$ ) [123] with a thickness of 0.63 mm at 2.6 kHz ( $\delta = 1.6$  mm) will have the same current distribution when re-scaled as a 40  $\mu\text{m}$  wide copper trace with a thickness of 0.32  $\mu\text{m}$  at 6.8 GHz ( $\delta = 0.8$   $\mu\text{m}$ ).

The round wire admits the only known exact analytic solution to Eq. 8.1 in a finite volume [112].<sup>4</sup> The round wire solution for the current density is given by  $J(r) = C\mathcal{J}_0(\frac{(1-i)r}{\delta})$ , valid at all frequencies, where  $r$  is the radial coordinate,  $\mathcal{J}_0(r)$  is the Bessel function of the first kind, and  $C$  is a normalization constant. In the high frequency limit ( $\delta \ll R$  for radius  $R$ ), this solution reduces to  $J(r) \simeq$

---

<sup>4</sup>The infinite half-space conductor can also be solved analytically [124]

$J_{max}e^{-(1+i)\frac{R-r}{\delta}}$  for  $r \simeq R$ , with  $J_{max}$  the current density at the edge of wire. Notably, this example shows that the phase of the current distribution also varies with  $r$  across the conductor, a fact that is often overlooked in discussions of the skin effect. Specifically, the phase wraps by  $2\pi$  for every  $\delta$  of penetration into the wire as its amplitude decreases by  $1/e$ . N.B.: At a given time, the current flow is not all in the same direction.

A ribbon-like conductor, with thickness  $2T$  much smaller than the width  $2W$ , is in the *lateral skin effect* regime for  $\delta \gg T$  [107]. In this case, the current distribution falls off from the two ribbon edges to a finite value in the middle with a  $1/e$  characteristic decay length  $\lambda$  that is larger than the skin depth  $\delta$ . While the fall off does not have a closed form, at low frequency ( $\delta^2 > WT$ ), it is roughly polynomial, while at high frequency ( $\delta^2 < WT$ ) it is more exponential-like. In the very high frequency limit ( $\delta^2 \ll WT$ ), the lateral current distribution has an analytic form (see Appendix 8.7.1), which is plotted in black in Fig. 8.2(b). Notably, the phase also varies across the conductor width, but less so than in the round wire case (see Appendix 8.7.2 and Fig. 8.10).

We have provided a supplemental online animation which illustrates the time-evolving nature of the current density's phase and amplitude across a wide range of frequencies. The lateral current density is shown to advance by rotating around the position axis in complex space (as in Fig. 8.3(e)). The instantaneous amplitude is projected onto the real axis to show the measured value. Generally, the phase (and current) at the edges leads the current at the center of the strip. At very high frequencies, the total current lags  $90^\circ$  behind the near-DC phase (and current).

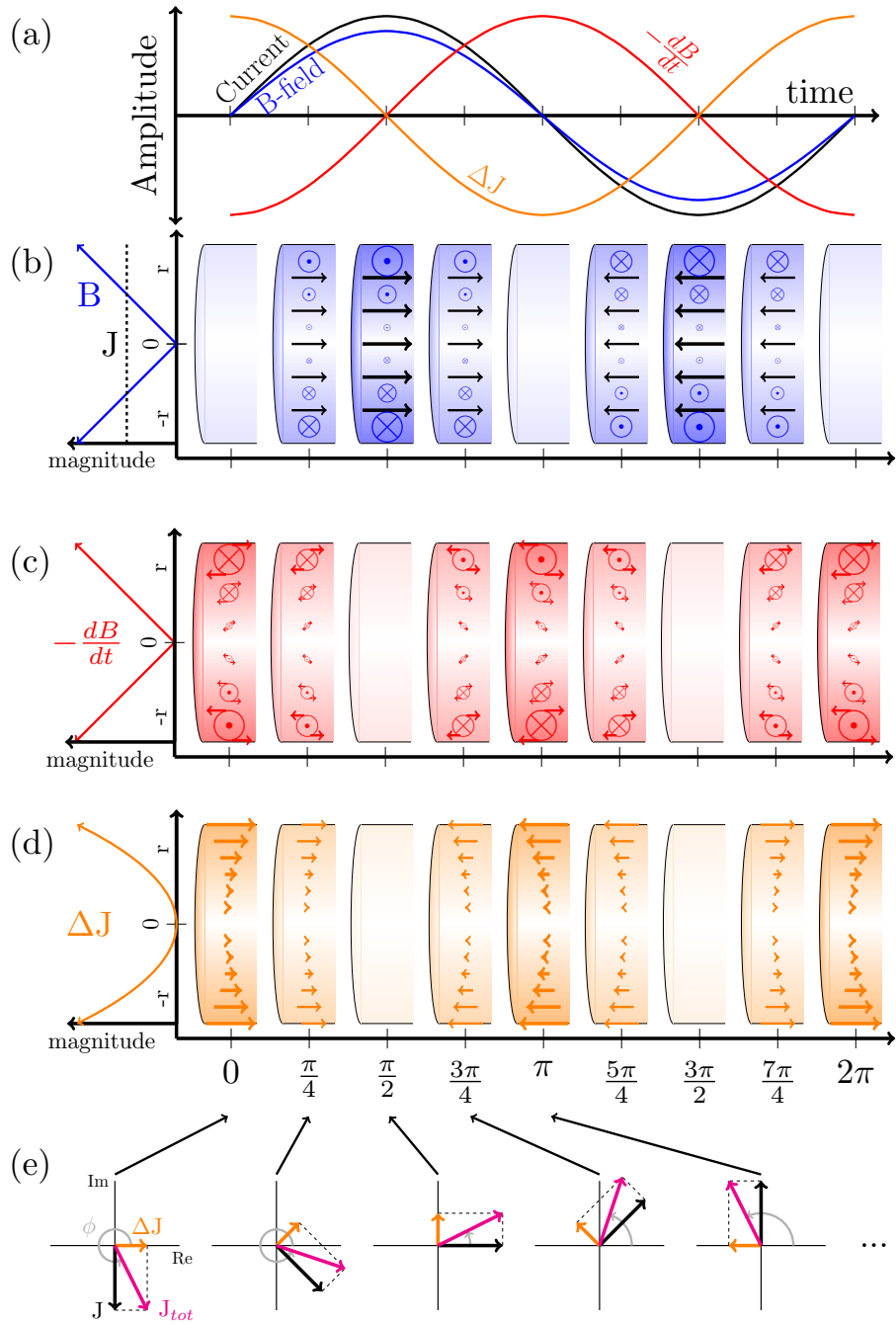


FIG. 8.3: Visual explanation of the AC skin effect at low frequency in a round wire.  
 (a) Plot versus time of the input current, associated quasi-static magnetic field  $B$ , and the first order contributions to the induced EMF and eddy current  $\Delta J$ . (b) Quasi-static magnetic field  $B$  (blue) due to a uniform AC input current density  $J$  (black arrows) versus oscillation phase. (c) First order  $-dB/dt$  contribution (red) to the induced EMF from (b) versus phase. (d) Induced eddy current density  $\Delta J$  (orange arrows) from EMF in (c). (e) Complex-plane representation of the uniform input current density  $J$ , the first order eddy current density  $\Delta J$  contribution from (d) at fixed  $x$ , and resulting total current density  $J_{tot}$  (magenta) at various phases.

### 8.3.1 Pedagogical Explanation

We present a pedagogical explanation for the AC skin effect in Fig. 8.3 by expanding on an approach given by Zangwill [125]. The reason that an AC current hugs the skin of a conductor is because the driving current creates a magnetic field which is largest at the edge, which in turn generates opposing eddy currents. The net result is a current distribution that is largest in amplitude at the skin, and out of phase with the source. To demonstrate further, we begin by considering a round wire (radius  $R$ ) driven by a low enough frequency AC current such that the skin effect is a small perturbation on the uniform current distribution (i.e.  $\delta \gg R$ ). We can use the following steps illustrated in Fig. 8.3 to calculate the first order correction to a uniform input current distribution  $J$  with a low frequency  $\omega$ .

- (a) shows the sinusoidal time dependence of the uniform input AC current, its associated magnetic field  $B$ , the first order contribution to the induced electric field  $\vec{\nabla} \times \vec{E}_{ind} = -d\vec{B}/dt$ , and the resulting eddy current  $\Delta J = \sigma E_{ind}$ .
- (b) shows the uniform input AC current density  $J = J_0 \sin(\omega t)$  and its in-phase quasi-static magnetic field  $B = B_0 \sin(\omega t)$ . The field  $B_0 = \mu J_0 r / 2$  increases linearly outwards from the center.
- (c) shows the spatial dependence of  $-dB/dt = -\omega B_0 \cos(\omega t)$ , which then generates an induced electric field  $E_{ind}$  (first order) via Faraday's law.
- (d) shows the eddy current distribution  $\Delta J$  generated by  $E_{ind} = \mu J_0 \omega (r^2/4) \cos(\omega t)$  along the wire axis. Applying Ohm's law, we obtain the first order correction to the current density  $\Delta J = (J_0/2)(r/\delta)^2 \cos(\omega t)$ , which increases quadratically from the wire center.
- (e) shows the resulting total current density  $J_{tot}$  from the quadrature sum of the input current  $J$  and the first order correction  $\Delta J$ .

Thus, to first order the AC skin effect results in a current density  $J_{tot}$  that varies radially in *magnitude* as  $1 + (r/\delta)^4/8$  and radially in *phase* as well. As the drive frequency  $\omega$  is increased, higher order contributions in  $(r/\delta)^2$  must be included. The physics is similar for a strip conductor, however the computation of  $J_{tot}$  is more involved.

### 8.3.2 Simulations

Numerical approaches are required for calculations of  $J_{tot} = J(x, y)$  with an arbitrary conductor profile, and often begin by converting Eq. 8.1 into an integral equation [84],

$$J(x, y) = J_{DC} - \frac{i}{\pi\delta^2} \iint_A J(\tilde{x}, \tilde{y}) \ln \sqrt{(x - \tilde{x})^2 + (y - \tilde{y})^2} d\tilde{x}d\tilde{y} \quad (8.2)$$

where the  $J_{DC}$  term is the uniform current density expected for a DC current. The second term generates the skin effect by which the strip's self-inductance redistributes the current in the wire.

We compute  $J(x)$  using four different methods and then calculate the corresponding  $x$ -component of the magnetic near-field  $B_x(x, y_h)$ , evaluated at the effective height  $y_h$  of our pickup coil. Models which consider vertical extent of  $J$  show less than a part in  $10^3$  variation vertically for our parameters, and this extent is averaged over for  $J(x)$  values.

We use two commercial electromagnetic solvers to compute  $J(x)$  and  $B(x, y_h)$ . FEKO uses a method of moments (MoM) approach to solve a finite-length model of our strip, giving the only longitudinal current description, but the current sheet model gives no vertical information. FLUX uses a finite element method (FEM) to solve a 2D transverse cross section of the strip, without longitudinal information.<sup>5</sup>

We have also directly implemented two numerical algorithms that model an

---

<sup>5</sup>Both FEKO and FLUX are distributed by Altair Inc.

infinite length strip in the transverse plane. The first algorithm is by P. Silvester [84] and solves Eq. 8.2 by decomposing the strip cross section onto a Cartesian grid of square  $dxdy$  elements, and calculating the mutual induction between them. The second algorithm by V. Belevitch et al. [111] uses a flat line of current expanded in even polynomial powers to solve the same equation (See Appendix 8.7.1 for a summary of this method).

We find that the four numerical models give comparable results for phase and amplitude of the current density  $J(x)$  and magnetic field  $B(x)$  (see Fig. 8.2). Three of the models give very similar results, but we find that the FEKO phase results deviate somewhat from the others and depend on the discretization mesh geometry.<sup>6</sup> We note that the phase offsets of each model in Fig. 8.2(d, e) have been adjusted so that the phase over the center portion of the strip corresponds to  $0^\circ$ . In the case of FEKO, the small contribution to the AC magnetic field from the supply wires is subtracted out in Fig. 8.2(c, e).

## 8.4 Experimental Method

We measure the AC current distribution  $J(x)$  (in A/m) laterally across a thin aluminum strip via the AC magnetic near-field that it produces at the surface of the conductor. We use a lab-built pickup coil located just above the strip to sample the AC magnetic field via the voltage induced in the coil.

The basic experimental set-up (see Fig. 8.4(a) and (d)) consists of a thin strip of aluminum driven by a sinusoidal current source. The pickup coil is scanned transversely across the surface of the conducting strip, and its induced emf signal

---

<sup>6</sup>Older versions of FEKO (before 2019) appeared to use a pseudo-random arrangement of mesh elements, which led to overall continuous and comparable results. Newer versions use regions of aligned rows of uniform triangle mesh elements, and we observe deviations, such as those evident in the amplitude and phase at the center of the strip in Fig. 8.2, occurring at the borders between these uniform regions.

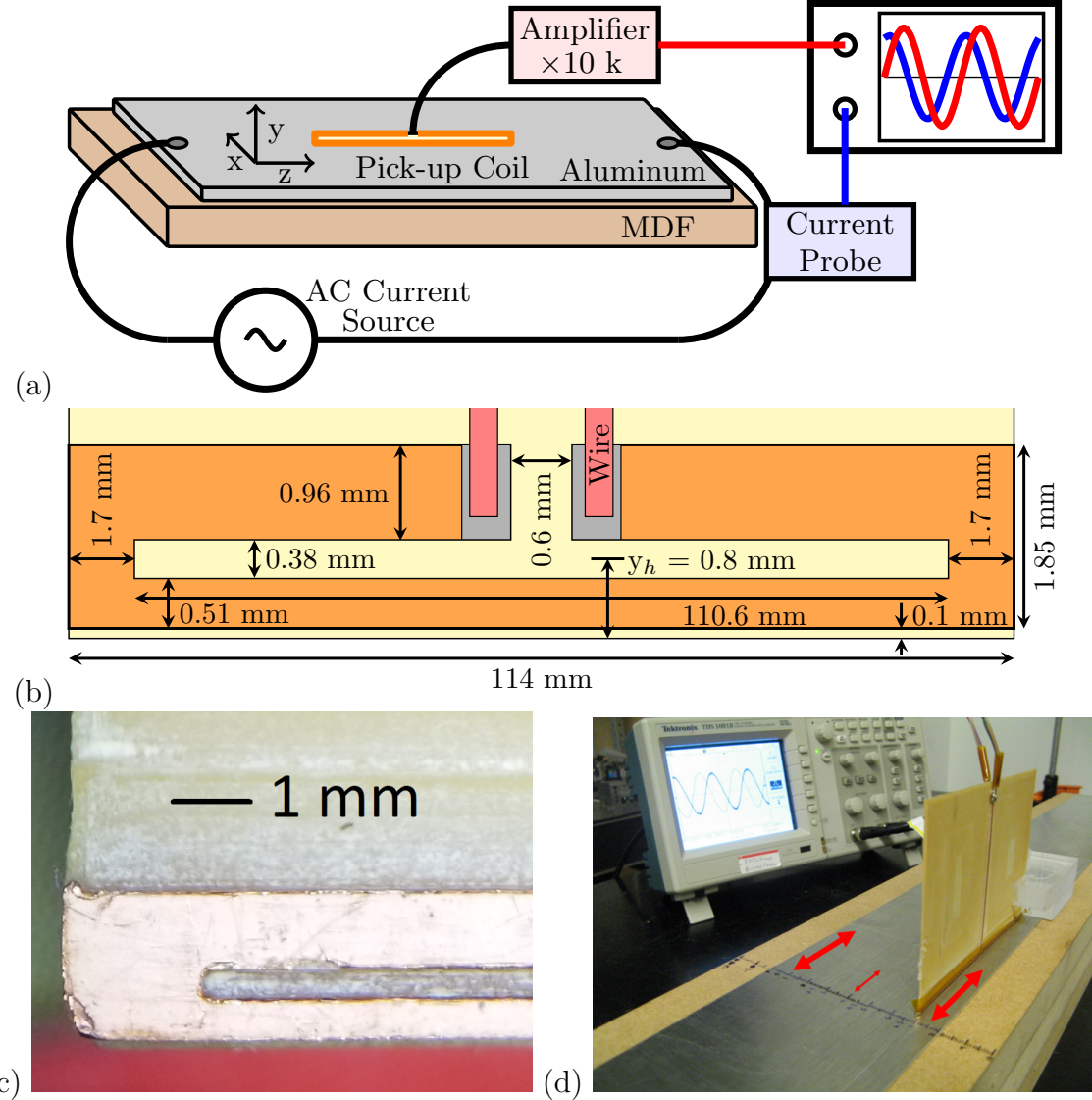


FIG. 8.4: Experimental system. (a) Experimental setup showing the aluminum strip, AC current source, Hall effect current sensor, and the pickup coil, which is scanned in the  $x$ -direction. Changes in amplitude and phase between the amplified  $V_{sig}$  and the total current can be seen by plotting both on an oscilloscope. (b) Schematic diagram of the pickup coil. All dimensions have a nominal error of 0.05 mm. (c) The end portion of the pickup coil, showing the milled center channel and length scale. (d) A photo of the table-top set-up. Arrows (red) indicate current direction and magnitude. The pickup coil PCB is shown with two twisted-pair signal wires attached at the top: final measurements were conducted with only one twisted-pair, which was connected directly onto the pickup coil loop for better fidelity and lower noise.

is sent to a battery-powered amplifier (gain  $\sim 10^4$  with 10 kHz bandwidth, based on two OP27E op-amp gain stages). The output of the amplifier is then displayed on an oscilloscope, along with the signal from an isolated Hall sensor (LEM model HX 10-NP) that monitors the total current through the strip. A series ammeter provides an additional rms measurement of the AC current.

The aluminum alloy strip has width  $2W = 80.1(1)$  mm and thickness  $2T = 0.63(1)$  mm. We measure its DC conductivity to be  $\sigma = 2.50(6) \times 10^7 (\Omega \cdot \text{m})^{-1}$  with a four-point measurement. The aluminum strip is mounted on medium density fiberboard (MDF) with double-sided tape, and electrical connections soldered on washers are bolted to the strip with through holes at its two ends. The strip is about 0.9 m long, but could be much shorter, since the pickup coil measures very little variation in signal along the strip's length, except at the ends.

We direct an AC current with amplitude 1.85 A ( $1.3 \text{ A}_{\text{rms}}$ ) through the strip using a voltage controlled current source driven by the sinewave output of a function generator. At near-DC frequencies, the current density is essentially uniform at  $J_{DC} = 1.85 \text{ A}/8 \text{ cm} \approx 23.1 \frac{\text{A}}{\text{m}}$ , which corresponds to a surface magnetic field of  $B_{DC} \approx 0.145 \text{ G}$ . We use drive frequencies in the range of 0.25-5 kHz. Our current source (lab-built, based on a LM675 op-amp) operates up to 5 kHz, while below 250 Hz the small pickup coil signal is too noisy.

The amplified pickup coil is very sensitive to environmental noise, such as RF communication signals (e.g. Bluetooth, WiFi) and the 60 Hz noise (and associated harmonics) emanating from nearby electrical devices. We found that for low noise measurements, the overhead fluorescent lights and cellphones had to be turned off while taking data. Alternatively, in a noisy environment, directing the battery-powered amplifier signal to a lock-in amplifier could provide a cleaner signal.

Care was taken to route the AC current supply wires away from the pickup coil to minimize crosstalk. We suspect that the placement of these supply wires on

one side of the conductor may contribute to the slight asymmetry in the current distribution observed in Fig. 8.6.

### 8.4.1 Pickup coil

The pickup coil (Fig. 8.4(b–c)) consists of a machined, highly elongated rectangular copper loop of external dimensions 114 mm × 1.85 mm with an inner gap measuring 110.6(1) mm × 0.38(5) mm, centered at a height of 0.80(5) mm. The base for construction was a 114 mm × 79 mm double-sided copper-clad electronics prototyping circuit board (PCB). We initially used two loops on the front and back in series for higher sensitivity but switched to a single loop for improved spatial resolution. The PCB construction ensures that the pickup loop is flat in a plane, and that the two coil planes are parallel.

We machined the PCB into the pickup coil using a desktop CNC milling machine (Carvey, Inventable Inc.). Bulk copper removal was done with a regular end mill bit (1/8" fishtail upcut bit), while a specialized 0.1 mm diameter bit (P3.2501) was used for the regions directly adjacent to the wire loop and within it.

We note that alternative single-turn and multi-turn pickup coils based on wrapping a thin wire around a plastic card were effective at producing a signal. However, the signal amplitude showed a significant asymmetry when the coils were rotated 180° around the vertical  $y$ -axis. The PCB-based coil minimizes this asymmetry.

### 8.4.2 Measurement Theory

According to Faraday's law, the voltage induced in the pickup coil by the magnetic near-field  $\vec{B} = \vec{B}(x, y)e^{i\omega t}$  is given by

$$V_{coil} = -\frac{d}{dt}(\vec{A} \cdot \vec{B}) = -i\omega AB_x \quad (8.3)$$

where  $\vec{A} = A\hat{x}$  gives the effective area of the pickup coil. In order to relate current density  $J(x)$  to the induced pickup coil voltage  $V_{coil}$ , we note that  $\vec{B}(x, y)$  is given by the Biot-Savart integral in the quasi-static limit:

$$\vec{B}(x, y) = \frac{\mu_0}{2\pi} \int \frac{J(x')(-y\hat{x} + (x - x')\hat{y})}{(x - x')^2 + y^2} dx' \quad (8.4)$$

However, in the limit that the pickup coil is at the surface of the aluminum strip (i.e.  $y \rightarrow 0$ ), then  $\vec{B}(x) \simeq \mu_0 J(x)\hat{x}/2$  from Ampère's law for  $|y| \ll \delta$ . Figure 8.6 shows that the current distribution  $J(x)$  and the horizontal component  $B_x(x)$ , less than a millimeter from the surface, are proportional to each other (by  $\frac{\mu_0}{2}$ ) near the center of the conductor, but deviate from each other at the edges, as shown in Fig. 8.5.

Therefore, across the middle of the conductor, we have to a good approximation

$$V_{coil}(x) = -i\omega AB_x(x) \simeq -i\omega A \frac{\mu_0}{2} J(x) \quad (8.5)$$

Since we measure an amplified signal  $V_{sig} \approx V_{coil} \times 10^4$ , calibrations relating  $V_{sig}$  to  $B_x$  and  $J$  are required.

### 8.4.3 Calibration

We used a two-part calibration procedure. First, the frequency-dependent gain of the coil-amplifier system was examined using the pickup coil to measure the magnetic field near an aluminum rod of circular cross section. For a known current in the rod, the drop in signal at higher frequencies can be attributed to the bandwidth of the coil-amplifier system, independent of the skin effect in the rod. Second, we measure the field above the rectangular strip at a low frequency (250 Hz), where the current is nearly evenly distributed. Averaging over the middle region of a

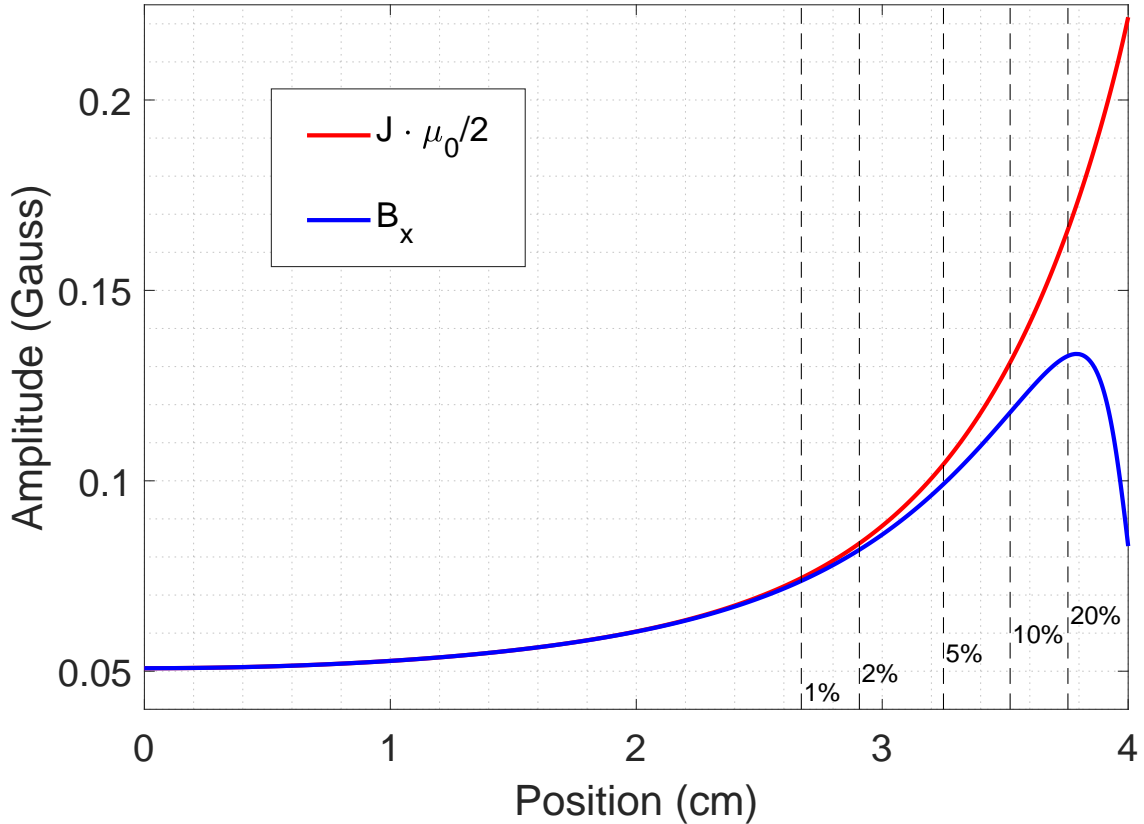


FIG. 8.5: Plot of the magnetic near field  $B_x$  (blue) and current density  $J$  (red) multiplied by  $\mu_0/2$  to demonstrate the close relationship between the two quantities. Values are for 1 A magnitude at 5 kHz, where  $B_x$  is taken at  $y_h = 0.8$  mm. Dashed vertical lines indicate the relative magnitude difference between the two values. We see excellent agreement in the central region, with less than 1% deviation. The difference grows towards the edges, where it exceeds 20%. The relative phases of  $J$  and  $B_x$  (not shown) have similar agreement, within  $\approx 1^\circ$  across the center, and diverging to about  $15^\circ$  at the edges.

known current density allows us to relate the amplified voltage  $V_{sig}$  to the known average current density and the surface magnetic field strength. Measurements of  $V_{sig}$  are divided by the linear  $\omega$  scaling, corrected for frequency dependent amplifier gain, and multiplied by the voltage-to-J and voltage-to-B factors to produce real values of  $J$  and  $B_x$  for the data in Figs. 8.6 and 8.7. The full calibration procedure is detailed in Appendix 8.7.3.

Phases are measured using the time delay between the zero crossings of the Hall current sensor and  $V_{sig}$ . Phase is presented relative to the  $x = 0$  center phase ( $\equiv 0^\circ$ ), since pickup ( $-90^\circ$ ), inversion ( $180^\circ$ ), and bandwidth (unique to frequency) were not studied with sufficient precision.

## 8.5 Results

The main results of this paper are shown in Figs. 8.6 and 8.8, where we plot the amplitude and phase, respectively, of the pickup coil signal versus transverse position  $x$ . The amplitude measurements in Fig. 8.6 clearly show the AC skin effect: at high frequency (5 kHz) the current is highest at the edges of the conducting strip, while at a much lower frequency (250 Hz), the current density is essentially uniform. We use two vertical axes in Fig. 8.6 to show the surface magnetic field  $B_x(x)$  (left) and the current density  $J(x)$  (right) that we convert from the pickup coil signal based on our calibration procedure (see Sec. 8.4.2 and appendix 8.7.3). We have also plotted the theoretical expectations for the current density (solid) and surface magnetic field (dashed), and find good agreement with the data in the center portion of the strip. For completeness, we also present all of our measured data in Fig. 8.7. At the edges of the strip, the data is lower than the theoretical expectation, possibly due to high field curvature, or misalignment of the coil in a region with a significant  $B_y$  component.

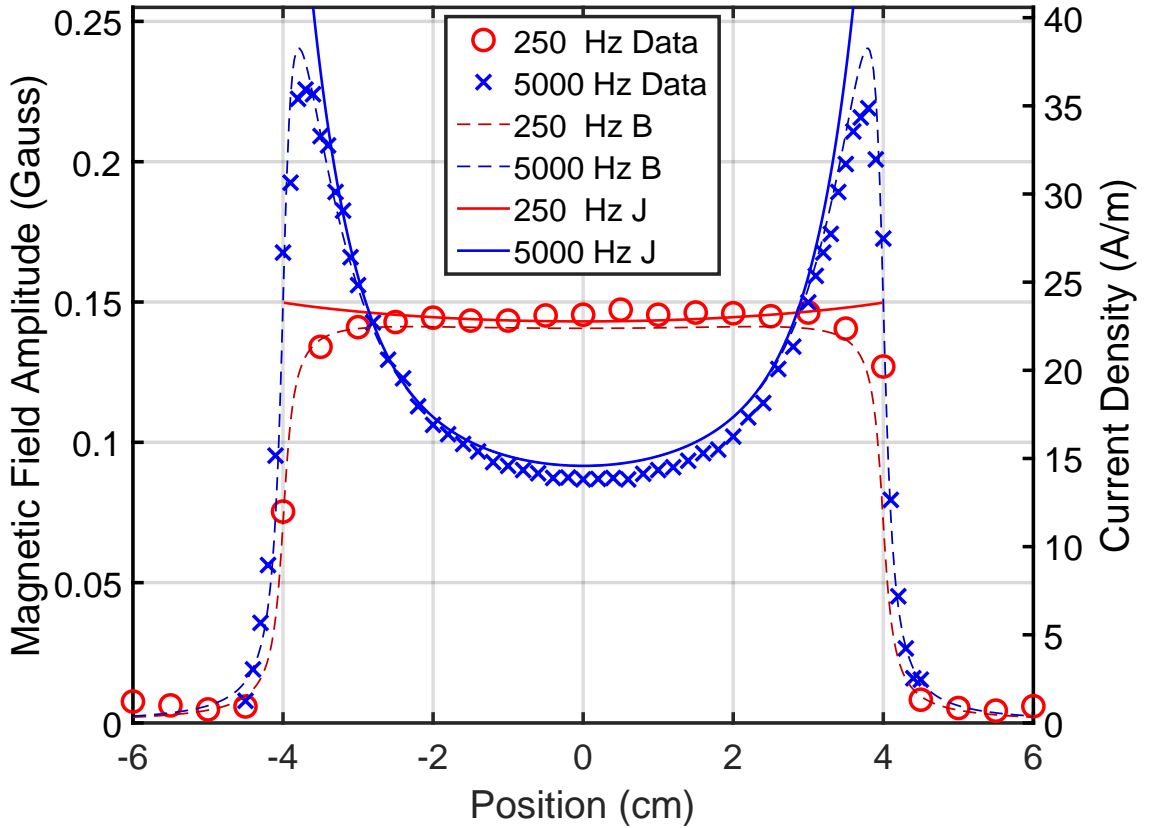


FIG. 8.6: Pickup coil measurements versus transverse position at 250 Hz (red circles) and 5 kHz (blue crosses) for 1.3 A rms of current. The pickup coil measurements are given in terms of the calibrated surface magnetic field  $B_x$  (left axis) and calibrated current density  $J$  (right axis). The theoretical current density predictions (solid lines) and the surface magnetic field  $B_x$  predictions (dashed lines) at a detector of height  $y_h = 0.8$  mm are shown for the Silvester numerical method [84] without any free parameters, using our conductor width 80.1 mm, height 0.63 mm, and conductivity  $\sigma = 2.50 \times 10^7 (\Omega \cdot \text{m})^{-1}$ . Theoretical current density values reach 62.3 A/m at the edge. Error bars are smaller than the symbol size and are omitted.

Freq (Hz)	$\delta$ (mm)	$WT/\delta^2$	$\lambda_J/\delta$	$\lambda_{B_{th}}/\delta$	$\lambda_{B_{exp}}/\delta$
250	6.37	0.31	2.3	1.8	[no fit]
500	4.50	0.62	3.2	3.3	2.9 (1.3)
1000	3.18	1.25	4.4	4.8	4.8 (0.3)
2000	2.25	2.49	5.2	6.0	5.6 (0.5)
3000	1.84	3.74	5.1	6.3	5.5 (0.9)
4000	1.59	4.98	4.8	6.3	5.8 (1.0)
5000	1.42	6.23	4.6	6.3	7.0 (1.1)

TABLE 8.1: Comparison of the decay constant  $\lambda$ , i.e. the lateral skin “width,” for theory and experiment in units of the skin depth  $\delta$  for data in Fig. 8.7. The theoretical values for the current density and surface magnetic field (at the probe) are given by  $\lambda_J$  and  $\lambda_{B_{th}}$  respectively. The experimental value for the surface magnetic field is given by  $\lambda_{B_{exp}}$ , with one standard deviation given in parentheses.

The amplitude of the current density and associated surface magnetic field follow a roughly exponential fall off (with an offset) from the edges towards the middle of the strip. We define the characteristic decay constant  $\lambda$  as the distance from the maximum magnitude position to the position where the magnitude falls to  $1/e$  above the minimum value at the center. Table 8.1 shows  $\lambda$  for the data at all the frequencies shown in Fig. 8.7. The theoretical values for the current density and surface magnetic field,  $\lambda_J$  and  $\lambda_{B_{th}}$ , are extracted from numerical simulations (Silvester method [84] for Table 8.1). For interpolation of the data, both a fourth order polynomial and an exponential function yield the same  $1/e$  values for  $\lambda_{B_{exp}}$ . We note that the fall off constant  $\lambda$  is significantly larger than the skin depth  $\delta$ , as expected for the lateral skin effect regime. For example, across the few kHz region of our data, we find that  $\lambda \sim 5\delta$ . Generally,  $\lambda$  depends on the geometry of the strip, which we parameterize by  $WT/\delta^2$  [107].

In Fig. 8.8, we plot the phase of the pickup coil signal (relative to the  $x = 0$  phase) versus position  $x$  across the strip for a 5 kHz current. The data clearly show that the phase of the current density varies by more than  $30^\circ$  across the strip, in tandem with the magnitude. In other words, for short portions of the AC cycle, the current in the center is going in the opposite direction to the current on the edges of

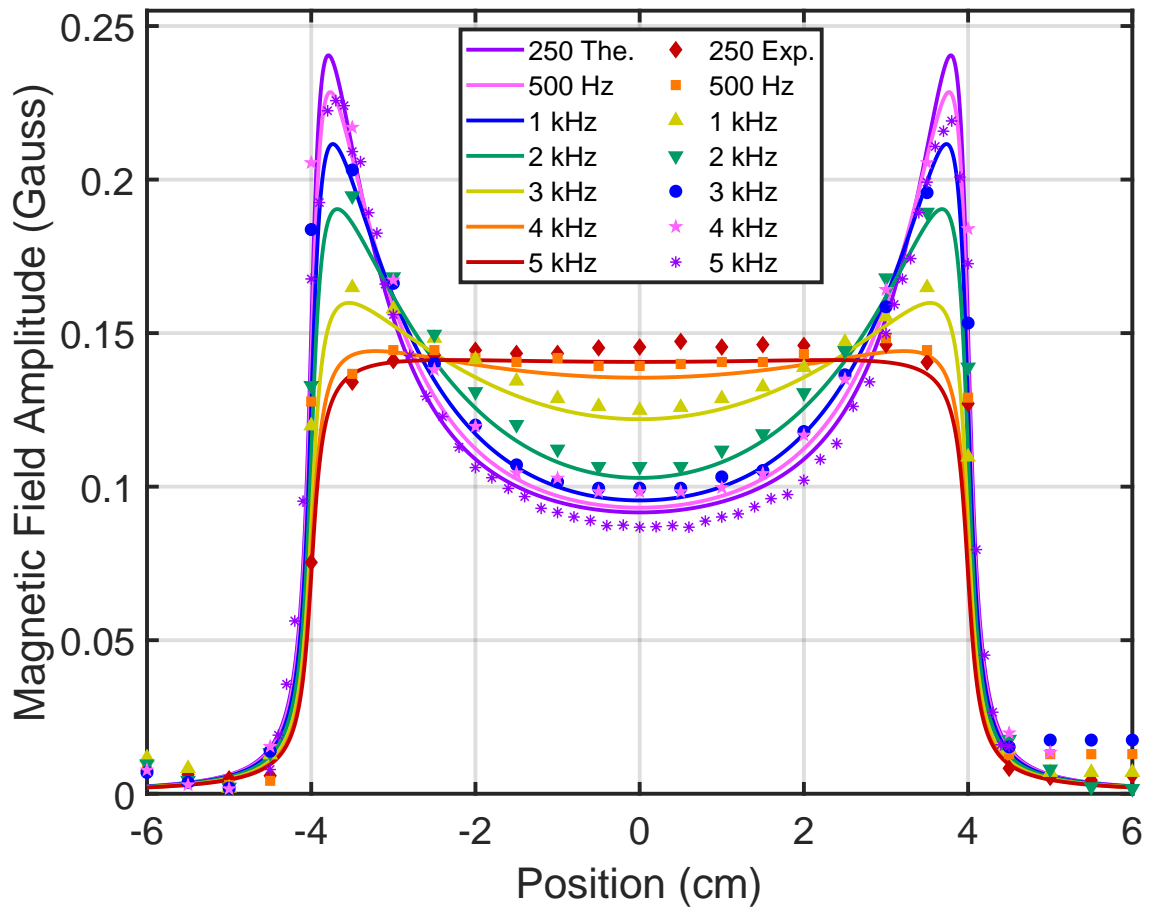


FIG. 8.7: Comparison of data and theory for all measured frequencies, 250 Hz through 5 kHz. Theory curves use the same parameters as Fig. 8.6.

the strip. The theory curve for the phase agrees reasonably well with the data over the breadth of the strip. Past the strip edges, the overall pickup coil signal is weaker, and the data deviates from theory, possibly due to interference in the pickup coil from other parts of the apparatus. Furthermore, in contrast with the magnitude, the phase across the conductor, when plotted, displays a modest “bump” at the center of the strip. This non-monotonic behavior means that for brief moments in the cycle, the current at the center and along the edges of the strip are going in the same direction, but the current between these regions is going in the opposite direction. This counterflow behavior is examined in detail in Appendix 8.7.2.

## 8.6 Conclusion

We have directly observed the AC skin effect at kHz frequencies in a rectangular aluminum strip. We have shown experimentally that the current increasingly hugs the edges of the strip as the frequency increases, and that the phase of the current density varies significantly across the strip. We have calculated the theoretical distribution of the current across the strip by four different methods and find good agreement between these and the data, with modest deviations at the edge.

Conveniently, our simple experimental setup is well suited to an in-class demonstration. The setup requires standard laboratory equipment (analog controlled current source, function generator, op-amp-based amplifier, current sensor, and oscilloscope) and a lab-built elongated pickup coil. A possible upgrade to the pickup coil is to use two perpendicular elongated coils so that  $B_x$  and  $B_y$  can be measured simultaneously. Such a pickup coil would provide more information when probing the edges of the strip, as well as the circular polarization in the case of phased currents in multiple strips.

This kHz-level work is a stepping stone towards accurate engineering of GHz-

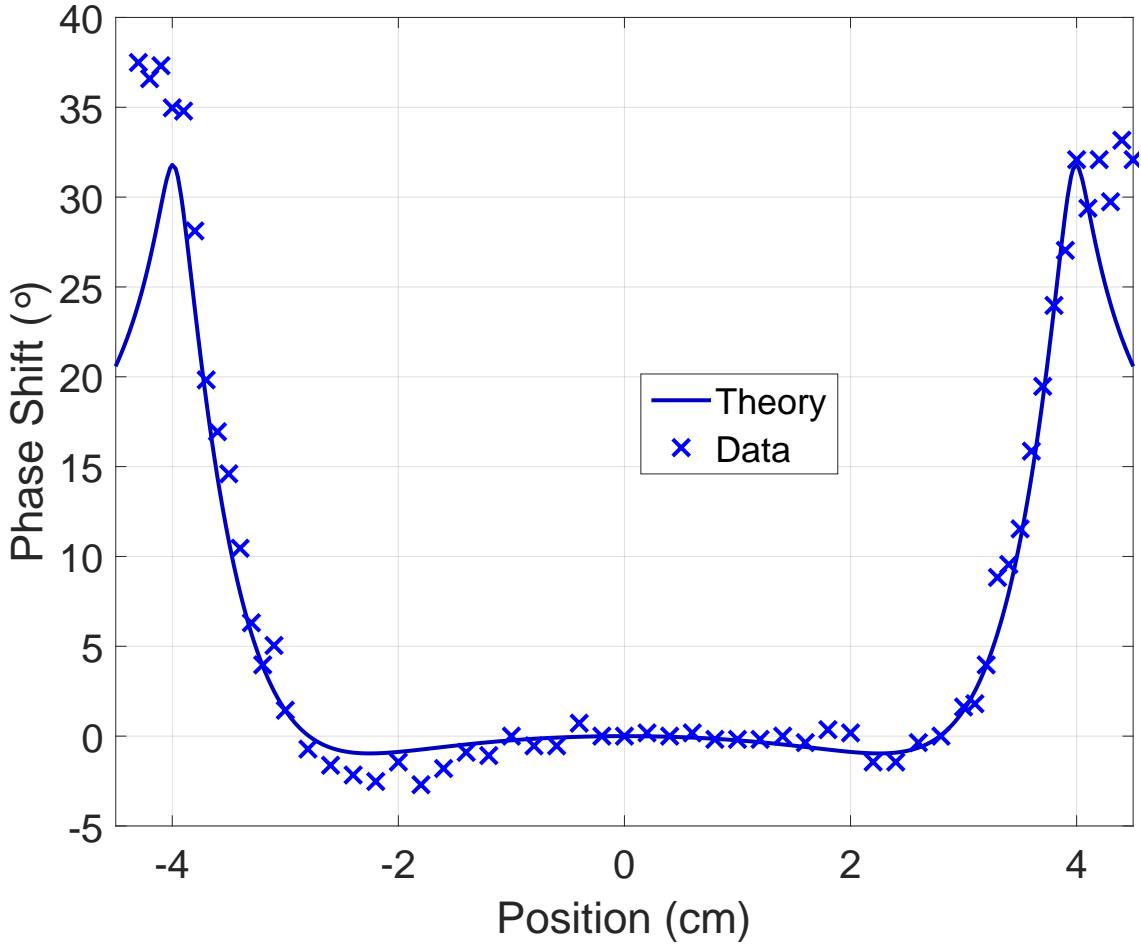


FIG. 8.8: Pickup coil phase measurements versus transverse position at 5 kHz. The pickup coil measurements (crosses) are compared to the theoretical prediction (line) of the phase of the surface magnetic field  $B_x$  (at a height  $y_h = 0.8$  mm) based on the same numerical calculation employed for the theory curves in Fig. 8.6. The phases are given relative to the center value at  $x = 0$ . Errors are smaller than the symbol size and are omitted.

level microwave magnetic near-fields with much smaller conducting strips ( $\sim 100 \mu\text{m}$ ) on an atom chip. Based on the principle of similitude, the agreement between theory and experiment in this kHz work provides confidence that our numerical computation methods for the AC skin effect and related magnetic near field can be extended to microwave frequencies.

## 8.7 AC Skin Appendix

### 8.7.1 Analytic Forms

In the interest of supplying useful analytic functions to the experimenters with similar flat wires, here we reproduce two functions from the paper by Belevitch et al. [111] for the case of a flat, 1-d ‘ribbon’ conductor of width  $2W$  and thickness  $2T$ , where  $W \gg T$ . Solutions assume the form of an infinite sum of even powers of the normalized  $x$  coordinate  $s = \frac{x}{W}$ ,

$$J(s) = \sum_{n=0}^N C_n \cdot s^{2n} \quad (8.6)$$

where increasing the order  $N$  of the sum yields higher accuracy. To simplify some expressions Belevitch et al. [111] use the dimensionless variable  $k = \frac{i\omega\sigma\mu WT}{\pi} = i\frac{2WT}{\pi\delta^2}$  and DC linear current density  $J_{DC} = I_{ext}/2W$ . In our experiment,  $|k| \approx 0.2$  at 250 Hz and  $|k| \approx 4$  at 5 kHz. This method’s first-order ( $N=1$ ) solution yields a complex quadratic equation:

$$J(s) = \frac{1 + k + ks^2}{1 + \frac{4}{3}k} \cdot J_{DC}$$

which applies only for sufficiently low frequencies (i.e.  $|k| < 0.1$ ). For larger  $|k|$  more terms in Eq. 8.6 must be included.

In Fig. 8.9 we plot  $C_n$  terms in the sum of Eq. 8.6 for different values of  $|k|$

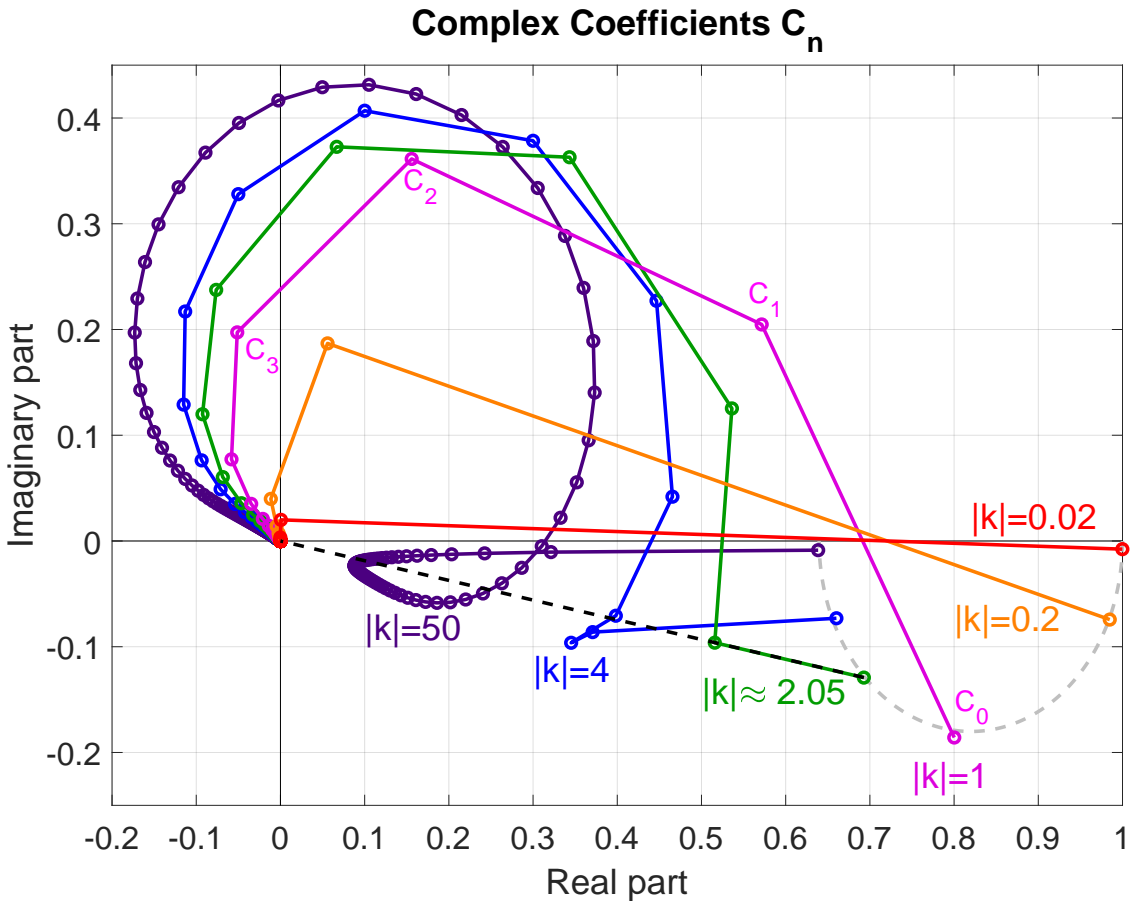


FIG. 8.9: Sequential complex values of the coefficients  $C_n$  for  $N = 500$ . Each colored line connects consecutive terms for a single frequency, labeled by  $|k|$ . Selectively shown are the lowest and highest experimental frequencies used ( $|k| = 0.2, 4$ ), and  $|k| \approx 2.05$ , the value at which the ‘counterflow’ effect begins.

with  $N = 500$ . Each segmented line connects consecutive  $C_n$  terms in sequence, beginning in the lower right with the  $C_0$  or DC value, and ending for converged sequences with many values near the origin, contributing very little. Solutions require many powers of  $s$  for convergence at high frequency, while only a few are needed for low frequency convergence. At low frequencies (e.g.  $|k| = 0.02$ ), similar to the discussion in Sec. 8.3.1, the primary contribution is largely real, with a small imaginary  $s^2$  contribution. The leading  $C_0$  terms describe a semi-circle of diameter  $\approx 0.36 \approx 1 - \frac{2}{\pi}$ , a feature also described in Casimir and Ubbink's analysis [86].

In the high frequency limit of a thin ribbon conductor, e.g.  $|k| \gg 50$ , Belevitch also provides an exact solution for the magnitude of the current distribution:

$$|J(s)| = \frac{2}{\pi\sqrt{1-s^2}} \cdot J_{DC} \quad (8.7)$$

This function appears, scaled to our parameters, in Fig. 8.2. This expression also shows that in the center of a very thin strip, the minimum  $J$  will only drop to  $2/\pi \approx 0.63662$  times the DC value. Our other simulations reinforce the trend toward this curve at higher frequencies. The phase in the high frequency limit approaches a uniform distribution, lagging the driving current by  $90^\circ$  (for a very thin ribbon).

### 8.7.2 The Counterflow Effect

Due to the phase-shifting of the skin effect, the dominant outer current always precedes the rest of the current (see Fig. 8.10). However, above some frequency, the phase in the center slightly precedes the area surrounding it. As seen in Fig. 8.8, a slight bump in phase is present at the center of the strip.

As shown in Fig. 8.10 (3, 4, and 5 kHz curves), for a small portion of time (about  $1^\circ$ , twice per cycle), the current in the center and edge are going in the same direction, but currents at points between are flowing in the opposite direction, near

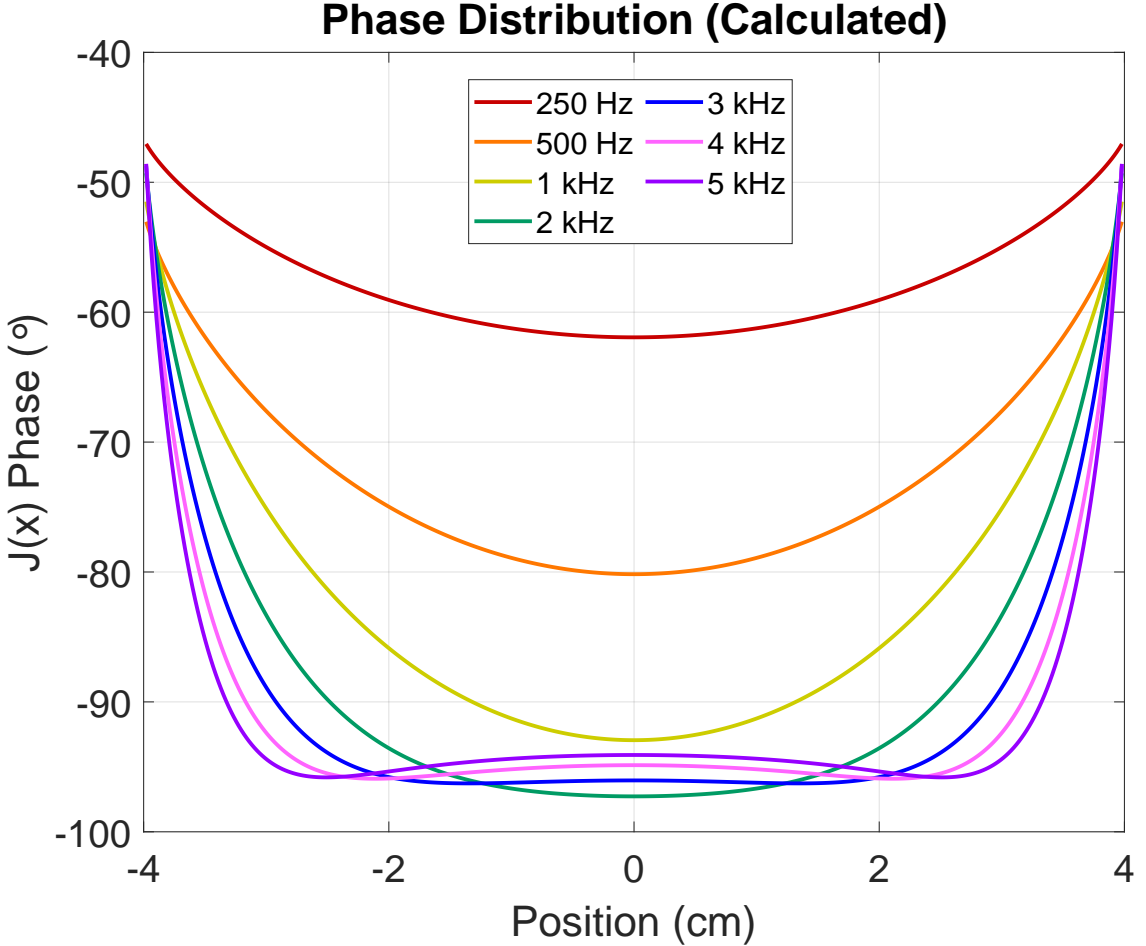


FIG. 8.10: Phase distributions calculated using the Silvester model [84] for the experimental parameters given in Fig. 8.6. Note that the counterflow effect is visible for 3 kHz and higher.

the zero crossing of a current oscillation. Our calculations show that this effect begins at  $|k| \approx 2.0514$ , which corresponds to about 2.6 kHz in our experiment. The effect grows and then diminishes at very high frequencies, and we predict no higher order phase reversals.

We find that we are able predict this crossing point analytically, using the Belevitch model. Using  $s = \frac{x}{W}$ , the current at any point can be represented by the expression

$$J(s) = a(s) + ib(s) = \sum_{n=0}^N (a_n + ib_n) s^{2n}$$

with phase  $\phi$  given by

$$\phi = \tan^{-1} \left( \frac{b(s)}{a(s)} \right)$$

The phase bump appears when the curvature of  $\phi$  at  $s = 0$  flips from negative to positive. Setting  $d^2\phi/ds^2 = 0$ , we obtain at  $s = 0$  : (a prime represents a derivative with respect to  $s$ )

$$\frac{a''}{a} = \frac{b''}{b}$$

where we have used the fact that  $d\phi/ds = 0$  at  $s = 0$  due to the even symmetry of  $J(s)$ . We can translate the above conditions into statements about relative curvature of the real and imaginary parts of the current density at the center:

- If  $\frac{a''}{a} > \frac{b''}{b}$ , the center phase always follows locally.
- If  $\frac{a''}{a} = \frac{b''}{b}$ , the center is in phase with its surroundings.
- If  $\frac{a''}{a} < \frac{b''}{b}$ , the center phase precedes locally.

Using the summation  $J(s) = C_0 + C_1 s^2 + C_4 s^4 + \dots$  we can identify  $C_0 = a + ib|_{s=0}$  and  $C_1 = \frac{1}{2!}(a'' + ib'')|_{s=0}$ . We only need to compute two complex terms of equation 8.6's solution,  $C_0$  and  $C_1$ , to know whether the current has this phase reversal at the center. The equality condition  $a''/a = b''/b$  implies that  $C_0$  and  $C_1$  lie on a line through the origin (see dashed line in Fig. 8.9). Numerically, we find this happens for  $|k| = 2.0514 \approx 2$ . The frequency required for this central phase reversal effect is then roughly  $f_\phi \gtrsim \frac{1}{WT\mu\sigma}$ . At higher frequencies, the effect is at most only a few degrees, which is sufficient for observation (see Fig. 8.8).

### 8.7.3 Calibration

In principle, we can extract values of  $J(x)$  or  $B(x)$  via Eq. 8.5, a measurement of  $V_{coil}(x)$ , the frequency  $\omega$ , and the coil area  $A$ , but this approach is problematic. First, the coil area is not well defined, because the coil's enclosed area is comparable to the

wire area (see Fig. 8.4(b–c)). Second, the signal we measure on the oscilloscope  $V_{sig}$  is also modified by the bandwidth of the amplifier. Finally,  $V_{coil}$  may have additional magnetic gradient dependence or  $\omega$ -dependence beyond the linear  $\omega$  scaling in Eq. 8.3.

We resolve these difficulties by using a collective model for the gain of the pickup coil system (coil, amplifier, etc.) that relates  $V_{sig}$  to the current density and magnetic field at the surface:

$$J(x) = \frac{\alpha_J(\omega)V_{sig}(x)}{\omega}, \text{ and } B_{surf}(x) = \frac{\alpha_B(\omega)V_{sig}(x)}{\omega}$$

The proportionality constants  $\alpha_J(\omega)$  and  $\alpha_B(\omega)$  are determined via calibration experiments at known  $J$  and  $B_{surf}$ . These two constants also have the same frequency dependence, so for two different frequencies  $\omega$  and  $\omega_0$ , we expect  $\alpha_J(\omega)/\alpha_J(\omega_0) = \alpha_B(\omega)/\alpha_B(\omega_0)$ . From this relation, we see that we have  $\alpha_J(\omega) = \alpha_J(\omega_0)(\alpha_B(\omega)/\alpha_B(\omega_0))$ , so we can obtain  $\alpha_J(\omega)$  from measurements of  $\alpha_J(\omega_0)$  and  $\alpha_B(\omega)/\alpha_B(\omega_0)$ .

We measure  $\alpha_J(\omega_0)$  at a very low frequency with  $\omega_0 = 2\pi \times 250$  Hz, where the AC skin effect is near negligible, yet high enough in frequency to be visibly picked up by the coil. The current density  $J(x)$  is near-constant across the middle of the strip as seen in Fig. 8.6.

We determine  $\alpha_B(\omega)/\alpha_B(\omega_0)$ , i.e. the frequency dependent gain of the pickup coil system, by measuring  $V_{sig}$  at the surface of an aluminum rod of circular cross section driven by a known AC current for different frequencies. Due to its geometry, the external magnetic field of the rod is frequency independent (unlike the strip), so we can use  $\alpha_B(\omega)/\alpha_B(\omega_0) = (V_{sig}(\omega_0)/\omega_0)/(V_{sig}(\omega)/\omega)$  to determine the  $\alpha_B(\omega)/\alpha_B(\omega_0)$  calibration ratio.

# CHAPTER 9

## Outlook

While I had hyped up the AC Zeeman a bit in the introduction as a revolutionary Swiss army knife, what has been demonstrated so far is a proof-of-principle search into this new trapping technology. We have performed additional demonstrations like evaporation and the ‘throw and catch’ technique in this two-wire trap, and it demonstrates the resonant and state-dependent nature we had expected. While the categorical existence of a trap suggests the motivating theory is sound, we found a few empirical results which violate expectations. This knowledge gap suggests we look again at the approximations we have asserted [126], such as  $\Omega \ll \omega_{rf}$ ,  $\omega_0 - \omega_{RF} \ll \omega_0 + \omega_{RF}$ , and experimental nuances which need to be grappled with. This demonstration of a few hundred Hz of trap frequency using < 1 W, and half second lifetimes, I hope serves as a diving board into any number of more complex experiments.

We still search for a good rationale for trap losses, which appear to prefer shedding hotter atoms, but aren’t visible in the  $|+\rangle$  state, as we had expected. This points to simple free evaporation, when the ensemble temperature is nearly the order of the trap depth, as in our case. In addition, we suspect something analogous

to Majorana losses, spin-flips from trapped into anti-trapped states at the central zero of the trapping field. At the  $B_{\pm}$  field zero, the coupling  $\Omega$  goes to zero, and the detuning  $\delta$  alone gives the difference in energies. Atoms moving in simple trap oscillations through this central zero might find themselves re-projected into other un-trapped states, although we did not directly observe this. I believe a proper model would be something like the Landau-Zener formula for a harmonic oscillating  $\Omega$  coupling instead of linear sweeps over detuning, weighted by the energy curvature at trap bottom, linear or harmonic to leading order.

Having demonstrated an AC Zeeman trap for a relatively small investment, we encourage other atom-chip experimenters to consider adding this technique to their toolbox. One main hurdle is a frequency sweeping, phase-controlled multi-RF source, but one can use arbitrary waveform generators at MHz frequencies or specialized commercial products like we used. In terms of power consumption, we observed trapping nearly  $100 \mu\text{m}$  from the chip using 0.1 Watts per  $\approx 8 \Omega$  trace (usually 400 mW though), and less power would be needed in low-gravity [58] or with inverted chip orientation (opening upwards). Further, microstrip transmission lines allow more microwave power for inter-manifold state-selective trapping, and counter-propagating microwave fields can create an ACZ standing wave to confine atoms in an axial ‘microwave lattice.’ Shifting phase in this microwave lattice can shift atoms along the axial direction, adding distance and an enclosed area to an AC Zeeman trapped atom interferometer.

In terms of spin-selection, we have shown here polarization selection between the  $F_+ = 2$  and  $F_- = 1$  manifolds, using only one AC Zeeman state of each manifold. Using microwaves, we can target two-level inter-manifold transitions by polarization *and resonance*, allowing for atoms in any hyperfine state to become a high- or low-field seeking AC Zeeman state [44]. While the two-trace geometry precludes it, other geometries generate both  $B_+$  and  $B_-$  traps co-located outside the chip,

moving differentially away from each other as the phase is varied. Additionally, arbitrary independent trap movement is available using multiple microwave transitions sufficiently detuned from one another.

## 9.1 The Proposed Interferometer

An atom interferometer can be constructed using a single frequency RF in combination with a three-trace trapping geometry from Sec. 6.4.3 and Fig. 6.10. Beginning with one of the clock states  $|2, +1\rangle \& |1, -1\rangle$  at 3.23 Gauss,<sup>1</sup> one can co-locate both RF AC Zeeman traps for  $|+\rangle \& |+\rangle'$  using red detuning (from Fig. 7.2), where each state is trapped by opposite polarization  $B_{\pm}$  field. Detuning and power can be fine-tuned to match trap frequencies in these two traps, a crucial step. From a pure population, an RF and  $\mu$ w two-photon  $\pi/2$  pulse [127] (spatially a saddle-point using the same chip wires) can put equal populations in the two clock states, each in a different trap. Then, we separate these  $|+\rangle \& |+\rangle'$  traps (seeing opposite RF polarizations) differentially side-to-side (vis-a-vis Fig. 6.10) by shifting phase from  $180^\circ$ . While we employ linear phase sweeps, different separation protocols can improve interferometric performance [128]. After some interrogation time, possibly with controlled axial motion, these separated traps are recombined spatially, and a second  $\pi/2$  pulse is applied. To read the output states, a DC Stern-Gerlach field would move them the same direction, so we require a differential  $B_+/B_-$  gradient to separate them, or an ARP sweep to a different value of  $m_F g_F$ . While there remains  $\approx 6.8$  GHz of energy separation in the arms, any noise in background magnetic field is made common-mode at ‘magic’ magnetic field values, e.g. 3.23 G for  $^{87}\text{Rb}$ . The states probe fields at distances on par with trace separation or enclose

---

<sup>1</sup>Experimental conditions may preclude operation at such a low frequency. The scheme proposed here would work at higher field, simply losing magnetic insensitivity.

an area with trace length, using an axial ACZ lattice as well.

This is just a toy example, but the spin-targeting ability of the AC Zeeman effect can enable new categories of experiments in existing hardware, as is already happening in trapped ion experiments [129, 130, 131, 132]. Stepping beyond a spin-targeting force or microwave field, this spin-targeting trap, we think, is a transformative tool for chip-based atomic physics.

## 9.2 Chip Design

The next generation of chips to continue this work will need decent power coupling near 6.8 GHz. Other atomic isotopes and species offer different target ranges, so designing for broadband 0-20 GHz might be a good target range. This approach requires a ground plane forming a microstrip transmission line, which we wrote a separate publication about [80], and is largely an engineering hurdle. We employ many 3-D electromagnetic simulations in FEKO to simulate designs and building blocks toward the goal of a microwave AC Zeeman trapping chip.

I have done a handful of early simulations, but the bulk of our lab's work on atom chip design and can be found in forthcoming Ph.D. theses from Shuangli Du and William Miyahira, or the undergraduate theses of Chloe Lewelling [133] and Kameron Sullivan [134] (as of 2021).

## 9.3 Questions

I also want to voice some remaining questions which seem within reach at the moment, and may have answers known to other physicists, but perhaps mark a new unknown endeavor for a future graduate student or post-doc in this field.

- What causes number loss from the AC Zeeman trap, especially at low detuning?

- Is there an extension to Landau-Zener transitions, where we oscillate  $\delta$  across or near resonance? What about oscillating  $\Omega$  as thermal atoms sample the (linear, parabolic, and beyond) gradient at the trap bottom?
- Do transitions analogous to Landau-Zener occur for off-resonant non-adiabatic sweeps?
- Empirical spin mixing showed that higher power preserved states longer, but in the trap, higher power has lower lifetime, why the apparent paradox? (Possible explanations: gravitational trap sag with lower power brings trap center off the zero point, or that higher velocities in a tight trap pass more non-adiabatically through the field zero.)
- How can one quantize the trap energy levels in a quasi-linear/quadratic/beyond AC Zeeman trap, a precursor to dynamic matter wave simulations? Is it easy numerically in 2D or 3D? This will be important for simulating the phase evolution of trapped atom interferometers [135].
- Is there a single, simple sweeping procedure for the RF trap hold frequency plus a microwave field to quickly set up a  $F_+/F_-$  trapped superposition in co-located traps?
- Can one design a chip around inductively coupled microwaves generating stationary traps, as we accidentally performed? (like [136])
- Am I accidentally ‘double dipping’ factors of  $\frac{1}{2}$  in the AC Zeeman analysis by taking the rotating wave approximation, when I start with  $B_{\pm}$  fields? Or, using  $\hat{x} \rightarrow \frac{\hat{e}_+ + \hat{e}_-}{2}$  and the RWA? I believe the  $\Omega$  definition I have adopted might differ by a factor of 2 from a conventional definition. Explicitly, I define  $\Omega_0 = \mu_B |B_{\pm}|/\hbar$  so that each off-diagonal element in the Hamiltonian used is  $\Omega_0 \cdot (CG)/2$ , where

$(CG)$  is  $\frac{\langle F', m'_F | g_S S_{\pm} | F, m_F \rangle}{2\hbar}$ . Keeping the ‘/2’ in the off-diagonal elements matches interpretation to the Rabi definition in the two-level case.

- What mathematical intuition properly resolves the Hermitian  $\Omega_{eg}^*$ ’s abandoned polarization flip? Or, how does one properly formulate the inverse  $S_{\pm}$  transition elements (stimulated emission vs.  $S_{\mp}$  absorption) so that it knows about  $g_F$ ’s sign?  $\langle 1, 1 | S_- B_+ | 2, 2 \rangle^* \stackrel{?}{=} \langle 2, 2 | S_+ B_- | 1, 1 \rangle$
- Is there a nice Bloch-sphere picture for three or five levels? [137]
- Can one simply inject complex phases into the Silvester model?
- In the high-frequency limit of the AC skin effect, do the lateral results apply to the edges of a rectangular conductor? Or is there always magnitude in the center, as with the linear case?

## APPENDIX A

# Five-level Hamiltonian Derivation

This appendix goes with Chapter 3, working through the five-level dressed atom system to find a time-independent Hamiltonian which we can diagonalize to get AC Zeeman energy.

In this appendix, I will extend the two-level dressed atom approach into the five-level ladder-like system of the  $F_+ = 2$ , being more explicit about the quantum mechanics.

Let us begin with the bare atomic energies and eigenstates, here for the  $F_+$  manifold, which we label as  $|m_F\rangle$ . In this case, we order them from least DC Zeeman energy to most from the top to bottom row. In this basis, a state  $|\Psi\rangle$  can be written as:

$$|\Psi\rangle = \begin{pmatrix} C_{-2} \cdot e^{-i\omega_{-2}t} \\ C_{-1} \cdot e^{-i\omega_{-1}t} \\ C_0 \cdot e^{-i\omega_0 t} \\ C_{+1} \cdot e^{-i\omega_{+1}t} \\ C_{+2} \cdot e^{-i\omega_{+2}t} \end{pmatrix} \cdot \begin{pmatrix} | -2 \rangle \\ | -1 \rangle \\ | 0 \rangle \\ | +1 \rangle \\ | +2 \rangle \end{pmatrix} \quad (\text{A.1})$$

where each  $\omega_i$  is  $E_i/\hbar$ . We also have the bare state Hamiltonian in this basis:

$$\hat{H} = \begin{pmatrix} \hbar\omega_{-2} & 0 & 0 & 0 & 0 \\ 0 & \hbar\omega_{-1} & 0 & 0 & 0 \\ 0 & 0 & \hbar\omega_0 & 0 & 0 \\ 0 & 0 & 0 & \hbar\omega_{+1} & 0 \\ 0 & 0 & 0 & 0 & \hbar\omega_{+2} \end{pmatrix} \quad (\text{A.2})$$

As with the two level case, the interaction between a ground and excited state is given by  $\langle e | -\mu \cdot B | g \rangle$  where we take  $g_S = 2$ ,  $\vec{\mu} = \frac{-2\mu_B}{\hbar} \vec{S}$ ,  $\vec{B} = B_{RF} \cos(\omega_{RF}t) \hat{x}$ ,  $\hbar\Omega_x = \mu_B B_{RF}$ . From Sec. 3.2, we use the low- $B_{DC}$  Clebsch-Gordan coefficients  $\frac{\sqrt{4}}{4}$  (for  $|2\rangle \leftrightarrow |1\rangle$  and  $| -1 \rangle \leftrightarrow | -2 \rangle$ ) and  $\frac{\sqrt{6}}{4}$  (for  $|1\rangle \leftrightarrow |0\rangle$  and  $|0\rangle \leftrightarrow | -1 \rangle$ ).

These values, along with their complex conjugates (all real here, displayed for the general case), yields an interaction Hamiltonian:

$$\hat{H}_{int} = \hbar \begin{pmatrix} 0 & \frac{\sqrt{4}}{4}\Omega_x & 0 & 0 & 0 \\ \frac{\sqrt{4}}{4}\Omega_x^* & 0 & \frac{\sqrt{6}}{4}\Omega_x & 0 & 0 \\ 0 & \frac{\sqrt{6}}{4}\Omega_x^* & 0 & \frac{\sqrt{6}}{4}\Omega_x & 0 \\ 0 & 0 & \frac{\sqrt{6}}{4}\Omega_x^* & 0 & \frac{\sqrt{4}}{4}\Omega_x \\ 0 & 0 & 0 & \frac{\sqrt{4}}{4}\Omega_x^* & 0 \end{pmatrix} \cdot \cos(\omega_{RF}t) \quad (\text{A.3})$$

Now, taking the combined Hamiltonian into the time-dependent Schrödinger equation gives

$$i\hbar \frac{d}{dt} |\Psi(t)\rangle = \hat{H} |\Psi(t)\rangle \quad (\text{A.4})$$

$$i\hbar \frac{d}{dt} \begin{pmatrix} C_{-2}e^{-i\omega_{-2}t} \\ C_{-1}e^{-i\omega_{-1}t} \\ C_0e^{-i\omega_0t} \\ C_{+1}e^{-i\omega_{+1}t} \\ C_{+2}e^{-i\omega_{+2}t} \end{pmatrix} = \hbar \begin{pmatrix} \omega_{-2} & \frac{\sqrt{4}}{4}\Omega_x & 0 & 0 & 0 \\ \frac{\sqrt{4}}{4}\Omega_x^* & \omega_{-1} & \frac{\sqrt{6}}{4}\Omega_x & 0 & 0 \\ 0 & \frac{\sqrt{6}}{4}\Omega_x^* & \Omega_x & \frac{\sqrt{6}}{4}\Omega_x & 0 \\ 0 & 0 & \frac{\sqrt{6}}{4}\Omega_x^* & \omega_{+1} & \frac{\sqrt{4}}{4}\Omega_x \\ 0 & 0 & 0 & \frac{\sqrt{4}}{4}\Omega_x^* & \omega_{+2} \end{pmatrix} \cdot \cos(\omega_{RF}t) \begin{pmatrix} C_{-2} \cdot e^{-i\omega_{-2}t} \\ C_{-1} \cdot e^{-i\omega_{-1}t} \\ C_0 \cdot e^{-i\omega_0t} \\ C_{+1} \cdot e^{-i\omega_{+1}t} \\ C_{+2} \cdot e^{-i\omega_{+2}t} \end{pmatrix} \quad (\text{A.5})$$

where with a bit of lazy short hand, the cos term is only on the off-diagonal coupling terms. Taking the time derivative on a product  $C \cdot e^{i\omega t}$ , and canceling in each equation the left side's

$$(-i^2\hbar\omega_i) \cdot C_i(t) \cdot e^{-i\omega_i t} \quad (\text{A.6})$$

with the diagonal energy elements on the right

$$\hbar\omega_i \cdot C_i(t) \cdot e^{-i\omega_i t} \quad (\text{A.7})$$

we obtain the system of equations:

$$\begin{aligned} i\hbar e^{-i\omega_{-2}t} \frac{d}{dt} C_{-2}(t) &= +C_{-1}(t)e^{-i\omega_{-1}t} \hbar\Omega_x \frac{\sqrt{4}}{4} \cos(\omega_{RF}t) \\ i\hbar e^{-i\omega_{-1}t} \frac{d}{dt} C_{-1}(t) &= C_{-2}(t)e^{-i\omega_{-2}t} \hbar\Omega_x^* \frac{\sqrt{4}}{4} \cos(\omega_{RF}t) + C_0(t)e^{-i\omega_0t} \hbar\Omega_x \frac{\sqrt{6}}{4} \cos(\omega_{RF}t) \\ i\hbar e^{-i\omega_0t} \frac{d}{dt} C_0(t) &= C_{-1}(t)e^{-i\omega_{-1}t} \hbar\Omega_x^* \frac{\sqrt{6}}{4} \cos(\omega_{RF}t) + C_1(t)e^{-i\omega_1t} \hbar\Omega_x \frac{\sqrt{6}}{4} \cos(\omega_{RF}t) \\ i\hbar e^{-i\omega_1t} \frac{d}{dt} C_1(t) &= C_0(t)e^{-i\omega_0t} \hbar\Omega_x^* \frac{\sqrt{6}}{4} \cos(\omega_{RF}t) + C_2(t)e^{-i\omega_2t} \hbar\Omega_x \frac{\sqrt{4}}{4} \cos(\omega_{RF}t) \\ i\hbar e^{-i\omega_{-2}t} \frac{d}{dt} C_2(t) &= C_1(t)e^{-i\omega_1t} \hbar\Omega_x^* \frac{\sqrt{4}}{4} \cos(\omega_{RF}t) \end{aligned}$$

Now, we wish to remove the  $e^{-i\omega_i t}$  dependence on the left by multiplying by its inverse ( $e^{+i\omega_i t}$ ) on both sides. This factor introduces new dependence on differences in  $\omega$ , which prompts the definition of a double subscripted  $\omega_{ab} = \omega_a - \omega_b$ . Performing

this, we come to the system

$$\begin{aligned}
i\hbar \frac{d}{dt} C_{-2}(t) &= +C_{-1}(t) e^{-i\omega_{-1-2}t} \hbar \Omega_x \frac{\sqrt{4}}{4} \cos(\omega_{RF}t) \\
i\hbar \frac{d}{dt} C_{-1}(t) &= C_{-2}(t) e^{+i\omega_{-1-2}t} \hbar \Omega_x^* \frac{\sqrt{4}}{4} \cos(\omega_{RF}t) + C_0(t) e^{-i\omega_{0-1}t} \hbar \Omega_x \frac{\sqrt{6}}{4} \cos(\omega_{RF}t) \\
i\hbar \frac{d}{dt} C_0(t) &= C_{-1}(t) e^{+i\omega_{0-1}t} \hbar \Omega_x^* \frac{\sqrt{6}}{4} \cos(\omega_{RF}t) + C_1(t) e^{-i\omega_{10}t} \hbar \Omega_x \frac{\sqrt{6}}{4} \cos(\omega_{RF}t) \\
i\hbar \frac{d}{dt} C_1(t) &= C_0(t) e^{+i\omega_{10}t} \hbar \Omega_x^* \frac{\sqrt{6}}{4} \cos(\omega_{RF}t) + C_2(t) e^{-i\omega_{21}t} \hbar \Omega_x \frac{\sqrt{4}}{4} \cos(\omega_{RF}t) \\
i\hbar \frac{d}{dt} C_2(t) &= C_1(t) e^{+i\omega_{21}t} \hbar \Omega_x^* \frac{\sqrt{4}}{4} \cos(\omega_{RF}t)
\end{aligned}$$

Now, we perform the Rotating Wave Approximation (RWA), where we make the substitution

$$\cos(\omega_{RF}t) = \frac{e^{-i\omega_{RF}t} + e^{+i\omega_{RF}t}}{2} \quad (\text{A.8})$$

and then drop terms which contain in the exponential the sum of two frequencies ( $\omega_{RF} + \omega_i$ ) and retain the difference of two frequencies ( $\omega_{RF} - \omega_i$ ). We are near the edge of this being a valid assumption when we work at low RF frequencies. However, this counter-rotating term can be added again later as a Bloch-Siegert shift, effectively re-dressing the system from far off-resonance [70, 71, 72]. Checking signs, we examine the product

$$\left( \frac{e^{-i\omega_{RF}t} + e^{+i\omega_{RF}t}}{2} \right) \cdot e^{\pm i\omega_i t} \quad (\text{A.9})$$

Pulling out the minus sign, we flip the sign on the whole term:  $e^{\mp i(\omega_{RF} - \omega_i)t}$ . Applying

the RWA, we have:

$$\begin{aligned}
i\hbar \frac{d}{dt} C_{-2}(t) &= +C_{-1}(t)e^{+i(\omega_{RF}-\omega_{-1-2})t}\hbar\Omega_x \frac{\sqrt{4}}{8} \\
i\hbar \frac{d}{dt} C_{-1}(t) &= C_{-2}(t)e^{-i(\omega_{RF}-\omega_{-1-2})t}\hbar\Omega_x^* \frac{\sqrt{4}}{8} \\
i\hbar \frac{d}{dt} C_0(t) &= C_{-1}(t)e^{-i(\omega_{RF}-\omega_{0-1})t}\hbar\Omega_x^* \frac{\sqrt{6}}{8} \\
i\hbar \frac{d}{dt} C_1(t) &= C_0(t)e^{-i(\omega_{RF}-\omega_{10})t}\hbar\Omega_x^* \frac{\sqrt{6}}{8} \\
i\hbar \frac{d}{dt} C_2(t) &= C_1(t)e^{-i(\omega_{RF}-\omega_{21})t}\hbar\Omega_x^* \frac{\sqrt{4}}{8}
\end{aligned}$$

And, for convenience we define each transition's detuning  $\delta_{ij} = \omega_{RF} - \omega_{ij}$ :

$$\delta_{-1-2} = \omega_{RF} - \omega_{-1-2}, \quad \delta_{0-1} = \omega_{RF} - \omega_{0-1}, \quad \delta_{10} = \omega_{RF} - \omega_{10}, \quad \delta_{21} = \omega_{RF} - \omega_{21}$$

Which leaves us with:

$$\begin{aligned}
i\hbar \frac{d}{dt} C_{-2}(t) &= +C_{-1}(t)e^{+i(\delta_{-1-2})t}\hbar\Omega_x \frac{\sqrt{4}}{8} \\
i\hbar \frac{d}{dt} C_{-1}(t) &= C_{-2}(t)e^{-i(\delta_{-1-2})t}\hbar\Omega_x^* \frac{\sqrt{4}}{8} \\
i\hbar \frac{d}{dt} C_0(t) &= C_{-1}(t)e^{-i(\delta_{0-1})t}\hbar\Omega_x^* \frac{\sqrt{6}}{8} \\
i\hbar \frac{d}{dt} C_1(t) &= C_0(t)e^{-i(\delta_{10})t}\hbar\Omega_x^* \frac{\sqrt{6}}{8} \\
i\hbar \frac{d}{dt} C_2(t) &= C_1(t)e^{-i(\delta_{21})t}\hbar\Omega_x^* \frac{\sqrt{4}}{8}
\end{aligned}$$

We then perform the rotating frame transformation, intending to remove all explicit time dependence in the new detuning exponential terms by redefining the

$C_i$  terms. Defining new coefficients  $C$  and Delta terms:

$$\begin{aligned}
\tilde{C}_{-2} &= C_{-2} \cdot e^{i\Delta_{-2}t} & \Delta_{-2} &= 0 \\
\tilde{C}_{-1} &= C_{-1} \cdot e^{i\Delta_{-1}t} & \Delta_{-1} &= \Delta_{-2} + \delta_{-1-2} \\
\tilde{C}_0 &= C_0 \cdot e^{i\Delta_0 t} & \Delta_0 &= \Delta_{-1} + \delta_{0-1} \\
\tilde{C}_1 &= C_1 \cdot e^{i\Delta_1 t} & \Delta_1 &= \Delta_0 + \delta_{10} \\
\tilde{C}_2 &= C_2 \cdot e^{i\Delta_2 t} & \Delta_2 &= \Delta_1 + \delta_{21}
\end{aligned}$$

We use a different convention later with fewer terms, but this version is equivalent and follows from this theory section. Plugging these in, we obtain the system

$$\begin{aligned}
i\hbar \frac{d}{dt} \tilde{C}_{-2}(t) &= +\Delta_{-2} \tilde{C}_{-2}(t) + \tilde{C}_{-1}(t) \hbar \Omega_x \frac{\sqrt{4}}{8} \\
i\hbar \frac{d}{dt} \tilde{C}_{-1}(t) &= \tilde{C}_{-2}(t) \hbar \Omega_x^* \frac{\sqrt{4}}{8} + \Delta_{-1} \tilde{C}_{-1}(t) + \tilde{C}_0(t) \hbar \Omega_x \frac{\sqrt{6}}{8} \\
i\hbar \frac{d}{dt} \tilde{C}_0(t) &= \tilde{C}_{-1}(t) \hbar \Omega_x^* \frac{\sqrt{6}}{8} + \Delta_0 \tilde{C}_0(t) + \tilde{C}_1(t) \hbar \Omega_x \frac{\sqrt{6}}{8} \\
i\hbar \frac{d}{dt} \tilde{C}_1(t) &= \tilde{C}_0(t) \hbar \Omega_x^* \frac{\sqrt{6}}{8} + \Delta_1 \tilde{C}_1(t) + \tilde{C}_2(t) \hbar \Omega_x \frac{\sqrt{4}}{8} \\
i\hbar \frac{d}{dt} \tilde{C}_2(t) &= \tilde{C}_1(t) \hbar \Omega_x^* \frac{\sqrt{4}}{8} + \Delta_2 \tilde{C}_2(t)
\end{aligned}$$

In the  $\tilde{C}$  basis, we can re-write the system in a Hamiltonian matrix form:

$$i\hbar \frac{d}{dt} \begin{pmatrix} \tilde{C}_{-2} \\ \tilde{C}_{-1} \\ \tilde{C}_0 \\ \tilde{C}_{+1} \\ \tilde{C}_{+2} \end{pmatrix} = \hbar \begin{pmatrix} \Delta_{-2} & \frac{\sqrt{4}}{8} \Omega_x & 0 & 0 & 0 \\ \frac{\sqrt{4}}{8} \Omega_x^* & \Delta_{-1} & \frac{\sqrt{6}}{8} \Omega_x & 0 & 0 \\ 0 & \frac{\sqrt{6}}{8} \Omega_x^* & \Delta_0 & \frac{\sqrt{6}}{8} \Omega_x & 0 \\ 0 & 0 & \frac{\sqrt{6}}{8} \Omega_x^* & \Delta_{+1} & \frac{\sqrt{4}}{8} \Omega_x \\ 0 & 0 & 0 & \frac{\sqrt{4}}{8} \Omega_x^* & \Delta_{+2} \end{pmatrix} \begin{pmatrix} \tilde{C}_{-2} \\ \tilde{C}_{-1} \\ \tilde{C}_0 \\ \tilde{C}_{+1} \\ \tilde{C}_{+2} \end{pmatrix} \quad (\text{A.10})$$

Having performed some transformations on a time-dependent setup, this Hamilto-

nian is now time-independent, as the  $\tilde{C}(t)$  terms now oscillate instead. The diagonal terms depend on the applied frequency  $\omega_{RF}$ , detuning  $\delta$  as  $\Delta_i$ , and energies of the bare states set by  $B_{DC}$ . Off diagonal, we have adjacent state couplings driven by the amplitude  $B_{RF}$  of the external field.

## APPENDIX B

### Microwave Lattice

With an eye towards future microstrip atom chip design, we have constructed a macro-sized demonstration model to test different features, among them the microwave lattice. A number of undergraduate researchers in our lab have developed methods of etching away copper to leave traces for testing, shown in Fig. B.1(top). Together with our post-doc researcher Doug Beringer, we made a measurement of magnetic field power along these traces. We inserted microwaves into either end port, generated by a SynthHD Pro signal generator, with directional coupler ports to prevent reflections.

We show data from this experiment in Fig. B.1(bottom). Each connected colored curve shows the spatial measurements of microwave magnetic field power. The data show roughly sinusoidal position dependence, forming the magnetic ‘microwave lattice’ we had expected. Each different color curve shows a new insertion phase difference, in steps of  $\pi/4$ . We can see a continuous shift in phase should translate atoms confined in one of these axial minima along the trace.

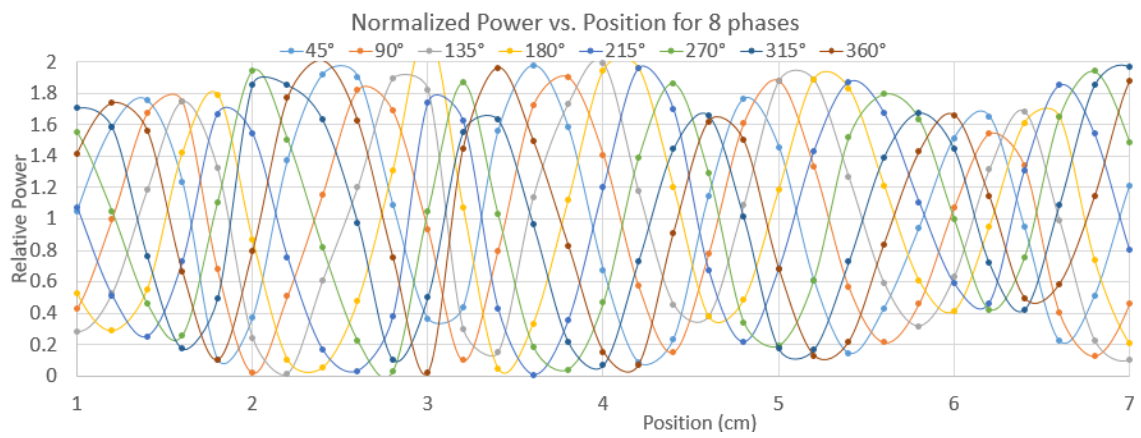
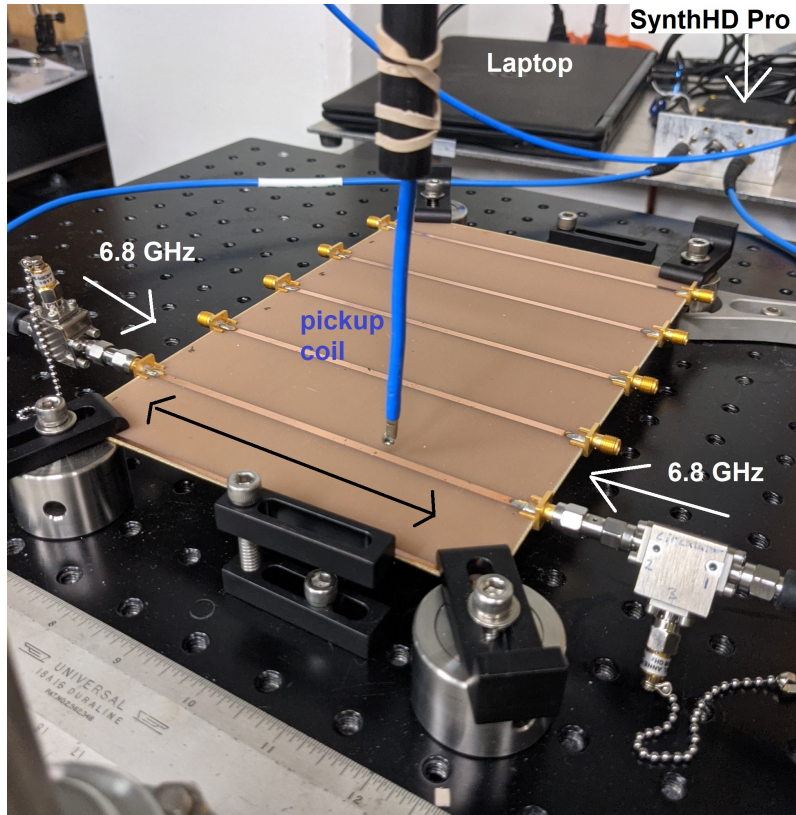


FIG. B.1: Demonstration of a microwave lattice. Microwaves are inserted into both microstrip ports (top), and we measure pick-up magnetic field power along the microstrip trace, across a range of phases. Measurements are normalized to account for measurement artifacts, and demonstrate the translation of the sinusoidal lattice field with insertion phase differences (bottom).

# APPENDIX C

## Rabi Maps

Here, we showcase more time steps of the ‘Rabi map’ procedure [82] used to map the AC Zeeman  $\Omega(x, y)$  field contours by imaging only the initial  $|2, +2\rangle$  state. In each figure, we show a new  $+2 \mu\text{s}$  time step using 20 mW in each of two wires in the U-U configuration with insertion phase labeled in each cell. This represents some initial low-power exploration from July 27, 2020.

Plots like these have the moniker ‘zebra’ plots (or here ‘bulls-eye’ plots) because a gradient in RF power flops atoms at different rates spatially, and when we image one state, a gradient is mapped by stripes in the resultant atom density. Each dark and light band marks contours of ‘iso- $\Omega_0$ ’ as atoms in the  $F_+ = 2$  state react to the generated  $B_-$  near field.

These dark and bright contour lines are illustrated in Fig. C.1, where we take an illustrative case ( $10 \mu\text{s}$ ,  $130^\circ$ ) and draw on black and white iso-Rabi contour lines. Each black line shows atoms in the initial state, either before a Rabi flop (the black circle), or because it has flopped out of, then back to the initial state, or out and in again, and so on. Each white line shows a ‘half-flop,’ where atoms are not visible, as they have flopped into states ( $m_F \neq 2$ ) other than the imaged

initial state ( $m_F = 2$ ), along with repetitions of this behavior over successive flops. Approaching the atom chip at the top of the image, the lines become more dense, as the Rabi gradient is steepest near the chip.

We could analyze these images by fitting the atom number at any location over time to the Rabi fits of Chap. 4. We don't elect to do this, we simply use these Rabi map images to illustrate the power gradients over space, especially when they show a trapping field. In these illustrations, a trap looks like a small bright region of atoms which haven't Rabi flopped, surrounded by atoms that have.

An animation containing these frames and some others are in the GitHub repo:  
<https://github.com/drewrotunno/ThesisCode>

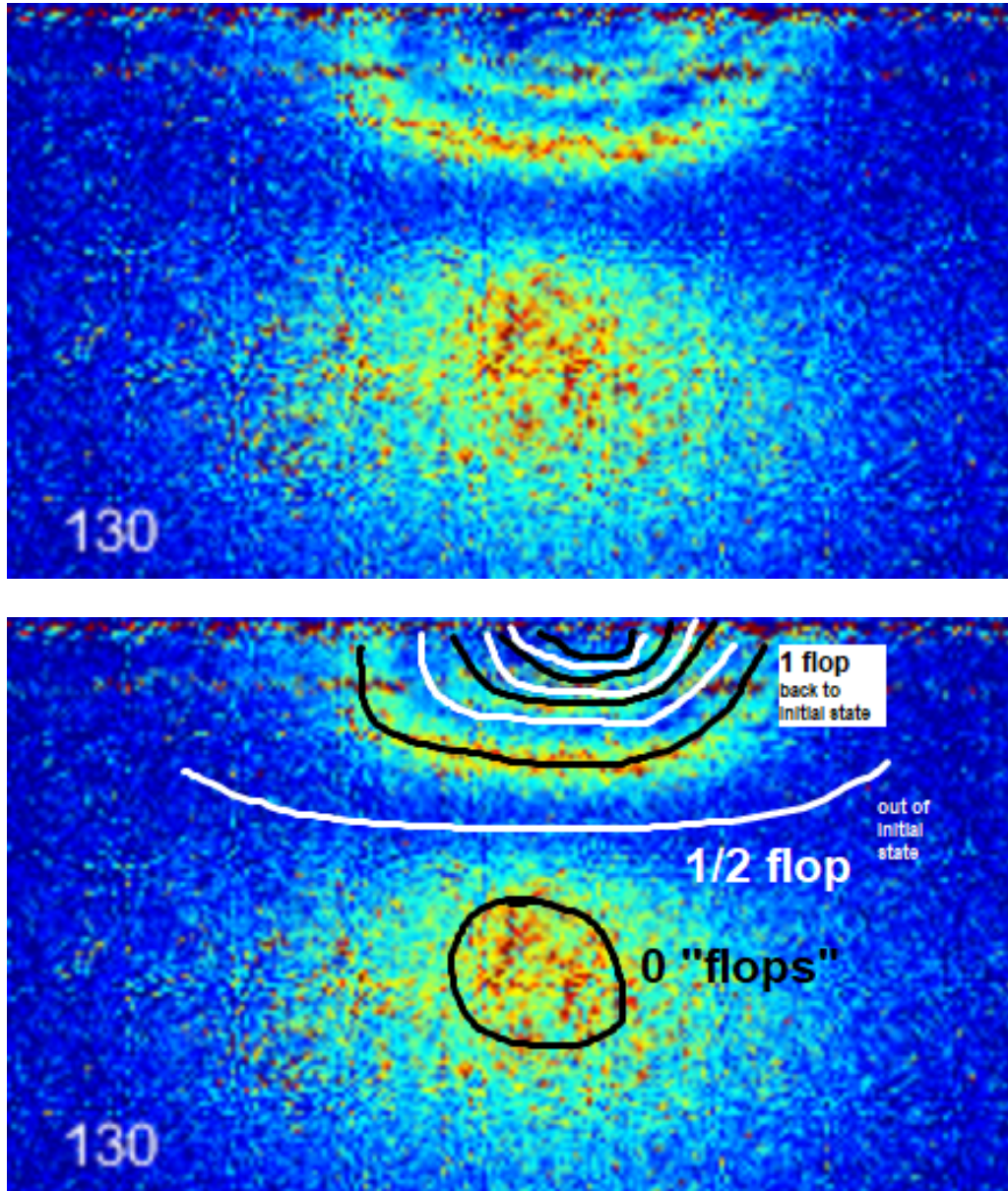


FIG. C.1: Illustration of the Rabi Map's ability to map contour lines of the Rabi frequency, with (top) the original image and (bottom) with annotations. Atoms are subject to a varying-duration pulsed RF two-wire field, and the atoms are imaged in the initial  $|2, +2\rangle$  state. Atoms in the initial state are marked by black lines, either because the atoms have not flopped or have flopped back into their initial state. Areas marked by white lines have atoms which are not visible, and represent a 'half' flop, out of the initial state.

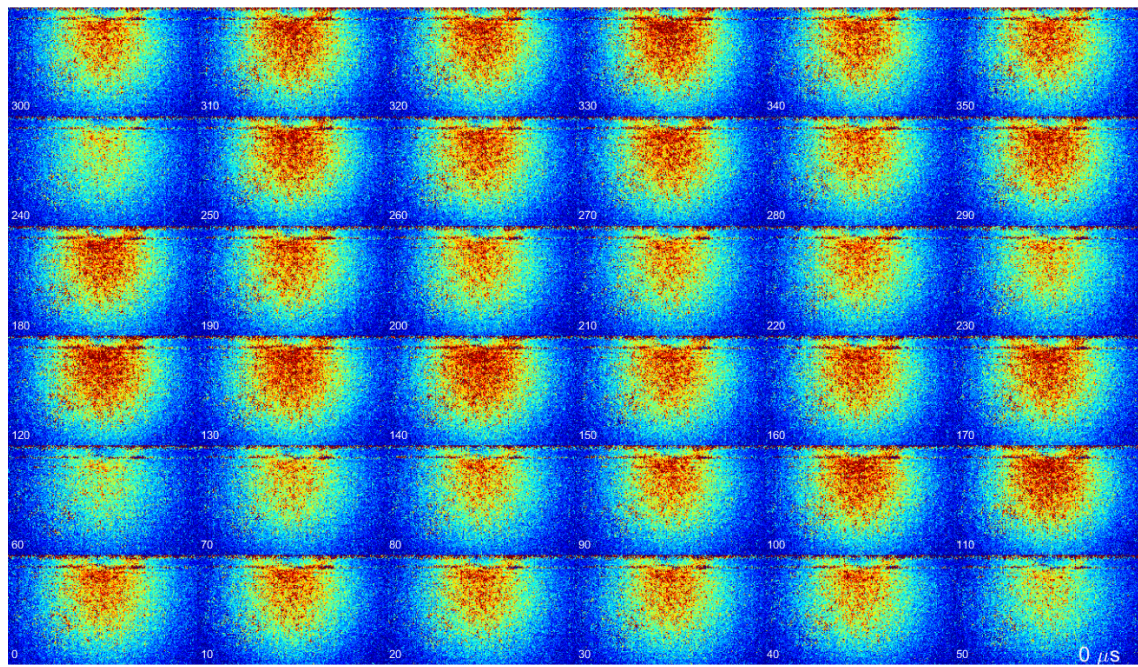


FIG. C.2: Rabi map image, before any pulse.

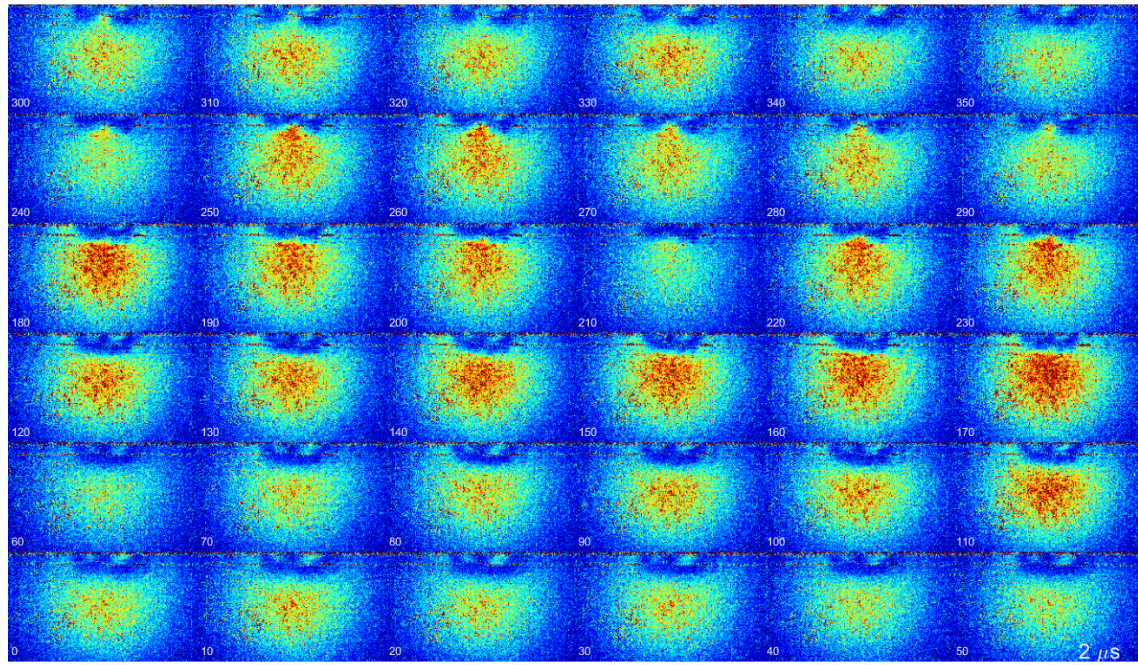


FIG. C.3: Rabi map image, using a 2  $\mu$ s pulse.

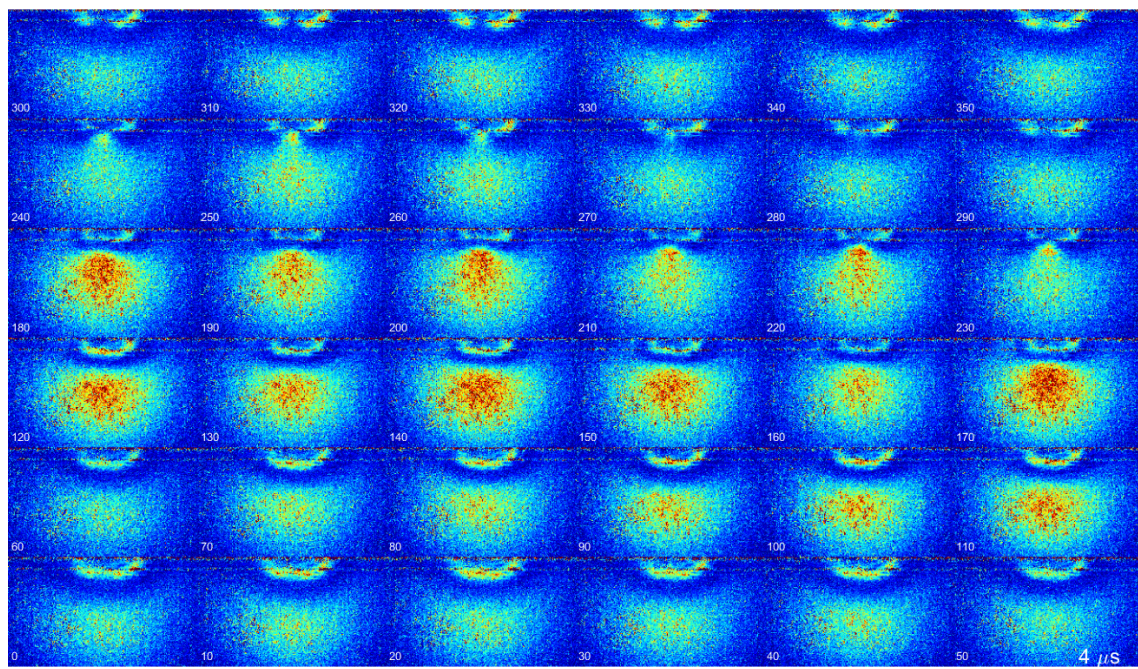


FIG. C.4: Rabi map image, using a  $4 \mu\text{s}$  pulse.

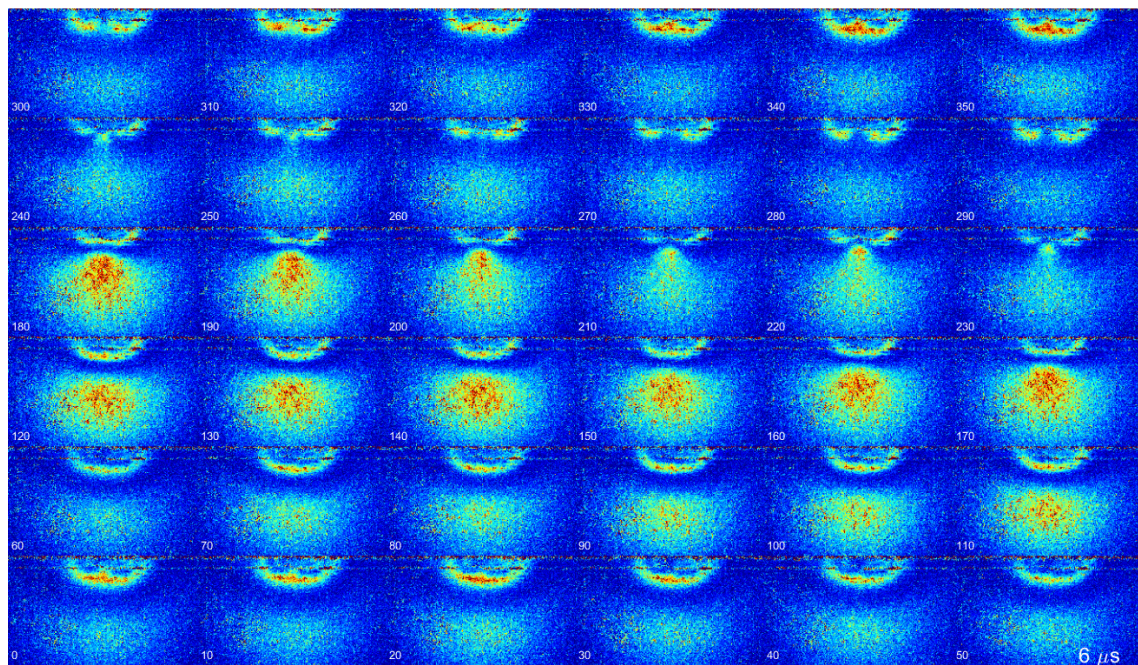


FIG. C.5: Rabi map image, using a  $6 \mu\text{s}$  pulse.

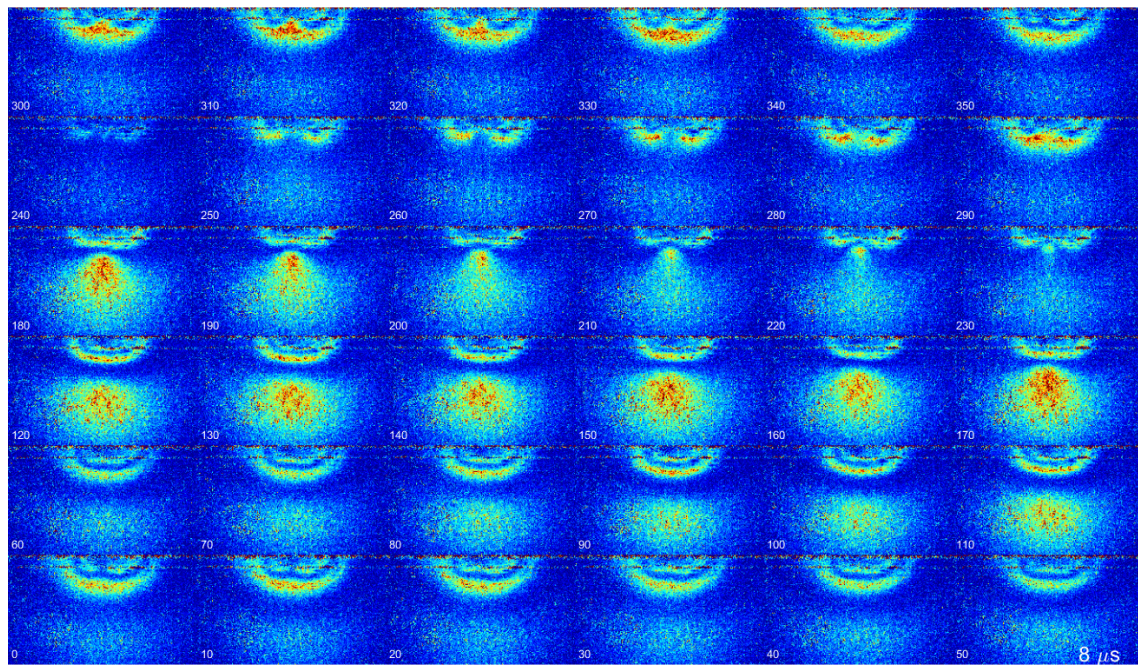


FIG. C.6: Rabi map image, using a  $8 \mu\text{s}$  pulse.

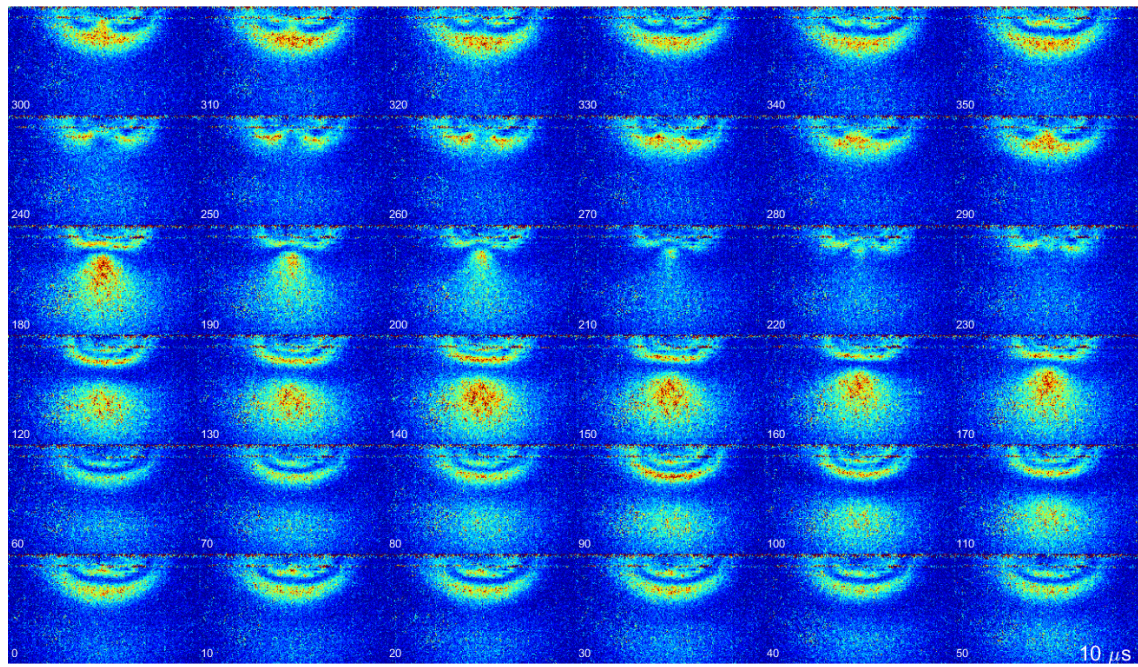


FIG. C.7: Rabi map image, using a  $10 \mu\text{s}$  pulse.

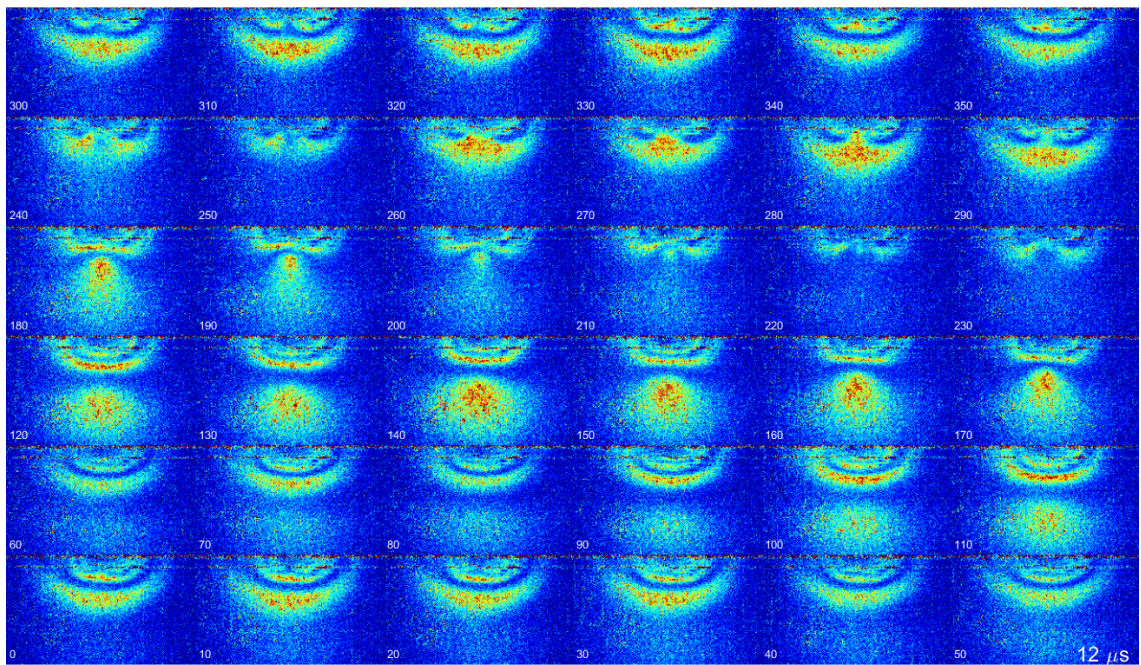


FIG. C.8: Rabi map image, using a 12  $\mu\text{s}$  pulse.

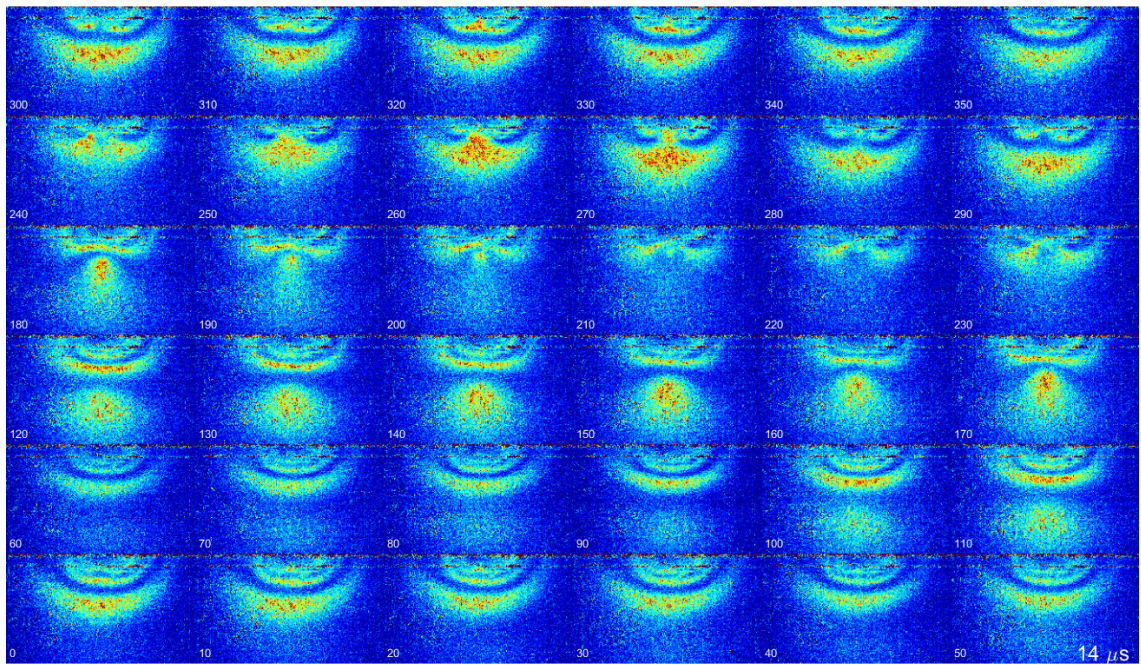


FIG. C.9: Rabi map image, using a 14  $\mu\text{s}$  pulse.

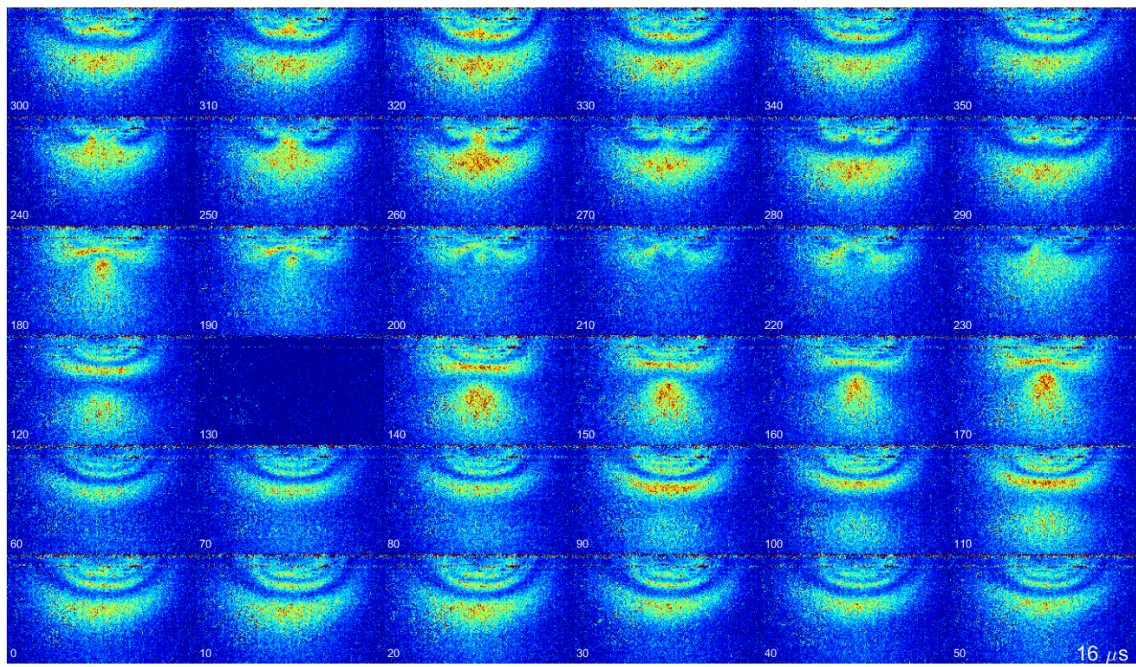


FIG. C.10: Rabi map image, using a  $16 \mu\text{s}$  pulse.

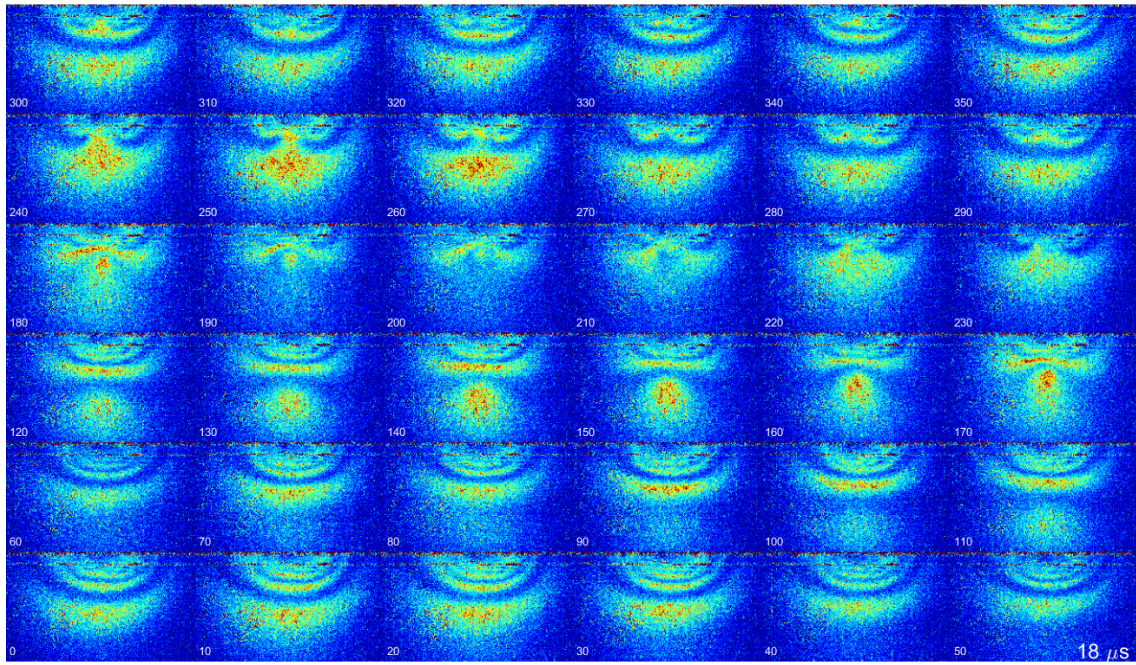


FIG. C.11: Rabi map image, using a  $18 \mu\text{s}$  pulse.

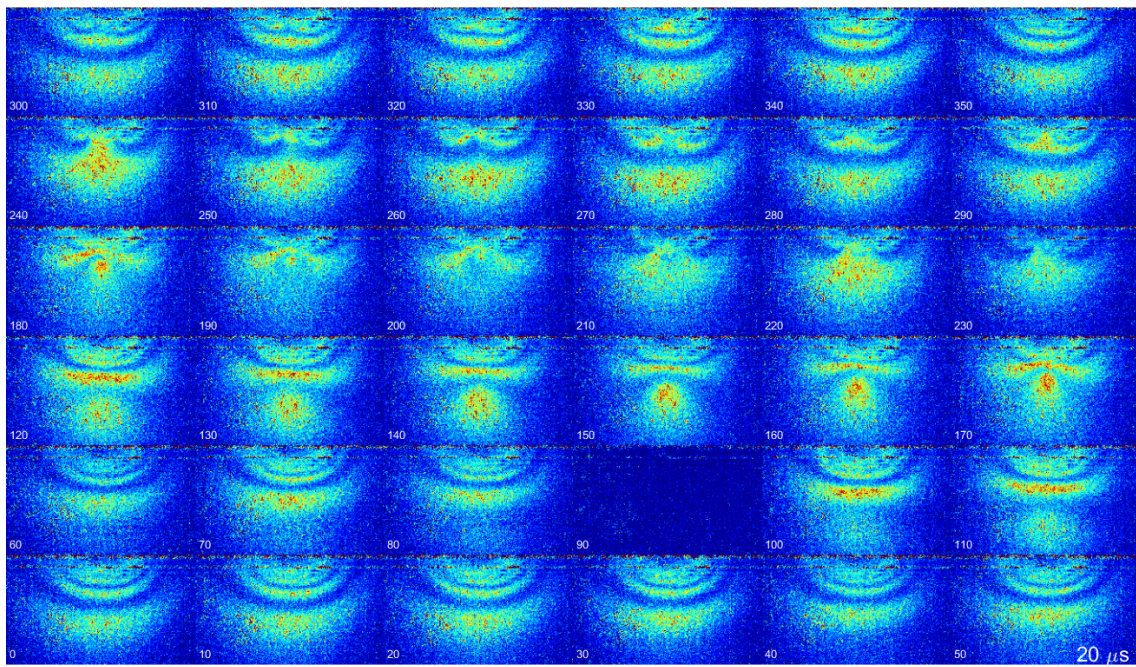


FIG. C.12: Rabi map image, using a  $20 \mu\text{s}$  pulse.

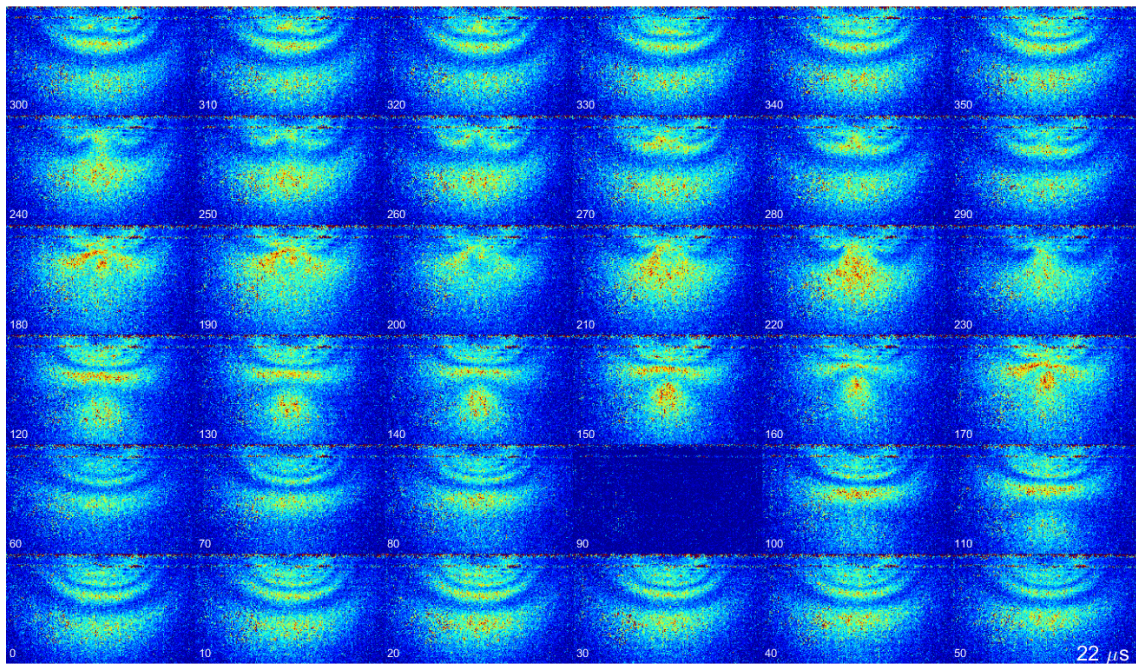


FIG. C.13: Rabi map image, using a  $22 \mu\text{s}$  pulse.

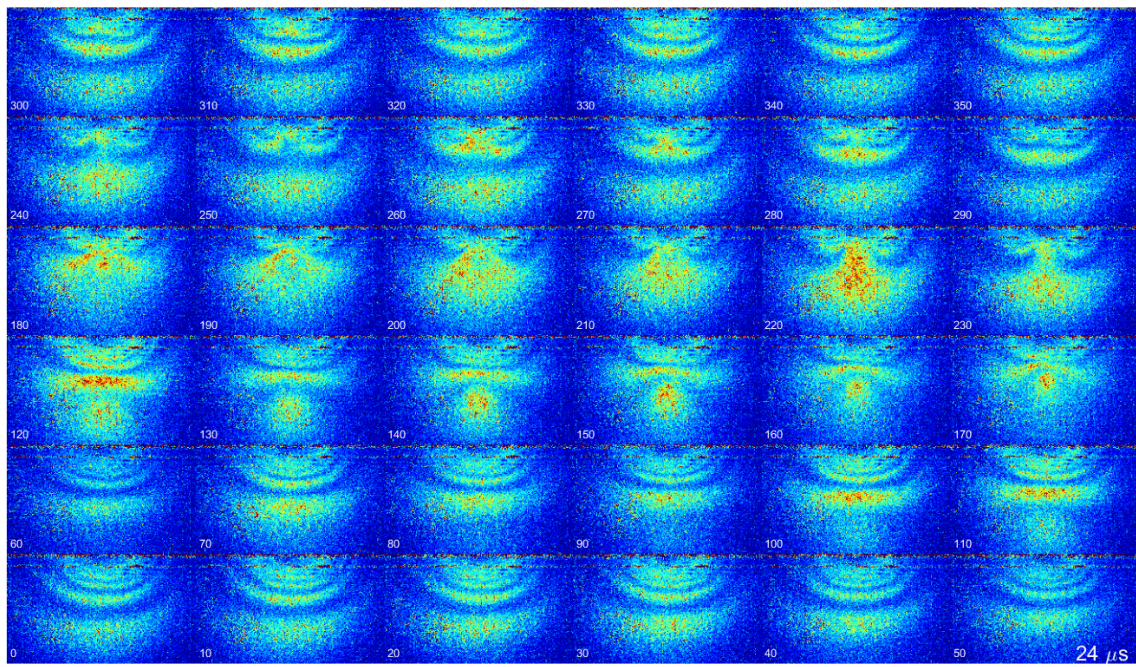


FIG. C.14: Rabi map image, using a  $24 \mu\text{s}$  pulse.

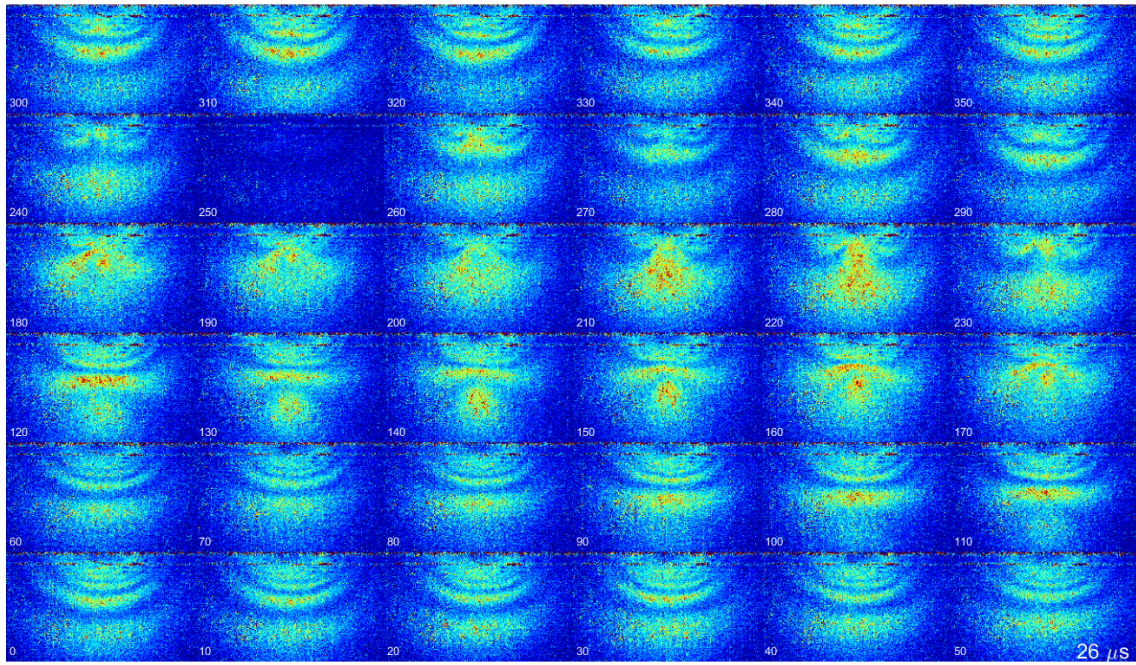


FIG. C.15: Rabi map image, using a  $26 \mu\text{s}$  pulse.

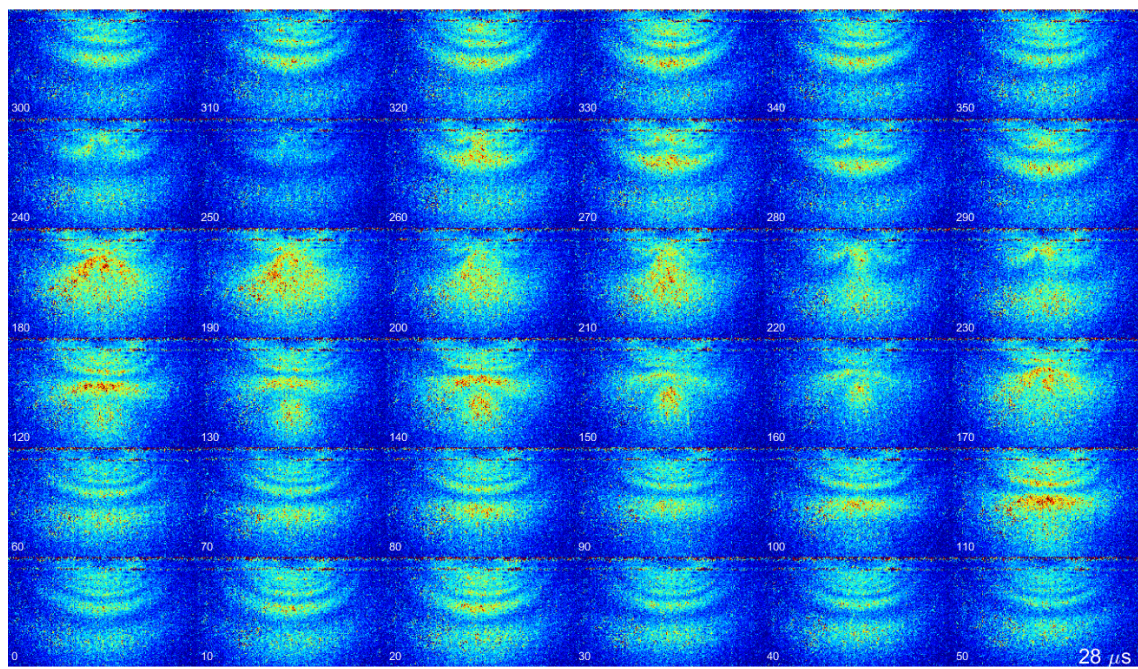


FIG. C.16: Rabi map image, using a  $28 \mu\text{s}$  pulse.

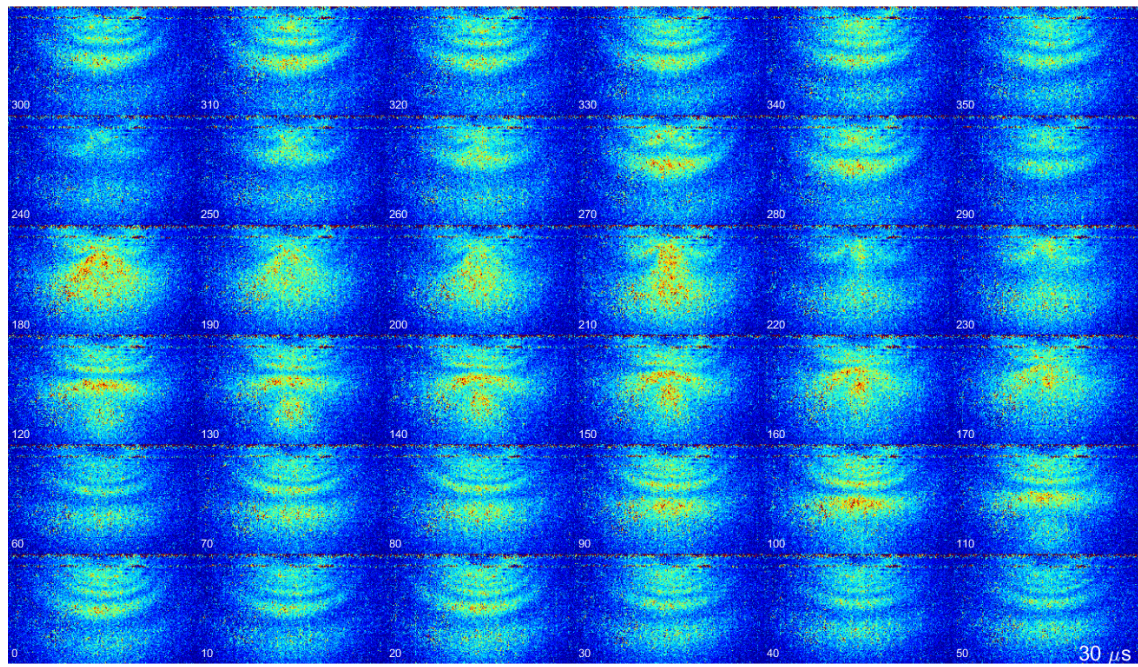


FIG. C.17: Rabi map image, using a  $30 \mu\text{s}$  pulse.

## BIBLIOGRAPHY

- [1] N. Hinkley, J. A. Sherman, N. B. Phillips, M. Schioppo, N. D. Lemke, K. Beloy, M. Pizzocaro, C. W. Oates, and A. D. Ludlow, “An atomic clock with 10–18 instability,” *Science*, vol. 341, no. 6151, pp. 1215–1218, 2013.
- [2] A. Wicht, J. M. Hensley, E. Sarajlic, and S. Chu, “A preliminary measurement of the fine structure constant based on atom interferometry,” *Physica scripta*, vol. 2002, no. T102, p. 82, 2002.
- [3] R. H. Parker, C. Yu, W. Zhong, B. Estey, and H. Müller, “Measurement of the fine-structure constant as a test of the standard model,” *Science*, vol. 360, no. 6385, pp. 191–195, 2018.
- [4] L. Morel, Z. Yao, P. Cladé, and S. Guellati-Khélifa, “Determination of the fine-structure constant with an accuracy of 81 parts per trillion,” *Nature*, vol. 588, no. 7836, pp. 61–65, 2020.
- [5] D. Hanneke, S. Fogwell, and G. Gabrielse, “New measurement of the electron magnetic moment and the fine structure constant,” *Physical Review Letters*, vol. 100, no. 12, p. 120801, 2008.
- [6] A. Peters, K. Y. Chung, and S. Chu, “High-precision gravity measurements using atom interferometry,” *Metrologia*, vol. 38, no. 1, p. 25, 2001.
- [7] J. B. Fixler, G. Foster, J. McGuirk, and M. Kasevich, “Atom interferometer measurement of the newtonian constant of gravity,” *Science*, vol. 315, no. 5808, pp. 74–77, 2007.
- [8] M. Snadden, J. McGuirk, P. Bouyer, K. Haritos, and M. Kasevich, “Measurement of the earth’s gravity gradient with an atom interferometer-based gravity gradiometer,” *Physical review letters*, vol. 81, no. 5, p. 971, 1998.
- [9] M. G. Tarallo, T. Mazzoni, N. Poli, D. Sutyrin, X. Zhang, and G. Tino, “Test of einstein equivalence principle for 0-spin and half-integer-spin atoms: search for spin-gravity coupling effects,” *Physical review letters*, vol. 113, no. 2, p. 023005, 2014.

- [10] D. Schlippert, J. Hartwig, H. Albers, L. L. Richardson, C. Schubert, A. Roura, W. P. Schleich, W. Ertmer, and E. M. Rasel, “Quantum test of the universality of free fall,” *Physical Review Letters*, vol. 112, no. 20, p. 203002, 2014.
- [11] M. Jaffe, P. Haslinger, V. Xu, P. Hamilton, A. Upadhye, B. Elder, J. Khouri, and H. Müller, “Testing sub-gravitational forces on atoms from a miniature in-vacuum source mass,” *Nature Physics*, vol. 13, no. 10, pp. 938–942, 2017.
- [12] G. Rosi, G. D’Amico, L. Cacciapuoti, F. Sorrentino, M. Prevedelli, M. Zych, Č. Brukner, and G. Tino, “Quantum test of the equivalence principle for atoms in coherent superposition of internal energy states,” *Nature communications*, vol. 8, no. 1, pp. 1–6, 2017.
- [13] V. Xu, M. Jaffe, C. D. Panda, S. L. Kristensen, L. W. Clark, and H. Müller, “Probing gravity by holding atoms for 20 seconds,” *Science*, vol. 366, no. 6466, pp. 745–749, 2019.
- [14] A. Lenef, T. D. Hammond, E. T. Smith, M. S. Chapman, R. A. Rubenstein, and D. E. Pritchard, “Rotation sensing with an atom interferometer,” *Physical review letters*, vol. 78, no. 5, p. 760, 1997.
- [15] F. Riehle, T. Kisters, A. Witte, J. Helmcke, and C. J. Bordé, “Optical ramsey spectroscopy in a rotating frame: Sagnac effect in a matter-wave interferometer,” *Physical review letters*, vol. 67, no. 2, p. 177, 1991.
- [16] T. Gustavson, P. Bouyer, and M. Kasevich, “Precision rotation measurements with an atom interferometer gyroscope,” *Physical review letters*, vol. 78, no. 11, p. 2046, 1997.
- [17] B. Canuel, F. Leduc, D. Holleville, A. Gauguet, J. Fils, A. Virdis, A. Clairon, N. Dimarcq, C. J. Bordé, A. Landragin, *et al.*, “Six-axis inertial sensor using cold-atom interferometry,” *Physical review letters*, vol. 97, no. 1, p. 010402, 2006.
- [18] J. I. Cirac and P. Zoller, “Quantum computations with cold trapped ions,” *Physical review letters*, vol. 74, no. 20, p. 4091, 1995.
- [19] D. Nigg, M. Mueller, E. A. Martinez, P. Schindler, M. Hennrich, T. Monz, M. A. Martin-Delgado, and R. Blatt, “Quantum computations on a topologically encoded qubit,” *Science*, vol. 345, no. 6194, pp. 302–305, 2014.
- [20] C. Ospelkaus, U. Warring, Y. Colombe, K. Brown, J. Amini, D. Leibfried, and D. J. Wineland, “Microwave quantum logic gates for trapped ions,” *Nature*, vol. 476, no. 7359, pp. 181–184, 2011.

- [21] T. Harty, D. Allcock, C. J. Ballance, L. Guidoni, H. Janacek, N. Linke, D. Stacey, and D. Lucas, “High-fidelity preparation, gates, memory, and read-out of a trapped-ion quantum bit,” *Physical review letters*, vol. 113, no. 22, p. 220501, 2014.
- [22] A. Rastogi, E. Saglamyurek, T. Hrushevskyi, S. Hubel, and L. J. LeBlanc, “Discerning quantum memories based on electromagnetically-induced-transparency and autler-townes-splitting protocols,” *Physical Review A*, vol. 100, no. 1, p. 012314, 2019.
- [23] J. Prodan, A. Migdall, W. D. Phillips, I. So, H. Metcalf, and J. Dalibard, “Stopping atoms with laser light,” *Physical review letters*, vol. 54, no. 10, p. 992, 1985.
- [24] M. A. Kasevich, “Coherence with atoms,” *Science*, vol. 298, no. 5597, pp. 1363–1368, 2002.
- [25] H. J. Metcalf and P. Van der Straten, “Laser cooling and trapping of neutral atoms,” *The Optics Encyclopedia: Basic Foundations and Practical Applications*, 2007.
- [26] J. Reichel, W. Hänsel, and T. Hänsch, “Atomic micromanipulation with magnetic surface traps,” *Physical Review Letters*, vol. 83, no. 17, p. 3398, 1999.
- [27] S. Leslie, J. Guzman, M. Vengalattore, J. D. Sau, M. L. Cohen, and D. Stamper-Kurn, “Amplification of fluctuations in a spinor bose-einstein condensate,” *Physical Review A*, vol. 79, no. 4, p. 043631, 2009.
- [28] K. B. Davis, M.-O. Mewes, M. R. Andrews, N. J. van Druten, D. S. Durfee, D. Kurn, and W. Ketterle, “Bose-einstein condensation in a gas of sodium atoms,” *Physical review letters*, vol. 75, no. 22, p. 3969, 1995.
- [29] M. W. Zwierlein, C. A. Stan, C. H. Schunck, S. M. Raupach, S. Gupta, Z. Hadzibabic, and W. Ketterle, “Observation of bose-einstein condensation of molecules,” *Physical review letters*, vol. 91, no. 25, p. 250401, 2003.
- [30] J. Ensher, D. S. Jin, M. Matthews, C. Wieman, and E. A. Cornell, “Bose-einstein condensation in a dilute gas: Measurement of energy and ground-state occupation,” *Physical Review Letters*, vol. 77, no. 25, p. 4984, 1996.
- [31] J. R. Anglin and W. Ketterle, “Bose-einstein condensation of atomic gases,” *Nature*, vol. 416, no. 6877, pp. 211–218, 2002.

- [32] R. Folman, P. Kruger, J. Schmiedmayer, J. Denschlag, and C. Henkel, “Microscopic atom optics: from wires to an atom chip,” *arXiv preprint arXiv:0805.2613*, 2008.
- [33] M. F. Riedel, P. Böhi, Y. Li, T. W. Hänsch, A. Sinatra, and P. Treutlein, “Atom-chip-based generation of entanglement for quantum metrology,” *Nature*, vol. 464, no. 7292, pp. 1170–1173, 2010.
- [34] T. Schumm, S. Hofferberth, L. M. Andersson, S. Wildermuth, S. Groth, I. Bar-Joseph, J. Schmiedmayer, and P. Krüger, “Matter-wave interferometry in a double well on an atom chip,” *Nature physics*, vol. 1, no. 1, pp. 57–62, 2005.
- [35] S. Du, M. B. Squires, Y. Imai, L. Czaia, R. A. Saravanan, V. Bright, J. Reichel, T. Hänsch, and D. Z. Anderson, “Atom-chip bose-einstein condensation in a portable vacuum cell,” *Physical Review A*, vol. 70, no. 5, p. 053606, 2004.
- [36] S. Schneider, A. Kasper, C. Vom Hagen, M. Bartenstein, B. Engeser, T. Schumm, I. Bar-Joseph, R. Folman, L. Feenstra, and J. Schmiedmayer, “Bose-einstein condensation in a simple microtrap,” *Physical Review A*, vol. 67, no. 2, p. 023612, 2003.
- [37] C. Sackett, “Limits on weak magnetic confinement of neutral atoms,” *Physical Review A*, vol. 73, no. 1, p. 013626, 2006.
- [38] M. Bloom and K. Erdman, “The transverse stern–gerlach experiment,” *Canadian Journal of Physics*, vol. 40, no. 2, pp. 179–193, 1962.
- [39] M. Bloom, E. Enga, and H. Lew, “Observation of the transverse stern–gerlach effect in neutral potassium,” *Canadian Journal of Physics*, vol. 45, no. 4, pp. 1481–1495, 1967.
- [40] C. C. Agosta, I. F. Silvera, H. T. C. Stoof, and B. J. Verhaar, “Trapping of neutral atoms with resonant microwave radiation,” *Physical review letters*, vol. 62, no. 20, p. 2361, 1989.
- [41] R. J. Spreeuw, C. Gerz, L. S. Goldner, W. D. Phillips, S. Rolston, C. Westbrook, M. Reynolds, and I. F. Silvera, “Demonstration of neutral atom trapping with microwaves,” *Physical review letters*, vol. 72, no. 20, p. 3162, 1994.
- [42] P. Böhi, M. F. Riedel, J. Hoffrogge, J. Reichel, T. W. Hänsch, and P. Treutlein, “Coherent manipulation of bose–einstein condensates with state-dependent microwave potentials on an atom chip,” *Nature Physics*, vol. 5, no. 8, pp. 592–597, 2009.

- [43] C. Xin-zhao, L. Shu-qin, and D. Tai-qian, “Experimental study of ac zeeman effect in 87rb atomic frequency standard,” *Acta Physica Sinica (Overseas Edition)*, vol. 5, no. 6, p. 423, 1996.
- [44] C. Fancher, A. Pyle, A. Rotunno, and S. Aubin, “Microwave ac zeeman force for ultracold atoms,” *Phys. Rev. A*, vol. 97, no. 4, p. 043430, 2018.
- [45] S. Du and S. Aubin, “Suppression of potential roughness in atom chip ac zeeman traps,” 2021.
- [46] A. D. Cronin, J. Schmiedmayer, and D. E. Pritchard, “Optics and interferometry with atoms and molecules,” *Reviews of Modern Physics*, vol. 81, no. 3, p. 1051, 2009.
- [47] O. Garcia, B. Deissler, K. Hughes, J. Reeves, and C. Sackett, “Bose-einstein-condensate interferometer with macroscopic arm separation,” *Physical Review A*, vol. 74, no. 3, p. 031601, 2006.
- [48] E. Moan, R. Horne, T. Arporntip, Z. Luo, A. Fallon, S. Berl, and C. Sackett, “Quantum rotation sensing with dual sagnac interferometers in an atom-optical waveguide,” *Physical review letters*, vol. 124, no. 12, p. 120403, 2020.
- [49] B. Barrett, P. Cheiney, B. Battelier, F. Napolitano, and P. Bouyer, “Multidimensional atom optics and interferometry,” *Physical review letters*, vol. 122, no. 4, p. 043604, 2019.
- [50] M. Zimmermann, M. A. Efremov, W. Zeller, W. P. Schleich, J. P. Davis, and F. A. Narducci, “Representation-free description of atom interferometers in time-dependent linear potentials,” *New Journal of Physics*, vol. 21, no. 7, p. 073031, 2019.
- [51] M. Ammar, M. Dupont-Nivet, L. Huet, J.-P. Pocholle, P. Rosenbusch, I. Boucchoule, C. I. Westbrook, J. Estève, J. Reichel, C. Guerlin, *et al.*, “Symmetric microwave potentials for interferometry with thermal atoms on a chip,” *Physical Review A*, vol. 91, no. 5, p. 053623, 2015.
- [52] M. Dupont-Nivet, C. I. Westbrook, and S. Schwartz, “Effect of trap symmetry and atom-atom interactions on a trapped-atom interferometer with internal state labeling,” *Physical Review A*, vol. 103, no. 2, p. 023321, 2021.
- [53] V. Ivannikov and A. I. Sidorov, “Phase diffusion in trapped-atom interferometers,” *Journal of Physics B: Atomic, Molecular and Optical Physics*, vol. 51, no. 20, p. 205002, 2018.

- [54] N. Lundblad, D. Trypogeorgos, A. Valdes-Curiel, E. Marshall, and I. Spielman, “Synthetic clock states generated in a bose-einstein condensate via continuous dynamical decoupling,” in *APS Division of Atomic, Molecular and Optical Physics Meeting Abstracts*, vol. 2017, pp. K1–122, 2017.
- [55] I. Kruse, K. Lange, J. Peise, B. Lücke, L. Pezzè, J. Arlt, W. Ertmer, C. Lisdat, L. Santos, A. Smerzi, *et al.*, “Improvement of an atomic clock using squeezed vacuum,” *Physical review letters*, vol. 117, no. 14, p. 143004, 2016.
- [56] S. Jenkins, T. Zhang, and T. Kennedy, “Motional dephasing of atomic clock spin waves in an optical lattice,” *Journal of Physics B: Atomic, Molecular and Optical Physics*, vol. 45, no. 12, p. 124005, 2012.
- [57] G. Roati, E. De Mirandes, F. Ferlaino, H. Ott, G. Modugno, and M. Inguscio, “Atom interferometry with trapped fermi gases,” *Physical Review Letters*, vol. 92, no. 23, p. 230402, 2004.
- [58] K. Frye, S. Abend, W. Bartosch, A. Bawamia, D. Becker, H. Blume, C. Braxmaier, S.-W. Chiow, M. A. Efremov, W. Ertmer, *et al.*, “The bose-einstein condensate and cold atom laboratory,” *EPJ Quantum Technology*, vol. 8, no. 1, pp. 1–38, 2021.
- [59] A. J. Pyle, *Scattering of a Bose-Einstein Condensate off a Modulated Barrier*. PhD thesis, College of William and Mary, 2016.
- [60] C. T. Fancher, *AC Zeeman Force with Ultracold Atoms*. PhD thesis, College of William and Mary, 2016.
- [61] A. R. Ziltz, *Ultracold rubidium and potassium system for atom chip-based microwave and RF potentials*. PhD thesis, College of William and Mary, 2015.
- [62] M. K. Ivory, *Experimental Apparatus for Quantum Pumping with a Bose-Einstein Condensate*. PhD thesis, College of William and Mary, 2016.
- [63] D. A. Steck, “Rubidium 87 d line data,” 2001.
- [64] H. Perrin and B. M. Garraway, “Trapping atoms with radio frequency adiabatic potentials,” *Advances in Atomic, Molecular, and Optical Physics*, vol. 66, pp. 181–262, 2017.
- [65] N. Lundblad, R. Carollo, C. Lannert, M. Gold, X. Jiang, D. Paseltiner, N. Sergay, and D. Aveline, “Shell potentials for microgravity bose-einstein condensates,” *npj Microgravity*, vol. 5, no. 1, pp. 1–6, 2019.

- [66] O. Zobay and B. Garraway, “Two-dimensional atom trapping in field-induced adiabatic potentials,” *Physical review letters*, vol. 86, no. 7, p. 1195, 2001.
- [67] G. Breit and I. Rabi, “Measurement of nuclear spin,” *Physical Review*, vol. 38, no. 11, p. 2082, 1931.
- [68] I. I. Rabi, “Space quantization in a gyrating magnetic field,” *Physical Review*, vol. 51, no. 8, p. 652, 1937.
- [69] M. Bloom, “B loom, m yer: Personal views of nmr history,” *eMagRes*, 2007.
- [70] F. Bloch and A. Siegert, “Magnetic resonance for nonrotating fields,” *Physical Review*, vol. 57, no. 6, p. 522, 1940.
- [71] C. Wei, A. S. Windsor, and N. B. Manson, “A strongly driven two-level atom revisited: Bloch-siegert shift versus dynamic stark splitting,” *Journal of Physics B: Atomic, Molecular and Optical Physics*, vol. 30, no. 21, p. 4877, 1997.
- [72] Z. Lü and H. Zheng, “Effects of counter-rotating interaction on driven tunneling dynamics: Coherent destruction of tunneling and bloch-siegert shift,” *Physical Review A*, vol. 86, no. 2, p. 023831, 2012.
- [73] M. Matthews, B. P. Anderson, P. Haljan, D. Hall, M. Holland, J. Williams, C. Wieman, and E. Cornell, “Watching a superfluid untwist itself: Recurrence of rabi oscillations in a bose-einstein condensate,” *Physical review letters*, vol. 83, no. 17, p. 3358, 1999.
- [74] C. Menotti, A. Smerzi, and A. Trombettoni, “Superfluid dynamics of a bose-einstein condensate in a periodic potential,” *New Journal of Physics*, vol. 5, no. 1, p. 112, 2003.
- [75] V. Galitski and I. B. Spielman, “Spin-orbit coupling in quantum gases,” *Nature*, vol. 494, no. 7435, pp. 49–54, 2013.
- [76] S. Inouye, M. Andrews, J. Stenger, H.-J. Miesner, D. M. Stamper-Kurn, and W. Ketterle, “Observation of feshbach resonances in a bose-einstein condensate,” *Nature*, vol. 392, no. 6672, pp. 151–154, 1998.
- [77] P. Courteille, R. Freeland, D. Heinzen, F. Van Abeelen, and B. Verhaar, “Observation of a feshbach resonance in cold atom scattering,” *Physical Review Letters*, vol. 81, no. 1, p. 69, 1998.

- [78] B. M. Garraway and H. Perrin, “Recent developments in trapping and manipulation of atoms with adiabatic potentials,” *Journal of Physics B: Atomic, Molecular and Optical Physics*, vol. 49, no. 17, p. 172001, 2016.
- [79] A. E. Blackwell, A. P. Rotunno, and S. Aubin, “Demonstration of the lateral ac skin effect using a pickup coil,” *American Journal of Physics*, vol. 88, no. 8, pp. 676–684, 2020.
- [80] W. Miyahira, A. Rotunno, S. Du, and S. Aubin, “Microwave atom chip design.” in preparation.
- [81] M. Ivory, A. Ziltz, C. Fancher, A. Pyle, A. Sensharma, B. Chase, J. Field, A. Garcia, D. Jervis, and S. Aubin, “Atom chip apparatus for experiments with ultracold rubidium and potassium gases,” *Rev. Sci. Instrum.*, vol. 85, no. 4, p. 043102, 2014.
- [82] P. Böhi, M. F. Riedel, T. W. Hänsch, and P. Treutlein, “Imaging of microwave fields using ultracold atoms,” *Applied Physics Letters*, vol. 97, no. 5, p. 051101, 2010.
- [83] W. Ketterle and N. Van Druten, “Evaporative cooling of trapped atoms,” *Advances in atomic, molecular, and optical physics*, vol. 37, pp. 181–236, 1996.
- [84] P. Silvester. Englewood Cliffs, N.J.: Prentice Hall, 1968.
- [85] T. J. Higgins, “The origins and developments of the concepts of inductance, skin effect and proximity effect,” *Am. J. Phys.*, vol. 9, no. 6, pp. 337–346, 1941.
- [86] H. Casimir and J. Ubbink *Philips Tech. Rev.*, vol. 28, p. 271, 1967.
- [87] J. C. Maxwell. Oxford: Oxford University Press, 1873.
- [88] J. J. Thomson. Oxford: Clarendon Press, 1893.
- [89] O. Heaviside *The Electrician*, vol. 17, p. 88, 1886.
- [90] J. W. Strutt *Phil. Mag.*, vol. 21, p. 381, 1886.
- [91] W. Thomson. London: Clay, 1890.
- [92] E. Rutherford *Trans. New Zealand Insti.*, vol. 27, p. 481, 1894.
- [93] P. Silvester *IEEE Trans. Power Apparatus and Systems*, vol. 87, p. 735, 1968.

- [94] P. Sylvester *Proc. IEEE*, vol. 54, p. 1147, 1966.
- [95] P. Sylvester *IEEE Trans. Power Apparatus and Systems*, vol. 86, p. 770, 1967.
- [96] P. Sylvester *IEEE Trans. Power Apparatus and Systems*, vol. 86, p. 241, 1967.
- [97] G. Antonini, A. Orlandi, and C. R. Paul, “Internal impedance of conductors of rectangular cross section,” *IEEE Trans. Microw. Theory Techn.*, vol. 47, no. 7, pp. 979–985, 1999.
- [98] T. Vu Dinh, B. Cabon, and J. Chilo, “New skin-effect equivalent circuit,” *Electron. Lett.*, vol. 26, no. 19, pp. 1582–1584, 1990.
- [99] S. Mei and Y. I. Ismail, “Modeling skin and proximity effects with reduced realizable rl circuits,” *IEEE Trans. VLSI sys.*, vol. 12, no. 4, pp. 437–447, 2004.
- [100] R. Faraji-Dana and Y. Chow *IEE Proceedings*, vol. 137, p. 133, 1990.
- [101] D. Kajfez, J. Guo, and A. W. Glisson *Microw. Opt. Technol. Lett.*, vol. 20, p. 272, 1999.
- [102] J. Guo, D. Kajfez, and A. W. Glisson *Electron. Lett.*, vol. 33, p. 966, 1997.
- [103] M. Vitelli *IEEE Trans. Electromagn. Compat.*, vol. 44, p. 529, 2002.
- [104] M. Matsuki and A. Matsushima *Prog. Electromagn. Res. M*, vol. 23, p. 139, 2012.
- [105] R. Faraji-Dana and Y. L. Chow, “The current distribution and ac resistance of a microstrip structure,” *IEEE Trans. Microw. Theory Techn.*, vol. 38, no. 9, pp. 1268–1277, 1990.
- [106] V. Belevitch *Philips Res. Rep.*, vol. 31, pp. 199–215, 1976.
- [107] V. Belevitch *Philips Tech. Rev.*, vol. 32, pp. 221–231, 1971.
- [108] G. S. Smith, “On the skin effect approximation,” *Am. J. Phys.*, vol. 58, no. 10, pp. 996–1002, 1990.
- [109] N. Gauthier, “Explaining the skin effect simply, with  $v = ri + l(d i/dt)$ ,” *Am. J. Phys.*, vol. 54, no. 7, pp. 649–650, 1986.

- [110] D. Gerling, “Approximate analytical calculation of the skin effect in rectangular wires,” in *Int. Conf. Electr. Mach. Sys., ICEMS 2009.*, pp. 1–6, IEEE, 2009.
- [111] V. Belevitch, P. Gueret, and J. C. Lienard *Rev HF*, vol. 5, pp. 109–115, 1962.
- [112] G. S. Smith, “A simple derivation for the skin effect in a round wire,” *Eur. J. of Phys.*, vol. 35, no. 2, p. 025002, 2014.
- [113] J. MacDougall, “An experiment on skin effect,” *Am. J. Phys.*, vol. 44, no. 10, pp. 978–980, 1976.
- [114] P. Böhi, M. F. Riedel, T. W. Hänsch, and P. Treutlein, “Imaging of microwave fields using ultracold atoms,” *App. Phys. Lett.*, vol. 97, no. 5, p. 051101, 2010.
- [115] H. Tsuboi and K. Kunisue, “Eddy current analysis of thin plates taking account of the source current distributions and its experimental verifications,” *IEEE transactions on magnetics*, vol. 27, no. 5, pp. 4020–4023, 1991.
- [116] T. H. Petersen, K. H. Carpenter, and C. M. May, “Comparison of experimental measurements of current distribution in a flat conductor with simulated results from the partial inductance method,” *IEEE Trans. Electromagn. Compat.*, vol. 51, no. 2, pp. 345–350, 2009.
- [117] M. Kosek, M. Truhlar, and A. Richter, “Skin effect in massive conductors at technical frequencies,” *Przeglad Elektrotechniczny (Electrical Review)*, vol. 5, pp. 179–185, 2011.
- [118] M. Kosek, M. Truhlar, and A. Richter, “Skin effect in conductor of rectangular cross-section—approximate solution,” *Przegl AD Elektrotechniczny (Electrical Review)*, vol. 88, pp. 23–25, 2012.
- [119] I. Manke, N. Kardjilov, M. Strobl, A. Hilger, and J. Banhart *J. Appl. Phys.*, vol. 104, p. 076109, 2008.
- [120] A. J. Ilott, S. Chandrashekhar, A. Kloeckner, H. J. Chang, N. M. Trease, C. P. Grey, L. Greengard, and A. Jerschow, “Visualizing skin effects in conductors with mri: 7li mri experiments and calculations,” *Journal of Magnetic Resonance*, vol. 245, pp. 143–149, 2014.
- [121] J. Wagner and M. Syed, “Investigation of skin effect in mercury using a simple solenoid setup,” *Am. J. Phys.*, vol. 79, no. 8, pp. 850–855, 2011.

- [122] H. B. Dwight, “Skin effect in tubular and flat conductors,” *Transactions of the American Institute of Electrical Engineers*, vol. 37, no. 2, pp. 1379–1403, 1918.
- [123] D. R. Lide, *CRC handbook of chemistry and physics*, vol. 79. CRC press, 1998.
- [124] Z. Popovic and B. Popovic, *Introductory electromagnetics*. Prentice Hall, 2000.
- [125] A. Zangwill, *Modern Electrodynamics*. Cambridge University Press, 2013.
- [126] S. Hofferberth, B. Fischer, T. Schumm, J. Schmiedmayer, and I. Lesanovsky, “Ultracold atoms in radio-frequency dressed potentials beyond the rotating-wave approximation,” *Physical Review A*, vol. 76, no. 1, p. 013401, 2007.
- [127] T. R. Gentile, B. J. Hughey, D. Kleppner, and T. W. Ducas, “Experimental study of one-and two-photon rabi oscillations,” *Physical Review A*, vol. 40, no. 9, p. 5103, 1989.
- [128] A. Duspayev and G. Raithel, “Tractor atom interferometry,” *arXiv preprint arXiv:2103.05071*, 2021.
- [129] U. Warring, C. Ospelkaus, Y. Colombe, R. Jördens, D. Leibfried, and D. J. Wineland, “Individual-ion addressing with microwave field gradients,” *Physical review letters*, vol. 110, no. 17, p. 173002, 2013.
- [130] G. Zarantonello, H. Hahn, J. Morgner, M. Schulte, A. Bautista-Salvador, R. Werner, K. Hammerer, and C. Ospelkaus, “Robust and resource-efficient microwave near-field entangling be+ 9 gate,” *Physical review letters*, vol. 123, no. 26, p. 260503, 2019.
- [131] H. Hahn, G. Zarantonello, M. Schulte, A. Bautista-Salvador, K. Hammerer, and C. Ospelkaus, “Integrated 9 be+ multi-qubit gate device for the ion-trap quantum computer,” *npj Quantum Information*, vol. 5, no. 1, pp. 1–5, 2019.
- [132] Z. D. Romaszko, S. Hong, M. Siegele, R. K. Puddy, F. R. Lebrun-Gallagher, S. Weidt, and W. K. Hensinger, “Engineering of microfabricated ion traps and integration of advanced on-chip features,” *Nature Reviews Physics*, vol. 2, no. 6, pp. 285–299, 2020.
- [133] C. Lewelling, “Electromagnetic simulations of microwave trapping structures,” *Bachelor of Science Thesis, William and Mary*, 2018.
- [134] K. Sullivan, *Simulation and Prototype Construction of Microwave Atom Chip Components*. PhD thesis, College of William and Mary, 2019.

- [135] A. Bertoldi, F. Minardi, and M. Prevedelli, “Phase shift in atom interferometers: Corrections for nonquadratic potentials and finite-duration laser pulses,” *Physical Review A*, vol. 99, no. 3, p. 033619, 2019.
- [136] G. A. Sinuco-León, K. A. Burrows, A. S. Arnold, and B. M. Garraway, “Inductively guided circuits for ultracold dressed atoms,” *Nature communications*, vol. 5, no. 1, pp. 1–7, 2014.
- [137] S. K. Goyal, B. N. Simon, R. Singh, and S. Simon, “Geometry of the generalized bloch sphere for qutrits,” *Journal of Physics A: Mathematical and Theoretical*, vol. 49, no. 16, p. 165203, 2016.

## VITA

### Andrew Peter Rotunno

Drew Rotunno was born in 1992 in Syracuse, NY, and lived in the suburb Liverpool for 20 years. His first job was delivering newspapers, before spending 5 years employed as a maintenance worker at a church. He attended grade school within walking distance, and later drove across town to attend Christian Brothers Academy, where an exceptional science department fostered his interest and abilities in the sciences. He went to Fordham University in the Bronx, NY, where he served as president of the Fordham Experimental Theatre club, and took extra classes in philosophy. His physics pursuits during college include digital holography in Dr. Stephen Holler's lab at Fordham, and developing an ion neutralizing system under Dr. Itzik Ben-Itzhak at Kansas State. He went on to become a graduate student at William & Mary, making some of Seth Aubin's ideas come to life, adding some of his own, and fabricating a number of personal projects in the Small Hall Makerspace. Pending this defense, he will research Rydberg atoms as calibrated RF sensors as a postdoc researcher in Chris Holloway's lab at NIST. Drew, his wife Sarah, and their three rabbits ('the boys') will move to Boulder, CO this summer.